Institute of Aeronautics and Astronautics: Scientific Series Band 12

Hrsg./Eds.: Robert Luckner, Dieter Peitsch, Andreas Bardenhagen, Klaus Brieß, Julien Weiss

Merlin F. Barschke

Systems architecture of a modular microsatellite family

ISSN (online) 2512-515X

Technische Universität Berlin

Systems Architecture of a Modular Microsatellite Family

vorgelegt von

M. Sc.
Merlin F. Barschke
ORCID: 0000-0001-5552-0984

an der Fakultät V – Verkehrs- und Maschinensysteme
der Technischen Universität Berlin
zur Erlangung des akademischen Grades

Doktor der Ingenieurwissenschaften
Dr.-Ing.

genehmigte Dissertation

Promotionsausschuss:

Vorsitzender: Prof. Dr. ir. Maarten Uijt de Haag
Gutachter: Prof. Dr.-Ing. Klaus Brieß
Gutachter: Prof. Dr.-Ing. Stefanos Fasoulas

Tag der wissenschaftlichen Aussprache: 25. Oktober 2022

Berlin 2023

Contents

List of Figures

List of Tables

Glossary

Availability

Measure of the fraction of time a system is operating according to the specification [1]. 25, 26, 28

BEESAT series

CubeSat series of Technische Universität Berlin [2]. Currently, spacecraft in the range of 0.25 U to 2 U are based on the BEESAT series. 5, 64, 240

Board support package (BSP)

Software layer used in embedded systems that contains the hardware-specific code. 64

Cold redundancy

One or several spare units of a device that are switched off in nominal operations to replace the primary unit in case of a failure [3]. 67, 69, 77, 79, 96, 190

Consultative Committee for Space Data Systems (CCSDS)

A multi-national forum for the development of communications and data systems standards for spaceflight.. 58, 60

Control area network (CAN)

Multi-master serial bus standard defining a message based protocol for inter-device communication [4]. 69, 74, 77

Control moment gyroscope (CMG)

Attitude actuator consisting of a spinning mass whose angular momentum can be tilted by one or more gimbals to create a gyroscopic torque. 56

CubeSat

Satellite form factor based on a number of cuboids with an edge length of 10 cm, called "U" [5, 6]. 1–5, 8–10, 13–16, 18, 19, 22–24, 29, 37, 51, 58, 59, 69, 71, 135, 136, 151, 171, 175, 187, 189, 191, 242

Depth of discharge (DoD)

Parameter for battery dimensioning, which indicates the maximum fraction of the total battery capacity that will actually be used by the spacecraft. 52, 53, 165, 166, 183, 184, 186

Direct energy transfer (DET)

Power system topology that implements no active elements between solar arrays the load [7]. 38

Diverse redundancy

Technique to improve the reliability of a system by the implementation of two or more diverse components to execute the same task [8]. 28

Duplicating redundancy

Technique to improve the reliability of a system by the implementation of two or more instances of the same component [8]. 28

Error

A part of a system's state that can lead to a failure of the system [1]. 26–28

Ethernet

Specification of hardware and protocols for the data transmission within cable connected networks. 70, 78, 96, 153, 155, 159, 160, 163

Failure

The delivery of a service that is not according to the specification [1]. 25–28

Fault

The cause of a latent error in a system [1]. 26–28

Fault avoidance

Measures applied to avoid faults from manifesting in a system [1]. 27

Fault tolerance

A systems ability to continue its service according to the specification despite the occurrence of one or several faults [1]. 27, 34, 69, 74, 96

Fluid-dynamic actuator (FDA)

Attitude actuator using a magnetic fluid that is circulated in a ring-shaped tube to create an angular momentum [9]. Demonstrated in orbit for the first time within the TechnoSat mission [10, 11]. 56, 58, 103, 108

Generational platform

A platform targeting at updating the product between variants. 25

HiSPiCO

S-band transmitter developed by IQ wireless GmbH from Berlin, Germany together with Technische Universität Berlin [12]. Demonstrated in orbit within the TechnoSat mission [13]. 104, 252

Hot redundancy

Two or more devices that perform the same task in such a manner that the operation is not disrupted if one unit is lost [3]. 53, 69, 74, 77, 96, 106, 190

Inter-integrated circuit (I2C)

Serial data bus that was developed for the communication between different ICs [14]. 69, 76, 77

Ka band

Frequency range from 27 to 40 GHz, which is commonly used for satellite communications or radar applications (33.4 to 36 GHz) [15]. 11

Kelly cosine

Power-angle curve for solar cells that deviates from the mathematical prediction for values above 50 degrees illumination angle [16]. 47, 124

Logical node

Describes a TUBiX20 node according to its function and regardless of which physical node is active. 68

Maximum power point tracking (MPPT)

Power generation mode in which a solar panel's voltage is constantly adjusted to guarantee the maximum power output. The MPPT technique is also referred to as Peak power tracking (PPT) [7]. 38–40, 43–45, 47, 49, 50, 115, 172, 180, 182, 183, 185, 191

Microsatellite

A satellite, which is characterised by a launch mass that is between 10 and 100 kg [17]. 2–4, 7, 14, 23, 190

Modular platform

A platform that supports adding or removing capabilities to form different variants of a product. 25

Multi-layer insulation (MLI)

Thermal insulation material composed by a variable number of thin metallised synthetic films. 32

Nanosatellite

A satellite, which is characterised by a launch mass that is between 1 and 10 kg [17]. 2, 7, 105

OSIRIS

Optical data transmission terminal developed by the German Aerospace Center (DLR) [18]. 171, 174

Peak power tracking (PPT)

Power generation mode that adjusts the output voltage of a solar array such that the panel is always generating the maximum possible power [7]. The PPT technique is also referred to as maximum power point tracking (MPPT). 38, 48

Physical node

One of the two processing units of a logical node within the TUBiX20 platform. 68, 93

Product platform

"A product platform is a set of subsystems and interfaces that form a common structure from which a stream of derivative products can be efficiently developed and produced" [19]. 20

QUEEN mission

Microsatellite mission of Technische Universität Berlin implemented in cooperation with of Humboldt-Universität zu Berlin and the Ferdinand-Braun-Institut, Leibniz-Institut für Höchstfrequenztechnik (FBH) to demonstrate an optical Rb frequency reference payload and advanced small satellite platform technology in orbit [20, 21]. 5, 6, 30, 32, 101, 169–172, 174–177, 180–182, 184, 186, 187, 189–191, 240

Reliability

Measure of the likelihood for a given system to continuously perform according to specification for a defined duration of time [1]. 25–28

S band

Frequency range from 2 to 4 GHz, which is commonly used for satellite communications [15]. 20, 58–60, 96, 104, 105, 108, 125, 126, 130, 131, 133, 140, 160, 163, 171, 172, 174, 182, 252, 253

Scalable platform

A platform that allows for adjusting certain performance parameters of the system. 24

Single event effect (SEE)

Fault in an electronic component caused by a single ionising particle interaction [22]. 111

Single event latchup (SEL)

Radiation induced high current condition that may damage an electronic circuit [16]. 111

Single event upset (SEU)

Radiation induced change in the state of a memory cell (bit-flip) [16]. 111

Solar generator based Impact Detector (SOLID)

Novel detector concept developed by the Institute of Space Systems of the German Aerospace Center (DLR) in Bremen, Germany. It uses the solar arrays of a satellite as sensor areas to detect impacts of particles larger than 100 µm [23–25]. Demonstrated in orbit for the first time within the TechnoSat mission. 105, 108

STELLA

S tar tracker designed for nanosatellite applications by the University Würzburg, Germany [26, 27]. Was integrated as payload on the TechnoSat mission [13]. 105

TechnoSat mission

In-orbit demonstration mission of Technische Universität Berlin carrying seven technology payloads [28]. TechnoSat launched in 2017 and is the first mission to implement the TUBiX20 platform [13, 28]. 5, 6, 30, 36, 38, 49, 52, 55, 56, 58, 59, 62, 65, 73, 75, 77, 94, 101–106, 108–111, 114, 115, 120, 127–131, 133, 135–139, 141, 155, 156, 161, 163–165, 172, 174–176, 179, 180, 182, 185, 187, 189–191, 240

Time-triggered CAN (TTCAN)

Higher level protocol layer for the CAN bus that enables real-time communications [29]. 74

Total ionising dose (TID)

Energy deposited by charged particles per mass for a specific material quantified in Gray or rad [22]. 30, 110, 111, 114, 190, 191

Triple modular redundancy

Technique to improve the reliability of a system by triplicating modules within the system, which are to be operated in hot redundancy and allow for majority voting [30, 31]. 27

TUBIN mission

Microsatellite Earth observation mission targeting the detection of wildfires with a payload implementing two infrared microbolometer cameras and one imager for the visible spectrum [32]. 5–7, 30, 33, 36, 38, 49, 53, 55, 59, 60, 62, 64, 65, 73, 75, 77, 83, 94, 101, 105, 139–143, 147, 148, 150, 152, 156–161, 163–165, 167, 168, 171, 172, 174–176, 179, 180, 182, 187, 189–191, 240

TUBiX platform series

A small satellite platform series of Technische Universität Berlin formed by the nanosatellite platform TUBiX10 and the microsatellite platform family TUBiX20 [33]. 5

TUBiX10 platform

Nanosatellite platform of Technische Universität Berlin targeting missions in the 10 kg range [34]. 5

TUBiX20 platform family

Microsatellite platform family of Technische Universität Berlin targeting missions in the range of 10 to 50 kg [35–37]. 5, 23–26, 28–31, 33, 34, 36, 37, 49, 51, 53–58, 60–71, 73–77, 79, 80, 83, 84, 86, 89, 90, 94, 96–99, 101, 103, 105, 108–110, 115, 136, 138, 140, 148, 163, 169, 172, 174–176, 187, 189–192, 243

TUBSAT series

Small satellite series of Technische Universität Berlin within which seven spacecraft were launched between 1991 and 2007 [38]. 4, 5, 240

Ultra high frequency (UHF)

Frequency range from 300 to 1 000 MHz, which is commonly used for satellite communications [15]. 58–60, 96, 106, 121, 131, 163, 165, 172, 175, 177, 181, 182, 185, 253

Very high frequency (VHF)

Frequency range from 30 to 300 MHz, which is commonly used for satellite communications [15]. 253

Warm redundancy

One or several spare units that are powered but are not performing the same tasks as the primary unit. 68, 76, 77, 91, 190

X band

Frequency range from 8 to 12 GHz, which is commonly used for satellite communications [15]. 59, 60, 73, 96, 140, 141, 160, 167, 171, 174, 181, 187, 191, 252, 253

XLink

Four channel SDR X-band transceiver developed by IQ wireless GmbH together with Technische Universität Berlin [39]. 139, 140, 143, 155, 158–160, 163, 165, 167, 171, 174, 253

Acronyms

ADCS Attitude determination and control system.

AI Artificial intelligence.

AIT Assembly, integration and testing.

ANN Artificial neural networks.

ASTER Advanced Spaceborne Thermal Emission and Reflection Radiometer.

AVHRR Advanced Very-High-Resolution Radiometer.

BEESAT Berlin Experimental and Educational Satellite.
Glossary: BEESAT series.

BIT Built-in test.

BMWi Federal Ministry for Economic Affairs and Energy.

BOL Begin-of-life.

BSP Board support package.
Glossary: Board support package (BSP).

CAN Control area network.
Glossary: Control area network (CAN).

CCR Corner cube reflectors.

CCSDS Consultative Committee for Space Data Systems
Glossary: Consultative Committee for Space Data Systems (CCSDS).

CIRC Compact Infrared Camera.

CMG Control moment gyroscope.
Glossary: Control moment gyroscope (CMG).

CMOS Complementary metal-oxide-semiconductor.

COM Communications system.

COTS Commercial off-the-shelf.

DET Direct energy transfer.
Glossary: Direct energy transfer (DET).

DLR German Aerospace Center.

DoD Depth of discharge.
Glossary: Depth of discharge (DoD).

ECDL Extended cavity diode lasers.

EDAC Error detection and correction.

EGSE Electrical ground support equipment.

EOL End-of-life.

EPS Electrical power system.

EQM Engineering qualification model.

ESA European Space Agency.

ESPA EELV Secondary Payload Adapter.

FDA Fluid-dynamic actuator.
Glossary: Fluid-dynamic actuator (FDA).

FDIR Fault detection, isolation and recovery.

FEM Finite element method.

FOR Fibre optic rate sensor.

FoV Field of view.

FPGA Field programmable gate array.

GCP Ground control point.

GFZ German Research Centre for Geosciences.

GMC Gas multiplier counter.

GNB Generic Nanosatellite Bus.

GNSS Global navigation satellite system.

GPS Global Positioning System.

GRB Gamma-ray bursts.

GSD Ground sampling distance.

GUI Graphical user interface.

GW Gravitational wave.

HD High definition.

HIROS High resolution InfraRed Occultation Spectrometer.

HSDI Hyperspectral Solar Disc Imager.

IC Integrated circuit.

IOD In-orbit demonstration.

IoT Internet of things.

ISL Inter-satellite link.

ISOC Inter-Satellite Optical Communicator.

ISS International Space Station.

JAXA Japan Aerospace Exploration Agency.

JPL Jet Propulsion Laboratory.

LAPAN Indonesian National Institute of Aeronautics and Space.

LEO Low-Earth orbit.

LEOP Launch and early operations phase.

Li-ion Lithium–ion.

LNA Low-noise amplifier.

LoS Line of sight.

LTAN Longitude of the ascending node.

MCU Micro controller unit.

MEMS Microelectromechanical system.

MLI Multi-layer insulation.
Glossary: Multi-layer insulation (MLI).

MMS Multimission Modular Spacecraft.

MODIS Moderate Resolution Imaging Spectroradiometer.

MOPA Master-oscillator-power-amplifier configuration.

MPP Maximum power point.

MPPT Maximum power point tracking.
Glossary: Maximum power point tracking (MPPT).

NASA National Aeronautics and Space Administration.

NEMO Next-generation Earth Monitoring and Observation.

NETD Noise equivalent temperature difference.

NUDT National University of Defense Technology.

OBC On-board computer.

OEAW Austrian Academy of Sciences.

OS Operating system.

PCB Printed circuit board.

PCU Power conditioning unit.

PDH Payload data handling.

PPS Pulse per second.

PPT Peak power tracking.
Glossary: Peak power tracking (PPT).

PSF Point spread function.

QKD Quantum key distribution.

RBF Remove before flight .

RF Radio frequency.

RMS Root mean square.

ROIC Readout integrated circuit.

SDR Software-defined radio.
Glossary: Software-defined radio (SDR).

SEL Single event latchup.
Glossary: Single event latchup (SEL).

SEM Scanning electron microscope.

SFL Space Flight Laboratory.

Si Silicon.

SLR Satellite laser ranging.

SOLID Solar generator based Impact Detector.
Glossary: Solar generator based Impact Detector (SOLID).

SPENVIS Space ENVironment Information System.

SSMS Small Spacecraft Mission Service.

SSO Sun-synchronous orbit.

SSTL Surrey Satellite Technology Ltd.

TBC To be confirmed.

TBIRD Terabyte Infrared Delivery.

TC Telecommand.

TCS Thermal control system.

TID Total ionising dose.
Glossary: Total ionising dose (TID).

TIR Thermal infrared.

TM Telemetry.

TM/TC Telemetry and telecommand.

TMM Thermal mathematical model.

TTCAN Time-triggered CAN.
Glossary: Time-triggered CAN (TTCAN).

UHF Ultra high frequency.
Glossary: Ultra high frequency (UHF).

UTC Universal Time Coordinated.

UTIAS University of Toronto Institute for Aerospace Studies.

VLEO Very low Earth orbit.

VOx Vanadium oxide.

1 Introduction

Within the first chapter of this thesis the motivation for the research work is presented. Furthermore, this chapter gives an overview of the evolution of the research project and outlines the structure of the thesis.

1.1 Motivation and Problem Statement

The recent decades have seen significant progress in the field of small satellites characterised by a launch mass below 1 000 kg. Sweeting [40] has presented a comprehensive recapitulation of the small satellites' development from the beginning of the space age to the mega-constellations that are considered today. In this context, especially the launch numbers of satellites below 50 kg increased significantly in recent years [41, 42].

The growing interest in satellites of this mass range was decisively shaped by two factors. Firstly, the introduction of the CubeSat standard by California Polytechnic State University and Stanford University in 1999 promoted a unified form factor [43]. The standard defines different satellite sizes based on units of 10 cm called "U". CubeSats are launched in containerised dispensers from which the satellite is ejected once the target orbit is reached, which significantly simplifies the interface to the launcher. Secondly, the growing supply of consumer grade electronic components offering high performance at comparatively low cost facilitated this trend. It was mainly due to these two factors that universities all over the world were now in the position to develop and operate their own satellite missions. As a result of the rising activity in this field, the performance of such spacecraft increased continuously and eventually aroused commercial interest which ultimately led to the three-figure launches per year that are registered today.

Recently, satellites below 50 kg have demonstrated extraordinary capabilities in orbit including pointing accuracies below 0.5 arcsec [44], payload data downlink rates above 1.6 $\mathrm{Gbit\,s^{-1}}$ [45] and the successful support of Mars exploration [46].

Figure 1.1 gives an overview over the number of satellites with a launch mass of 1 to 50 kg that have been launched between the years 2009 and 2018, as well as predicted numbers until 2021 based on data presented by SpaceWorks [47]. This mass range includes nanosatellites that are characterised by a launch mass between 1 and 10 kg as well as a part of the launched microsatellites characterised by launch masses of 10 to 100 kg. Here, the overall numbers of satellites with a mass between 1 and 50 kg that will be launched in the three subsequent years is predicted to rise steadily with reaching 400 launched spacecraft in 2021.

According to Villela et al. [42], the majority of the spacecraft below 50 kg that launched to date are triple unit CubeSats with a mass of around 5 kg. However, with an increasing number of demanding missions successfully demonstrating the capabilities of such small spacecraft more and more payloads with increased mass and volume requirements were being considered. This ultimately lead to the proposal to extend the original CubeSat standard towards 6, 12 and even 27 U satellites with launch masses up to 12, 24 and 54 kg, respectively, brought forward by Hevner et al. [48]. In this context, Barnhart and Sweeting [49] found a launch mass of 30 kg to be optimal when considering spacecraft utility, mission utility, and optimum cost as figures of merrit. A trend towards larger numbers of launched microsatellites below 50 kg can also be observed in the data presented in Figure 1.1. While the overall amount of launched nanosatellites decreased slightly in 2018 compared with the prior year, the numbers rose by more than 25 percent for launched microsatellites in the 10 to 50 kg mass range.

The rising interest in the use of small satellites for commercial applications also promoted the development of small launchers characterised by a maximum payload capability of 1 000 kg to provide more flexibility in launch schedule and target orbit for small payloads. In this context, Niederstrasser [50] published a comprehensive overview of the current state in small launcher development.

For the cost effective implementation of competitive small satellite missions the development efforts for each individual spacecraft need to be kept at a minimum. This is customarily achieved by implementing platform concepts that facilitate reuse between individual missions. Small satellite platform designs for various spacecraft sizes have for example been presented by Kingston [51], Dannemann and Jetzschmann [52], Song, Kim, and Chang [53], and Grau [54].

Generally, the architectures of such platforms range from highly integrated designs to modular architecture that focus on scalability. However, according to Erens and Verhulst [55] modularity and integration can result in conflicting requirements.

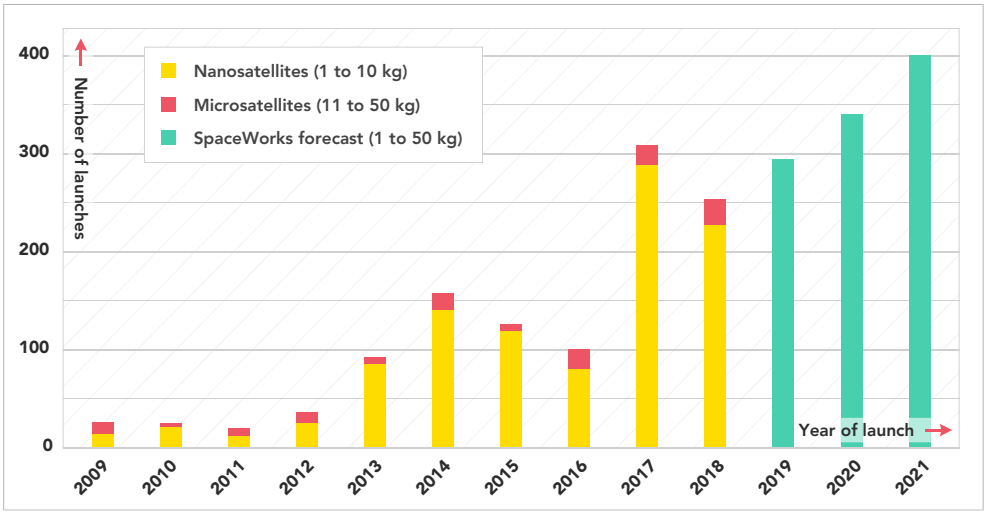

Figure 1.1: Overview of nanosatellites and microsatellites that have been launched between 2009 and 2018 and predicted numbers until 2021. The number of nanosatellites with a launch mass between 1 and 10 kg is shown in yellow, while microsatellites with a launch mass between 10 and 50 kg are depicted in red. The predicted number of total launches until 2021 for both groups are coloured green (figure modified from [47]).

Therefore, the choice of architecture needs to be matched with the aspired application. According to Jetzschmann et al. [56], the advantages of a modular platform architecture take affect if the platform is applied to missions with diverging requirements, while the modular platform may be outperformed by an integrated design if a large number of spacecraft are to be produced based on similar requirements. In this context, the single unit CubeSat platform design presented by Grau [54] is an example for a highly integrated design. In contrast, scalable platform designs, as presented by Dannemann and Jetzschmann [52], allow for largely tailoring the performance of each subsystem according to the needs of a specific mission.

Falkenhayn [57] found that a modular platform design will initially generate higher costs when being compared to a satellite developed with only considering a single use-case. However, cost savings can be expected if several spacecraft build on the same modular platform. Therefore, scalable platform designs target application scenarios in which changes in the requirements can be expected between missions and several spacecraft are to based on the same platform. When additionally

considering the use of the CubeSat form factor the containerised launch adapter imposes rigid boundaries for mass and volume on the spacecraft. Here, the applicability of a platform would greatly benefit if several CubeSat sizes are supported by the architecture.

Today, spacecraft components that were specifically developed for the implementation within spacecraft complying with the CubeSats standard are widely commercially available. However, the variety of the implemented interfaces and communication protocols was reported to complicate the combination of components from different manufacturers. For the implementation of components from multiple vendors within a single 14 kg spacecraft Nohka, Drobczyk, and Heidecker [58] found that the overall complexity of the satellite was increased by mismatching interfaces. Furthermore, the implementation of redundancy was not feasible. Similar findings have been published by Horch, Schimmerohn, and Schäfer [59] for the development of a 12 U CubeSat based on commercially available components. Here, mainly the lack of standardization of the electrical interfaces has been named.

Based on the above assessment of the evolution of satellites in the 10 to 50 kg mass range the following key objectives are formulated for the research presented in this thesis:

1. To define a systems architecture for a scalable microsatellite platform that supports missions between 10 and 50 kg and focusses on reuse between missions and reduced development times.
2. To analyse exemplary spacecraft implementations based on the platform to demonstrate the advantages that result from such an approach.

1.2 Evolution of the Research Project

The research presented in this thesis was conducted at the Chair of Space Technology of Technische Universität Berlin. With the launch of 26 satellites since 1991, the university has a long and successful history of small satellite development and mission operations [60]. A complete record of past and current small satellite missions of Technische Universität Berlin can be found in Appendix A.

Satellite development at Technische Universität Berlin was initiated by the TUBSAT series. Between 1991 and 2007 seven TUBSATs with launch masses between 3

and 56 kg were launched, mainly focussing on applications from the field of Earth observation and satellite communications [38]. One notable achievement here are interactive attitude control capabilities in combination with live-video feeds from a satellite that were first demonstrated by DLR-TUBSAT in 1999 [61]. These features enabled the operator to manipulate the attitude of the satellite according to the received live footage.

After the last TUBSAT was launched in 2007 the development shifted towards single-unit CubeSats within the Berlin Experimental and Educational Satellite (BEESAT) series. Within this series 13 CubeSats have been launched to date. BEESAT-1 [62] was the first CubeSat that demonstrated reaction wheels on orbit and these wheels have been used for performing three-axis attitude control on later BEESAT missions.

While the BEESAT-series is continued to date, it was additionally approached to transfer the heritage in technology miniaturisation back into larger spacecraft to allow for serving more sophisticated payloads with more demanding requirements in mass, power, and volume. To this end, the TUBiX platform series has been established. Here, the TUBiX10 platform targets missions of approximately 10 kg, while the TUBiX20 platform family was originally developed to support spacecraft in the 20 kg range and its scope was later extended to a range of 10 to 50 kg. The TUBiX10 platform was implemented within the missions S-Net [63, 64] and SALSAT [65] to date, while, the TUBiX20 platform is the basis for the missions TechnoSat (cf. Section 4.1), TUBIN (cf. Section 4.2) and QUEEN (cf. Section 4.3).

The research project presented in this thesis addresses the definition of the systems architecture of the TUBiX20 platform and its implementation for the missions TechnoSat, TUBIN and QUEEN. The author of this thesis served as systems engineer and project manager for the development of the TUBiX20 platform in general and the afore mentioned missions in particular.

1.3 Thesis Outline

This thesis is structured in five chapters. In the following, a brief summery of each chapter is given.

Chapter 1 introduces the thesis with presenting the problem statement, which defines the scope of the research. The introduction further gives an overview over

the evolution of the research project and concludes with this outline of the thesis's structure.

Chapter 2 gives an overview of the state-of-the-art of microsatellites between 10 and 50 kg. To this end, it introduces application areas for this class of spacecraft by presenting state-of-the-art missions in the respective areas. Finally, it discusses product platforms and gives an overview of microsatellite platforms that are available on the market today.

Chapter 3 presents required key characteristics of the platform and identifies suitable scaling-ranges of key subsystem performance parameters. Furthermore, the overall systems architecture is defined and motivated.

Chapter 4 contains a collection of three use cases in which the developed platform architecture is applied to different mission scenarios. This includes the TechnoSat mission that launched in 2017, the TUBIN mission brought to orbit June 2021, and the QUEEN mission that is currently in the phase of the preliminary design.

Chapter 5 presents a conclusion for the entire research project.

2 State of the Art

In this chapter the state of the art of small satellites with launch masses between 10 and 50 kg is presented. As an introduction, definitions and characteristics associated with this satellite class are introduced. In the following, the state of the art in different application areas for microsatellites, such as Earth observation, communications, science, or close proximity and robotics is outlined. As a conclusion, this section examines the term *platform* and discusses commercially available microsatellite platforms.

With the rising interest in small satellite missions, the need for a classification emerged to distinguish different satellite sizes within this class of spacecraft. Here, the satellite's launch mass prevailed as primary distinguishing criterion. Table 2.1 shows the division of small satellites according to their launch mass as proposed by Sweeting [17, 40]. Following these definitions, spacecraft with a launch mass between 10 and 100 kg qualify as microsatellites.

Table 2.1: Satellite classification by their launch mass according to Sweeting [17, 40]. Here, the mass range of 10 to 50 kg that is studied in this thesis belongs to the microsatellite class.

Satellite class	Launch mass kg	Exemplary missions
Large satellite	above 1 000	ENVISAT of ESA [66]
Small satellite	500 to 1 000	CryoSat of ESA [67]
Minisatellite	100 to 500	TET-1 of the DLR [68]
Microsatellite	10 to 100	TUBIN of Technische Universität Berlin [32]
Nanosatellite	1 to 10	GOMX-3 of GomSpace [69]
Picosatellite	0.1 to 1	Delfi-PQ of Delft University of Technology [70]
Femtosatellite	below 0.1	Stardust of the NUDT [71]

For simplicity, the term *microsatellite* denotes the mass range of 10 to 50 kg in the remainder of this thesis, unless otherwise stated.

As discussed in the introduction, the majority of microsatellites of the mass range studied in this thesis that were launched to date adhere to the CubeSat standard. One of the most notable features of the CubeSat specification is the closed dispenser that is foreseen for the separation of the CubeSat from the upper stage of the launcher. The dispenser was originally designed by the California Polytechnic State University for the separation of three single-unit CubeSats [43]. However, the increased popularity of larger CubeSats, i.e 3 U, 6 U and 12 U satellites, led to updated dispenser designs to accommodate also these sizes of spacecraft. Nowadays, 12 U dispensers are widely spread and most of those allow for separating a single 12 U satellite and alternatively also two 6 U or four 3 U CubeSats. An overview of different CubeSat deployment systems has been published by Aslan, Bernal, and Puig-Suari in [72].

The introduction of the dispenser greatly simplified the launch of CubeSats up to 16 U. However, while a launch container for 27U CubeSats has been proposed [48], the first separation of a 27U CubeSat with such a dispenser has yet to take place and microsatellites larger then 16 U have been separated using traditional separation systems until now.

Figure 2.1 illustrates different launcher separation system options for microsatellites by showing a number of small spacecraft mounted to the Small Spacecraft Mission Service (SSMS) structure of the VEGA rocket [73]. On the lower module one can see several CubeSat deployers mounted onto the structure, whereas the larger spacecraft on the upper modules make use of ring type separation systems.

2.1 Application Areas

This section presents a short review of the current state and future developments in the application areas relevant to microsatellites. To this end, launched missions, as well as missions still in development are briefly introduced for different application areas. Furthermore, subsystem performance parameters are derived from analysing these missions to illustrate the range of requirements a microsatellite platform may be confronted with.

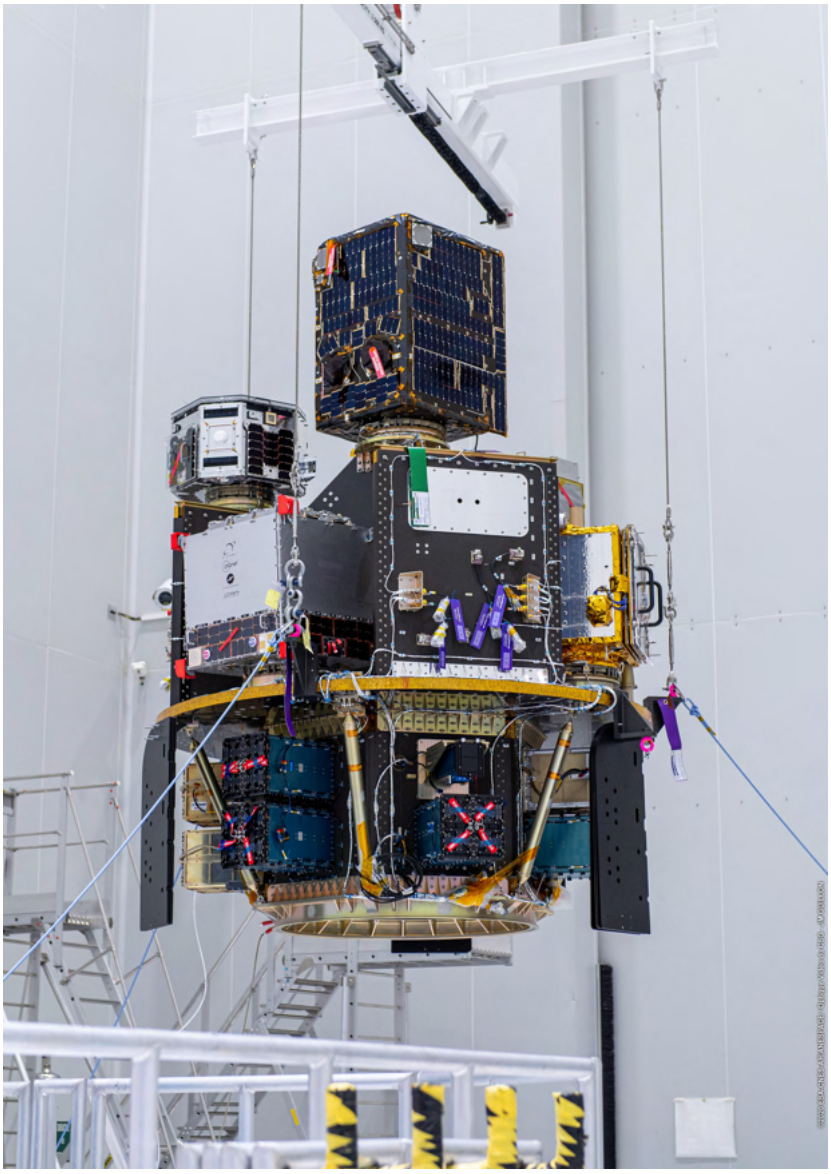

Figure 2.1: Small satellites mounted on Vega's Small Spacecraft Mission Service (SSMS). At the lower end one can see several 12 U CubeSat dispensers mounted to the adapter, while the larger satellites on the upper deck make use of traditional separation systems (Image credit: ESA/CNES/Arianespace/Optique Video du CSG - JM Guillon).

2.1.1 Technology Demonstration

The in-orbit demonstration (IOD) of new technology has been the dominating application area at the beginning of the CubeSat era and still plays an important role as can be seen in the numbers presented by Villela et al. [42].

However, in order to prevent duplications, technology demonstration missions are assigned to the respective application area they are targeting at in the following.

2.1.2 Earth Observation

There has been considerable development in the performance satellites from the lower end of the microsatellite mass range can provide when it comes to Earth observation tasks. In 2012 Selva and Krejci [74] analysed the performance of such spacecraft and related it to different Earth observation technologies. They concluded that only a smaller part of the considered Earth observation applications, like disaster monitoring or ocean surface temperature measurements, could be accommodated on a CubeSat.

Only four years later in 2016 Freeman [75] found that the performance that can be expected from a CubeSat significantly increased. As a result of this, Freeman considered most of the tasks that were ruled out for the implementation on the basis of CubeSats by Selva and Krejci to now be within the capabilities of this satellite class. This, for example, includes cloud profile and rain radars, hi-resolution optical imagers, and scatterometers.

A concept that may open additional application scenarios in Earth observation for microsatellites in the future is the operation in very low Earth orbit (VLEO), i.e. below 450 km. While VLEO missions are also proposed for other application areas, the advantages are especially evident for Earth observation missions. Here, significantly lower costs are predicted for small Earth observation missions operating in VLEO by Shao, Koltz, and Wertz [76] when being compared to missions with similar performance operating in higher altitudes. This is mainly because smaller instrument can be utilised in VLEO for achieving the same ground sampling distance (GSD). A comprehensive overview of the advantages VLEO operation may entail for Earth observation missions is presented by Crisp et al. [77].

In the following, present and future microsatellite Earth observation missions are introduced. Additionally, platform performance requirements are derived as a reference for the platform development that is presented in this thesis.

One recent mission that showcased new Earth observation capabilities on a microsatellite is RainCube, a precipitation radar mission based on a 6 U CubeSat. The RainCube payload was developed by Jet Propulsion Laboratory (JPL), while Tyvak Nano-Satellite Systems contributed the platform [78, 79]. Launched in 2018, RainCube demonstrated weather observations based on a newly developed Ka-band atmospheric radar using a deployable antenna that was equally designed for the mission. In the future, the technologies demonstrated by RainCube may pave the way for science missions to observe weather processes based on constellation of microsatellites. An artists impression of a satellite constellation based on the RainCube design is shown in Figure 2.2.

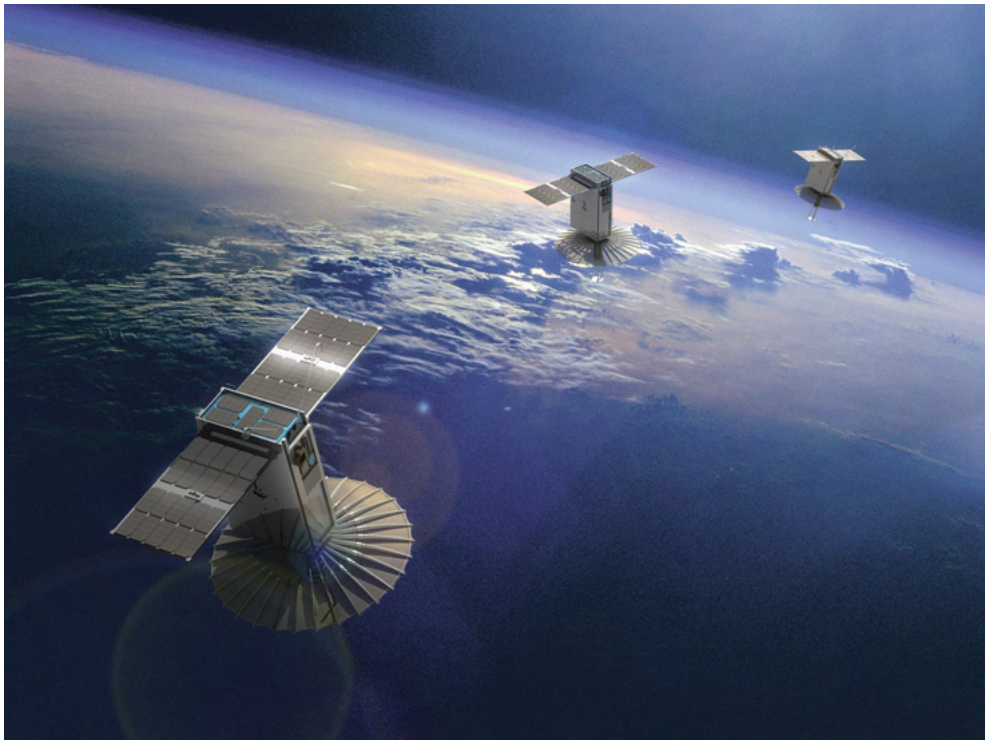

Figure 2.2: Artist's impression of a RainCube constellation with unfolded radar antennas and solar panels (Image credit: John MacNeill).

An example of a commercial Earth observation constellation based on microsatellites is GHGSat, that aims at measuring point sources of greenhouse gas emissions [80]. In 2016, GHGSat-D, a microsatellite with a mass of approximately 15 kg was launched as proof-of-concept technology demonstrator [81]. It was followed by GHGSat-C1 in 2020, which is the first satellite of an operational constellation that will eventually comprise of 10 satellites. The first three GHGSat satellites are based on the Next-generation Earth Monitoring and Observation (NEMO) platform of the Space Flight Laboratory (SFL) by University of Toronto Institute for Aerospace Studies (UTIAS) [82].

More towards the upper end of the considered mass range, the 39-kg Earth observation satellite Jilin-1gf03 provides multispectral images with a GSD below four meters and panchromatic imagery with a GSD of one meter [83]. Jilin-1gf03 represents the third generation of the Jilin satellites that shall form the basis for the Jilin-1 constellation comprising 108 satellites in 12 orbital planes. Figure 2.3 shows three images that were captured by Jilin-1gf03 in 2019.

(a) Shenzhen airport (b) Palm island (c) New Orleans

Figure 2.3: Images captured by the 39-kg microsatellite Jilin-1gf03A from a 571 kilometer orbit in 2019 [83] (Image credit: Chang Guang Satellite Technology Co., Ltd.).

In the following, typical values of platform performance parameters required for state-of-the-art Earth observation missions shall be collected. To this end, three future missions, namely MANTIS, CubeMAP, and HiREV, have been selected as reference that are briefly introduced in the following. The requirements the associated payloads impose on the spacecraft platform may serve as a general indicator for the capabilities that are demanded by a state-of-the-art Earth observation mission.

The MANTIS mission is based on a 12 U CubeSat carrying a Maksutov-Cassegrain imager with a focal length of 775 mm [84]. In a 500 km orbit the payload can deliver raw imagery with a GSD of 3.5 meters.

The CubeMAP constellation aims at studying the middle atmosphere with 12 U CubeSats [85]. To this end, each satellite of the constellation carries four payloads, namely three instances of the High resolution InfraRed Occultation Spectrometer (HIROS) and the Hyperspectral Solar Disc Imager (HSDI).

Another 6 U Earth observation mission is HiREV that is designed to generate 5 m color and 3 m monochromatic imagery as well as high definition (HD) videos [86].

Table 2.2 gives an overview of the payload mass, the pointing accuracy, the orbit average power consumption, the payload data downlink rate as well as the delta-v required by these missions.

Table 2.2: Selected subsystem requirements for exemplary future Earth observation microsatellite missions [84–86].

Parameter	MANTIS	CubeMAP	HiREV
Form factor	12 U	12 U	6 U
Pointing accuracy	1 arcmin	6 arcmin	unspecified
Power generation	15 W[a]	16.71 to 32.08 W[b]	41 W[c]
Payload data downlink	150 Mbit s^{-1}	7 Mbit s^{-1}	2 Mbit s^{-1}
Delta-v	n/a	213 m s^{-1}	n/a

[a] Average power available for the payload
[b] Average power available for platform and payload
[c] Maximum power available for platform and payload at end-of-life (EOL)

When evaluating the values given in Table 2.2, one needs to consider that while implementing state-of-the-art payloads, these missions target the demonstration of said payloads. Therefore, one can assume that the requirements for average power and data downlink capacity may vary considerably if the payloads shall be utilised continuously in an operational mission, while pointing accuracy and peak power are not affected by this fact.

2.1.3 Communications

An application area that recently gained more and more significance for microsatellites is the field of communications [42]. In this context, advantages and emerging trends in small satellite communications have been published by Saeed et al. [87] and Burleigh et al. [88].

Generally, the trend of continuously increasing downlink data rate facilitated a growing number of application areas for microsatellites. In this context, the rapidly increasing number of satellites in orbit lead to increasing competition for the use of the available radio frequency (RF) spectrum [89]. One approach to avoid this is moving towards optical laser communication systems. While optical laser communication is vulnerable to cloud coverage it promises very high data rates at moderate power consumption. A comprehensive overview of present developments and future prospects in laser communication has been published by Toyoshima [90].

Another application within the field of satellite communications that recently gained significance for the microsatellite class is quantum key distribution (QKD) that enables secure information exchange. In this context, an overview of recent and future QKD satellite missions was published by Bedington, Arrazola, and Ling [91].

Space-based internet of things (IoT) networks to enable the interconnection of devices via satellites is another emerging application area for CubeSats. Here, an overview of the current state of the art and projected future developments has been published by Birkeland and Palma [92] and by Akyildiz and Kak [93].

It has been highlighted that due to their comparatively smaller launch mass and lower associated production costs microsatellites are especially well suited for the utilisation in constellations. In this context, inter-satellite links (ISLs) are often required. Here, different inter-satellite communication technologies have been investigated Zaman et al. [94].

In the following, present and future microsatellites from the field of communications are presented. Furthermore, the subsystem requirements that originate from these missions are examined to understand the impact on the satellite platform's design.

An example of a microsatellite mission that carries capabilities required for QKD is SOCRATES that demonstrated quantum-limited laser communication from low-Earth orbit (LEO) to ground from a 50 kg class microsatellite [95].

NanoBob is a planned microsatellite mission that equally targets the demonstration of QKD, but in the much smaller envelope of a 12 U CubeSat [96]. Furthermore, NanoBob's payload may support a number of quantum physics experiments.

Further to single spacecraft, quantum communications constellations are being researched nowadays. Here, QUARC, a QKD constellation that is based on 15 six-unit CubeSats may serve as an example [97].

The 6 U CubeSat mission Q4 aims at demonstrating optical inter-satellite communications with up to 1 Gbit s^{-1} for distances of up to 200 km [98]. Here, four 6 U CubeSats equipped with the Inter-Satellite Optical Communicator (ISOC) shall be deployed from International Space Station (ISS) and use their propulsion systems to orbit as a swarm with one leader and three followers.

The 2 U Terabyte Infrared Delivery (TBIRD) payload, to be demonstrated on a 6 U National Aeronautics and Space Administration (NASA) CubeSat shall demonstrate a communication link to a small ground terminal from LEO with burst rates up to 200 Gbit s^{-1} [99]. In this manner, the number of required ground stations for LEO missions that produce large amounts of data shall be drastically reduced.

Table 2.3: Selected subsystem requirements for exemplary future communications microsatellite missions [96, 98, 99]. Here, the data downlink rate is excluded from the list as only telemetry data is expected to be downlinked by the platform.

Parameter	NanoBob	Q4	TBIRD
Form factor	12 U	6 U	6 U
Pointing accuracy	25 arcsec[a]	25 arcsec[a]	0.5 arcsec[b]
Electrical power	21.5 W[c]	72 W[a,d]	130 W[e]
Delta-v	n/a	40 m s^{-1}[a]	n/a

[a] Capability of the selected components, but not specifically named as payload requirement
[b] Shall be realised with feedback from the payload
[c] Peak power consumption of the payload including contingency
[d] Power delivered by the solar panels
[e] Peak power consumption of the payload

Table 2.3 gives an overview of the subsystem requirements of the NanoBob and the Q4 missions as well as for the TBIRD payload. No payload data downlink requirements are shown as due to the nature of the payload only a comparatively small amount of telemetry data are expected to be downlinked using the satellite platform's means of communications.

As can be seen from Table 2.3 a communication mission may impose significant requirements on the satellite platform regarding power consumption and pointing accuracy.

2.1.4 Science

Microsatellites have been applied for various kinds of science missions successfully and increased activity can be expected for this sector in the future.

One emerging application area for microsatellites is the exploration of our solar system. In this context, an overview of the current status and future trends in the implementation of microsatellites for space exploration has been published by Freeman [100].

One of the most prominent examples for incorporating microsatellites into an exploration mission is Mars Cube One that involved the first CubeSats to be operated beyond Earth orbit. The mission comprised of the two six unit CubeSats MarCO-A and MarCO-B that supported the Insight Mars lander mission with by providing a real-time communication link to Earth while performing a Mars fly-by in 2018 [46]. Figure 2.4 shows an artist's impression of MarCO-A and MarCO-B over the surface of Mars.

A planned stand-alone Mars mission with a larger 16 U CubeSat form factor is MARIO. This mission shall perform thermal radiation imaging to analyse the upper atmosphere of Mars [101].

Another area of activity are scientific observation missions involving various different types of instruments.

A notable science observation mission is ASTERIA that was designed to demonstrate precision photometry on a six unit CubeSat and launched in 2017 [102]. Here, both attitude pointing accuracies on arcsecond level and highly stable focal plane temperature control are required to operate the spacecraft's telescope.

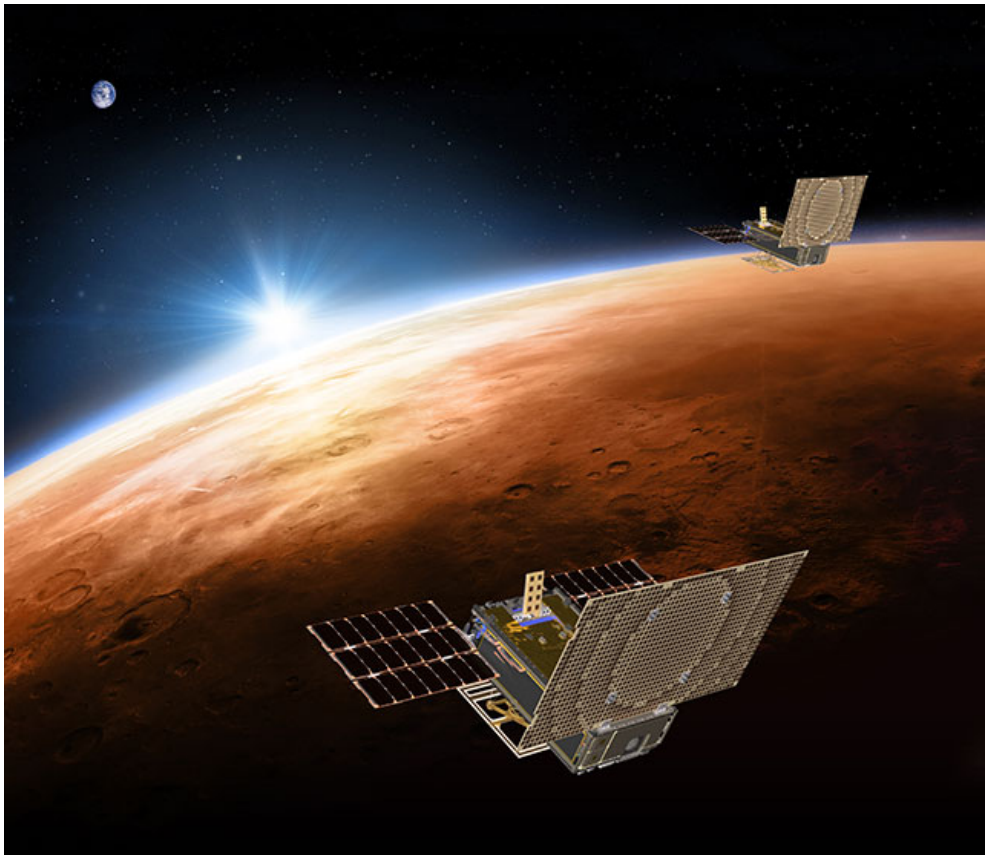

Figure 2.4: Artist's impression of the two Mars Cube One satellites MarCO-A and MarCO-B over the surface of Mars (Image credit: NASA).

BurstCube is a six unit scientific CubeSat with the mission objective to detect and localise gamma-ray bursts (GRBs) in the energy range of 10 to 1 000 keV that are predicted to be the counterparts of gravitational wave (GW) sources [103].

A mission that targets monitoring the time variability of bright x-ray sources is NinjaSat [104]. The NinjaSat payload comprises two gas multiplier counters (GMCs) sensitive to X-rays in the 2 to 50 keV range.

Further to the application areas mentioned above, quantum science recently showed a high level of activity in connection with microsatellites. Here, an overview of different quantum science applications has been presented by Oi et al. in [105].

One application relevant in this context would for example be gravity sensing. Here, one example is the CASPA project that developed and tested a 6 U CubeSat with a cold atom trap as payload [106].

Due to the variety of different application areas, science missions may impose highly diverse requirements on a microsatellite platform. Exemplary requirements for science missions are shown in Table 2.4 for the missions MARIO, ASTERIA and NinjaSat

Table 2.4: Selected subsystem requirements for exemplary future science microsatellite missions [101, 102, 104].

Parameter	MARIO	ASTERIA	NinjaSat
Form factor	16 U	6 U	6 U
Pointing accuracy	1 degree[a]	0.5 arcsec	0.5 degree
Power generation	220 W[b]	48 W[b]	18 W[c]
Payload data downlink	2.4 kbit s^{-1}[d]	1 Mbit s^{-1}	4 Mbit s^{-1}
Delta-v	445 m s^{-1}	n/a	n/a
Instrument thermal stability	unspecified	$\pm$0.01 K	unspecified

[a] Value not directly stated, 1 degree was given as pointing error for the downlink budget.
[b] At begin-of-life (BOL)
[c] Orbit average
[d] Mars to Earth

2.1.5 Robotics and Close Proximity

Further domains that have recently gained the attention of microsatellite developers are close proximity operations and robotics applications and various missions are planned in this fields.

In order to overcome the constraints imposed by size limits of the launch for space-based telescopes the AAReST mission aims at demonstrating the assembly of a telescope mirror in space using small satellites [107]. To this end, the AAReST mission involves two 3 U MirrorSats carrying an electrically actuated adaptive mirror, which can perform autonomous un-dock and re-dock manoeuvres on a 9 U CoreSat. Figure 2.5 shows an artist's concept of the fully assembled AAReST spacecraft in orbit.

Figure 2.5: Artist's concept of the two MirrorSats docked to the CoreSat of the AAReST mission in orbit (Image credit: Sergio Pellegrino/Caltech).

A central prerequisite for many robotic satellite missions are rendezvous and docking capabilities. In this context, the CPOD mission has the objective to demonstrate a miniaturised docking mechanism and the corresponding sensor suite for rendezvous, close proximity operations and docking with two 3 U spacecraft [108].

A topic that is nowadays gaining more and more relevance, especially in the context of the raising numbers of satellite launches that can be observed today, is orbital debris removal. Here, Mark and Kamath presented a comprehensive review of active space debris removal methods [109].

An example for a microsatellite-based mission to address the problem of space debris is Deorbiter CubeSat, a 8U CubeSat[1] designed to remove debris objects from LEO [110]. The mission concept involves a mother ship carrying several of these 8 U CubeSats that are capable of removing one debris object each.

[1] Despite not being one of the CubeSat form factors defined in the CubeSat Design Specification [5, 6], 8 U designs are sometimes suggested in the form of two by two units.

Table 2.5 gives an overview of the subsystem requirements of three reference robotics and close proximity microsatellite missions, namely AAReST, CPOD, and Deorbiter CubeSat.

Table 2.5: Selected subsystem requirements for exemplary future close proximity and robotics microsatellite missions [107, 108, 110].

Parameter	AAReST	CPOD	Deorbiter CubeSat
Form factor	9 U plus two 3 U	Two 3 U	8 U
Pointing accuracy	1.2 arcmin	15 arcmin	Approx. 1 degree[a]
Power generation	10 W[b]	unspecified	48.1 W[c]
Payload data downlink	9.6 kbit s^{-1}[d]	S band	n/a
Delta-v	n/a[e]	30 m s^{-1}[f]	Mission specific

[a] Derived from the accuracies stated for the attitude sensors
[b] Peak power consumption of payload and MirrorSats
[c] Platform peak power generation
[d] Telemetry downlink, no dedicated payload downlink channel provided
[e] While each MirrorSat carries a propulsion system delivering 5 to 10 m s^{-1}, this propulsion system is required for docking and is not intended for orbit manoeuvres
[f] For each satellite

2.2 Satellite Platforms

The concept of platform-based satellite development is nowadays widely used in space industry. It dates back to the development of the Multimission Modular Spacecraft (MMS) of NASA that started in the early 1970's [57]. The term *product platform* has been defined by Meyer and Lehnerd [19] as follows:

> "A product platform is a set of subsystems and interfaces that form a common structure from which a stream of derivative products can be efficiently developed and produced."[2]

The development of platforms in satellite design is motivated by the increased level of reuse that can be achieved between missions, which in turn enables reductions in cost and development time for the individual spacecraft. Research on satellite

[2] In the field of spacecraft development the term *subsystem* is already occupied by a common definition so that *component* would be a more suitable term in this context.

platforms has been presented for example by Gonzalez-Zugasti, Otto, and Baker [111], Caffrey et al. [112] and Kingston [51, 113, 114].

As the terms and definitions that are used in platform-based product development widely diverge in literature, the following definitions gathered by Jiao, Simpson, and Siddique in [115] are used throughout this thesis. Here, a *product family* comprises of products that share common components and interface definitions but are tailored to the requirements of a certain use-case. A specific implementation of the product family is referred to as *variant*, while the common elements shared between variants are called the *product platform*. Such product platforms can be designed with different objectives. A *scalable platform* allows for adjusting certain performance parameters of the system, while a *modular platform* supports adding or removing capabilities to form different variants of a product. A platform that targets updating the product between variants is referred to as *generational platform*.

Figure 2.6: M16P 16 U microsatellite platform developed by NanoAvionics in flight configuration (Image credit: NanoAvionics).

There is a wide variety of small satellite platforms with launch masses in the range of 10 to 50 kg that have been developed by different vendors. As an exemplary microsatellite platform available on the market, the M16P 16 U platform developed by NanoAvionics is shown in Figure 2.6.

In order to obtain an overview of the market availability of microsatellite platforms in the 10 to 50 kg range, 51 commercial platforms from 26 vendors have been analysed[3]. Figure 2.7 shows the distribution of both form factor and launch mass among those platforms. One can see that with 33 and 27 percent, respectively, the majority of the platforms that adhere to the CubeSat standard are either 6 or 12 U designs. Another 18 percent are either 8, 16 or 27 U platforms and 22 percent do not adhere to the CubeSat form factor at all. When looking at the maximum launch masses, 80 percent of the platforms are below 30 kg[4].

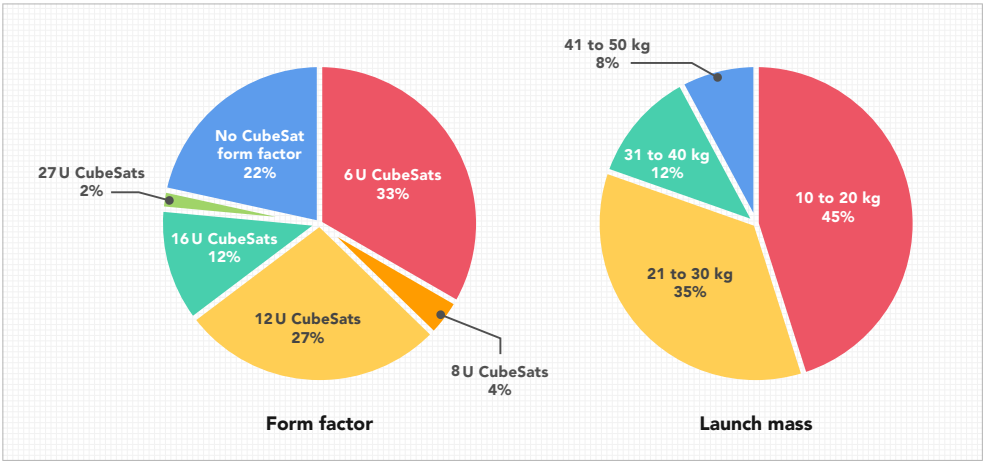

Figure 2.7: Distribution of form factor and maximum launch mass among 51 commercially available microsatellite platforms in the 10 to 50 kg range offered by 26 different vendors. A list of the individual platforms can be found in Appendix B.

[3]The complete list can be found in Appendix B.
[4]For all CubeSats a maximum mass of 2 kg was assumed per unit.

3 Platform Architecture

In this chapter, the requirements and constraints of the microsatellite platform TUBiX20 for missions with a launch mass between 10 and 50 kg targeting towards a broad range of applications including science, Earth observation, and technology demonstration are examined. Furthermore, scaling ranges for the most significant performance parameters of the satellite's subsystems are analysed and key design parameters of the platform are defined. Finally, a generic systems overview of a TUBiX20-based spacecraft is presented to illustrate the overall architecture of the platform. An overview of the considerations presented in this chapter has been published by the author in [116].

3.1 Requirements and Constraints

In the following, a number of generalised requirements and constraints that apply to the TUBiX20 platform and influence its overall architecture are outlined and motivated.

3.1.1 Form Factor

A small satellite's launcher interface has a significant impact on the launch logistics. Especially for spacecraft with a launch mass below 25 kg adhering to the CubeSat form factor significantly simplifies the launcher interface and can reduce launch costs and integration times. To be able to exploit the advantages offered by the CubeSat form factor regarding a streamlined launch process, the TUBiX20 platform shall offer 6, 12, 16 and 27 U CubeSat compatible designs (cf. Section 1.1).

However, especially for the larger form factors, launching from a CubeSat dispenser may not always be the most effective solution as the dispenser adds significant mass to the launch and prohibits extensions exceeding the specified dimensions. Therefore, launching from a container is not mandatory for TUBiX20 satellites and a launch using a traditional separation system is a foreseen option, especially

for the larger implementations. Table 3.1 gives an overview of the TUBiX20 form factors, their CubeSat equivalent as well as of the maximum allowable mass.

Table 3.1: Form factors of the TUBiX20 platform family with equivalent CubeSat volume, as well as limits of mass and volume.

Platform configuration	CubeSat units U	Maximum mass kg	Volume[a] cm^3
TUBiX20-S	6	12	$10 \times 20 \times 30$
TUBiX20-M	12	24	$20 \times 20 \times 30$
TUBiX20-Mp	16	32	$20 \times 20 \times 40$
TUBiX20-L	27	54	$30 \times 30 \times 30$

[a] Only stated as reference for the configuration, the effective volume is larger

Generally, a CubeSat's mass is restricted to 2 kg per unit [5, 6, 48]. According to this, the maximum allowable mass per unit for the TUBiX20 platform is specified with 2 kg which may, however, be exceeded for specific missions if allowed by the launcher interface.

3.1.2 Scaling, Modularity, and Reuse

In order to establish a better understanding of the capabilities the TUBiX20 platform is required to implement, the author analysed the requirements derived in Section 2.1 regarding their impact on the platform's characteristics.

Given the diverse application areas foreseen for the TUBiX20 platform, significant differences in the requirements for performance parameters such as available payload power, attitude knowledge, pointing accuracy, or payload data downlink rate are to be expected between individual missions. To account for this, the platform needs to provide scalability regarding such parameters. The range that need to be covered for each parameter was already examined in Section 2.1 and is further detailed in Section 3.2. This boundary condition relates to the term *scalable platform* introduced in Section 2.2.

Some features provided by the satellite platform may only be required for certain missions. One example here is a propulsion system which may be essential to a

specific mission but will not be required for others. Therefore, the TUBiX20 platform additionally needs to be able to serve as a *modular platform* (cf. Section 2.2) allowing to add and remove features as required by the mission.

While the modular architecture chosen for the platform enables a high level of scalability it also increases the parts count (cf. Section 2.2). In this context, the potential for reuse shall be maximised within a single spacecraft as well as between different missions to decrease the effort associated with development, maintenance and extension of the platform.

3.1.3 Component Selection and Technology Update

To stay abreast with state-of-the-art terrestrial technology and to limit the cost associated with a mission based on the TUBiX20 platform, the implementation of consumer grade commercial off-the-shelf (COTS) components is permitted. However, the short development cycles of such components increase the risk that key components are being discontinued. Furthermore, updating components may be required for the platform to maintain competitive performance. Therefore, the platform shall enable continuous component update, i.e. it shall be implemented as *generational platform* as defined in Section 2.2.

3.1.4 Fault Tolerance

In the context of fault tolerance, two terms can generally be distinguished, namely *availability* and *reliability*. According to Laprie [1], availability specifies the fraction of time in which a service according to the specification was provided by a system, while reliability is a measure of the time to failure. Following this, a platform with relatively frequent but short disruptions of service might have a low reliability but nevertheless a high availability. In general terms, different missions may have different requirements for both aspects. While an Earth observation mission may primarily focus on availability, an interplanetary mission might require a high level of reliability for crucial mission phases.

In order to work out fundamental boundary conditions for the implementation of fault tolerance capabilities for the TUBiX20 platform, the author evaluated relevant publications and examined the missions presented in Section 2.2. Furthermore, the operation of the platform in a university environment was taken into account.

In the context of fault tolerance for small satellites, Shirasaka and Nakasuka [117] propose the concept of *reasonably reliable systems engineering* for small satellites, focussing on availability instead of reliability. This concept also concentrates the efforts to improve reliability on the components that are strictly necessary to communicate with the spacecraft, i.e. the communications system (COM), the electrical power system (EPS), and the on-board computer (OBC). For the remainder of the spacecraft, including the payload, it is expected that recovery from an interrupted service can be accomplished via power cycling or ground intervention. A similar approach was furthermore proposed by Jackson in [118]. Here, a multi-level fault protection system allows for graceful degradation upon the occurrence of a fault and is designed to keep the spacecraft in a thermally safe, power positive, and communicative state at all times.

Following this, the TUBiX20 platform targets to support variants that implement a high degree of system-level robustness. Furthermore, limiting the resources required for self-retaining the platform prevents that the satellite platform drives the requirements for missions with moderate payload requirements. Finally, when operating TUBiX20-based missions within the university environment, continuous supervision of the spacecraft may not be guaranteed especially if several missions are operated in parallel.

Based on the above, a number of boundary conditions are formulated which are listed in the following:

1. The platform shall support satellite configurations that survive extended periods of time without being operated from the ground.
2. It shall be possible to configure a spacecraft such that it may survive extended periods of time without active attitude control.
3. Platform configurations that guarantee availability for communication at all times and regardless of the satellite's attitude shall be supported.

While these boundary conditions may not apply to each and every TUBiX20 mission, they shall generally be supported by the platform.

In order to describe means of increasing a system's reliability, a number of definitions need to be clarified. As the terms used in this context diverge in literature, definitions presented by Laprie [1] are employed within the remainder of this thesis. According to Laprie, a *fault* is a deviation from the desired state within a system. A fault may result in an *error*, which may in turn cause a *failure*. A

disconnected line within a cable of a spacecraft's harness, for example, is denoted as a fault. If a device shows incorrect behaviour due to the affected signal, the fault resulted in an error. This error may now lead to the delivery of a service by the spacecraft that is not according to the specification, which is then referred to as failure.

Preventing errors that could impact the service of a system can be improved by enhancing the reliability of its components or through the implementation of redundancy [119]. According to Laprie [1], this is referred to as fault avoidance and fault tolerance, respectively. Here, the former approach is not applicable, as it was established already that the platform shall rely on a extensive implementation of COTS components to enable a high performance at comparatively low cost. In contrast, the latter concept is in line with the usage of COTS components. Another disambiguation related to fault tolerance that is relevant in this context is *static* and *dynamic* fault tolerance [120]. In the case of static fault tolerance, the development of an error from the fault is prevented by design. This may for example apply to the interrupted cable from the above example, if another line passes the same signal as the affected one. In contrast to that, dynamic fault tolerance requires an activity. If two sensors that measure the same signal would, for example, deliver diverging results, tests could be run on both sensors to identify the incorrect value.

To achieve fault tolerance in non-repairable systems, different forms of redundancy are commonly implemented. The most common classification of redundancy, which is for example presented by Amari and Dill [121], divides redundancy implementations into *active* and *stand-by* redundancy. Active redundant components perform the same tasks in parallel so that a failing unit would not lead to an interruption of service. Here, active redundancy provides large potential for contributing to fault tolerance in the implementation of computer systems, as the result generated by several units in parallel can be compared. However, this is only possible if more than two units are available for performing the same task as no conclusion could be drawn if two units are contradicting each other. Therefore, active redundancy is commonly implemented as triple modular redundancy [30, 31]. Standby redundancy, on the other hand, is again divided into *hot*, *warm* and *cold* standby redundancy according to the failure rate of the redundant component.

However, due to the launch loads and the space environment a satellite is exposed to, the failure rate of a redundant component is hard to determine especially if COTS components are implemented. Here, alternative definitions to describe

redundancy are suggested by Sharma [3], who is referring to a powered component as *hot redundant* and calls a component that is switched off *cold redundant*. As these definitions are considered to be better suited for the use in space technology, they will be used for the remainder of the thesis. In addition, a powered component, which is not performing the same task as the active one is referred to as *warm redundant*.

While the replication of hardware, referred to as *hardware redundancy*, is the most common redundancy implementation, Johnson [122] claims that also *software redundancy* and *time redundancy* can be applied. The first one denotes parts of a software implementation such as validity checks that are not strictly necessary to perform the required task but shall improve reliability of the execution. The second one is used to distinguish between *permanent* and *transient* faults. Here, a processor may for example repeat a computation if an error was detected in the result to determine if a fault is permanent.

Another disambiguation relevant in this context is *duplicating* and *diverse redundancy*. As pointed out by Mok, Goh, and Segaran [8] duplicating a device is an appropriate measure against random failures, but will not protect against design weaknesses of the component in question. Here, a failure due to a design weakness that may affect all instances of the same component is referred to as systematic failure. Implementing two units of a different design, however, will require a larger implementation effort but can also protect against shortcomings in the design of one of the components.

Resulting from the considerations made in this section, the author concludes that the systems architecture of the TUBiX20 platform is to be designed towards a high level of availability, while interruptions of the mission service are generally tolerated. However, the critical subsystems, i.e. the COM, the EPS, and the OBC shall be configurable towards higher reliability. The platform shall therefore allow for the implementation of diverse redundancy for these critical subsystems. Furthermore, no single fault shall lead to a terminal failure of one of the critical subsystems or to a failure of any other subsystem that cannot be recovered by intervention from the ground. Finally, variants shall be supported that comply to a number of boundary conditions regarding system-level robustness to ensure that the overall complexity can be reduced sufficiently for missions with generally moderate requirements.

3.2 Subsystems Architecture and Scalability

According to the findings presented by the author in Section 2.1, diverging requirements will be imposed on the individual satellite variants of a platform by a specific mission. Therefore, a number of the spacecraft's performance parameters need to allow for scaling and certain features may need to be added or removed. In the following, the individual subsystems and the satellite's software are analysed regarding required scaling options and their associated performance range. At the same time, high-level implementation details are presented and motivated.

3.2.1 Structure and Mechanisms

The structure of a satellite arranges the components according to their individual requirements, provides heat conduction paths within the spacecraft as well as shielding against radiation. Thereby, it needs to withstand the mechanical loads the satellite is subjected to during launch. Another aspect that is strongly influenced by the structure is the satellite's integration process.

For the TUBiX20 platform, the design of the structure is furthermore influenced by the requirement to support different CubeSat form factors (i.e. 6, 12, 16 and 27 U).

Within a masters thesis supervised by the author, different structure concepts for 12 and 16 U CubeSats were evaluated focussing on a maximised payload volume and a time-optimised integration process [123]. Based on the findings of this thesis, a structural design that gathers all components on the six outer panels of the primary structure was derived. Furthermore, it could be shown that secondary structure such as mounts for sensors or avionics compartments may be designed for the use across different form factors to maximise the potential for reuse.

In order to optimise the integration process for TUBiX20-based spacecraft, a harness concept developed by the author was implemented into the structure design realised in the thesis. Here, interconnections between the panels are realised such that each panel including all mounted components can be detached from the satellite without releasing any cables or other elements. The components that are attached to the panels are in turn interconnected by means of printed circuit board (PCB) distribution boards and board-to-board connectors, facilitating

straightforward integration or removal of any single component. For more details of the described harness approach, the reader is referred to Section 4.3.3.

The design approach developed in the thesis was extended towards 6 and 27 U form factors to establish a unified design philosophy of primary and secondary structure that can be applied across all TUBiX20 platform variants. It could be shown that while a number of structural elements are directly affected by the dimensions of the spacecraft, a common design and simulation approach may be established between the different form factors. The presented structure design is being implemented for the first time within the QUEEN mission (cf. Section 4.3.3). Here, it could be shown that especially the harness concept can be applied widely independent from the spacecraft's form factor.

For 27 U spacecraft, launch containers are currently not applied and separation systems are used instead. Nevertheless, implementing a standardised form factor promotes standardisation and may thus reduce development time. On the other hand, customisation of the form factor may be desired for specific missions. Examples here are the missions TechnoSat (cf. Section 4.1) and TUBIN (cf. Section 4.2) that build on an individual form factor.

The total ionising dose (TID) received by a component within the spacecraft can be simulated as a function of the provided shielding. The result is customary given in millimetres representing the uniform wall thickness of a aluminium sphere around the device in question.

For an evaluation of the TID values that can be expected and to analyse the impact of shielding, a simulation in the Space ENVironment Information System (SPENVIS) of the European Space Agency (ESA) [124] is performed by the author. Apart from the applied shielding, the TID is mainly affected by the mission duration, the orbit, as well as by the launch date that defines the solar activity within the mission. Here, the mission duration is set to be 1 year and the launch date is assumed to be the first of January, 2025 as the current solar cycle 25 is expected to peak in this year according to Labonville, Charbonneau, and Lemerle [125].

Figure 3.1 shows the radiation dose deposited in silicon (Si) as a function of the orbital height for different inclinations and shielding thicknesses. According to Sinclair and Dyer [22], it can generally be expected that the impact of increasing the thickness of aluminium shielding beyond 5 mm is low. Therefore, Figure 3.1 plots the TID values for 1 mm shielding for inclinations of 0, 30, 60 and 90 degrees,

while the largest value received for these inclinations is plotted against the orbital altitude in grey for shielding thicknesses of 2 and 5 mm.

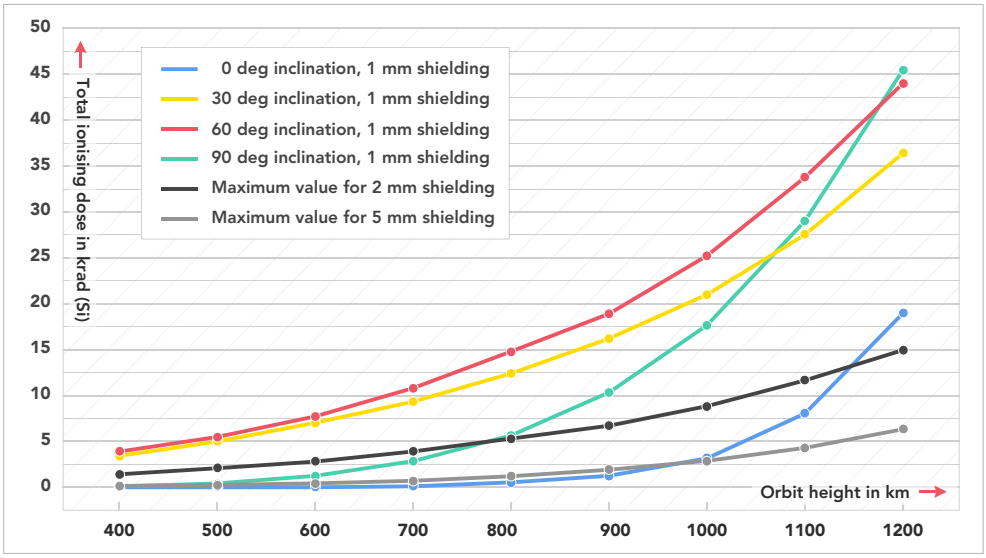

Figure 3.1: Simulation results for the TID received by a silicon component of a satellite for different orbital altitudes and inclinations assuming shielding of an aluminium sphere with 1 mm wall thickness and one year mission duration. Additionally, the highest values received for either 0, 30, 60 or 90 degrees inclination for an aluminium sphere with 2 and 5 mm wall thickness are plotted against the orbital altitude in grey.

In Section 4.1.3 the calculation of the shielding thicknesses at various points within the structure of the TechnoSat spacecraft is presented.

Mechanisms are mainly required for the platform to unfold solar panels or antennas. The design of the latter is independent of the form factor and can thus be used across all platform variants without modification. While the solar panel area may relate to the form factor, elements such as hinges and release mechanisms can be designed such that they can be applied regardless of the panel size (cf. Section 3.2.3).

In this context, a deployable solar panel for 6, 12 and 27 U TUBiX20-based satellites was developed in a masters thesis supervised by the author [126]. The outcome of the thesis is a design for a modular solar panel that supports the implementation as single, double or triple variant to support all power generation

options discussed in Section 3.2.3. The developed design will be implemented in the single-deployable-panel variant within the QUEEN mission for the first time.

3.2.2 Thermal Control System

The thermal control system (TCS) is responsible for maintaining a thermal environment within the spacecraft that allows for the operation of satellite platform and payload. Implementations of the thermal control system can be divided into two categories, namely passive and active systems (cf. [127, 128]) that are briefly introduced in the following.

Passive thermal control systems aim at maintaining thermal conditions that agree with the requirements of the spacecraft's components without the use of active elements such as heaters or pumped fluid loops. This can be achieved by optimising the arrangement of the spacecraft's individual components to match their heat dissipation, as well as by adjusting the thermal resistance within the interfaces of certain elements. Here, thermal films can be used to increase the thermal coupling while isolating plates or cloth facilitate a reduction of the heat exchange at selected interfaces. Furthermore, structure materials can be selected according to their heat transfer capacity to aid the TCS.

More stringent thermal requirements of the payload, increased heat dissipation within the satellite or a limited thermal capacity of the structure may rule out the use of entirely passive thermal control for specific missions. Here, active control elements, such as heaters or thermo-electric coolers can be added to the system.

Elliott [129] found that another distinction can be made in the use of the outer surfaces independently of whether active elements are used or not. The outer surfaces of larger satellites are commonly covered with multi-layer insulation (MLI) to the greater extent to limit the heat exchange with the environment. Furthermore, the solar panels are usually realised as deployable structures that are thermally decoupled from the spacecraft. Radiators that are pointed towards free space are used to dissipate the excess heat energy produced by the spacecraft. Here, heaters may be required to realise operational modes with reduced internal energy dissipation. In contrast, small satellites often implement TCS that use coatings, films, paintings, or other finishes to adjust the optical properties of the spacecraft's outer surfaces. In this manner, the heat flux between the satellite and the environment can be adjusted to a certain extend. This is especially required to

compensate the impact of the optical properties of the solar cells if body-mounted solar panels are implemented.

Small satellites are usually targeting mainly passive TCS implementations to limit complexity and power consumption [130, 131]. However, Tuttle, Barraclough, and Dudziak [132] claim that the complexity of the TCS of small satellites will increase in the future, which will also lead to the consideration of active thermal control elements. This is due to the ever-increasing requirements being imposed on the TCS of small satellites as these spacecraft are considered for more and more sophisticated applications. In this context, the requirement to survive extended periods without active attitude control (cf. Section 3.1) may impose additional challenges to the thermal design especially for variants with high energy turnover.

Due to the nature of their application, passive thermal control design measures can be applied largely independent for different platform variants. In order to be able to support a broad variety of payloads, active thermal control elements are expected to be required for certain TUBiX20 missions. In this context, Yang et al. [133] have shown that unit-level active thermal control efforts can effectively stabilise the thermal environment for dedicated payloads without having a large impact on the remainder of the platform. Therefore, active thermal control elements and their respective control software that may be implemented for specific missions are expected to be largely independent from the remainder of the TCS implementation.

The simulation tool chain that is used for simulating the TCS for TUBiX20-based satellites comprises a self-developed pre-calculation tool that outputs time series of the heat flux for all outer surfaces of the satellite which are then fed into a finite-element-method (FEM) simulation. In this manner, the same FEM model that is used for the thermal simulations can also be used to investigate the thermo-elastic behaviour of the structure for the case of high heat loads or demanding relative position accuracy requirements of certain elements. This was for example used in the TUBIN mission (cf. Section 4.2) to evaluate the thermo-elastic behaviour of the structural elements between the payload cameras and the star trackers to analyse the impact on the attitude determination accuracy.

The overall work flow for the TCS simulations was developed by Kühn in a masters thesis that was supervised by the author [134] and later published in [135][1].

[1] Publication with contributions of the author.

3.2.3 Electrical Power System

The electrical power system (EPS) of a satellite fulfils four major tasks, namely power generation, storage, conditioning, and distribution. Furthermore, the system needs to be monitored and controlled. Figure 3.2 illustrates the tasks of the EPS along with their power interconnections and the monitor and control flow between the different tasks.

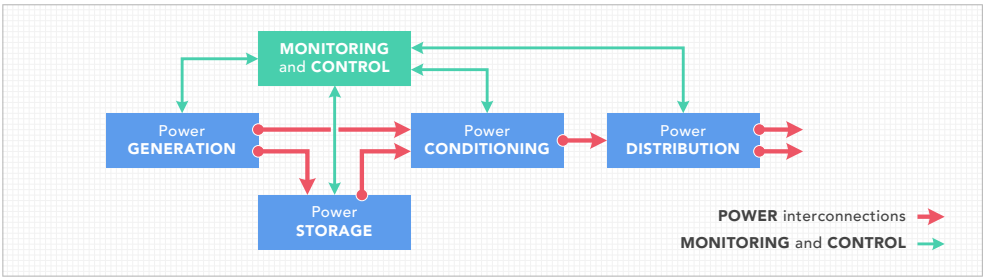

Figure 3.2: Tasks of a satellite's power system along with the power, as well as the monitor and control flow between the different tasks

As customary for satellites operating in LEO, solar cells are used for power generation, while secondary batteries are implemented to realise power storage for the TUBiX20 platform. In the following, the EPS is analysed in more detail and major design decisions are motivated. To this end, general aspects like the system's overall architecture and fault tolerance considerations are discussed before each task of the power system is analysed regarding its potential for scaling.

Fault Tolerance

Following White and Miles [136], fault tolerance in power systems can be achieved by the implementation of redundancy. Here, protection against any single fault may be realised by duplicating the entire system. Figure 3.3 shows the two paths of a completely redundant EPS. Keeping both paths of the system fully independent of each other would eliminate the risk that a fault on one path may influence the other path. However, a single fault may now disable one entire path. By introducing links between the power paths, the impact of a single fault may be reduced down to the affected function itself. While the effect of the links may

vary for different power system implementations, a generalised discussion is given in the following.

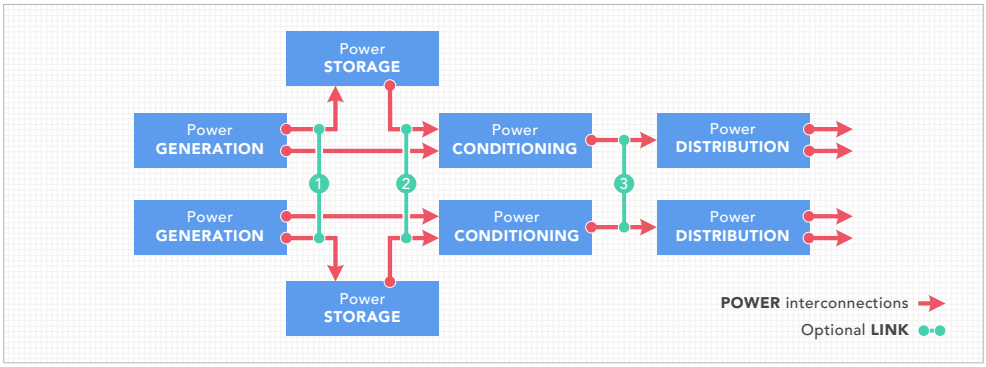

Figure 3.3: Diagram of a redundant power system indicating the points were links between the two power paths can be introduced into the system. These links can decouple a fault in a single block from certain other blocks in the same path.

If established in the design, the link that is denoted with (1) in Figure 3.3 would enable battery charging, even if power generation on this path is disabled. Furthermore, both solar paths would still contribute to charging the remaining battery if one battery is lost. However, as power generation and power storage capacities are usually closely matched, this would only be relevant for very specific mission scenarios. By introducing the link that is labelled with (2) in Figure 3.3 it can be achieved that power conditioning is still performed by both paths during eclipse in the case that one battery fails. More importantly, the entire power generation and storage potential can still be used, if one of the power conditioning units fails. If the last link, that is marked with (3), would be present in a system, power distribution would be unaffected by any fault on both paths. However, this link needs to be implemented individually for each power level provided by the EPS.

While limiting the impact of a single fault on the overall system, each link between the two redundant paths in the power system introduces significant complexity. Furthermore, there is a risk associated with cross-strapping the two power paths. The fact that both power paths can supply the next module of the power supply chain in turn also means that a short circuit on the input of the module in question may affect both power paths. This can be mitigated with the introduction of fuses that would separate the faulty module from the rest of the system in case

of a short circuit. However, when considering a fault that results in a module drawing an increased amount of power that is still below the fuses threshold, this may be considered as single failure that may at least degrade the overall system's performance.

Based on this considerations, only the link denoted with (2) in Figure 3.3 will nominally be considered for the TUBiX20 power system, as it significantly improves the robustness of the system, while complexity and parts count are lower than for realising the link denoted with (3).

The described overall architecture of the EPS was implemented and demonstrated in orbit within the missions TechnoSat (cf. Section 4.1) and TUBIN (cf. Section 4.2).

Power Generation

The power generation capacity of a specific platform option is defined by the number of solar cells that can be directed towards Sun simultaneously. A selection of solar cells that are suitable for the application in small satellites is listed in Appendix C. For the TUBiX20 platform, the 3G30C solar cell of AZUR SPACE Solar Power GmbH with a size of $40 \times 80\,\mathrm{mm}^3$ [137] is selected as reference.

For the further considerations, the following notions are being defined for solar power generation based on solar cells. To obtain the desired voltage, a number of solar cells is connected in series. This group of cells is called a *string*. A number of these strings are then connected in parallel to form the two solar *paths* required to provide redundancy. Each path may include strings on several *solar panels*, while each panel in turn may host strings from both paths. Finally, all solar panels that are aligned towards the same direction form a solar *array*.

As a trade between generated power and complexity, five different options are considered for the primary solar array of each platform variant, namely one single body-mounted panel, as well as one, two, four, or six deployable panels in addition to the body-mounted one. Additional panels may be mounted to the remaining sides of the spacecraft to ensure that sufficient power is generated even in if the primary solar array is not directed towards the Sun.

Figure 3.4 exemplary shows the TUBiX20-S, the TUBiX20-M, and the TUBiX20-L variant of the platform with one body-mounted and six deployable panels each.

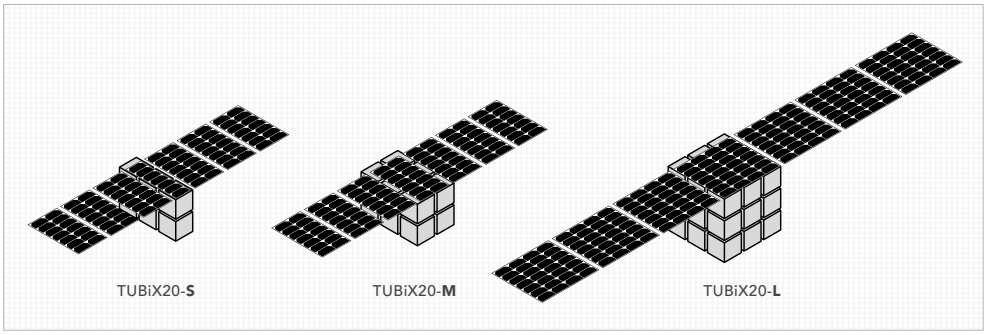

Figure 3.4: Exemplary display of the TUBiX20-S, the TUBiX20-M, and the TUBiX20-L platform variant, each with one body-mounted and six deployable panels. All spacecraft are shown using the same scale.

To determine the maximum number of solar cells a certain solar panel can be equipped with, the amount of cells per string needs to be defined. On the one hand, this number needs to be high enough to limit the current for larger panel configurations. On the other hand, it needs to be small enough to allow for the optimal use of the given space for different panel options. In order to preserve flexibility in combining different solar panel sizes within a single spacecraft, the number of solar cells in one string shall be the same for all panel sizes.

There are four panel sizes being considered in this context, which are indicated by the involved number of CubeSat unit surfaces, $3 \times 1\,\mathrm{U}$, $3 \times 2\,\mathrm{U}$, $4 \times 2\,\mathrm{U}$, and $3 \times 3\,\mathrm{U}$. As mentioned before, solar cells with a size of $40 \times 80\,\mathrm{mm}$ are assumed for dimensioning of the panels. From these constraints a string length of seven cells, delivering a voltage of 17.1 V at peak power [137] is found as a suitable compromise. The different panel configurations that are considered for the TUBiX20 platform-based on this string size are presented in Table 3.2.

The electrical peak power values given in Table 3.2 assume BOL operation of the cells at the maximum power point (MPP), a panel temperature of 28 °C, and perpendicular irradiation with $1\,367\,\mathrm{W\,m^{-2}}$ [137]. However, to estimate the electrical power generated on orbit within a specific mission the panel's temperature, the radiation induced degradation, the irradiation angle, as well as the radiation power of the Sun need to be considered. Furthermore, the amount of power generated by a satellites solar panel is influenced by the way the solar panel is operated.

Table 3.2: Power generation capabilities of the solar panel configurations considered for the TUBiX20 platform. The values are considering MPP operation at BOL, a panel temperature of 28 °C, and perpendicular irradiation with 1 367 W m^{-2} [137].

Area of the panel[a] cm^2	Number of strings	Number of cells	Peak power W
10×30	1	7	8.51
20×30	2	14	17.03
20×40	3	21	25.54
30×30	4	28	34.05

[a] Only intended as reference for the configuration, the effective area is larger

To effectively exploit the area provided from their individual form factor the missions TechnoSat and TUBIN deviated from this specification and implemented six instead of seven solar cells per string. However, this difference does not result in a significant deviation from the presented EPS architecture.

According to Dakermanji and Sullivan [7], satellite power systems can be divided into two major groups, namely direct energy transfer (DET) and maximum power point tracking (MPPT)[2] systems. Here, DET implementations are characterised by the fact that the energy generated by the solar panels is directly supplied to the loads without series regulation. MPPT systems are capable of varying the solar panel voltage to maximise the panel's power generation capabilities independently of influencing factors such as the temperature. Both approaches can be implemented in different variants. An overview over power implementations that are traditionally applied for satellite applications can be found in [138].

However, with the introduction of modern COTS components additional power system architecture variants have been implemented that may not comply with the aforementioned classification. One example here is the power system of the University of Toronto's Generic Nanosatellite Bus (GNB). According to Bonin, Sinclair, and Zee [139], the system qualifies as DET system despite the fact that it is capable of performing MPPT. Therefore, the distinction is here rendered more precisely between systems that operate the solar panels at a fixed voltage when under load and systems that implement MPPT capabilities.

[2] MPPT is also often also referred to as peak power tracking (PPT) in literature.

Generally, the voltage at which the maximum power can be retrieved from the solar cells is dependent on the cell's temperature and also changes, to a lesser extent, over the spacecraft's lifetime due to cell degradation induced by radiation. Therefore, the efficiency of fixed-voltage operation reduces with larger temperature variations of the cells. This is accounted for by MPPT systems that adjust the cells' output voltage to always operate it at the MPP. A drawback for MPPT implementations is their potentially higher complexity as well as additional efficiency factors that may for example be introduced by the applied algorithm or the implementation of dedicated regulators. As larger solar array temperature fluctuations are to be expected for small satellites that are operated in LEO, MPPT systems are more suited for these missions according to Clark and Mazarias [140].

To illustrate the performance of both approaches when being operated at different temperatures, the behaviour of a single solar cell shall be analysed. According to Dakermanji and Sullivan [7], the cells current as a function of its operation voltage can be obtained by the following equation:

$$I_{\mathrm{op}} = I_{\mathrm{sc}} \left\{ 1 - C_1 \left[e^{\left(\frac{V_{\mathrm{op}}}{C_2 V_{\mathrm{oc}}} \right)} - 1 \right] \right\} \tag{3.1}$$

with:

$$C_1 = \left(1 - \frac{I_{\mathrm{mp}}}{I_{\mathrm{sc}}} \right) e^{\frac{-V_{\mathrm{mp}}}{C_2 V_{\mathrm{oc}}}}, \tag{3.2}$$

and:

$$C_2 = \frac{\frac{V_{\mathrm{mp}}}{V_{\mathrm{oc}}} - 1}{\ln\left(1 - \frac{I_{\mathrm{mp}}}{I_{\mathrm{sc}}} \right)}. \tag{3.3}$$

Here, the open-circuit voltage V_{op}, the short-circuit current I_{sc}, as well as current and voltage at the maximum power point (V_{mp} and I_{mp}) are characteristics of the specific solar cell that is implemented. As established before, 3G30C solar cells of the AZUR SPACE Solar Power GmbH are used as reference [137] for the following considerations. According to the cell's data sheet the temperature dependence of the cell voltage is described by:

$$V(T) = V + (T - 28°\text{C})\Delta V, \tag{3.4}$$

while the cell current's temperature dependence is given by:

$$I(T) = I + (T - 28°\text{C})\Delta I. \tag{3.5}$$

Table 3.3 lists the constants that are required to analyse the cell's performance as a function of its temperature.

Table 3.3: Performance and temperature dependency parameters of the 3G30C solar cell at BOL. The values assume perpendicular irradiation with 1 367 W m^{-2} [137].

Parameter	Symbol	Value	Unit
Average open-circuit voltage	V_{oc}	2 700	mV
Open-circuit voltage temperature gradient	ΔV_{oc}	−6.2	mV K^{-1}
Voltage at maximum power	V_{mp}	2 411	mV
Voltage at maximum power temperature gradient	ΔV_{oc}	−6.7	mV K^{-1}
Average short-circuit current	I_{sc}	520.2	mA
Short-circuit current temperature gradient	ΔI_{sc}	0.36	mA K^{-1}
Current at maximum power	I_{sc}	504.4	mA
Current at maximum power temperature gradient	ΔI_{mp}	0.24	mA K^{-1}

In Figure 3.5 a comparison between fixed-voltage and MPPT operation of a single solar cell is shown. The blue curve represents the power generated by the solar cell while being operated at 2 V over a temperature range of −20 to 120 °C with 100. The green curve shows the same efficiencies while the cell is operated at 2.2 V. MPPT operation with 100 overall efficiency over the given temperature range is represented by the red curve. It can be observed from the figure that for cases in which only small temperature changes are anticipated, the trade between MPPT and fixed-voltage performance is down to the efficiencies that can be achieved with both approaches. Additionally, it is confirmed that MPPT is generally expected to outperform fixed-voltage operation if larger changes in temperature of the solar arrays occur during operation.

When combining solar cell strings located on body-mounted and deployable solar panels in the same solar path, the differences of the temperature between both panel types needs to be considered. As the body-mounted panels cant radiate

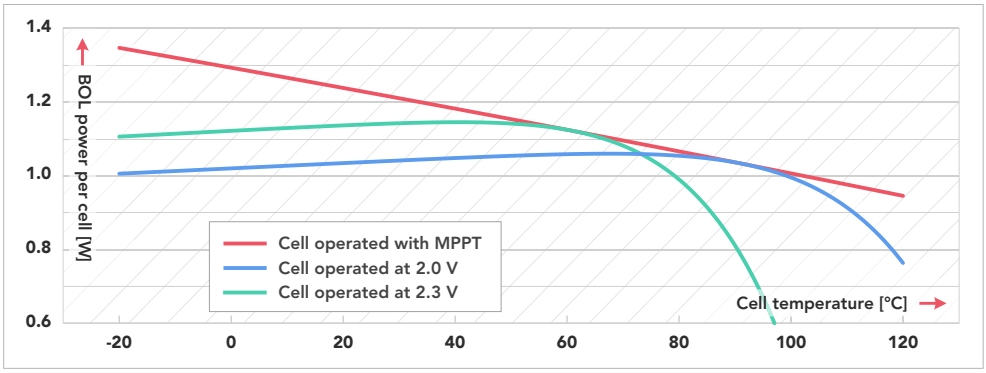

Figure 3.5: Comparison between fixed-voltage (2.0 and 2.2 V) and MPPT power generation of a single cell at BOL for a temperature range of −20 °C to 120 °C.

excessive heat towards free space, their temperature might be significantly higher when being compared to deployable panels.

To evaluate the influence of the diverging panel temperatures on the power generation capabilities, a single node thermal mathematical model (TMM) of both panel types shall be employed. To further simplify the model, it consists only of a single cell glued on a 1.6 mm PCB that is representing the panel structure and is covered with white paint on the back side. The panel is perpendicularly irradiated by the Sun while the backside is pointed towards free space for deployable panels and towards the spacecraft for body-mounted ones.

Figure 3.6 illustrates the solar panel TMM and indicates incoming and outgoing heat fluxes. While the larger part of the solar radiation is absorbed by the panel while being illuminated by the Sun, a smaller fraction is transformed into electrical energy that is supplied to the satellite. The panel radiates heat towards free space on the side the cells are mounted to. From the backside, radiation towards free space occurs for deployable panels, while body-mounted panels exchange heat radiation with the spacecraft.

The heat balance equation for a node of a TMM representing a spacecraft can generally be written as [141]:

$$
\begin{aligned}
m_i C_i \frac{\mathrm{d}T_i}{\mathrm{d}t} = {} & J_\mathrm{s}\alpha_i A_{\mathrm{solar},i} + J_\mathrm{a}\alpha_i A_{\mathrm{albedo},i} + J_\mathrm{p}\alpha_i A_{\mathrm{planetary},i} \\
& + Q_i - \sigma\epsilon_i A_{\mathrm{space},i} T_i^4 - \sum_{j=1}^{n} h_{ij}(T_i - T_j) \\
& - \sigma \sum_{j=1}^{n} A_i F_{ij} \epsilon_{ij} (T_i^4 - T_j^4).
\end{aligned}
\tag{3.6}
$$

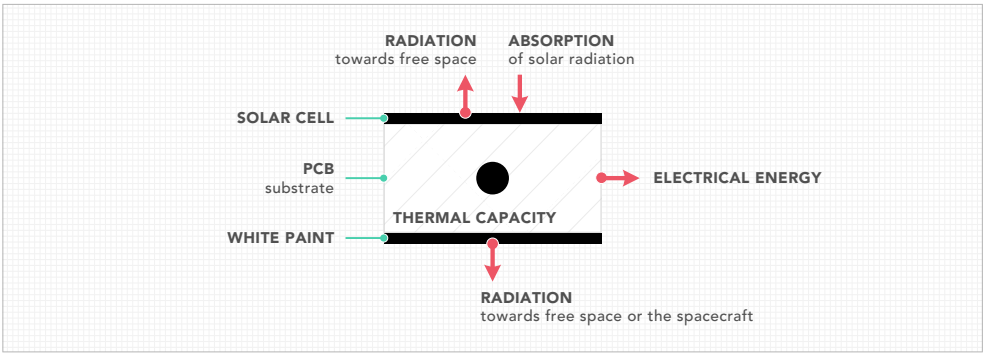

Figure 3.6: Overview of the simplified TMM representing a solar panel. Heat is absorbed from solar radiation and radiated into free space and additionally towards the spacecraft for body-mounted panels. Furthermore, a fraction of the solar radiation is transformed into electrical energy.

For the model at hand, heat input from albedo ($J_\mathrm{a}\alpha_i A_{\mathrm{albedo},i}$) and planetary radiation ($J_\mathrm{p}\alpha_i A_{\mathrm{planetary},i}$) are neglected and the dissipated heat (Q_i) is negative as it describes the fraction of the solar energy that is transformed into electrical energy. Furthermore, as a worst-case assumption and as its influence is expected to be minor for most designs, heat conduction ($\sum_{j=1}^{n} h_{ij}(T_i - T_j)$) is generally neglected for both panel variants. The view-factor F_{ij} for the heat absorption of the surfaces is not required, as all radiation is assumed to be perpendicular to the surface. Following these considerations, a transient calculation of the node's temperature can be performed with:

$$T_i = T_{i-1} + \frac{1}{mC}\Bigg[J_s\alpha_{\text{cell}}A_{\text{cell}} - Q_{\text{elec}} - \sigma\epsilon_{\text{cell}}A_{\text{cell}}T_{i-1}^4 - \sigma\epsilon_{\text{panel}}A_{\text{panel}}\left(T_{i-1}^4 - T_{\text{spacecraft}}^4\right)\Bigg], \tag{3.7}$$

for the body-mounted panel and with:

$$T_i = T_{i-1} + \frac{1}{mC}\Big(J_{\text{s}}\alpha_{cell}A - Q_{\text{elec}} - \sigma\epsilon_{\text{cell}}AT_{i-1}^4 - \sigma\epsilon_{\text{panel}}AT_{i-1}^4\Big), \tag{3.8}$$

for the deployable panel. Here, the emissivity for calculating the heat radiated by the body-mounted panel towards the spacecraft is approximated with 0.82 by using the following equation [141]:

$$\epsilon_{ij} = \frac{\epsilon_i\epsilon_j}{\epsilon_i + \epsilon_j - \epsilon_i\epsilon_j} \tag{3.9}$$

with both ϵ_i (solar panel side) and ϵ_j (spacecraft side) assumed to be 0.9. An overview of the parameters and values that were used for the simulation is given in Table 3.4.

Figure 3.7 gives an overview of the temperature development of both the body-mounted and the deployed solar panel. As the panels' temperatures converge to a fixed number during the Sun period regardless of the start temperature, this value can be used as initial condition for the eclipse simulation. In turn, the initial condition for the Sun period is derived from the end value of the eclipse simulation. Furthermore, the power generated by the solar panels when assuming lossless MPPT at BOL is plotted in the figure. It can be seen, that the power is comparatively higher at low panel temperatures right after entering the Sun phase and develops proportionally to the temperature throughout the Sun period.

The TMM, along with the solar cell equations, can now further be used to evaluate the impact of the MPPT implementation on the generated power for a combination of body-mounted and deployable solar panels. Here, one body-mounted together with one single deployable solar panel can be considered as a worst case if a

Table 3.4: Parameters of the single-node TMM build to evaluate the temperature of body-mounted and deployed solar panels. Here, the panel is represented by a single solar cell.

Parameter	Symbol	Value	Unit	Reference
Duration of Sun period	t_{sun}	3 600	s	-
Duration of eclipse period	t_{eclipse}	1 800	s	-
Area of the panel	A	$3.018\,0 \times 10^{-3}$	m^2	[137]
Mass of the panel	m	$9.657\,6 \times 10^{-3}$	kg	-
Panel's specific heat capacity	C	1 200	$\mathrm{J\,kg^{-1}\,K^{-1}}$	[142]
Absorptivity of the cell	α_{cell}	0.91	-	[137]
Emissivity of the cell	ϵ_{cell}	0.80	-	[141]
Panel's emissivity (paint)	$\epsilon_{\mathrm{panel}}$	0.82	-	[141]
Spacecraft's temperature	$T_{\mathrm{spacecraft}}$	30	°C	-
Heat radiated from the Sun	J_{s}	1 360.8	$\mathrm{W\,m^{-2}}$	[143]
Stefan–Boltzmann constant	σ	$5.670\,4 \times 10^{-8}$	$\mathrm{W\,m^{-2}\,K^{-4}}$	-

common voltage level is assumed for all panels. By identifying the operational voltage at which both panels together deliver the largest amount of electrical energy for every time step of the simulation MPPT applied to both panels in parallel can be simulated. In contrast, the MPP power value for both panels at their individual temperature is added up to simulate MPPT on panel level.

Here, the amount of electrical energy produced by both panels within one Sun period while performing MPPT on panel level is found to be 2.42 W h, while the value amounts to 2.29 W h for central MPPT. Thus it can be concluded that the power income of MPPT applied on panel level is 5.2 percent higher when being compared to a central tracking approach for this specific example. If the cell's voltage is constrained to 2.23 V, the optimal value for fixed-voltage power generation in this example, the power generated is 2.26 W h. This value is 6.7 percent below the energy generated with the panel level MPPT implementation. However, it needs to be noted in this context that while both MPPT implementations would be able to adopt to a change in the temperature environment the variation in temperature from the design values would degrade the performance of the fixed-voltage approach. It can be seen from Figure 3.5 that this would especially be relevant for the case where the panel's temperature is higher than anticipated as the power generation capabilities strongly decrease above a certain temperature. A countermeasure against this would be to lower the voltage the cell is operated

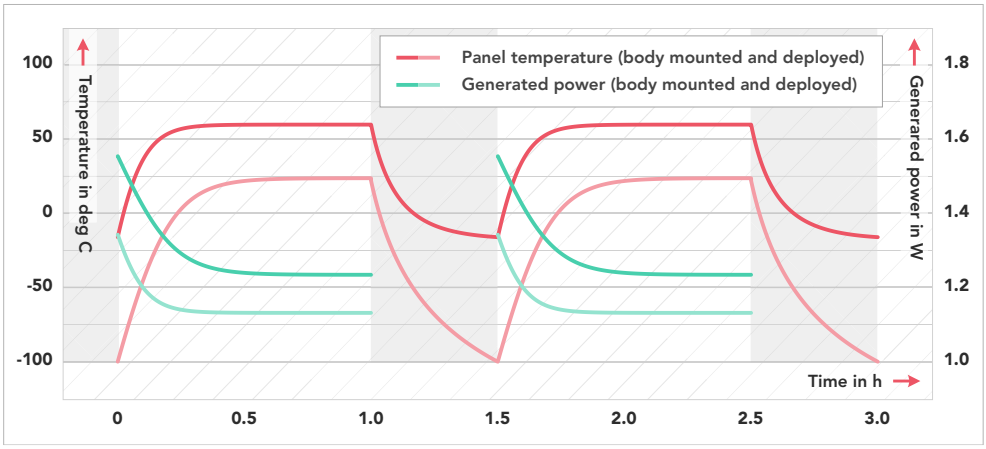

Figure 3.7: Temperature of a body-mounted and a deployed solar panel during two Sun and two eclipse periods along with the power generated by both panel types while being illuminated by the Sun.

at the expense of the power yield. If the voltage the panel is operated at is for example lowered to 2.0 V for the given setup, the power generated is already 13.1 percent below the value for MPPT applied on panel level. Furthermore, it needs to be noted that the presented simulation does not include any losses which may vary between the specific implementations and thus impact the comparison.

Another influencing factor that needs to be considered when evaluating the generation of electrical power by means of solar cells is the cells' degradation due to radiation. Here, the relevant parameters of the solar cell are given for several levels of damage equivalent fluence of 1 MeV particles in [137]. To obtain a worst-case value of the damage equivalent fluence for selecting the appropriate set of parameters a simulation in the SPENVIS tool of the ESA [124] is performed. The most significant parameters that influence the particle fluence a satellite is subjected to are the mission duration, the orbit, as well as the launch date as it defines the solar activity during the mission. For a worst-case estimate, the mission duration is assumed to be 5 years. Furthermore, the mission is set to start at the first of July, 2022 to cover the maximum of solar cycle 25, that is to be expected to peak in 2025 according to Labonville, Charbonneau, and Lemerle [125]. To determine the worst-case orbit in this context, different altitudes and inclinations are examined.

Here, it needs to be noted that the damage equivalent fluence can be given for different parameters of the solar cell, namely the maximum power, the open-circuit voltage and the short-circuit current. This is due to the fact that the 1 MeV particle fluence used for specifying the impact of radiation on the cells' performance produces a different degradation pattern than the radiation present on orbit and can therefore only be tuned to one of the aforementioned parameters. As the open-circuit voltage and the short-circuit current will be used to calculate the EOL performance of the cell, all three parameters are analysed in the following.

Figure 3.8 depicts the maximum power (P_{max}), open-circuit voltage (V_{oc}), and short-circuit current (I_{sc}) damage equivalent particle fluence values over altitudes between 400 to 1 200 km in steps of 100 km. Here, circular orbits and a mission duration of 5 years are considered. For each data point, the highest value from inclinations of 0, 30, 60 and 90 degrees is plotted.

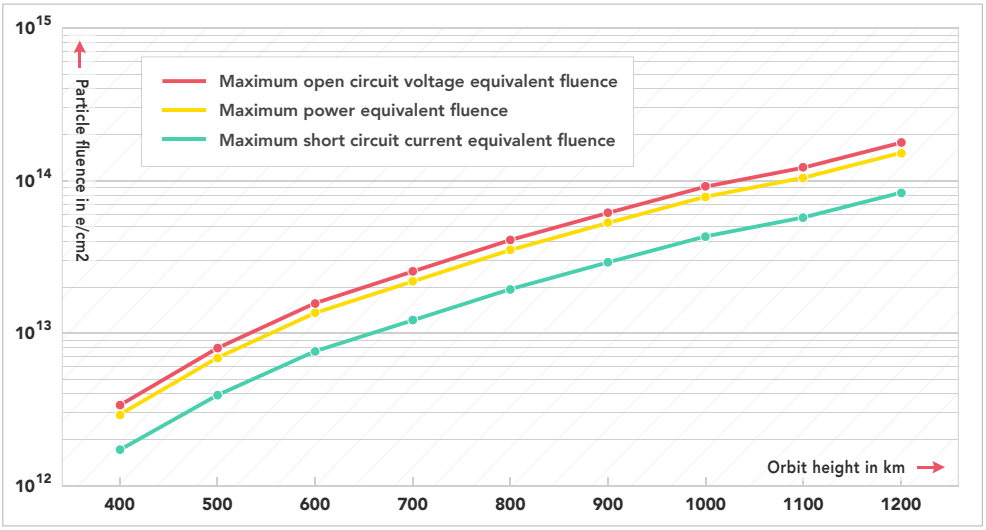

Figure 3.8: Particle fluence as a function of orbital altitude for a 5 year mission. The maximum power (P_{max}), open-circuit voltage (V_{oc}), and short-circuit current (I_{sc}) damage equivalent particle fluence are given for altitudes between 400 and 1 200 km. For each data point, inclinations between 0 and 90 degrees are considered, while only the maximum values are indicated in the plot.

For the maximum power equivalent fluence, the highest value of 1.521×10^{14} e/cm^2 can be found for a 1 200 km orbit with 60 degrees inclination. Furthermore, the highest values observed for the open-circuit voltage are 1.772×10^{14} e/cm^2 and

8.336×10^{13} e/cm^2 for the short-circuit current damage equivalent particle fluence. According to this, the lowest fluence value of 2.5×10^{14} e/cm^2 that is given in [137] is to be used for assessing the cell's EOL performance. Based on this, the parameters that describe the solar cell's characteristics at EOL are summarised in Table 3.5. It needs to be noted here that the maximum power equivalent fluence value obtained for a one year mission in orbits up to 600 km is only one percent of the lowest fluence values given in the solar cell's data sheet. Based on this, the radiation induced solar cell degradation for typical small satellite missions in LEO that are expected to operate for one to three years is expected to be insignificant.

Table 3.5: Parameters of the solar cell for the EOL. All values assume a panel temperature of 28 °C and a perpendicular irradiation with 1 367 W m^{-2} [137].

Parameter	Symbol	Value	Unit
Average open-circuit voltage	V_{oc}	2 616	mV
Open-circuit voltage temperature gradient	ΔV_{oc}	−6.5	mV K^{-1}
Voltage at maximum power	V_{mp}	2 345	mV
Voltage at maximum power temperature gradient	ΔV_{oc}	−6.8	mV K^{-1}
Average short-circuit current	I_{sc}	518.5	mA
Short-circuit current temperature gradient	ΔI_{sc}	0.33	mA K^{-1}
Current at maximum power	I_{sc}	503.2	mA
Current at maximum power temperature gradient	ΔI_{mp}	0.20	mA K^{-1}

By using the BOL and EOL parameters, the degradation of the solar cell's performance can now be depicted in Figure 3.9. Similar to Figure 3.5, here the effect is shown both for MPPT and fixed-voltage operation of the cell. It can be observed that while the MPP performance is nearly uniformly degraded, the effect is more perceivable at the higher end of the covered temperature range, while the power output is nearly unaffected at lower temperatures for fixed-voltage operation.

Another parameter that influences the generated power is sunlight's incident angle α, whose impact on the total power generated can be calculated by [16]:

$$P(\alpha) = P \cos(\alpha) \tag{3.10}$$

for angles up to 50 degrees. Above that value, the Kelly cosine is to be applied, as less power is generated than the mathematical prediction would suggest [16].

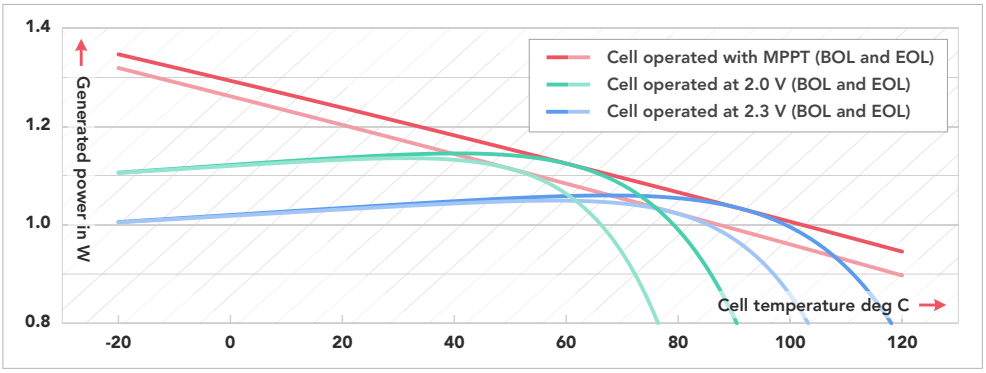

Figure 3.9: Visualisation of the impact of the radiation induced solar cell degradation. The blue and the green curves represent an operational voltage of 2.0 V and 2.2 V, respectively, while the red curves show the degradation when the cell is operated at the MPP.

Finally, seasonal variations of the solar flux will influence the power that is generated by the solar cells. According to Kopp and Lean [143], the average total solar irradiance in LEO was measured with $1\,360.8 \pm 0.5\,\mathrm{W\,m^{-2}}$ for the solar minimum in 2008 and the value will be higher by $1.6\,\mathrm{W\,m^{-2}}$ for the solar maximum. Based on this and with the seasonal variations that introduce a factor of 0.967 at the summer solstice and 1.034 at the winter solstice, a minimum of $1\,315.4\,\mathrm{W\,m^{-2}}$ and a maximum of $1\,409.2\,\mathrm{W\,m^{-2}}$ can be calculated [16]. Here, it needs to be noted that the efficiency of the solar cell is dependent on the irradiance. For the given cell, an average efficiency of 29.5 percent is stated for an irradiance of $1\,367\,\mathrm{W\,m^{-2}}$ while the efficiency is 29.8 percent for an irradiance of $1\,358\,\mathrm{W\,m^{-2}}$ according to that data sheet [137]. As no further data is available on the variation of the efficiency as a function of the irradiance and the given value suggest a minor influence, this correlation is neglected in the following.

Now the cell's overall performance can be obtained by Equation 3.11, where J_{Sun} is the irradiance of the Sun, α is the panels average Sun angle and $\eta_{\mathrm{PPT}} = 0.9$ is the overall efficiency of the PPT, that is assumed to be constant for all operating points [144]:

$$P(T) = \frac{V(T) \cdot I(T)}{1367W} \cdot J_{\mathrm{Sun}} \cdot \cos(\alpha) \cdot \eta_{\mathrm{PPT}} \tag{3.11}$$

It could be shown that, dependent on the efficiencies that can be achieved for both approaches, a fixed voltage operation of the solar cells can achieve similar efficiencies as the MPPT approach. However, despite the fact that the implementation of the fixed-voltage approach can be considered less complex it is regarded as less suited for a small satellite platform. This is due to the fact that such an approach requires very accurate knowledge of the temperature expected for the solar panels and, furthermore, needs to be tuned to each application individually, which in turn reduces the flexibility.

This could also be confirmed for the missions TechnoSat (cf. Section 4.1) and TUBIN (cf. Section 4.2), where the solar cells are operated with a fixed voltage. In order to mitigate the risk to exceed the maximum cell voltage at a certain operating point, a conservative threshold of 2.0 V per cell was selected, which effectively limits the power generation capabilities for these missions.

Therefore, it is concluded that MPPT shall generally be implemented for future missions based on the TUBiX20 platform. A discussion of known MPPT implementations and their advantages and disadvantages is beyond the scope of this thesis but were for example discussed by Esram and Chapman in [145] and by Nahak and Pal in [146].

In Figure 3.10 power options for the different TUBiX20 platform variants are illustrated. For each solar array configuration, three different values are calculated. The coloured bars that are given for each panel indicate the power that is generated under a generalised set of nominal conditions, while the error bars indicate the maximum and the minimum power that can be expected for the panel configuration at hand. More specifically, the following parameters were applied to generate the three different values for each configuration:

1. For deriving the reference value for the minimum power expected to be generated by a given panel configuration, the cell operated at EOL (assuming a damage equivalent fluence of 1 MeV particles of $2.5 \times 10^{14}\,\mathrm{e/cm^2}$) with a cell temperature of 100 °C and 20 degrees average pointing error. Furthermore, the minimum solar irradiation of $1\,315.9\,\mathrm{W\,m^{-2}}$ and MPPT applied on panel level with an efficiency of 0.9 (cf. [144]) is assumed.
2. For the nominal case, cell temperatures according to the presented solar panel TMM (cf. Figure 3.7) as well as BOL cell performance are assumed. The solar cells are irradiated with an average solar irradiation of $1\,361.0\,\mathrm{W\,m^{-2}}$ and the average pointing accuracy is 5 degrees. Here, the average power

over one Sun phase with MPPT applied on panel level with an efficiency of 0.9 (cf. [144]) is shown.

3. The maximum power that can be expected from the panels is determined by assuming MPPT operation of the solar cells at BOL and a temperature of $-100\,^{\circ}\mathrm{C}$ while being exactly aligned perpendicular to the Sun with $1\,405.7\,\mathrm{W\,m^{-2}}$ irradiation.

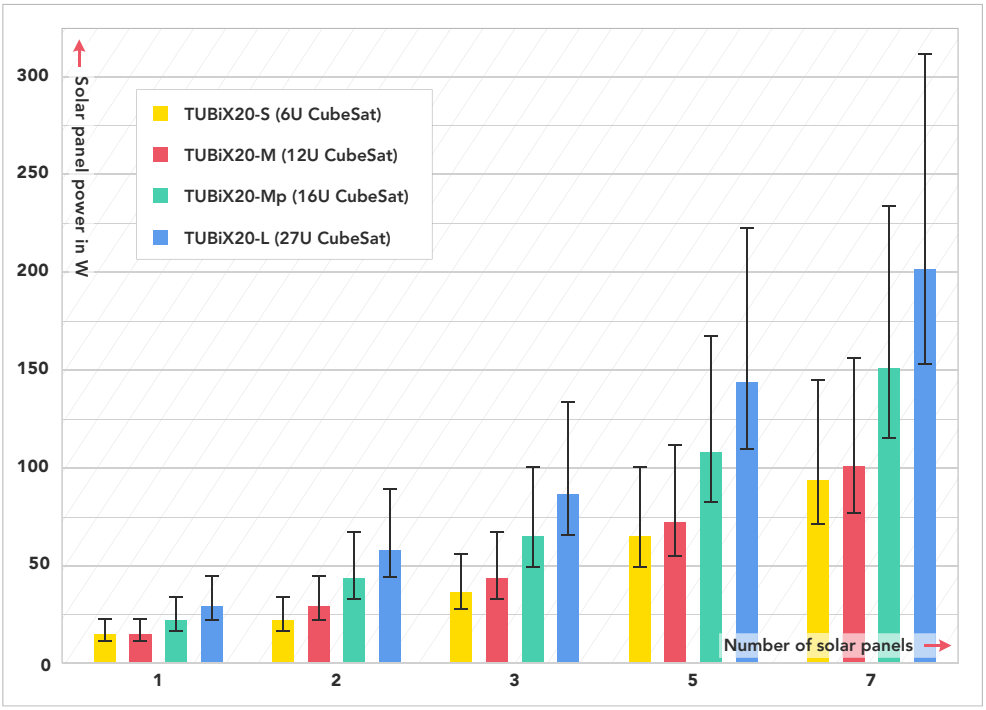

Figure 3.10: Output power in watt for the four solar panel configurations of each size variant of the platform. The coloured bars represent the expected average power for the presented scenario, while the error bars indicate minimum and maximum output power.

Safe Mode Platform Consumption

Based on the values presented above, a worst-case estimate of the power consumption allowed for the platform in safe mode can be performed. This is necessary to evaluate the requirement for the platform to survive larger periods of time in free

tumbling (cf. Section 3.1). Here, a TUBiX20-S-based satellite with four body-mounted solar panels each two accommodating 14 and 7 solar cells, respectively, is assumed. Furthermore, it is expected that all six surfaces of the satellite receive an equal amount of solar illumination when considering a longer period of time and that irregularities on a shorter time span are buffered by the batteries. Following these assumptions, the effective power generated in the Sun phase is one sixth of the minimum capacity of the four solar panels, which results into a maximum allowed safe mode power consumption of 5.47 W for the platform to guarantee a positive overall power balance.

Power Storage

While different battery technologies have been applied for satellite applications in the past, Chin et al. [147] claim that lithium–ion (Li-ion) is the energy storage option that is nowadays primarily used in NASA missions and that Li-ion batteries are likewise the preferred choice for CubeSat applications. This is mainly due to the combination of comparatively high operational lifetimes with very high specific energies offered by these kind of cells. Furthermore, there is a wide selection of COTS cells available that have successfully been used for small satellite applications. Based on these findings, Li-ion battery cells are chosen as energy storage technology for the TUBiX20 platform.

Generally, charging of a satellite's battery can be implemented by simply connecting battery, solar panel and loads in parallel or by implementing a charge regulator. While the first approach has been presented in conjunction with Li-ion battery technology by Patel in [16] in the past, modern COTS Li-ion cells are expected to require special charge profiles so that a charge regulator needs to be implemented.

Based on this, a set of at least one battery and the corresponding charge regulator is required for each of the two power paths of the platform. Here, scaling of the power storage capacity can either be realised by varying the number of battery packs with their associated chargers per path or by adjusting the size of the battery packs with one single pack per path. Here, the overhead in mass and volume that would be generated when following the first approach is expected to be comparatively large, therefore, a scaling of the battery packs is foreseen for the TUBiX20 platform.

A first estimate of the range of battery capacities that are required for different missions can be obtained if the power consumption of the spacecraft is assumed to be constant throughout the orbit. Now, the batteries' energy storage capacity (E_{battery}) can be calculated using Equation 3.12, with the depth of discharge (DoD), a combined charge efficiency of the battery cell and the charge regulator of (η_{charge}), as well as the duration of sunlight (t_{Sun}) and eclipse (t_{eclipse}):

$$E_{\text{battery}} = P_{\text{solar}} \frac{1}{DoD} \frac{1}{\eta_{\text{charge}}} \frac{t_{\text{eclipse}}}{t_{\text{Sun}}} \tag{3.12}$$

By assuming a DoD of 30 percent [148], a charging efficiency (η_{charge}) of 90 percent [144], and an orbit that provides one hour of sunlight and half an hour eclipse, the battery capacities as shown in Figure 3.11 can be obtained. It needs to be noted that no redundancy is considered here, i.e. a failure in one of the batteries would double the DoD.

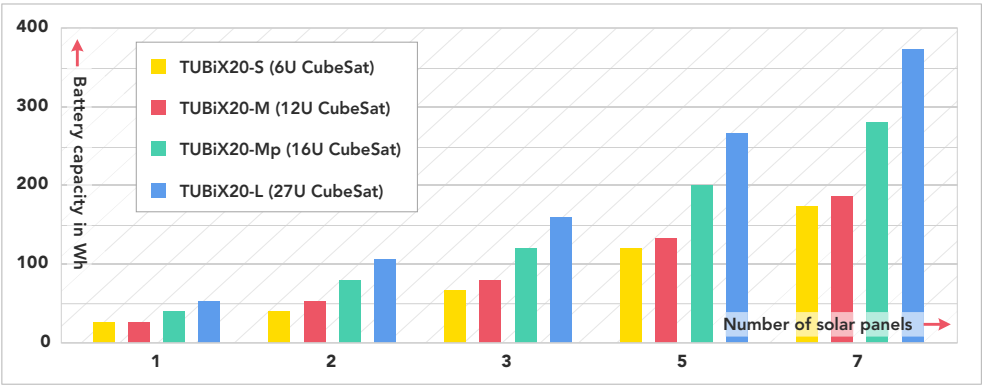

Figure 3.11: Estimated power storage capacities for the considered solar panel configurations of the different TUBiX20 platform size variants in watt-hours. The x-axis denotes the number of solar panels, while the y-axis indicates the power storage capacity required for the given option.

For the TechnoSat mission, a considerably lower DoD of five percent was chosen as the implemented battery cells had no flight heritage. However, this would result in a very high required battery capacity if the above methodology was used (i.e. 370 W h with 25 W average solar power during the Sun phase). Therefore, mission operations were planned such that the overall power consumption during eclipse was reduced to a maximum of 6.5 W h, resulting in a required battery capacity of

131 W h. Based on the available battery cell sizes, a total capacity of 144 W h was implemented for the mission (cf. Table 4.1).

For TUBIN a nominal DoD of 30 percent was defined and 30 W are generated in Sun pointing. According to this, a battery capacity of 74 W h would be required based on Equation 3.12. However, for TUBIN also scenarios in which the battery is not fully charged in one Sun phase before it is discharged again in eclipse were considered for battery dimensioning (cf. Section 4.2.5). Based on this, an overall storage capacity of 117 W h is implemented for TUBIN.

Power Conditioning and Distribution

Being systems-level considerations, the power conditioning and distribution requirements are discussed in-depth in Section 3.3 and the results are only briefly presented at this point. The EPS provides two independent power supply paths to the nodes, each comprising three regulated power lines of 3.3, 5.0 and 12.0 V (cf. Figure 3.17). Additionally, an unregulated power supply may be provided to components with high power consumption instead of the 12 V power line in order to minimise the conversion losses. Both power supply paths are operated in hot redundancy. In the case that other voltage levels are required by a component or payload to be connected to the platform, these are conditioned individually directly on the node the device is connected to.

Monitoring and Control

Monitoring and control of the EPS is performed by a dedicated computer, the EPS node (cf. Section 3.3.11). In order to be able to initiate and supervise the powering of the remainder of the spacecraft, the EPS node has a dedicated power supply, directly provided by the power conditioning units (PCUs). Furthermore, the EPS switches the power supply for the nodes (cf. Figure 3.18).

Conclusions

The power system of the of the TUBiX20 platform is based on two independent paths for power generation, storage, conditioning and distribution. Power generation is based on a variable number of solar cell strings comprising seven cells each.

The different platform size variants offer five different power generation options each ranging from a minimum nominal of 14 W for TUBiX20-S to a maximum nominal power of 201 W of generated power for TUBiX20-L.

Power storage is realised using a variable number of battery cells forming two battery packs, each one for both power paths. Here, the power storage capacities matching the generated power are estimated to be 27 to 373 W h. Both power paths each provide power buses with 3.3, 5.0 and 12.0 V to the nodes. If other voltages are required, they need to be generated directly on the node in question (cf. Section 3.3). However, for payloads or platform components with very high power consumption (e.g., propulsion systems or radio tranceivers) the 12 V supply might be exchanged in favour of an unregulated supply to reduce the conversion losses. The entire EPS is monitored, controlled and commanded via the EPS node.

3.2.4 Attitude Determination and Control System

The attitude determination and control system (ADCS) of a satellite uses sensors to establish the orientation of the spacecraft, while actuators are implemented to adjust its attitude. Varying requirements that concern the ADCS will mainly target the demanded accuracy in attitude knowledge and the precision, stability, and agility that is requested in pointing. A selection of commercially available attitude sensors and actuators that are suitable for the TUBiX20 platform are gathered in Appendix C.

Attitude Determination

Based on flight results of state-of-art missions (cf. the survey conducted in Section 2.1) and available sensor technology, three different attitude determination accuracy classes can be differentiated that are expected to meet the needs of the majority of missions in the investigated satellite mass range.

As shown by Slavinskis et al. [149] and Barschke et al. [150], coarse attitude knowledge in the range of several degrees can be achieved based on Microelectromechanical system (MEMS) magnetometers, Sun sensors and MEMS gyroscopes. This configuration would deliver sufficient accuracy for performing tasks such as Sun pointing for power generation, target pointing for data downlink or even low

resolution Earth observation. This configuration was successfully demonstrated in orbit for the TUBiX20 platform by the TechnoSat mission [151][3].

For missions that require arcminute attitude knowledge accuracy, star trackers are usually implemented [152, 153]. Due to the star trackers' significant exclusion angles for Sun, Moon, and Earth, two star trackers in a specific spatial arrangement may be required to minimise the periods where no star tracker attitude data is available. In the case that both star trackers are unavailable, gyroscopes are used to propagate the attitude, which imposes more stringent requirements on their accuracy when being compared to the coarse configuration. Arcminute accuracy will for example allow for performing most Earth observation or science missions. For the TUBiX20 platform, this configuration is implemented for the first time within the TUBIN mission (cf. Section 4.2).

Attitude determination accuracy in the range of arcseconds can be achieved, at least for limited periods of time, with the use of high-performance star trackers, as shown by Pong [44]. However, when aiming at such advanced determination accuracies, also effects like thermal expansion of the structure needs to be taken into account. This level of attitude determination accuracy will mainly be required for advanced science missions.

In addition to the sensor types that were already mentioned, there is number of less common attitude sensing approaches whose implementation may be suitable for specific missions. These include Earth horizon sensors [154] or stellar gyroscopes [155].

Attitude Control

Attitude control systems for small satellites are nowadays mainly implementing reaction wheels to deliver three-axis attitude control capabilities [156]. To desaturate the reaction wheels, magnetorquers are the most common design option. Depending on the implemented hardware, pointing accuracies in the range of arcminutes, as shown by Johnston-Lemke et al. [152] to arcseconds, as presented by Pong [44], can be achieved. Furthermore, specific requirements may target the pointing stability as well as the satellites agility, i.e. the time required for aligning an instrument towards a new target. These characteristics are influenced by the type and quality of the available sensors and actuators on the one hand,

[3] Publication with contributions by the author.

and the algorithms, filters, and controllers implemented in software on the other hand. Furthermore, calibration is an important factor for the accuracy that can be achieved with a given system.

In addition to the combination of reaction wheels and magnetorquers, there are less common actuator alternatives that are additionally considered for the TUBiX20 platform. Especially for missions beyond LEO, attitude control based on thrusters [157–159] is of interest, as magnetorquers cannot be applied for reaction wheel desaturation due to the absence of a sufficiently strong magnetic field. Furthermore, fluid-dynamic actuators (FDAs) have been demonstrated in space [11] and the combined use of fluid actuators with reaction wheels has been analysed by Grau et al. in [160]. Another actuator type that promises improved agility for small satellites are control moment gyroscopes (CMGs) [161, 162].

First orbit results of the attitude control capabilities that were generated with reaction wheels and magnetorquers as actuators within the TechnoSat mission are presented in Section 4.1.5.

Other attitude control methods that are less commonly implemented for small satellites include passive attitude control methods [163, 164] and spin stabilisation [165, 166].

Algorithms and Software

In order to support the proposed range of different sensor and actuator configurations, the attitude determination and control software architecture needs to support adding, removing, or exchanging hardware components according to the needs of a specific mission. Furthermore, a number of determination and control algorithms and filters need to be available to be able to support requirements imposed by different missions. A software architecture that was developed for the TUBiX20 platform and which offers the corresponding level of flexibility has first been published by Gordon and Barschke in [167] and is further detailed by Gordon in [168].

Fault Tolerance

Fault tolerance within the ADCS is mainly realised by redundancy both on the sensors' and on the actuators' side. Bos et al. [169] describe two general approaches

for fault tolerance in the ADCS system. The first method involves dedicated hardware for independent supervision of the attitude. If an unintended deviation is detected by the system, the spacecraft is transferred into safe mode. The second option, in contrast, seeks to identify failures using the given hardware and to reconfigure the system accordingly. Here, the first approach allows for straightforward design, but requires additional hardware. Furthermore, it may reduce the spacecraft's overall availability as interaction from the ground is required for recovery. The second method may allow the continuation of operation in case of an error and does not require independent hardware for supervision. However, these advantages come with a considerably larger implementation and verification effort.

The TUBiX20 platform shall support the implementation of both methods depending on the needs of a certain mission. Furthermore, hybrid approaches, that combine elements from both methods shall be possible. Sensors are mainly operated in hot redundancy as increasing the number of measurement points will result in higher accuracy. Furthermore, redundancy can be implemented by the use of different sensor types that measure different quantities, such as Sun sensors, magnetic field sensors or star trackers. The consistency of the sensor signals can also be revised by comparing different state quantities and by propagating the state quantities from the last determination cycle.

On the actuator side, redundancy can, for example, be implemented by the use of four reaction wheels that are arranged such that torque can still be applied to all axes in the case that one wheel fails [170]. For magnetorquers, redundant coils can be implemented in one single device [171], which may each be controlled by dedicated drive electronics.

Further insights into how fault tolerance is implemented for attitude determination and control within the TUBiX20 platform were detailed by Gordon in [168].

Conclusions

The most common scaling option for the attitude determination system is expected to be the addition of star trackers for missions with advanced accuracy requirements. Furthermore, rearranging the star trackers between missions might be required and less common sensor types may need to be introduced into the system. A combination of reaction wheels and magnetorquers will be the most common

set of actuators implemented to perform attitude control. However, alternative technologies, such as FDAs or thrusters may be considered as actuators for specific missions. Finally, fault tolerance will most commonly be implemented by operating a larger number of sensors and actuators than strictly required in hot redundancy.

3.2.5 Communications System

The communications system (COM) is associated with two major task, providing means to send telecommands to the spacecraft and receive its telementry as well as the transmission of payload data to the ground. While the telemetry and telecommand (TM/TC) link usually involves lower data rates and is designed towards reliability and availability, the payload data downlink is mainly characterised by the provided data throughput. A selection of commercially available transmitters, receivers, and transceivers that are suitable for the TUBiX20 platform are gathered in Appendix C.

Telemetry and Telecommand

According to Bouwmeester and Guo, the two most common frequency bands used for CubeSat TM/TC systems are ultra high frequency (UHF) and S band [172]. Here, an UHF link comes with the advantage that omnidirectional reception and transmission characteristics can be achieved with comparatively low power consumption. On the other hand, the much higher data rate of an S-band system allows to significantly streamline satellite operations. In order to minimize the power consumption, S-band systems are usually operated with directed antennas, which in turn requires low-accuracy pointing towards the ground station during operated passes.

Experience gathered within the operations of TechnoSat (cf. Section 4.1) showed that the UHF communications system carried by the spacecraft offered a very robust communications link, however, also some limitations were established. Here, a higher available data rate is expected to significantly reduce the effort required for satellite operations and a Consultative Committee for Space Data Systems (CCSDS) [173] compatible S-band system would simplify the use of foreign ground stations for commanding the spacecraft. Also, the increasing use of UHF frequencies for satellite operations may affect the link quality in the future according to Buscher [89].

Payload Data Downlink

If a downlink data rate of several megabits per second is sufficient for the payload, an S-band payload transceiver can be implemented for this task, as shown by Bradbury et al. in [174], or Frese et al. in [64]. Here, TM/TC system and payload data downlink are often combined using the same transceiver.

For missions that require higher data rates, an X-band transmitter may be considered. Data rates of up to several hundred megabits per second are usually provided by commercial X-band systems [39, 175]. Moreover, Devarajy et al. [45] presented the demonstration of data rates above 1.6 Gbps from orbit in X band using a triple unit CubeSat.

Optical data downlink systems provide data rates in the range of 100 Mbps to 1 Gbps [18, 82, 176] with comparatively moderate power consumption when being compared to RF systems. However, cloud coverage might reduce the total amount of data that can be downlinked as it affects the transmission. Furthermore, optical systems typically require pointing accuracies of around one degree, while less stringent requirements can be expected for RF systems.

Finally, some missions might not require a dedicated downlink channel for payload data, as the produced amount of data can be downlinked even by using only an UHF system. This was, for example, the case for the TechnoSat mission[4] (cf. Section 4.1).

Fault Tolerance

Fault tolerance for the communications system is achieved by the implementation of redundancy. Here, the communication system is generally suited for cold or warm redundancy and even hot redundancy can applied and may be used to increase the downlink bandwidth. This was, for example, implemented for the TUBIN mission (cf. Section 4.2), where both payload transceivers are configured to different frequencies to allow for simultaneous operation in order to increase the overall data rate.

[4] Here, the S-band transmitter was originally a technology demonstration payload and the use as regular platform element was later enabled via software update.

Another measure that has been proposed by Jackson [177] is to implement a secondary, independent command path to ensure that the spacecraft can still be accessed in case of a faulty primary communications system.

Conclusions

Based on the above considerations and the analysis on state-of-the-art missions the author conducted in Section 2.1, an S-band system is selected as the nominal system for TM/TC of the TUBiX20 platform, complemented by an UHF system as backup to enable reliable communications regardless of the satellite's attitude to increase the overall robustness.

To limit the amount of required RF units the TUBiX20 platform will combine TM/TC and payload data downlink system as a baseline. Here, X-band may replace the S-band downlink for missions that require higher payload data rates. Furthermore, also an X-band uplink may be considered if supported by the ground stations planned for the mission.

In this context, a newly developed CCSDS compatible transceiver that supports S-band and X-band uplink as well as an X-band downlink is currently tested in orbit as technology demonstration payload within the TUBIN mission (cf. Section 4.2.3).

Alternatively, an optical transmitter may deliver highest data rates at comparatively low power consumption but may require more accurate pointing.

3.2.6 On-Board Computer

In classical satellite architectures, a large proportion of the functionality that is implemented in software is usually embedded into the on-board computer (OBC) [178]. However, in favour of a higher level of flexibility, the required functionality can as well be distributed over a number of different computers (cf. Section 3.3.1). If all tasks associated to other subsystems are transferred to dedicated computers, the functionality of the OBC is reduced to system-level assignments. This includes for example telemetry storage, system-level mode management and fault detection, isolation and recovery (FDIR) tasks, as well as command list management. Performing systems-level tasks on a dedicated computer that is not engaged with subsystem tasks may improve reliability, reduce complexity, and simplify resource allocation. However, as these system-level tasks

are independent of external hardware components it might be sensible for a specific mission to combine the OBC with another subsystem's computer if the available processing power allows for this.

Based on these considerations, it can be concluded that the specific implementation of the OBC is largely dependent on the overall systems architecture of the platform. Therefore, the reader is referred to Section 3.3.1 for further details concerning the implementation of the OBC.

3.2.7 Payload Data Handling

The tasks that are attributed to the payload data handling (PDH) are mainly providing a data interface for the payload as well as payload data processing and storage. As could be shown in the survey performed in Section 2.1 for different application areas of small satellites, the requirements that result from these tasks highly rely on the nature of the payload. While some payloads may offer a widely used interface and produce only little data, others may require the implementation of specialised interfaces as well as processing and storage capabilities for large amounts of data. Due to this diverging requirements, the need to completely replace the PDH between missions can be expected. A further discussion about different option to integrate payloads into the TUBiX20 architecture was published by Barschke and Gordon in [179].

3.2.8 Orbit Determination and Control System

While orbit determination and control is commonly attributed to the ADCS it is considered as a separate subsystem for the TUBiX20 platform. This is due to the fact that a wide range of missions will not require a propulsion system. For that reason, the impact of adding propulsion to a specific mission on other subsystems shall be kept as small as possible.

An overview of commercially available global navigation satellite system (GNSS) receivers and propulsion systems that are suitable for providing orbit determination and control capabilities for the TUBiX20 platform is presented in Appendix C.

Orbit Determination

Orbit determination on satellites with a launch mass below 50 kg using GNSS receivers has been demonstrated in LEO with an accuracy in the range of meters [180, 181]. Furthermore, miniaturised COTS laser retro reflectors have been proposed for highly-accurate orbit determination from ground by Kirchner et al. [182][5].

Within the TechnoSat mission, miniaturised COTS laser retro reflectors have been demonstrated in orbit for the first time and results of the conducted experiments have been presented by Wang et al. [183][5] and Barschke et al. [13]. Adding a Global Positioning System (GPS) receiver while again implementing retro reflectors within the TUBIN mission will furthermore allow for assessing the accuracy achieved with the GNSS-based orbit determination.

Orbit Control

Orbit control and formation flight by means of drag control and propulsion systems has been demonstrated in LEO with small spacecraft [181, 184, 185]. Here, drag control solely requires the ability to control the spacecraft's attitude with an accuracy of several degrees, but only supports phasing on a given orbit. Propulsion systems, on the other hand, require higher pointing accuracies and may come with significant mass and volume. There is a wealth of mainly chemical or electrical propulsion systems that have been developed or proposed for the use in small satellites. An overview over propulsion technology proposed for small satellites, as well as over systems that are currently developed or are already commercially available can be found in [186–188].

The impact of integrating a propulsion system into a spacecraft based on the TUBiX20 platform is expected to be large for most technologies. This is mainly due to the significant mass and volume of the system, as well as due to specific requirements in mounting position and orientation. Furthermore, especially electrical systems may come with significant continuous power demand that may impact the sizing of solar panels and batteries. Overall, the requirements that result from the integration of a propulsion system are similar to those of a payload.

[5] Publication with contributions by the author of this thesis.

3.2.9 Software

Within the last decades, the importance of software for satellite systems increased continuously. While most functionality was implemented in hardware in the beginning of the space age, software solutions are nowadays often preferred to answer the need for increased performance and flexibility. A comprehensive introduction on the topic of software for aerospace systems has been presented by Sharp et al. in [189].

Software implementations can nowadays be found throughout the spacecraft from component to system level. On the component level, a star tracker may for example use software algorithms to identify star patterns and a payload data transmitter may be based on an SDR implementation. On subsystems and systems level, capabilities like control algorithms, higher-level communications protocols, or telemetry data management are commonly realised in software. Within the scope of this thesis, mainly the systems and subsystems software is of interest, as it is expected that most implemented components will be shipped with their own software.

Following the line of reasoning presented in Section 2.2, software reuse can be enabled by the implementation of software platforms, analogous to the approach followed for the hardware. In this context, a discussion of software product lines for satellite applications is presented by Gordon et al. in [190][6]. As highlighted by Gordon et al., software reuse is a key quality criterion for the development of a software platform for small satellite applications. Following Ferrari and Sangiovanni-Vincentelli [191], one can distinguish between two different forms of reuse in this context, *reuse in space* and *reuse in time*. Here, reuse in space refers to the implementation of the same software within different missions with varying requirements that are realised at the same time. Reuse in time, in turn, implies the application of the same code within several generations of the spacecraft, e.g. to support updated hardware. Both types of reuse are relevant for the TUBiX20 software platform.

Software platforms for space applications have for example been developed by the NASA [192], the German Aerospace Center (DLR) [193], Stuttgart University [194, 195], Tokyo University of Science [196], and Technische Universität Berlin [190].

[6] Publication with contributions by the author of this thesis.

Within such platforms, the software is commonly divided into different layers that fulfil specific tasks. Figure 3.12 shows a generic representation of the software layers that are customary implemented for a satellite flight software platform. While the terms vary here between the different platform implementations, the task distribution is similar. At the bottom of the figure, the blue box represents the hardware the software is running on. Above the operating system (OS) and the board support package (BSP), depicted as green boxes, are managing the hardware and software resources and provide common services. The next higher layer, the middleware, that is coloured in yellow, provides means of information exchange between the applications that are represented in red and which ultimately implement the aspired functionality and form the highest software level.

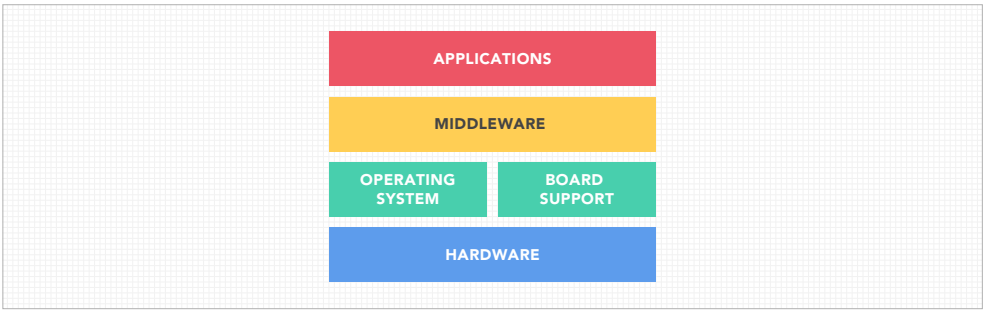

Figure 3.12: Generic representation that illustrates the four layers of a software platform as commonly used for satellite applications (Figure adapted from [190]).

This section gave a general overview of software platforms for small satellite applications. However, the specific software implementation for the TUBiX20 platform needs to take the platform's overall architecture into account. Therefore, implementation details on the TUBiX20 software platform are presented in Section 3.3.8 after key points of the platform's physical architecture were discussed.

3.3 Systems Architecture

This section examines the systems architecture of the TUBiX20 platform and motivates system-level design decisions. An initial draft of the systems architecture for the satellite platform to support the TUBIN mission that was based on heritage from picosatellite BEESAT [197] was published by Baumann et al. in [198]. It was then detailed for the TUBiX20 platform and implemented for the missions

TechnoSat and TUBIN by a group of researchers that was led by the author of this thesis. While a number of major requirements and constraints that concern the systems architecture of the platform were already discussed in Section 3.1, the analysis of the different subsystems in Section 3.2 revealed additional boundary conditions required to evaluate further architecture aspects that are discussed in the following.

3.3.1 Platform Topology

The topology that is selected for the avionics of a satellite platform strongly influences its scalability. Commonly, spacecraft avionics topologies are divided into three types, namely *star*, *ring*, and *bus* architectures [199, 200]. In the following, these architecture options are briefly discussed with focussing on their ability to support a scalable and modular satellite platform.

Star Architecture In this architecture, a central computer provides dedicated interfaces for all components to be controlled. However, for the TUBiX20 platform it could be shown that performance scaling is mostly realised by adding or removing components (cf. Section 3.2). This, in turn, results in a requirement for the platform to provide interfaces varying in number and type, which renders the star architecture less suitable for the given use case.

Ring Architecture Within a ring architecture, all components including the processing computer are interconnected in a ring. This arrangement can lead to a reduction in harness and decouple the component selection from the interfaces provided by the computer unit. However, as all information needs to be routed through all members of the network, a fault in one component might compromise the entire spacecraft.

Bus Architecture The bus architecture is based on a data bus interconnecting all components. As this topology combines most advantages of the star and the ring architecture, while avoiding their major disadvantages, it is nowadays widely implemented for satellite applications [201, 202].

Based on the presented considerations, a bus architecture is selected for the TUBiX20 platform for enabling the required scalability. However, there are still various degrees of freedom that allow to implement different bus architecture configurations. In order to evaluate which approach would be most suitable for the given use case, different aspects of the bus architecture implementation are discussed in the following.

Device Interfacing

The extent to which components are developed specifically to the needs of the platform, in contrast to being purchased with given power and data interfaces, has a strong influence on the platform's architecture. Here, it is obvious that the options to define the platform topology are limited, if all components are purchased. However, developing all required components like sensors, actuators, or radio transceivers in house in order for them to comply with the platform's interfaces will result in unacceptable development efforts. As a compromise between the two extremes, uniform modules that translate between the platform's data and power buses and devices that come with incompatible data and power interfaces can be implemented. A study of this approach in the context of small satellites has for example been presented by Pitterá and D'Errico in [201].

In order to allow for the use of a large variety of components available on the market, this approach is adopted for the TUBiX20 platform. Within the context of this thesis, the modules that translate between the platform's data and power bus and the devices to be integrated are called *nodes*. Figure 3.13 exemplary shows two nodes that connect two external devices to the platform's data and power bus. While devices could as well be supplied directly by the power bus in many cases, the power is routed through the interface nodes to maintain a standardised interface to power and data bus throughout the system. Furthermore, this configuration enables the nodes to directly perform power management and supervision for connected devices, which in turn abstracts the individual devices from the platform.

Processing Power

There are commonly two different options to provide the required processing capacity in a modular system. Federated architectures use one central computer

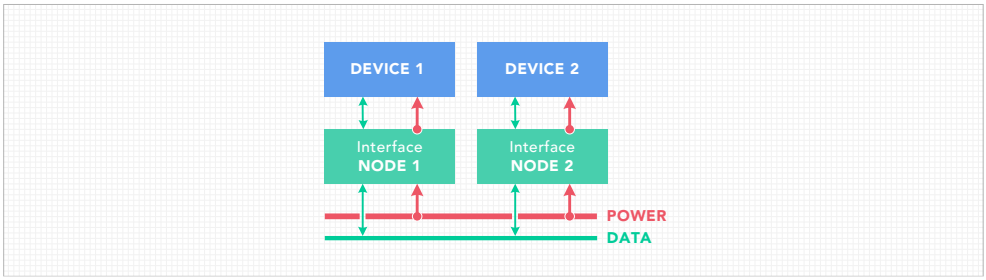

Figure 3.13: Representation of two interface nodes that connect two exemplary devices to the central power and data bus of the platform.

connected to the data bus that carries out all necessary processing tasks, while distributed systems consist of several computer units that share the tasks [199]. While the distributed approach increases the possible scaling options for processing power and allows for implementing various redundancy strategies, the federated approach offers reduced complexity.

With the interface node topology implemented by the TUBiX20 platform, a distributed computer network can also be realised without dedicated processing nodes but rather by using the interface nodes as processing engines. The advantages of this approach are manifold: the available processing power scales with the number of external components that are required and data can be preprocessed directly on the interface nodes which relieves the load on the central data bus. Furthermore, one or more dedicated processing nodes that offer higher performance when being compared to the nominal nodes of the system can still be integrated if required. This may for example be the case for payload data processing tasks.

3.3.2 Redundancy of the Nodes

In Section 3.1.4 it was established by the author that the reliability of the platform shall be increased by implementing redundancy. To limit the auxiliary mass and volume, as well as the overall complexity, the TUBiX20 computer nodes are operated in cold redundancy with two units implemented for each node.

However, one instance in the system is required to perform redundancy management for the cold redundant elements and can therefore not be operated in cold redundancy itself. This task is inevitably performed by the node responsible for

power switching of the nodes, e.g. the EPS node. To this end, the EPS node is operated in warm redundancy (cf. Section 3.3.10).

In this context, there are two different ways to refer to a node. Generally, each node provides a specific service, regardless of the redundant instance that is currently active. However, one can refer to one of the two hardware processing units specifically. For the remainder of this thesis, the term *logical node* refers to the entire node according to the attributed task, while the term *physical node A* and *B* refers to the individual processing units of the node.

3.3.3 Data and Power Buses

In order to realise a bus architecture for the platform (cf. Section 3.3.1), suitable data and power bus architectures need to be selected.

When considering the data to be transported on the data bus system, a classification into two types of data can be performed. The first type are status data generated by platform and payload components, as well as commands required to control the spacecraft. For these types of data, a bus with moderate data rate is required, which offers a high level of reliability and is widely used in consumer electronics to facilitate flawless integration as each and every node in the system needs to connect to this bus. The second category is payload data, which needs to be transported between the payload, the local storage location (typically a PDH or the OBC), and the payload data transmitter used for downlinking the data to the ground. Furthermore, payload data may also need to be transmitted between specific nodes for analysis. Here, a significantly higher data rate is required, while increased complexity might be tolerated as only selected devices and nodes need to connect to this data bus. Due to their diverging requirements, both buses are implemented separately as *control data bus* and *payload data bus* for the TUBiX20 platform. This limits the integration of the payload data bus to the devices that actually need to exchange payload data and even allows to remove the payload data bus completely in case it is not required by the mission to reduce its overall complexity.

Control Data Bus

A survey of data buses used for CubeSats presented by Bouwmeester, Langer, and Gill in [203] reveals that the most popular option for such spacecraft was the inter-integrated circuit (I2C) bus. However, reliability issues were reported for satellites using I2C as central data bus by the same survey. Furthermore, the buses master and slave setup restricts the potential to implement modularity when being compared to multi-master bus systems. For these reasons, the I2C-bus is not considered for the TUBiX20 platform.

Another data bus that has widely been studied regarding its applicability on small satellites is the control area network (CAN) bus [204, 205]. CAN is a multi-master message broadcast system offering data rates up to $1\,\mathrm{Mbit\,s^{-1}}$. Due to the wide distribution within the automotive industry there is a wealth of components available that support CAN communication. Furthermore, the use of CAN in space is widespread and satellites with launch masses from one to several hundred kilogram successfully demonstrated CAN technology in orbit [62, 206, 207]. Based on these findings, the CAN bus is implemented as control data bus for the TUBiX20 platform.

To achieve fault tolerance, the control data bus system is build by two CAN buses that are operated in cold redundancy. Such a configuration was for example described by Khurram, Muhammad, and Zaidi [208] and has been demonstrated within the X-SAT mission of Nanyang Technological University, Singapore [209]. While hot redundant operation of both buses would eliminate the risk of data loss in case of a bus failure, this would lead to significant increase in software complexity for the implementation of the interface, which shall be avoided. The implementation of redundancy management for cold redundant CAN buses by means of time limits has been presented by Woodroffe and Madle in [206]. This implementation has the advantage that no additional information needs to be distributed between the nodes, which, in turn, simplifies the hardware implementation. However, as no central decision over the active bus is made, complexity is expected in the implementation of the software interface and the overall verification. Another approach involves a hardware signal that selects the active data bus as it is for example realised in [197]. Implementing the latter method, redundancy management of the control data bus is performed by the EPS node for the TUBiX20 platform with a pair of dedicated select lines. Figure 3.14 illustrates the interface of the control data bus

system to an exemplary node. Here, active elements are depicted in colour, while deactivated ones are greyed out.

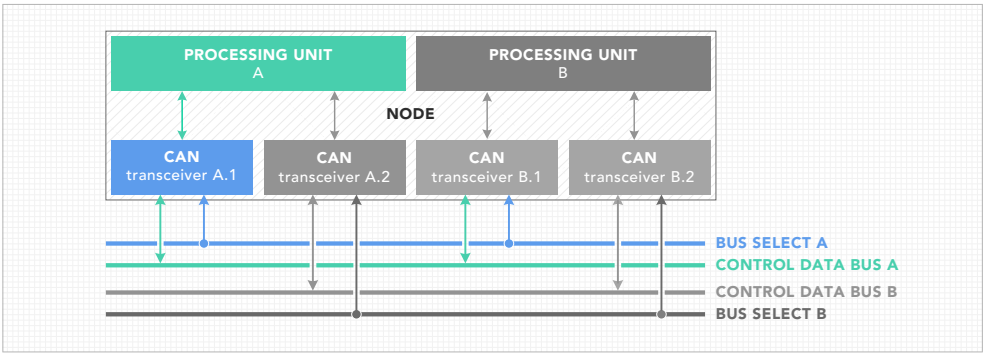

Figure 3.14: Representation of the control data bus system's interface to an exemplary node with CAN transceivers and bus select signal. Here, components that are greyed out are not supplied with power.

Payload Data Bus

For missions that need to exchange more data than can reasonably be distributed on the control data bus between the nodes, a dedicated payload data bus system is foreseen. A survey of candidate data bus systems performed in [210] resulted in the selection of Ethernet for the TUBiX20 payload data bus system. Here, the most significant advantage of Ethernet is its widespread distribution for commercial applications that result in a high availability of suitable COTS components and protocols. Furthermore, Ethernet has widely been considered and implemented for space applications [211–213]. However, as Ethernet is not a multi-master bus and only supports point-to-point connections, a switch is required if more than two participants are involved. Figure 3.15 illustrates the interface of the payload data bus between an exemplary payload, a PDH node, an OBC node, and a payload data transmitter that is realised with an Ethernet switch.

Power Buses

As a result of the distributed architecture of the platform, a variable number of nodes along with the devices controlled by these nodes need to be supplied with

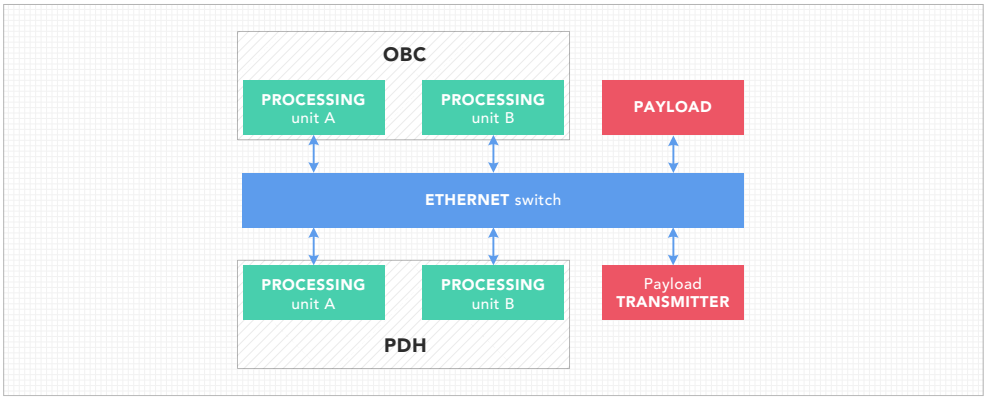

Figure 3.15: Interconnections of OBC, PDH, an exemplary payload, and a data downlink transmitter by the implementation of an Ethernet switch illustrating the TUBiX20 payload data bus architecture.

power. Here, two different approaches to power conditioning can be followed. Firstly, the nodes may be supplied with one single, unregulated or regulated power line only, while converting to all other required voltage levels is directly performed on the nodes themselves. Secondly, the most commonly required voltage levels can be centrally produced within the EPS and supplied to the nodes by the power bus system. As more than one common voltage level is expected to be required by most nodes, the first approach would increase mass and volume of the nodes and lead to a higher overall parts count for the platform. Therefore, centralised conditioning is performed for the most commonly used voltage levels within the TUBiX20 platform.

A first reference for the power levels that are chosen for central generation is a survey on CubeSat designs performed by Burt [214]. Within this survey it was shown that the most common voltage levels used in CubeSats are 3.3 and 5 V, followed by the unregulated battery power.

For a more detailed analysis the supply voltage requirements of 129 commercially available satellite components suitable for the application within the TUBiX20 platform were analysed by the author (cf. Appendix C). Here, the most common values among these components are 3.3, 5, 12 and 28 V, while several devices accept a certain range of supply voltages.

In order to determine if the platform may directly supply some of the devices with unregulated power, the worst-case voltage range of the platform's unregulated power bus needs to be estimated. Depending on the specific implementation of the power system, the unregulated power range may be driven by the power range the solar panels are operated at, as well as by the voltage range the batteries may provide.

For power generation, strings of seven solar cells are foreseen according to Section 3.2.3. Furthermore, it is expected that the cells are operated at the maximum power point. As a result, the strings' voltage is mainly influenced by the temperature of the solar cells and is also affected by radiation-induced degradation. As discussed in Section 3.2.3 the assumed design temperature range for the solar cells is -100 to $100\,^{\circ}\mathrm{C}$ and the values from the reference solar cell's data sheet [137] that correspond to $2.5 \times 10^{14}\,\mathrm{e/cm^2}$ damage equivalent fluence of 1 MeV particles at EOL are to be applied. With this, Equation 3.4 is used to obtain a minimum solar supply voltage of 12.99 V (EOL at $100\,^{\circ}\mathrm{C}$) and a maximum panel voltage of 22.88 V (BOL at $-100\,^{\circ}\mathrm{C}$).

Power storage is realised using strings of two to four battery cells. According to [16], the maximum battery cell voltage for Li-ion cells is the end-of-charge voltage with 4.2 V, while end of discharge cut-off voltage of 2.7 V is chosen as the minimum. Based on this, the battery's voltage range amounts to 5.4 to 16.8 V.

Resulting from these considerations, the worst-case unregulated power range is assumed to be 5 to 25 V, where the lower limit is defined by the batteries, while the upper limit is dictated by the solar cells.

In order to determine the power supply levels that offer the largest congruence with the devices' supply voltage requirements, two values have been determined for each of the considered levels. As a first parameter, the percentage of devices that can only be supplied by the given level or range is established. The second value that was determined is the number of devices that can be supplied by the given level or range among others.

Figure 3.16 gives an overview over the results of this analysis. Only two percent of the devices can be supplied by none of the given voltage levels and would therefore require local power conversion on the interface node in any case. While six percent of all analysed components may be supplied by an unregulated power supply of 5 to 25 V, all of these devices may naturally also be supplied by a 12 V supply. Two percent were found only to be compatible to an 28 V supply among the given

alternatives, while the same value is 18 percent for the 12 V supply, 33 percent for the 5 V and 10 percent for the 3.3 V supply.

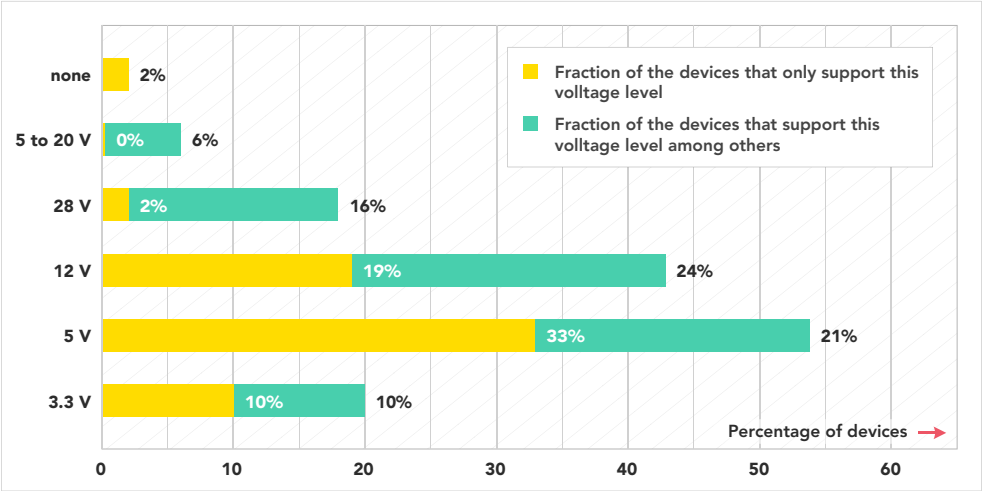

Figure 3.16: Analysis of the compatibility of commercially available microsatellite components to a number of candidate supply voltage levels.

The presented evaluation resulted in the selection of three regulated power lines of 3.3, 5 and 12 V for the power bus system.

A special case regarding the power supply requirements is the payload. As shown in Section 2.1, the payload might require significantly larger amounts of power than expected from the platform components. Therefore, the converter of the regulated power line that is used for supplying the payload might dissipate a significant amount of power. This could be prevented by supplying the payload directly with the unregulated power from the EPS. According to this, the TUBiX20 platform additionally supports supplying a node with an unregulated supply from the EPS that replaces the 12 V supply for the node in question. This adapted power interface might also be realised for platform components such as propulsion systems or radio transceivers to minimise the losses in the system.

The described power bus topology involving the mentioned supply voltage levels has been successfully demonstrated in orbit within the TechnoSat and the TUBIN mission. For both missions one of the payloads uses the unregulated power supply provided by the EPS (the reaction wheel system in the TechnoSat mission and the X-band transceiver in the TUBIN mission).

Similar to the data buses, fault tolerance for the power supply is achieved by implementing redundancy. To limit the number of switches and associated safeguard circuitry required to connect both redundant sides of a node to the power bus system, each side is only powered by one power path. As a result, avoiding that toggling the active side is only possible for all nodes simultaneously requires to operate both power buses in hot redundancy. Figure 3.17 illustrates how the power bus system interfaces to both redundant sides of an exemplary TUBiX20 node.

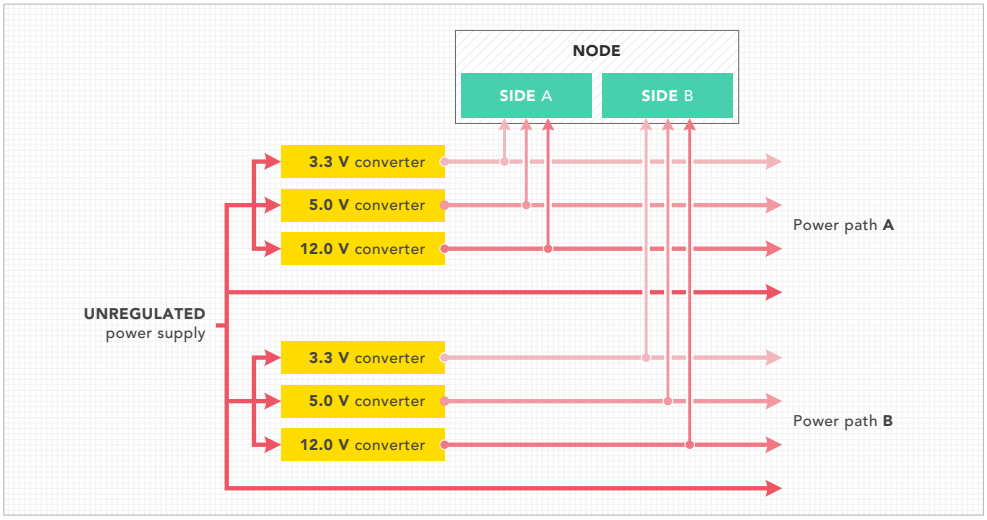

Figure 3.17: Power bus system with two hot redundant power paths offering three voltages each and exemplary node interfacing to the power bus system. Additionally, an unregulated supply line is provided per power path, that may replace the 12 V line for selected nodes with very high power consumption, such as payloads, propulsion systems or radio transmitters.

3.3.4 Time Synchronisation

Due to the distributed architecture of the platform, means for time synchronisation between the nodes are required. According to Ivkovic et al. [215] transmission on the CAN bus may be subject to time jitter that results from the priority-based scheduling of the transmission. To overcome this drawback for real-time applications, the time-triggered CAN (TTCAN) protocol was established [29, 216]. However, as using TTCAN strongly limits range of suitable components, it is not

considered for the TUBiX20 platform. Instead, a redundant pulse per second (PPS) hardware signal is provided for every node to enable time and task synchronisation.

3.3.5 Physical Segmentation

After defining the overall architecture of the platform the physical segmentation needs to be defined. This includes the nodes along with the connected components, the power and data bus system, as well as the different elements of the EPS.

Central Avionics Unit

The chosen architecture necessitates segmentation to support adding, removing, or replacing computational nodes to facilitate performance and capability scaling (cf. Section 3.1). This is realised by introducing a standardised form factor for the computational nodes and gather them together with selected elements of the EPS within a central avionics unit. This central avionics unit provides a mechanical frame to house a configurable number of slot-in cards. The interconnections between these cards and to external components are provided by a backplane. A similar design has, for example, also been presented by Navarathinam et al. [202] for the Surrey Satellite Technology Ltd (SSTL) X-series satellite platform.

The concept of the central avionics unit that houses the PCUs and the interface nodes was demonstrated in orbit within the missions TechnoSat and TUBIN. Furthermore, the form factor of the slot-in cards as well as the overall design of the central avionics unit has been optimised regarding mass and volume to allow the application in all size variants of the TUBiX20 platform within a thesis supervised by the author [217]. Here, the optimised design reduces the volume of the central avionics unit by 40 percent, while the mass is reduced by 32 percent. Furthermore, the optimised design supports an input power of up to 300 W to cover all power variants presented in Section 3.2.3.

Electrical Power System

Different levels of physical segmentation have been demonstrated for the EPS of small spacecraft. Johnston-Lemke et al. [218] presented a highly modular system, that implements physically distinct units for solar array and battery regulation,

power conditioning, and switching. Here, each one power conditioning module is foreseen for each required output voltage level and each one switching module is required for each component to be supplied. In contrast, the system presented by Notani and Bhattacharya [219] integrates the same functionality but the switches on one single PCB. In the following, the physical segmentation that was chosen for the TUBiX20 platform is described and motivated.

As analysed in Section 3.2.3, the EPS is required to provide solar panel regulation, charge control, power conditioning, switching, and power system management and supervision. The latter task is performed by the EPS node which also controls the redundancy of all other nodes as well as of the control data bus system. To this end, the EPS node is implemented in warm redundancy, operating in a worker and monitor configuration. While the worker is controlling the power system, the monitor is tasked with supervising the worker and claiming control if the worker fails to deliver a health signal towards the monitor. Another unique feature of the EPS node is that it commands a dedicated power supply, as it needs to be powered upon switching on the spacecraft, while the remainder of its interface is equal to the other nodes.

In the given architecture, the EPS node is required to switch and supervise a variable number of computational nodes within the central avionics unit. While all of these nodes will require the redundant 3.3 V supply to power the node's processing units, the other two power levels are expected to be utilised only by selected nodes. Therefore, only the switches that are used for a given configuration shall be physically implemented in order to limit the components count and to save mass and volume. To realise this, the switches and their associated supervision circuitry are located directly on the target node. This in turn requires a command interface for the EPS node to control the main power supply switches of the nodes. In order to limit the complexity of this interface and to ensure a large availability of suitable integrated circuits (ICs), the I2C bus is selected as EPS control bus.

As the battery will largely vary in volume and mass between missions it is, along with the associated supervision circuitry, located in a dedicated housing. The remaining tasks, namely solar panel regulation, power conditioning and charge regulation are gathered on two identical dedicated PCU PCBs, each one associated to one of the two power paths. This allocation is chosen as it results in two identical boards, on the one hand, and to enable the distribution of the thermal load over two PCBs, on the other hand.

The described segmentation of the EPS was successfully demonstrated in orbit within the missions TechnoSat and TUBIN.

3.3.6 Node Functional Scope

Following the preceding considerations, it is possible to summarise the functional scope of a TUBiX20 node. In the following, the major hard- and software features that have to be provided are listed:

- accommodate a set of two cold redundantly[7] operating processing units,
- implement a number of elementary software applications required to operate in the distributed system (cf. Section 3.3.8),
- implement further applications for fulfilling tasks specific to the node,
- provide hardware and software interfaces to a cold redundantly implemented pair of CAN buses that include a redundant bus select hardware signal,
- provide interfaces[8] to two hot redundantly operated paths of a power bus system,
- provide an I2C interface that allows to control the node's main power switches,
- receive a hot redundant hardware PPS signal,
- implement custom interfaces to components outside the central avionics unit that are controlled by the node, if applicable for the node in question.

An overview over the functionalities that are implemented on a TUBiX20 node is given in Figure 3.18. Here, it is assumed that side A of the node is active and all elements that are switched off in this configuration are greyed out. In this context, one can generally distinguish between two ways of operating external components. Firstly, each side of the node can be equipped with a dedicated instance of the component and, secondly, both processing units can access the same instance. In the case that is shown in Figure 3.18, the node connects to three external components. The first two of these components are two instances of the same device that are operated in cold redundancy and each of these devices only

[7] With the exception of the EPS node that is operated in warm redundancy.
[8] Only the power levels required by the node need to be implemented.

connects to one of the node's processing units. The third device is only present once and it therefore needs to interface to both processing units of the node. For this case, isolation of the power and data lines is required to prevent that a fault on one redundant side of the node may affect the other side. This is indicated by the box labelled *power switches, monitoring and isolation*. The standardised node interface is depicted as horizontal lines at the bottom of the figure. The node's PCB is indicated as a grey shaded box. The main switches that are controlled by the EPS node are denoted as *main switches path A* and *B*. Both control data buses are connected to both processing units.

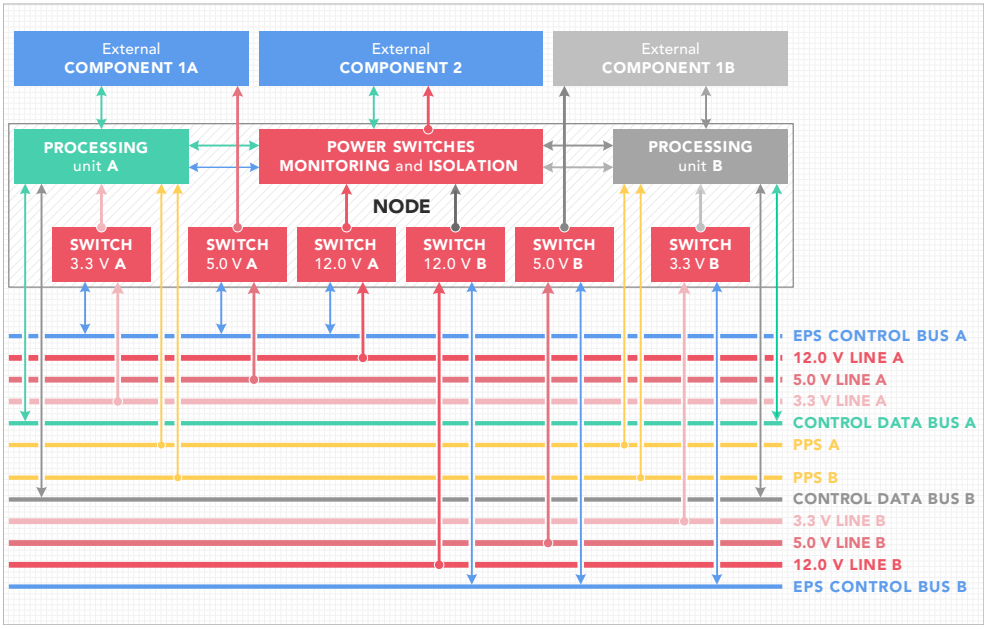

Figure 3.18: Schematic overview over the functionality implemented on a physical TUBiX20 node along with a representation of the standardised node interface.

Some external components to be used by the platform may solely require to be powered without necessitating to be controlled by a dedicated node. This may for example be the case for a radio transceiver that can directly be integrated via Ethernet. For this case, the power interface is realised by introducing a slot-in card that only carries the main switches controlled by the EPS node, while providing an electrical interfaces as required by the component in question. Such interfaces nodes, which are called *switching nodes* in the remainder of this thesis, may also

combine both power paths for components or payloads that are only present once in the system. A schematic overview over the functionality implemented on a switching node is given in Figure 3.19. There are two instances of component one, namely 1.A and 1.B, that are operated in cold redundancy. Therefore, each component can directly be connected to each of the power bus paths. Component 2, however, is only present once. To maintain fault tolerance of the provided power supply, the component needs to be connected to both power paths, which in turn requires that both supplies are coupled in an isolated manner to prevent that a fault on one bus may compromise the other.

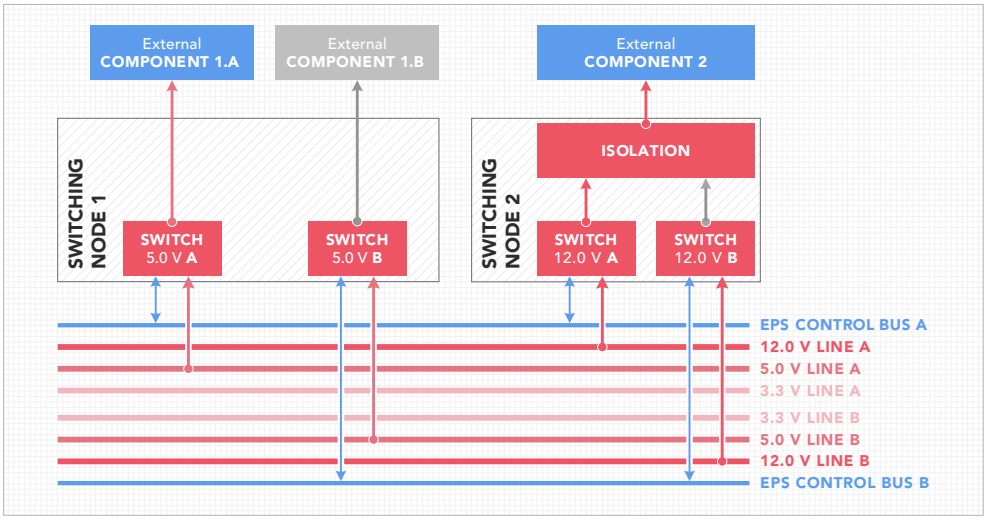

Figure 3.19: Schematic overview over the functionality implemented on two physical switching nodes along with the power paths of the standardised node interface. Greyed out components are not supplied with power.

3.3.7 Platform Levels and Layers

In order to aid the subsequent discussions, two classification strategies that target two distinct aspects of the platform's architecture are introduced in the following. The first concerns the segmentation of the platform into several levels, while the second one additionally divides the same into two layers. The classification of the TUBiX20 platform in layers and levels has first been published by Barschke et al. in [220] and will be discussed in more detail in the following.

Platform Levels

The TUBiX20 platform is divided into four different levels that are depicted in Figure 3.20. On the lowest level, components such as single sensors or actuators are situated, followed by the devices that form level one. A device may combine several hardware components along with a *device manager* application that provides the required software functionality.

As an example for the scope of component and device level, a reaction wheel system of four wheels may serve. Here, the single reaction wheels represent the component level. All four wheels along with the switches and sensors that are implemented on the node to control the wheels, as well as the software application that manages the mentioned hardware elements are referred to as device.

Following the device level, the subsystems are located at level two. A subsystem is typically formed by a number of devices along with the subsystem's core application that manages high-level tasks, such as running control algorithms or configuring the devices.

On system level, tasks concerning more than one subsystem are performed. This includes for example satellite mode management (cf. Section 3.3.9) or system-level FDIR tasks (cf. Section 3.3.10).

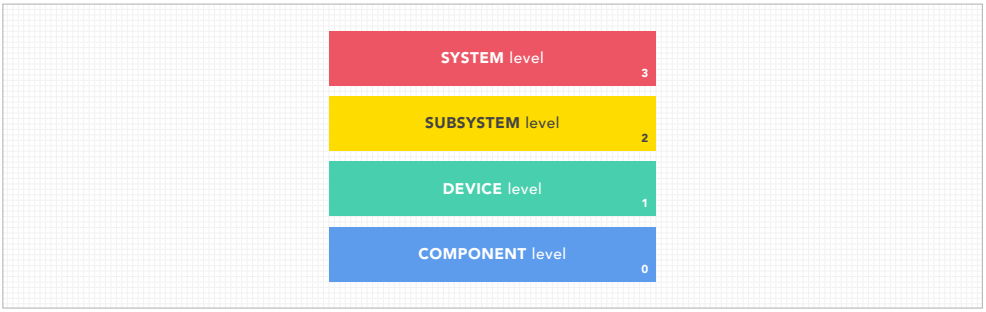

Figure 3.20: Representation of the four levels defined for the TUBiX20 platform. While system and subsystem level are commonly defined for spacecraft, device and component level take the distributed architecture of the TUBiX20 platform into account.

Platform Layers

In addition to the levels the platform may also be divided into two platform layers, namely the *service* and the *user* layer. Here, the service layer encompasses infrastructure as the node's hardware and all software required to operate and maintain the same. Abstracted from this the user layer comprises of devices, as well as device manager and subsystem core applications.

3.3.8 Distributed Software

In Section 3.2.9 a general overview of software platforms for satellite applications was presented. In this section, specific design choices to meet the requirements that originate from the distributed nature of the satellite platform's architecture are presented and motivated.

In order to provide the envisioned performance scaling capabilities, adding, removing, or rearranging nodes and components needs to be possible with minimal additional expense in software modification. To realise this, two major preconditions must be met:

1. The software must be structured in freely combinable modules that complement the hardware modules.
2. Communication between the software modules must be possible without a priori knowledge of the involved communication participants.

To address the first requirement, three different software module types have been identified:

1. Each device implements a *device manager* application providing abstraction from the specific implementation of the device by offering unified interfaces to the remainder of the satellite platform. The device managers are part of the software's user layer (cf. Section 3.3.7).
2. At the heart of each subsystem a *core application*, which also belongs to the user layer, performs subsystem specific tasks, subsystem-level mode management, and FDIR.

3. A number of *global applications* provide functionalities that are required on every node of the system. These global applications provide, for example, software upload capabilities, time management, or hardware watchdog triggers and are, thus, associated with the service layer (cf. Section 3.3.7).

The second requirement can be accomplished by implementing a publisher-subscriber design pattern as described by Buschmann et al. in [221] in an event channel variant. An illustration of the publisher-subscriber communication with event channels is shown in Figure 3.21. Here, two nodes are shown that implement a number of applications. These applications can publish messages on a number of channels, on the one hand, and may also subscribe to these channels, on the other hand. In this manner, messages can be exchanged between applications without prior knowledge of the involved communication partners.

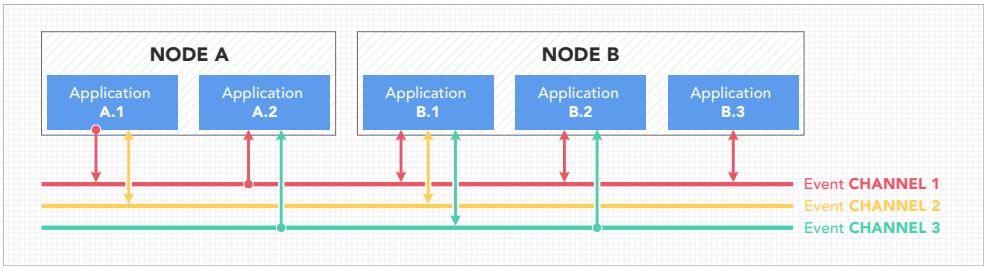

Figure 3.21: Illustration of the publisher-subscriber approach where applications can publish and may subscribe to different channels without a priori knowledge of the communication partners.

Based on the above it is evident that reuse is an important consideration for the modular software architecture. Here, the complexity that is introduced by fractionating the hardware in numerous computational nodes is responded to by standardisation of the nodes' service layer (cf. Section 3.3.7) with the aforementioned global applications.

In this context, the standardisation of the global applications in conjunction with the unified interfaces provided by the applications that are associated to the user layer also facilitates flexibility of the platform regarding the customisation for different variants.

Figure 3.22 shows an example in which reaction wheels and star trackers are implemented in two different configurations for two different missions. The first mission, denoted with (a), implements three reaction wheels and one star tracker

that interface to a single node. Hence, both device manager applications are implemented on this node. The configuration that is shown in (b) may be used by a mission with more stringent requirements in reliability and attitude pointing accuracy. Here, one node is used to interface to four reaction wheels, whereas the two star trackers connect to a separate node[9].

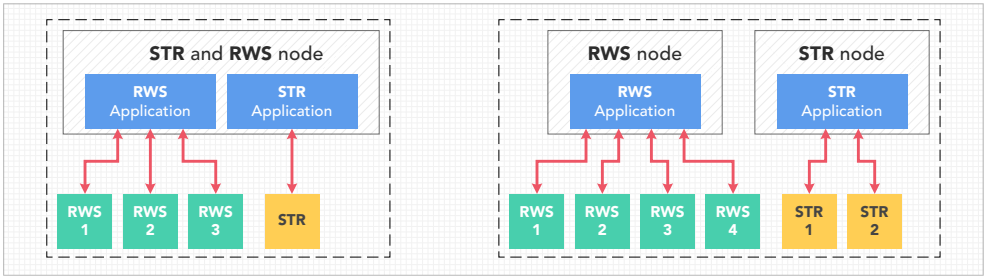

Figure 3.22: Flexible software support for different hardware configurations. The example on the left side shows three reaction wheels and one star tracker controlled by two applications on the same node, while the one on the right side shows the same applications located on two distinct nodes and controlling four reaction wheels and two star trackers.

Here, wheels and star trackers are controlled by the same device managers for both variants and parameters are used to distinguish between the different hardware configurations. Furthermore, the software layers above the device managers, i.e., the ADCS core application, solely requires knowledge about the different configurations to coordinate FDIR measures.

Generally, standardisation within the implementation (e.g. for device manager applications, drivers and FDIR functionality) streamlines the integration of new software elements by allowing to test against existing interfaces.

First considerations regarding the software to support the TUBiX20 platform were published by Barschke, Großekatthöfer, and Montenegro in [222]. Specific insights into the implementation and verification of the TUBiX20 software platform in the context of the ADCS were first presented by Gordon and Barschke in [167] and by Gordon, Lehmann, and Barschke in [223]. The concept was furthermore discussed in more detail by Gordon in [168]. Finally, a more generalised overview of the

[9] This configuration is for example implemented in the TUBIN mission (cf. Section 4.2). Here, both nodes are identical in hardware to reduce the production efforts.

implementation of software platforms for small satellite applications was published by Gordon et al. in [190][10].

The software development process applied within the development of the TUBiX20 platform was presented by Gordon, Graf, and Barschke in [224].

3.3.9 Mode Concept

Satellite modes are commonly implemented to establish a defined spacecraft configuration using a limited number of telecommands. According to Eickhoff [178], one can distinguish between the open and the closed mode concept. In both approaches, the satellite is configured by setting a global system mode, which will result in all subsystems being configured to the corresponding subsystem mode. However, while the open mode concept allows for reconfiguration of the spacecraft within a given mode, this is not permitted if a closed mode concept is implemented. Generally, the open mode concept offers more flexibility in satellite operations, while the closed mode concept is better suited for implementing on-board autonomy.

In order to complement the modular hardware approach of the TUBiX20 platform, the mode concept is required to support adding or removing devices to customise a spacecraft for a certain mission. Here, the efforts required to design and test a custom mode implementation need to be minimised. Following Klemich and Eickhoff [225], this can be achieved by extending the mode concept to include the device level. In this manner, the subsystem's core application can configure all devices associated to the subsystem solely by commanding the corresponding device modes.

For the TUBiX20 platform a closed mode concept that uses modes on all platform layers that were described in the previous section was developed and implemented by the research group. Here, the system modes are managed by the OBC. Figure 3.23 illustrates the systems level modes of an exemplary TUBiX20-based spacecraft designed for Earth observation. Here, the modes that are depicted in green are specific to the mission, while the other modes are platform inherent as they are required for any mission.

[10] Publication with contributions by the author of this thesis.

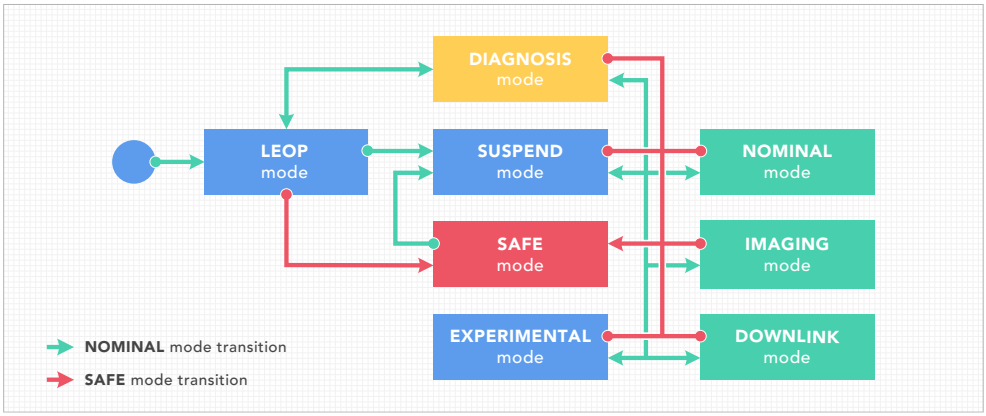

Figure 3.23: Exemplay implementation of the system modes for a TUBiX20-based spacecraft. Modes that are depicted in green are specific to the mission, while all other modes are standard platform modes.

Upon activation,[11] the satellite is booted into launch and early operations phase (LEOP) mode. Here, deployables are unfolded and the first contact to the ground station is established. After LEOP is concluded, the satellite is commanded into suspend mode where only a minimal equipment configuration is powered and commissioning is prepared. For performing commissioning, the experimental mode is used. Within this mode the spacecraft can be freely configured to test all equipment step by step. Furthermore, no reconfiguration is performed upon entering the experimental mode so that it inherits the configuration of the preceding mode. After platform and payload commissioning are concluded, three mission specific modes can be used for nominal operations.

Entering the safe mode is permitted from any other mode, either by telecommand or upon detection of an on-board anomaly. Upon transition into safe mode, a minimal equipment configuration is entered in which all non-essential hardware is switched off. From safe mode, only a transition into suspend mode is permitted.

The diagnosis mode is implemented to aid the platform's fault detection capabilities (cf. Section 3.3.10). The system-level diagnosis mode can be entered from all other modes except from safe mode. Similar to the experimental mode, the transition into the diagnosis mode will not alter the switching state of any equipment. Upon

[11] While larger spacecraft are often powered during launch [178], small satellites are usually switched off until being released.

commanding a diagnosis, all affected equipment will be temporary set to diagnosis mode to be able to perform testing.

An overview of the subsystem and device modes of an exemplary Earth observation satellite based on the TUBiX20 platform is given in Figure 3.24. It can be seen that the satellite is configured to imaging mode and each subsystem has its associated devices configured according to the corresponding subsystem-mode.

3.3.10 Fault Detection, Isolation and Recovery (FDIR)

The term fault detection, isolation and recovery (FDIR) is generally referring to the measures to be conducted upon the occurrence of a fault within a satellite system. As the exact terminology delimitation in connection with FDIR varies in literature, the following definitions in accordance with Tipaldi and Bruenjes [226] will be used throughout this thesis. Here, *fault detection* refers to the determination of the presence of a fault along with the time of the incidence, while *fault isolation* involves identifying type, severity and location of the fault. Finally, *fault recovery* denominates the application of appropriate measures to minimise the impact of the fault.

State of the Art

Similar to the fault tolerance approaches that were already described specifically for the ADCS in Section 3.2.4, two different FDIR strategies can generally be followed for the overall spacecraft, namely *fail to safe mode* and *fail operational* [178]. In the first case, a satellite is transferred to a safe configuration using available redundancies upon occurrence of a fault of sufficient severity. While this method may significantly reduce the availability of the spacecraft, as intervention from the ground is required for recovery, it involves comparatively low implementation and verification efforts. In contrast, a hierarchical FDIR strategy that targets fault detecting and autonomous recovery on the lowest possible level to keep the spacecraft operational in presence of a fault can be applied. Within such FDIR architectures, only faults that cannot be resolved by the spacecraft autonomously trigger a transition into safe mode. According to Olive [227], a hierarchical FDIR strategy requires significantly larger efforts for implementation and verification but, in turn, reduces the risk of failure for critical mission phases and generally increases the spacecraft's availability.

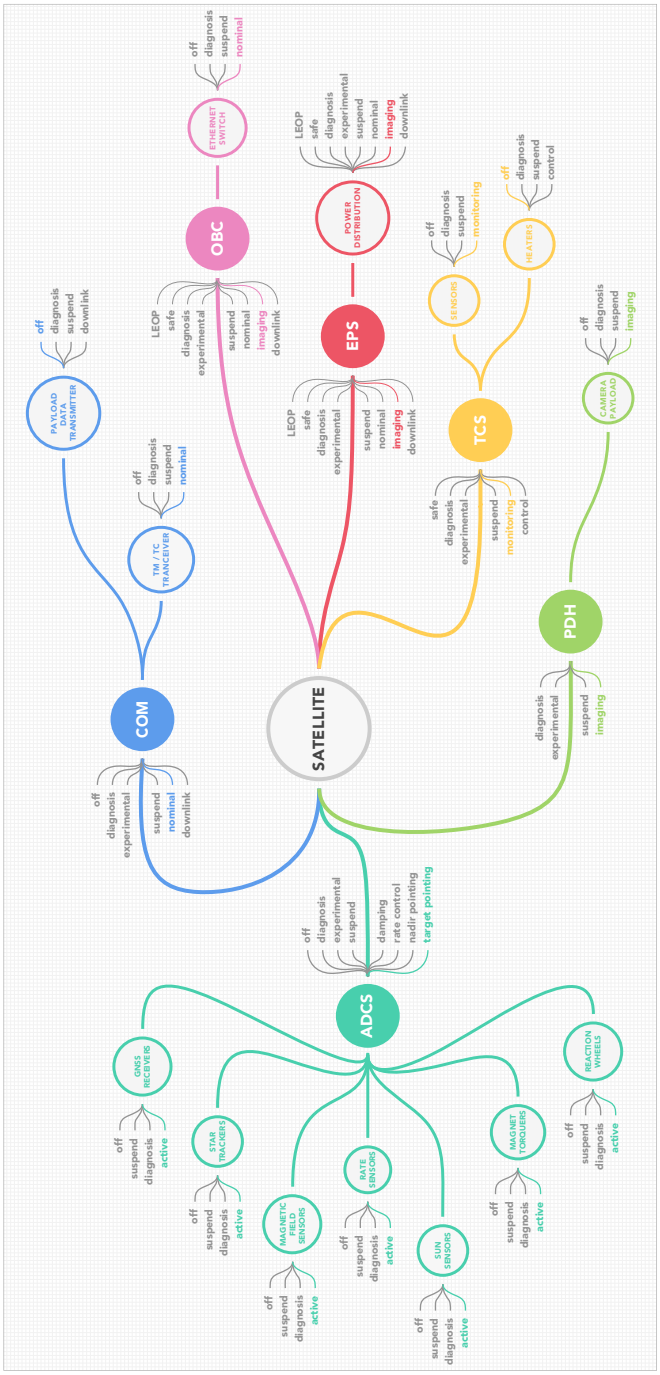

Figure 3.24: Exemplary mode configuration for the system, subsystem and device layer of a generic TUBiX20 Earth observation satellite.

For implementing a fail to safe mode strategy only fault detection needs to be performed autonomously as all subsequent measures are controlled by the operator from the ground. In this context, common approaches for fault detection in aerospace systems are cross checks, consistency checks, voting mechanisms, and build-in test techniques [228].

In contrast, additional measures targeting fault isolation and recovery that need to be performed by the spacecraft autonomously are required in order to implement a fail operational FDIR strategy. To limit the overall complexity, these measures are commonly organised in a hierarchical FDIR architecture. Here, relevant events are typically classified in five levels, as depicted in Figure 3.25.

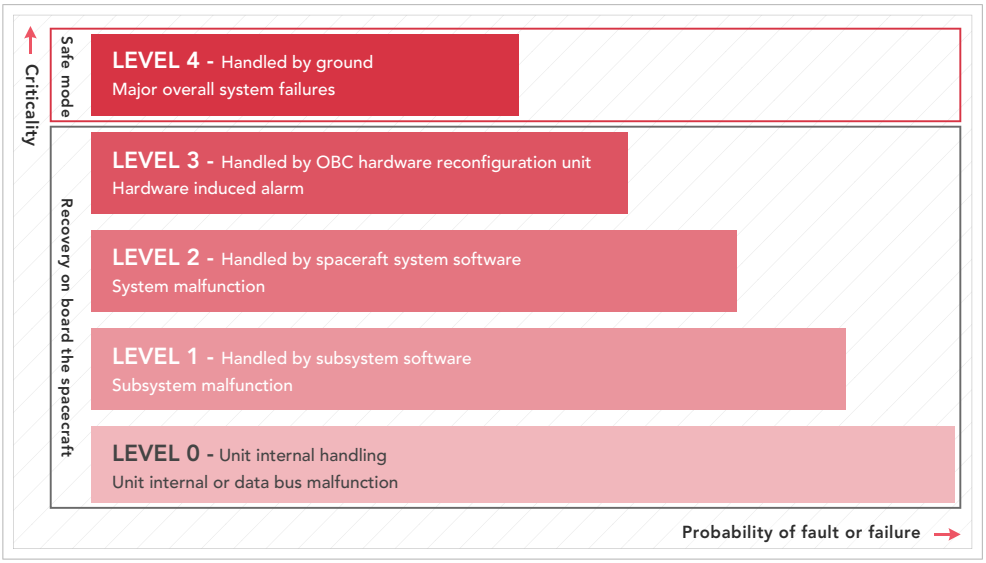

Figure 3.25: Representation a hierarchical FDIR architecture built by five levels with ascending critically. While the first four levels allow for on-board recovery, failures on level four initiate a transition of the spacecraft to safe mode and thus require intervention from the ground (Figure adapted from [178] and [229]).

FDIR level zero events are directly handled by the unit. This includes, for example, unit internal malfunctions like error detection and correction (EDAC) events or short-circuit protection events that require immediate reaction. On level one, malfunctions like equipment failures that can only be resolved on subsystem level are handled. Level two events are associated with the systems level. An example for such an incident are inconsistencies in attitude determination. The next higher

stage, FDIR level three, deals with malfunctions associated with FDIR related hardware failures and commonly involves hardware reconfiguration. The highest level is reserved for failures that cannot be resolved by the spacecraft autonomously and require intervention from the ground. To this end, the spacecraft is transferred into safe mode.

Current research in the field of FDIR for satellite applications involves the implementation of artificial intelligence (AI), e.g. in the form of Bayesian networks, cognitive automation, fuzzy logic, or artificial neural networks (ANN). For a more detailed discussion of the application of AI in FDIR for satellite systems, the reader is referred to a publication by Meß, Dannemann, and Greif [230].

TUBiX20 FDIR Implementation

Following Wander and Förstner [229], the degree of autonomy within the FDIR implementation required for a specific spacecraft strongly depends on the needs of the mission. According to this, the FDIR strategy for the TUBiX20 platform is to be selected in accordance with the requirements of a specific mission and the platform's architecture is therefore required to equally support both strategies. This is accommodated by implementing a hierarchical FDIR architecture that generally supports failure identification and recovery. However, here the prerequisites for an event to trigger a safe mode transition can be defined as required by a specific mission so that also a fail to safe mode approach can be implemented if demanded.

Within the TUBiX20 platform, built-in test (BIT) capabilities are realised by a modular hardware diagnosis framework that is embedded into the flight software to fault detection (cf. Section 3.4). A similar approach is also presented by Lian-Xiang, Ming-Rui, and Zhan-Guo [231, 232].

In contrast to the hierarchical FDIR architecture described before, the TUBiX20 FDIR design needs to account for the modular composition of the platform. More specifically, adding and removing devices to a given platform configuration shall be possible without requiring major changes of the FDIR structure. Another specific feature of the TUBiX20 platform that is relevant for the FDIR design is the fact that the equipment is connected to a number of independent computational nodes, as opposed to the OBC centred architecture that is conventionally implemented. This is accounted for by adding another FDIR layer between the unit and subsystem layer analogue to the layer structure introduced in Section 3.3.7. Furthermore,

the modular structure of the platform does not foresee a specific hardware reconfiguration unit for supervision of the OBC, which is conventionally running the system-level FDIR application. Instead, it is on the EPS to perform redundancy management of all nodes in the system equally. Based on this, the scope of FDIR level four is slightly adapted within the TUBiX20 FDIR implementation. Figure 3.26 gives an overview over the individual levels of the TUBiX20 FDIR architecture.

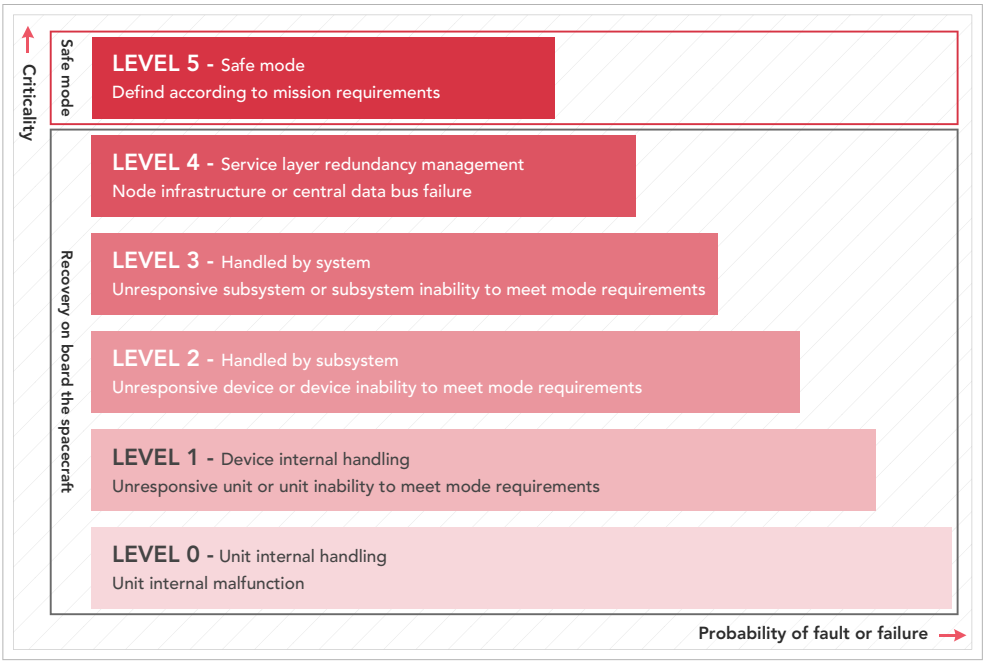

Figure 3.26: Representation the hierarchical TUBiX20 FDIR architecture built by six levels with ascending critically. Here, level one was included to account for the distributed architecture of the platform.

The general FDIR approach followed by the TUBiX20 platform was first published by Barschke et al. in [220].

For a better understanding of the presented FDIR architecture, an example is given in the following to illustrate the system's mode of operation. Considered is a reaction wheel system consisting of four wheels that is used for attitude control. If reading an internal sensor of one wheel fails and the problem is resolved by a reset of the data interface, this is classified as an FDIR level zero incident. While the event

may be reported to the device manager application for logging purposes, nominal operations resume. A sudden increase of a wheel's temperature in conjunction with the inability to reach the requested rotational rates may result in deactivation of the wheel in question along with a transition to a three wheel attitude control strategy that is performed on device level. This would be considered a level one FDIR event that is reported towards the ADCS subsystem. If, however, the current ADCS mode cannot be supported with three wheels, the subsystem may initiate a transition to a mode with less demanding agility requirements, which would elevate the given event to FDIR level two. As the ADCS subsystem naturally reports the mode change to the system level, where the OBC, in turn, may initiate a mode transition based on the given system-level requirements. In this case, the described event classifies as FDIR level three incident. If now a transition to safe mode is inevitable as the scheduled task cannot be fulfilled given the loss of one wheel, the event has triggered FDIR level four.

If a fail to safe mode strategy is envisaged for the mission, the FDIR implementation can be configured such that in the given example already the level one FDIR event is elevated to FDIR level five and a transition into safe mode is initiated. Furthermore, the prerequisites for safe mode transition can be adjusted as a function of the present state of the satellite, e.g. the current system mode.

In order to allow for greater insight into the purpose of FDIR level four, a closer description of the redundancy management approach for the service layer is given in the following. This entails a description of the worker and monitor configuration that is implemented to enable that redundancy control is being performed by the EPS node, on the one hand. On the other hand, the implementation of redundancy control for the nodes and the data bus system is detailed.

The two processing units of the logical EPS node are running in warm redundancy, each supervised by a dedicated hardware watchdog. Both physical nodes are powered upon activation of the spacecraft and side A claims the worker role upon boot-up, while side B takes on the monitor role. This is realised by a slightly longer waiting time of side B before the node would take over the worker role, so that a fault on side A would result in side B claiming the worker role. As long as side A considers itself operational it transmits a periodic health message towards side B, which in turn remains in monitor state while the health message is received as expected. As an additional hardware feature, only the current worker can access the platform's control data buses or the EPS's internal control communication

buses. Figure 3.27 depicts a simplistic representation of the implementation of the logical EPS node.

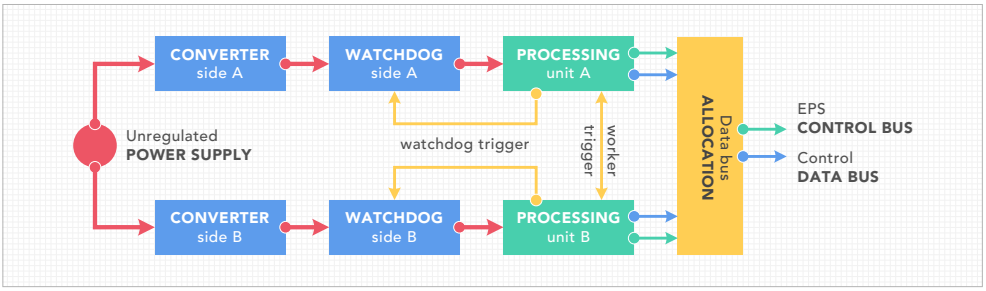

Figure 3.27: Schematic representation of the worker and monitor configuration of the two physical nodes of the logical EPS node.

In the following, the basic failure modes that lead to a worker change are listed:

- The worker fails to trigger its watchdog. As a consequence, and regardless of the question wether the health message is still delivered to the monitor, a hard reset is performed by the watchdog. The monitor takes over the worker role upon the non-appearance of the health message. The former worker now receives health messages upon initialisation and thus remains in monitor state.
- The communication on the platforms data bus system or the EPS control communication buses is compromised. Here, the node will perform a number of recovery attempts. If it fails to regain the ability to communicate upon its recovery attempts it will initiate a reset by suspending its watchdog trigger.
- The worker fails to configure the satellite as requested. After a defined number of attempts that did not result in a successful configuration of the spacecraft, the node will reset itself by ceasing to trigger its watchdog.

While there are a number of subordinate failure modes that were considered within the design of the warm redundant EPS node's architecture, their discussion would require a more detailed description of the node's hard- and software implementation and is therefore beyond the scope of this thesis.

As highlighted before, the EPS node has a particular role In the context of FDIR as it is responsible for supervising the redundancy of the computing nodes, as well as of the platform's data bus system. Following Section 3.3.7, the service

layer infrastructure including the data bus system can be seen as devices that are associated to the EPS. On unit level, each physical node is individually supervised by a hardware watchdog that performs power cycling if a registered software component fails to report nominal operation regularly. On device level, all nodes are expected to periodically register as operational upon requests issued by the EPS node. If these messages cease to arrive at the EPS node, FDIR measures as shown in Figure 3.28 are applied.

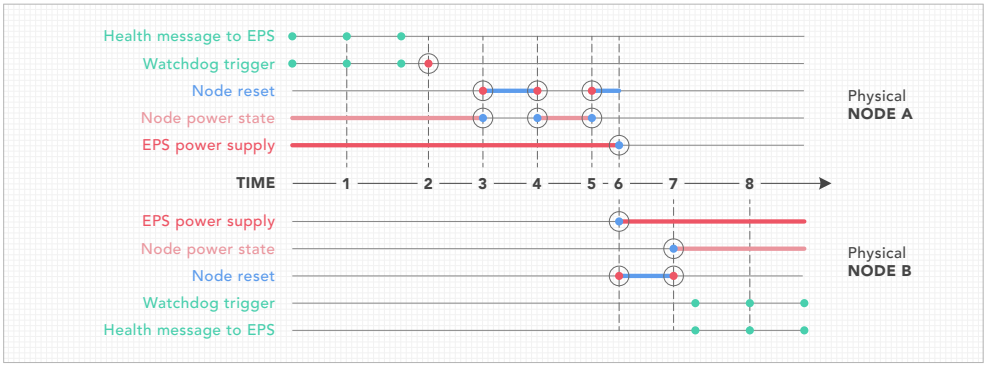

Figure 3.28: Overview of the sequence that is implemented by the EPS for supervision of the cold redundantly implemented nodes in the system (Figure adapted from [233]).

Point (1) marks nominal operations with physical node A being active. Now, the processing unit ceases to trigger its hardware watchdog at (2). In response, the watchdog interrupts the node's power supply for a specified period of time, which is marked with (3). At point (4) the node is again supplied with power but continues to fail triggering its watchdog. This, in turn, results in another reset attempt marked with (5) and an anomaly being triggered by the EPS. Before the node is powered again by the watchdog, the EPS switches off processing unit A and activates unit B (6). Now, after the reset period of the watchdog passed (7), physical node B is powered and takes over nominal operations (8).

In addition to the described FDIR measures, the EPS offers the option to define specific FDIR mechanisms for selected nodes. An example for such mechanism is toggling the active physical node of the TM/TC communications system if no telecommand has been received after a specific duration of time.

For the control data bus, toggling the active side is only considered if all periodic health messages from the nodes cease to arrive. With this, two failure modes are

being addressed. First, the EPS node may have lost its ability to receive messages. Secondly, the node may be unable to send out messages, which would equally stop the health messages from arriving at the EPS node, as these are only delivered upon request. If toggling the active control data bus does not resolve the issues, the current worker would initiate a reset of itself and the monitor would take over the worker role as result of this.

The design of the EPS software was the subject of a masters thesis executed by Keiser [233] that was supervised by the author. Within this thesis, the design of the TUBiX20 EPS software including the discussed FDIR capabilities was developed and a first implementation was realised. While it has been subject to continuous improvement after completion of the thesis, this software is currently applied within the missions TechnoSat and TUBIN (cf. the case studies that are presented in Chapter 4).

3.3.11 Systems Overview

Having analysed the individual aspects of the platform architecture in the preceding sections, the derived solutions can now be combined to form the overall systems architecture of the TUBiX20 platform. Figure 3.29 shows a generic systems architecture for a satellite that is based on the TUBiX20 platform. Horizontally spanning through the figure, the central power and data bus systems are shown. The computational nodes, depicted in green, interface to these bus systems via the standardised TUBiX20 hardware interface.

The EPS is divided into two power generation, storage and conditioning paths (cf. Section 3.2.3). According to the power requirements of a mission, each of the two solar paths comprise of a variable number of solar strings. Two battery packs provide electrical energy storage capabilities and can be adjusted to the mission requirements by varying their storage capacity. The two PCUs each accommodate a charge regulator on the one hand, and the power conditioning to supply one path of the power bus system on the other. In contrast to the other nodes in the system, the EPS node is directly powered by the PCUs, as it is required to command the switching of all other nodes in the system.

The ADCS comprises several nodes that connect to different components like sensors or actuators. Mostly, these components are solely requiring a power supply, an individual data interfaces and a device manager software application. However,

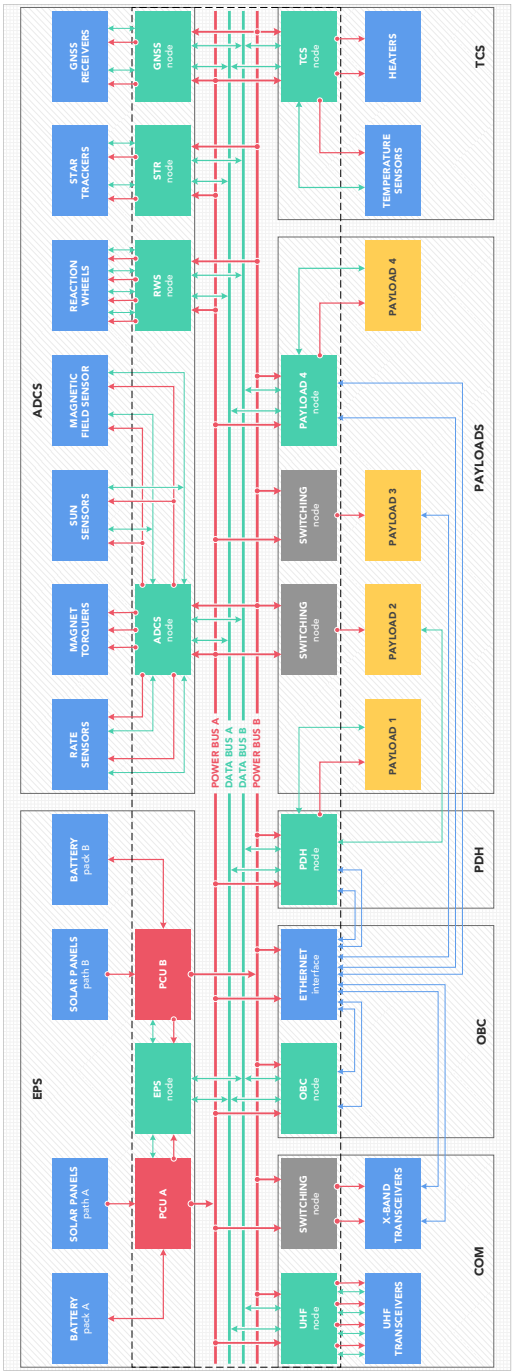

Figure 3.29: Generic systems design representation of the TUBiX20 platform depicting the central power and data bus system, the nodes, as well as the components and payloads (Figure adapted from [116]).

some components, like the magnetorquers, may require some specific hardware drivers that are also located on the node in question.

The baseline implementation of the COM system includes an S band uplink and an X band downlink, as well as a backup system in UHF. The nominal communication system comprises two cold redundantly operated units that are directly powered by the power bus system via a switching node and communicate via Ethernet. The backup system comprises a TUBiX20 node where each processing unit interconnects to two UHF transceivers that are operated in hot redundancy.

The OBC comprises a OBC node and an Ethernet switch. Here, the Ethernet lines are depicted in blue. In order to maintain fault tolerance, each physical node of the logical nodes is provided with an individual Ethernet line.

The PDH interfaces to the payloads and runs payload management software. In this generic overview, different possible payload interface options are shown. Apart from a payload that solely interfaces to the PDH, this includes for example the option to implement a dedicated payload node that provides an individual hardware interface and processing capabilities or a payload that connects with a data interface provided by the PDH but is supplied with electrical power by the central power bus system.

The overall architecture approach of the TUBiX20 platform was first published by Barschke and Gordon in [234].

3.4 Assembly, Integration and Testing

Assembly, integration and testing (AIT) activities make up a large proportion of the overall development time of a spacecraft. In this context Falkenhayn [57], claims that the cost advantages of NASA's MMS against non-modular designs could mainly be attributed to the reduced integration and test times. Additional advantages were reported by Townsend et al. [235] regarding the implementation of a modular distributed computing architecture in connection with the Emerald mission. Here, the reduced complexity of the single computer units were found to streamline parallel development and enable reuse.

In the following, reuse is discussed in more detail for two different aspects of the TUBiX20 platform's approach to AIT, namely the electrical ground support equipment (EGSE) architecture and functional hardware verification.

EGSE Architecture

Based on experiences that were gathered in previous missions of Technische Universität Berlin, the following high-level objectives for the TUBiX20 EGSE infrastructure have been derived:

- The applied software tools shall cover the entire development cycle of a spacecraft, including laboratory set-ups of ascending complexity.
- The same test implementations used to confirm hardware faultlessness shall be applicable at all integration steps from the single board to the fully integrated system.
- The implementation of the EGSE infrastructure shall foster synergies with other developments, especially from the field of satellite operations.

Especially the last point is also reflected in literature. Peccia et al. [236] claim that while there is a high degree of similarity between the requirements for the software used for satellite operations and the EGSE software, they are usually treated as individual developments. In this context, large potential for improving the overall product quality, while at the same time reducing the cost is generally attributed to the approach of combining both satellite operations and EGSE software [237–239]. As reported by Battelino and Svärd [240] this concept has also been implemented in the field of small satellites.

Figure 3.30 gives an overview over the TUBiX20 EGSE architecture. For interaction with the system under test, the central data bus system is directly accessed by the EGSE's interface board. This allows to monitor all data exchanged between the computer nodes on the central data bus system in real-time. Generally, the EGSE's interface board can either be connected to the ground support server via cable or via wireless data transmission. In the later case, which may, for example, be required for operating the spacecraft on an attitude test bed, the satellite may be supplied with electrical power from the internal batteries or a battery externally connected to the EGSE interface board.

A dedicated ground support server relays commands to the system under test and stores received telemetry within a TM/TC server. In this manner, all data generated by a test setup can be accessed, processed and analysed using the same tools that are already present for handling telemetry retrieved from the spacecraft in orbit. To interact with the system under test, most of the user

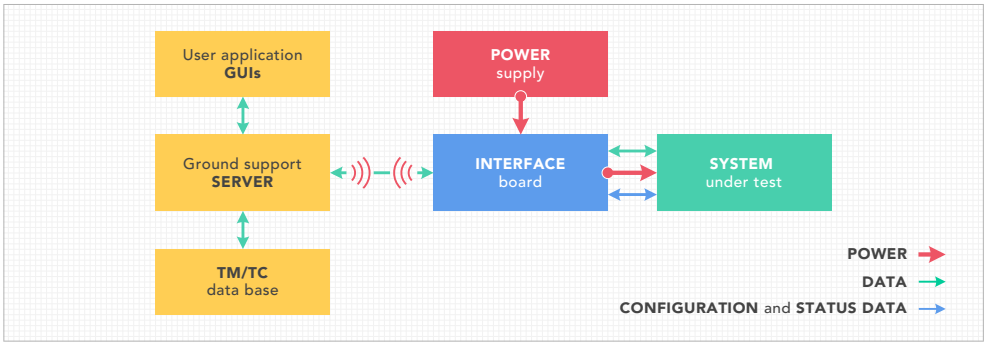

Figure 3.30: Overview of the power and information flow within the ground support set-up of the TUBiX20 platform. The set-up either supports direct interfacing to the system under test via cable or communications via wireless data transmission (Figure adapted from [241]).

application graphical user interfaces (GUIs) that are used for satellite operations can be applied. Here, a dedicated panel in the spacecraft command application allows configurations that are specific to the ground operations like for example powering the spacecraft. Additional tools are provided for monitoring and analysing the data exchanged of the platforms control data bus system. Owing to the central data bus system that is implemented by the platform, the same EGSE setup can be used for a broad variation of use cases ranging from a single computational node to a fully integrated spacecraft.

Generally, the same equipment can also be used to communicate via the satellite's radio interface for all setups that integrate a TM/TC transceiver.

An overview over the EGSE architecture for supporting the TUBiX20 platform has first been published by Werner et al. in [241][12].

Functional Hardware Verification

Within the development of a spacecraft, functional hardware verification is required at a number of occasions:

– for incoming inspections of newly produced hardware,

[12] Publication with contributions by the author of this thesis.

- for the verification of test setups of parts or the entire satellite,
- within environmental test campaigns,
- in the course of the assembly of the spacecraft,
- during the checkout campaign at the launch site,
- throughout the mission in orbit.

For the TUBiX20 platform, the topic of functional hardware verification is addressed by the introduction of a modular hardware diagnosis framework that is embedded into the flight software and facilitates hardware self-diagnosis based on BITs. The framework offers templates for a standardised definition of hardware tests that can be triggered via telecomand. In order to not interfere with the nominal operations of the spacecraft, tests are conducted in a dedicated diagnosis mode (cf. Section 3.3.9). While the tests are naturally defined per component, they can be combined to larger test scenarios that allow for testing entire devices, subsystems or even the complete spacecraft. Upon completion, the test results can be displayed within the telemetry visualisation GUI and are stored in the telemetry data base for future reference.

The described modular hardware diagnosis framework was developed within a masters thesis supervised by the author [242] and later published by Starke, Barschke, and Keiser in [243].

4 Platform Implementations

This chapter encompasses three case studies that detail the evolution of the TUBiX20 platform within the implementation for different application scenarios, namely the missions TechnoSat, TUBIN and QUEEN. A digital rendering of the three spacecraft is shown in Figure 4.1. Here, TechnoSat and TUBIN are two prove-of-concept missions that implement central aspects of the TUBiX20 platform architecture. For the QUEEN mission, experiences gained within the development of TechnoSat and TUBIN, as well as within the operations of TechnoSat were evaluated and the implementation of the platform was refined based on the findings. Within this chapter, the three missions are briefly introduced and relevant aspects of their implementation are discussed in more detail.

Figure 4.1: Digital rendering of the first three spacecraft that are based on the TUBiX20 platform, namely TechnoSat (left), TUBIN (middle) and QUEEN (right) in operational configuration (Image credit: Marc Lehmann).

4.1 The TechnoSat Mission

TechnoSat is a microsatellite technology IOD mission developed at Technische Universität Berlin[1] that was launched from Baikonur cosmodrome in Kazakhstan to LEO on the 14th of July, 2017 [28]. Orbit results gathered within the TechnoSat mission have been published within the proceedings of various scientific conferences by Barschke et al. and Gordon, Barschke, and Werner [150, 244, 245] and in a peer-reviewed journal article by Barschke et al. [37]. Furthermore, payload flight results can be found in [11, 13, 183]. Figure 4.2 shows the TechnoSat spacecraft while being integrated onto the Fregat upper stage of the Soyuz launcher.

Figure 4.2: Integration of the TechnoSat spacecraft onto the upper stage of the Soyuz launcher one week before launch [244] (Image credit: Roscosmos).

The primary mission objective of TechnoSat is testing new small satellite components in orbit. Secondary objective is the development and first application of

[1]The TechnoSat mission was funded by the Federal Ministry for Economic Affairs and Energy (BMWi) through the German Aerospace Center (DLR) on the basis of a decision of the German Bundestag (grant no. 50RM1219).

the TUBiX20 microsatellite platform. An overview of the main parameters of the TechnoSat mission is given in Table 4.1.

Table 4.1: Main parameters of the TechnoSat mission, as well as requirements and performance parameters of the satellite platform to support the mission.

Mission objective:	In-orbit technology demonstration
Orbit:	600 km Sun-synchronous orbit (SSO)
longitude of the ascending node (LTAN):	11:30
Launch date:	14^{th} of July, 2017
Launcher:	Soyuz with Fregat upper stage
Launch mass:	20 kg
Spacecraft volume[a]:	$465 \times 465 \times 305\,\text{mm}^3$
Design lifetime:	1 year
Power generation capabilities:	37 W (peak power in Sun pointing)
Power storage capabilities:	144 W h
Attitude knowledge:	3 deg (3 sigma)
Pointing accuracy:	4 deg (3 sigma)
Data downlink rate:	$1\,\text{Mbit}\,\text{s}^{-1}$

[a] Without antennas

4.1.1 TechnoSat Payloads

Figure 4.3 shows a digital rendering of the TechnoSat spacecraft with several solar panels removed to show the seven technology demonstration payloads inside the satellite. In the following, the individual payloads are briefly presented.

(1) Fluid Dynamic Actuator The FDA is an attitude actuator that uses fluid metal, which is pumped through a ring-shaped tube. The metal is accelerated and decelerated by means of an electromagnetic pump to create momentum for attitude alignment. The FDA demonstrated within the TechnoSat mission was developed at Technische Universität Berlin [9]. It has a diameter of 300 mm and a total mass of 1 175 g. Its maximum torque is 100 mN m s at 4.7 W power consumption [10][2].

[2] Publication with contributions by the author.

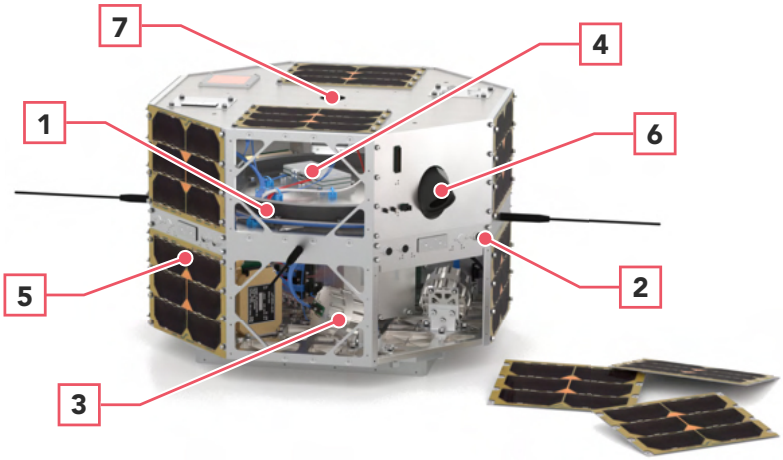

Figure 4.3: Digital rendering of the TechnoSat spacecraft with several solar panels removed to show the seven technology demonstration payloads the satellite is carrying (Image credit: Marc Lehmann).

(2) Satellite Laser Ranging TechnoSat carries fourteen corner cube reflectors (CCR) with a diameter of 10 mm for satellite laser ranging (SLR) [182, 246][3]. The objective is to demonstrate SLR using small COTS reflectors and the detection of the satellite's rotation axis and rate from ground [13, 183][2]. The experiment is designed and conducted by Technische Universität Berlin together with the German Research Centre for Geosciences (GFZ), the Austrian Academy of Sciences (OEAW), and the DLR.

(3) Reaction Wheel System A system of four reaction wheels that were developed at Technische Universität Berlin are demonstrated and tested within the TechnoSat mission. Each wheel has a mass of 330 g and can deliver an angular momentum of up to 46 mN m s at 1.35 W power consumption [247].

(4) S-Band Transmitter The S-band transmitter HiSPiCO was developed by IQ wireless GmbH from Berlin, Germany together with Technische Universität Berlin [12]. The transmitter has a mass of 75 g and offers a user data rate of 1.06 Mbps at 5 W power consumption.

[3] Publications with contributions by the author.

(5) Space Debris Detector The Solar generator based Impact Detector (SOLID) is a novel detector concept developed by the Institute of Space Systems of the DLR in Bremen, Germany [23, 24]. SOLID uses the solar arrays of a satellite as sensor areas to detect impacts of particles larger than 100 µm. TechnoSat implements SOLID detectors in four of its 17 solar panels [25][4].

(6) Star Tracker STELLA is a star tracker designed for nanosatellite applications by the University Würzburg, Germany [26, 27]. With a mass of 170 g and a power consumption of 250 mW, STELLA shall provide attitude measurements with an accuracy of 0.01 degrees in pitch and yaw and 0.04 degrees in roll.

(7) Camera TechnoSat carries a small complementary metal-oxide-semiconductor (CMOS) camera to generate payload data for experiments with the S-band transmitter and for evaluating the satellite's pointing performance. Furthermore, the camera is equipped with the same lens, that will later be used for the full-scale visible range camera within the TUBIN mission (cf. Section 4.2).

4.1.2 Spacecraft Systems Overview

In this section the configuration of the TUBiX20 platform implemented for the TechnoSat mission is described.

In order to allow for comprehending the orientation of the TechnoSat spacecraft for the remainder of this section, the satellite's coordinate frame is presented in Figure 4.4. Furthermore, the naming of the solar panels is indicated in the figure.

Figure 4.5 gives an overview over the systems design of TechnoSat. Here, grey boxes indicate the spacecraft's subsystems and the data flow is shown through green arrows, while power interconnections are plotted in red. Green boxes depict the computational nodes, while components such as sensors or actuators are shown as blue boxes and the payloads are represented in yellow. The dashed border contains all elements that are gathered in the spacecraft's central avionics compartment.

[4] Publication with contributions of the author.

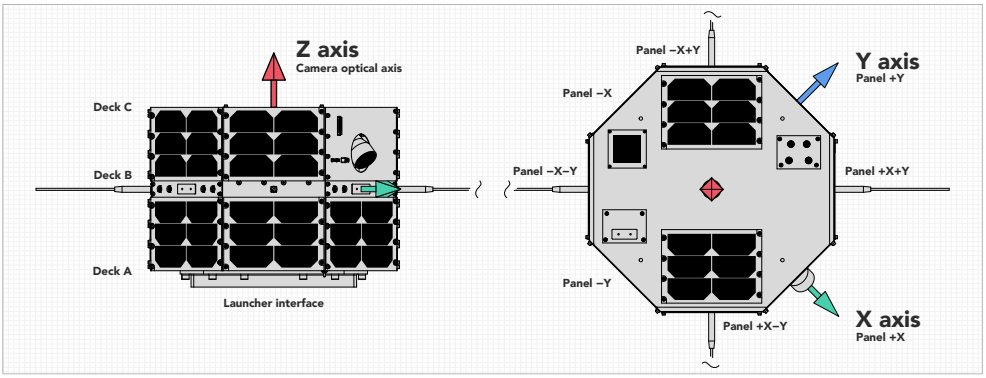

Figure 4.4: Satellite coordinate frame and solar panel naming conventions of the TechnoSat spacecraft. The Z axis is aligned with the optical axis of the camera payload, the X axis points towards the satellite's EGSE panel and the Y axis completes the right-handed coordinate system.

TechnoSat's two solar paths implemented for power generation are comprising eight and nine solar panels, respectively, carrying six solar cells each. Power storage is realised by two battery packs that are each build by four cells.

The ADCS implements two individual nodes. The ADCS node reads six hot redundant sensor panels equipped with Sun sensors, MEMS gyroscopes and MEMS magnetic field sensors. Furthermore, it controls the three magnetorquers for attitude control and executes the ADCS core software application. The fibre optic rate sensor (FOR) node interconnects three FORs to the power and data bus system of the spacecraft and performs preprocessing of the sensor data. Figure 4.6 exemplary shows the FOR computational node. At the rear side of the PCB, one can see the backplane connector, while the two mounting rails can be seen at the edges of the board. The division between the two halves of the board that are operated in cold redundancy is predominately indicated by the two micro controller units (MCUs) that are operated in cold redundancy. At the front side of the board, one can see the interface electronics for the operation of the FORs.

Communication capabilities are provided by the COM node. Each of the node's two MCUs is equipped with two UHF transceivers that are operated in hot redundancy. The UHF monopole antennas are aligned such that each of the two active ones are perpendicular to each other.

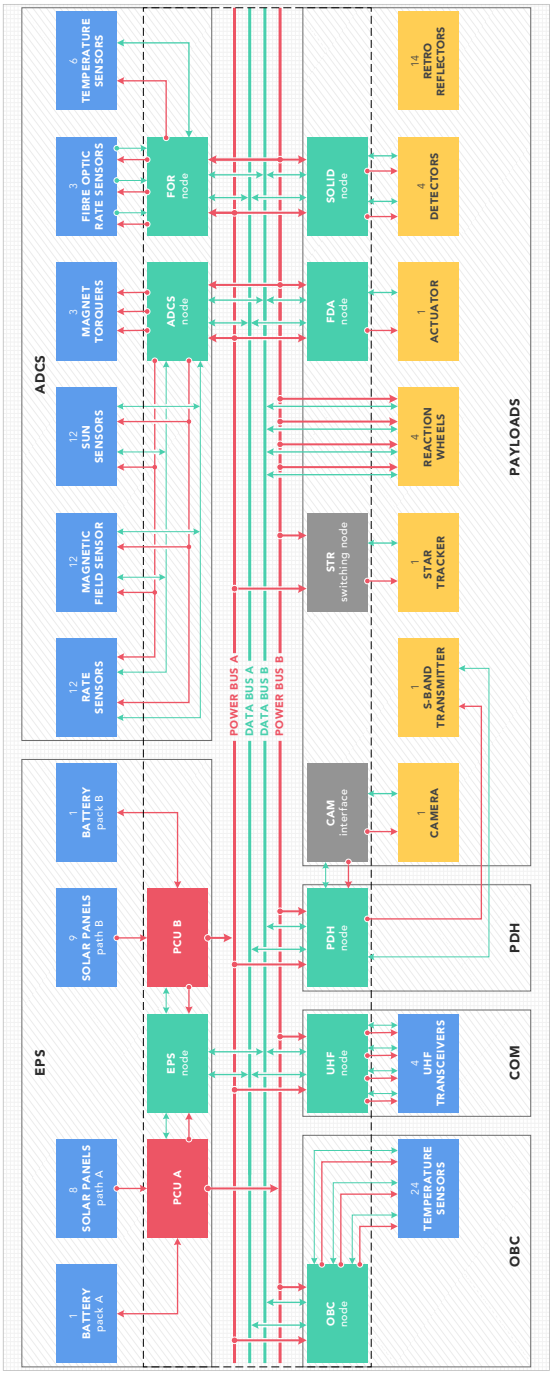

Figure 4.5: Systems design of the TechnoSat Spacecraft depicting the central power and data bus system, the nodes, as well as components and payloads. All elements within the dashed border are gathered in the central avionics compartment of the satellite (Figure adapted from [28]).

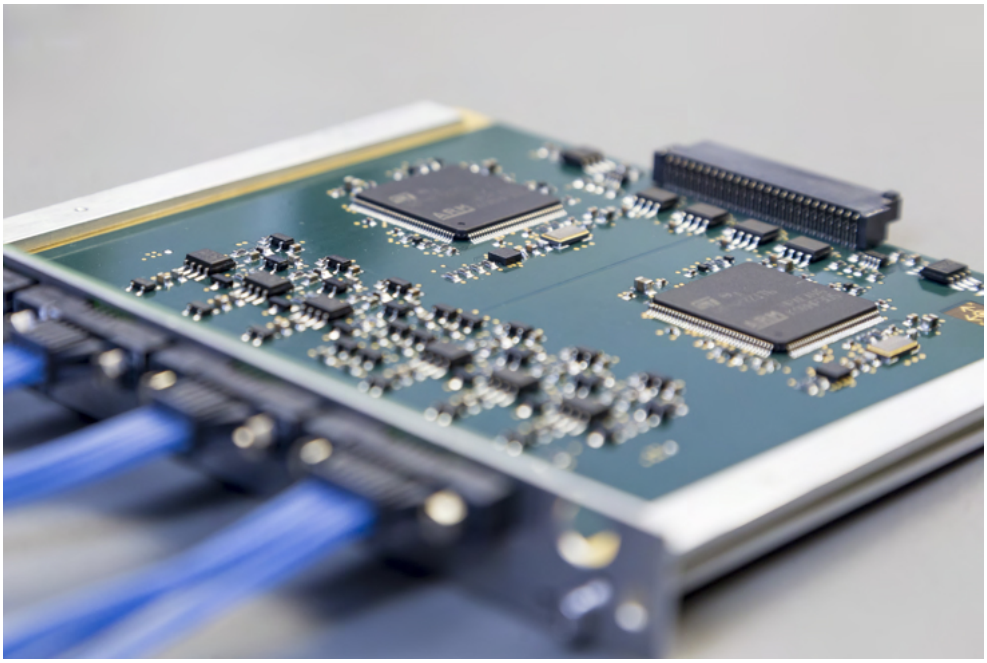

Figure 4.6: FOR computational node of the TechnoSat spacecraft [32]. The PCB is dominated by the two MCUs that are operated in cold redundancy (image credit: Philip von Keiser).

The OBC of TechnoSat comprises of a dedicated TUBiX20 node. Further to housing the software applications for tasks such as telemetry storage and system-level mode management and FDIR supervision, it also reads 24 sensors for monitoring the spacecraft's temperature.

The PDH provides hardware and software interfaces for two payloads, namely the S-band transmitter and the camera. While the FDA, the star tracker and the reaction wheel system are directly connected to the central data and power bus system of the spacecraft, they require dedicated software applications to integrate into the TUBiX20 software infrastructure. As the star tracker's power interface is not fully compatible with the interface provided by the satellite platform, a passive interface board is introduced that translates between both interfaces. The SOLID experiment uses a dedicated TUBiX20 node control computer so that no application on the PDH is required for this payload.

The system modes of the TechnoSat spacecraft are shown in Figure 4.7[5]. They comprise of the five standard TUBiX20 platform modes, as well as five mission specific modes. Four of these modes are both available in a nadir and a target pointing configuration to support different experiment scenarios of the mission.

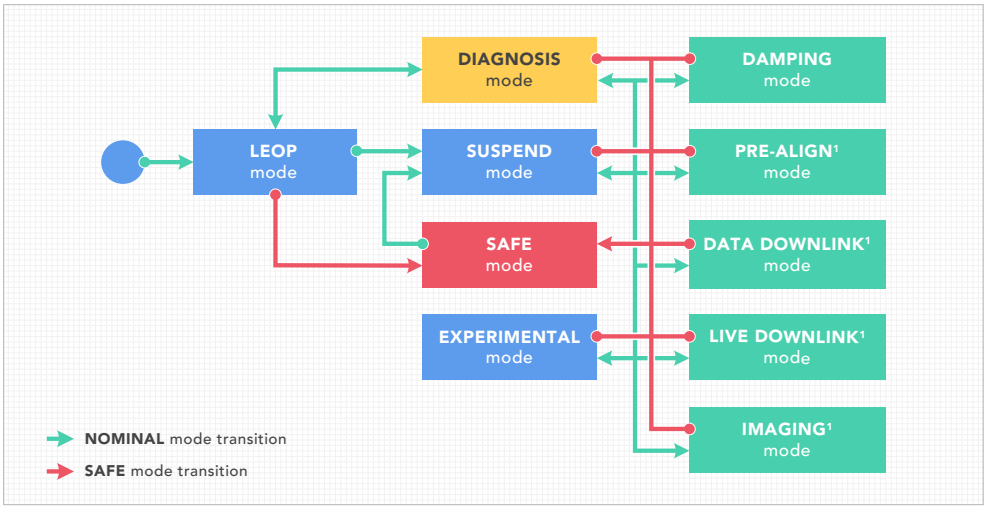

Figure 4.7: System modes of the TechnoSat spacecraft. The five modes that are depicted in green are specific to the mission and serve to operate the various payloads, while all other modes are standard platform modes. Here, the three modes that are indicated with a superscripted 1 are available both in a nadir and a target pointing configuration.

As the spacecraft is usually freely tumbling between experiments, the *damping mode* is required to slow down the rotation to a level were one of the modes that involve pointing can take over. The *pre-align mode* allows for coarse alignment of the spacecraft, which reduces the time required to establish pointing in one of the subsequent modes. The *data downlink mode* can be performed both with target pointing towards the ground station or with nadir pointing. Furthermore, TechnoSat supports a mode in which the spacecraft continuously captures images and sends them to the ground station without storing them on the satellite. This mode can for example be used for real-time visual confirmation of the spacecraft's attitude in operated passes. Furthermore, the imaging mode can be performed

[5] At the time of the satellite's launch, the system modes were not yet implemented as described here but were updated later via software upload. The modes that are described here represent the state-of-the software as it was active in orbit in July 2020.

in nadir or target pointing. Here, a target may be a point on the surface of the Earth or in inertial space.

In order to give an insight into the extend to which the satellite can be monitored and controlled, Table 4.2 lists the number of telecommands (TCs) and telemetry (TM) values available on the TechnoSat spacecraft with the software that was active in July 2020.

Table 4.2: Overview over the number of telecommands and telemetry values of TechnoSat for the software that was active on the spacecraft in July 2020 sorted by subsystems.

Subsystem	Number of telecommands	Number of telemetry values
EPS	77	881
OBC[a]	93	878
COM	60	509
ADCS[b]	219	2 194
PDH[c]	185	1 486
Total	634	5 948

[a] Includes the telemetry values for the satellite structure's temperature
[b] Includes telecommands and telemetry values for the reaction wheels
[c] Includes telecommands and telemetry values for all payloads save the reaction wheels

4.1.3 Spacecraft Specific Total Ionising Dose

Due to the fact that the TUBiX20 platform is based on consumer grade COTS electronics components, the radiation levels that different parts of the spacecraft are subjected to are of particular interest. In this context, a instructive introduction into the use of COTS electronics components for small satellites has been published by Sinclair and Dyer in [22].

Generally, two different radiation induced effects on electronics components can be distinguished:

1. The total ionising dose (TID) a component is subjected to may cause material damage that may in turn cause the device to diverge from its original specifications or stop functioning at all.

2. Single ionising particles may interact with a component and cause single event effects (SEEs) such as single event latchups (SELs) or single event upsets (SEUs) that may again lead to malfunctioning or failure of the device.

The TID a certain electronics unit of a satellite is subjected to can be determined based on two parameters. Firstly, the aluminium equivalent spherical shielding the unit is protected by and secondly the TID that is generally received in the given orbit depending on the available shielding.

To determine the first parameter, a worst-case estimation of the aluminium equivalent spherical shielding is derived for selected electronics units of the TechnoSat spacecraft. In this context, Palmerini and Pizzirani [248] have presented a methodology to perform a sector analysis to compute the uniform aluminium equivalent shielding for a defined point within a spacecraft.

For this analysis, the relevant elements are sectioned into triangles with uniform material thicknesses. Figure 4.8 shows a representation of the simulation model with two solar panels removed to show the its inner elements.

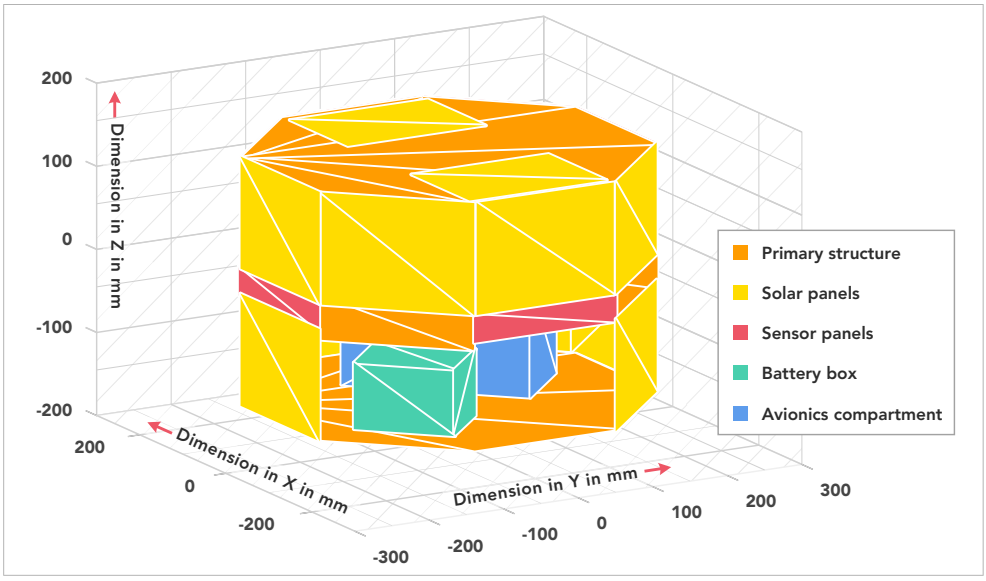

Figure 4.8: Geometry model developed for calculating the aluminium equivalent spherical radiation shielding for different electronics units inside the TechnoSat spacecraft.

For each triangle, the end-points are translated onto the same unit sphere by computing the unit vectors that originate at the point of interest and are orientated towards the corners of the triangle. As a next step, the triangle is transformed into spherical coordinates by applying the law of cosine (cf. Figure 4.9):

$$a = \arccos \frac{y^2 + z^2 - \left|\overrightarrow{BC}\right|^2}{2yz}. \tag{4.1}$$

Based on the fact that the length of x, y and z is 1 this can be simplified to:

$$a = \arccos \left(1 - \frac{\left|\overrightarrow{BC}\right|^2}{2}\right) \tag{4.2}$$

and the two other sides of the triangle can be obtained by:

$$b = \arccos \left(1 - \frac{\left|\overrightarrow{AC}\right|^2}{2}\right) \tag{4.3}$$

and:

$$c = \arccos \left(1 - \frac{\left|\overrightarrow{AB}\right|^2}{2}\right). \tag{4.4}$$

Now, the fraction of the sphere's surface area that is covered by the spherical triangle S can be calculated with (cf. Figure 4.9):

$$S = \alpha + \beta + \gamma - \pi \tag{4.5}$$

where:

$$\alpha = \cos \frac{\cos a - \cos b \cos c}{\sin b \sin c}, \tag{4.6}$$

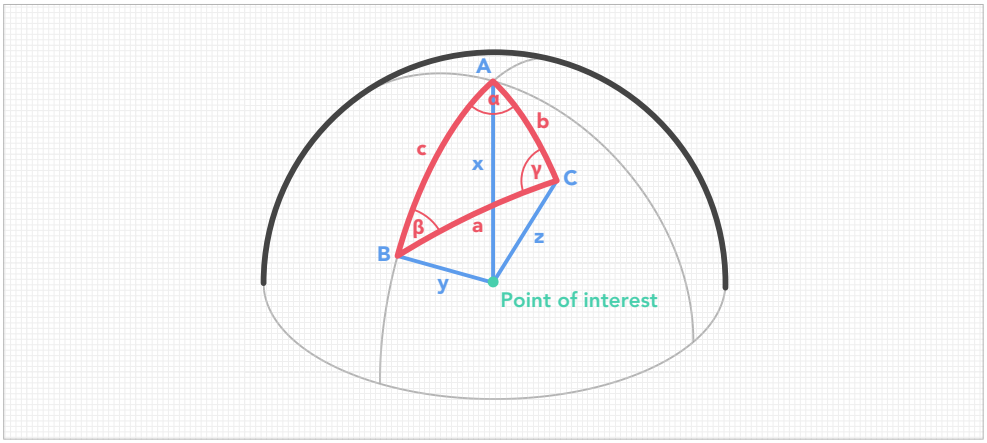

Figure 4.9: Representation of the spherical triangle derived from the planer triangle representing a structural element, along with the point of interest and the distances between the point of interest and the triangle's endpoints.

$$\beta = \cos \frac{\cos b - \cos a \cos c}{\sin a \sin c}, \tag{4.7}$$

and:

$$\gamma = \cos \frac{\cos c - \cos a \cos b}{\sin a \sin b}. \tag{4.8}$$

Finally, the representative, aluminium equivalent spherical shield thickness can be calculated using the density of aluminium ρ_{Al} of 2 710 kg m^3, as well as the individual densities ρ_n, the thicknesses σ_n, and the percentage of the sphere S_n covered by each triangle:

$$\sigma_{\mathrm{Al}} = \frac{1}{\rho_{\mathrm{Al}}}(S_1\sigma_1\rho_1 + S_2\sigma_2\rho_2 + \cdots + S_n\sigma_n\rho_n). \tag{4.9}$$

For TechnoSat, 75 parts that have been divided into 162 triangles were considered for a simulation to estimate the worst-case shielding at relevant reference points of the spacecraft. Out of the considered parts 42 are structure elements made of aluminium, 31 are PCBs with a density of 1 850 kg m^3 and two are the Li-ion

battery packs, whose density was assumed with 2 028 kg m^3 based on their mass and volume.

Table 4.3: Worst-case shielding thicknesses and TID levels for different electronics units within the TechnoSat spacecraft rounded to half millimetres.

Position	Shielding mm	TID per year krad(Si)
Satellite centre	5.0	0.4
Centre of battery compartment[a]	12.5	0.1
EPS node[b]	6.0	0.3
PDH node[b]	6.5	0.2
COM node[b]	6.0	0.3
Solar panel electronics (minimum value)	2.5	1.8
Solar panel electronics (maximum value)	4.5	0.5

[a] The Li-ion batteries' shielding is assumed according to their mass and volume
[b] Located inside the central avionics compartment

The TID for the design lifetime of one year as a function of the equivalent spherical aluminium shielding is obtained from a SPENVIS simulation. Table 4.3 lists the equivalent shielding values for an aluminium sphere with uniform wall thickness for several relevant positions within the TechnoSat spacecraft rounded to half a millimetre. Here, the lowest equivalent shielding of 2.5 mm is found for one of the solar panels' electronics boards. The highest shielding value is found for the battery monitor electronics board, which can mainly by attributed to the proximity to the battery packs. Furthermore, the table shows the corresponding TID values that are received at the position in question in the course of the satellites nominal mission of one year that range from 0.1 to 1.8 krad(Si).

Figure 4.10 shows the equivalent TID received by a component within an uniform aluminium sphere as a function of this sphere's wall thickness. Here, three spacecraft units have been indicated at the respective dose level they would receive within the nominal mission duration of one year.

Another SPENVIS simulation has been used to determine the power damage equivalent 1 MeV particle fluence values for the nominal mission duration of one year. The value was found to be 2.027×10^{12} e/cm^2, which is more than two orders of magnitude below the lowest value that is given in the solar cell's data

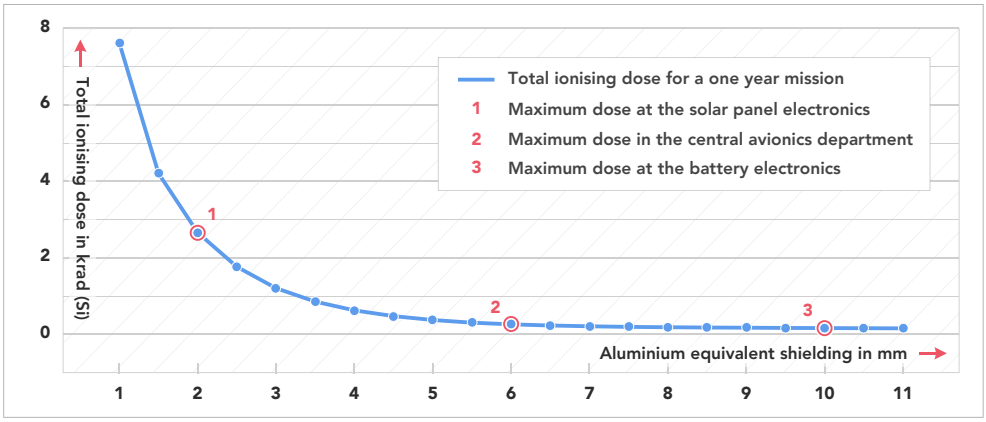

Figure 4.10: TID as a function of the aluminium equivalent shielding of a sphere with uniform wall thickness.

sheet [137]. based on this, it is assumed that the impact of solar cell degradation can be neglected for the TechnoSat mission.

4.1.4 Electrical Power System

To validate the function and to evaluate the capabilities of the TUBiX20 EPS, several orbit experiments were conducted within the TechnoSat Mission. In the following, these experiments along with the derived results are presented.

For a better understanding of the conducted experiments, the overall architecture of the TechnoSat EPS is depicted in Figure 4.11. Here, the charge regulator is the central element that manages battery charging based on the amount of energy supplied by the solar panels and guarantees at the same time that supplying the system is always prioritised.

The TechnoSat EPS does not support MPPT but implements a minimal solar string voltage of 12 V that takes effect at maximum load on the solar panels.

Power Generation

The first EPS experiment aimed at confirming the overall power generation capabilities of the spacecraft and at validating its behaviour within different system

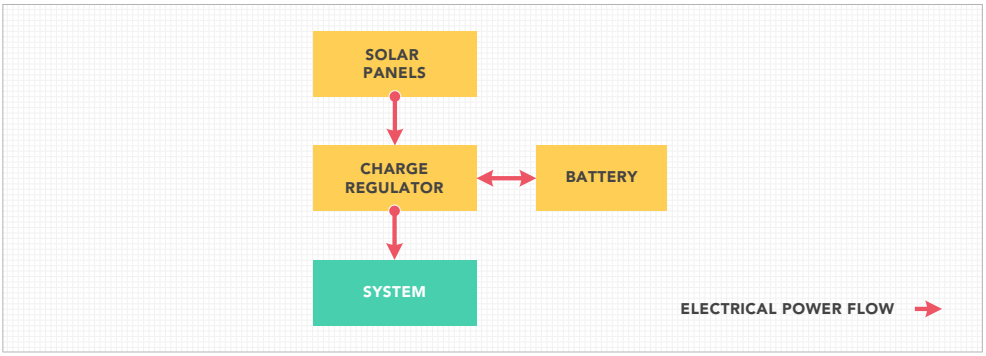

Figure 4.11: Schematic of the TechnoSat EPS topology with the charge regulator dividing the power generated by the solar panels between the system and the battery.

states regarding power generation and storage. It was performed on the 19th of December, 2018 and results from this experiment were first presented by Barschke et al. in [13]. The duration of the entire experiment was more than five hours in which 144 telemetry parameters were logged with individual periods resulting in 247 850 recorded telemetry values. In the following, two of the four orbits that were part of the experiment are analysed in more detail.

The experiment was divided into two main segments corresponding to two of the Sun phases. Within the first segment power generation was minimised by pointing the satellites −Z side, which carries the separation ring but no solar cells, towards Sun. The second segment, in contrast, aimed at maximising the power generation by performing Sun pointing with the −X solar array so that 12 solar cells were aligned nearly perpendicular to the Sun and 24 additional cells were illuminated with an angle. To allow for a better illustration of the correlation between illumination angle and generated power, the experiment was conducted with an five degrees offset, resulting into each two panels being illuminated with and angle of 5, 40 and 50 degrees, respectively.

Due to the cosine dependence of the generated power on the illumination angle the reduction in power generation is 9 percent when comparing an illumination angle of 45 and 50 degrees, while it only amounts to 0.5 percent between zero and five degrees illumination angle. Furthermore, the solar array that is illuminated with a 40 degree angle instead of an 45 degree angle produce 8 percent more power, so that the overall pointing loss amounts to 1.5 percent. Taking into account this illumination angles the power generation capability during Sun

pointing theoretically corresponds to 4.8 solar panels (29 solar cells) that are being illuminated perpendicular. Figure 4.12 illustrates the angles between the Sun vector and the normal vectors of the −X, the −X+Y and the −X−Y solar array by means of telemetry data. The peak in the middle of the second Sun phase corresponds to a small disturbance in the attitude.

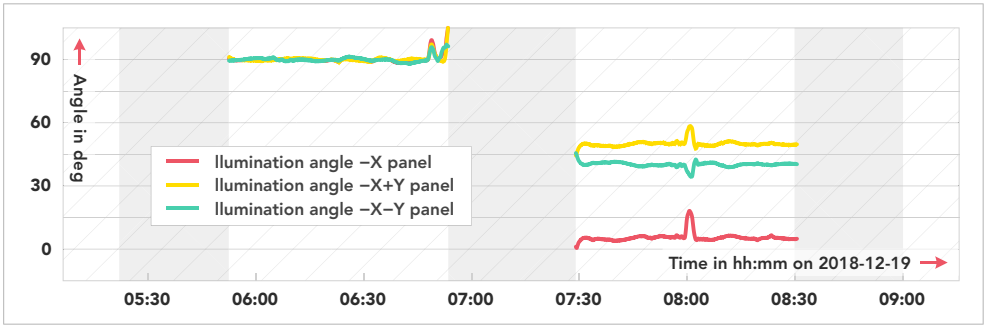

Figure 4.12: Angles between Sun vector and the normal vector of the −X, the −X+Y and the −X−Y solar array during the power generation experiment. The eclipse periods are indicated with a grey coloured background (Figure bases on data first presented in [13]).

Figure 4.13 gives and overview over voltages and currents of solar panels and the battery throughout the experiment as provided by the spacecraft's telemetry. For a better overview only solar path B is plotted within the figure. Furthermore, the curves are smoothened by means of a moving average over 10 measurements for better legibility, while the original telemetry data are plotted as narrower grey scale lines in the background.

Within the first Sun phase of the experiment, electrical power is solely generated from Earth albedo, as no solar array was illuminated by the Sun[6]. Due to the fact that more electrical power is consumed by the spacecraft (including battery charging) than can be generated by the solar arrays, the voltage of the solar path remains at 12 V throughout the first Sun phase. On the batteries' side it can be seen that voltage and current generally follow the pattern dictated by power generation. Here, current values below zero indicate the power the spacecraft draws from the batteries, while positive current values represent battery charging.

[6] According to Patel [16], no power is generated by a solar cell at illumination angles above 85 degrees, so that attitude alignment errors in the degree range will not result in power being generated by the solar cells.

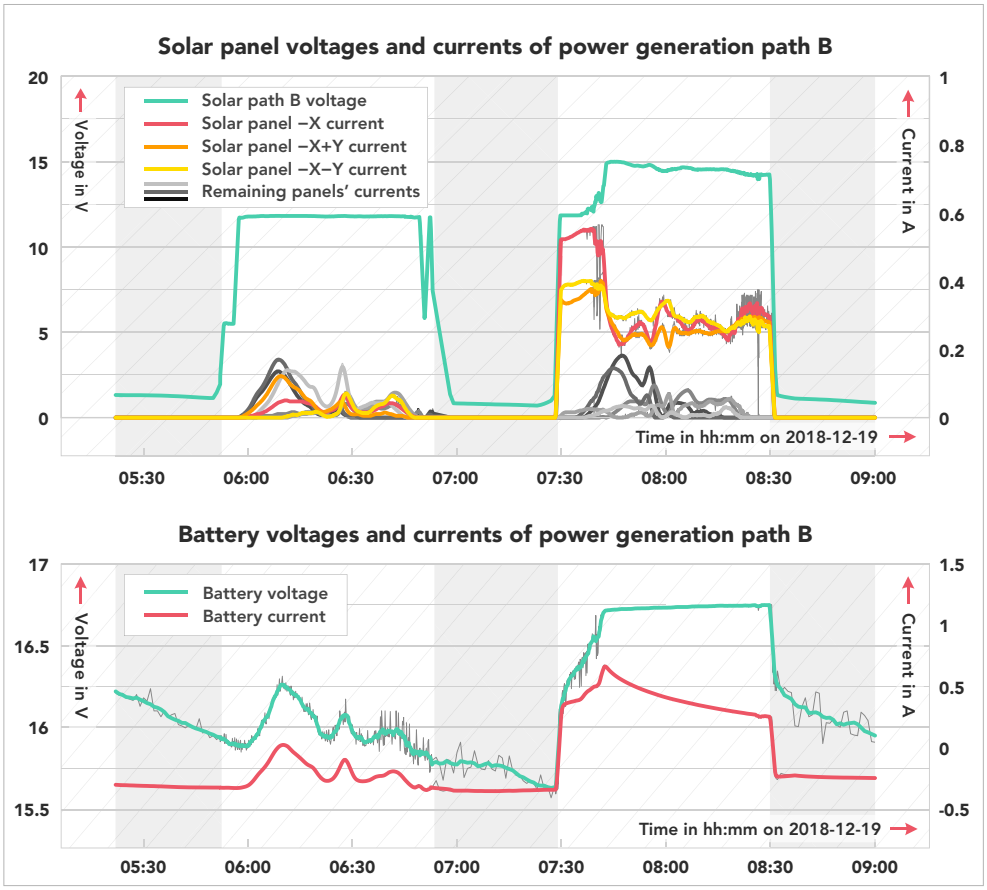

Figure 4.13: Telemetry data for voltage and current of solar path B (top) and battery B (bottom) during the power generation experiment. The currents of the −X solar panel, which is illuminated perpendicular during the experiment, as well as of the −X+Y and −X−Y panels are depicted in colour. All other solar panel's currents are plotted in grey scale and are only shown for completeness. For better visibility, the plotted lines are smoothed with a moving average over 10 data points. The eclipse periods are indicated with a grey coloured background. (Figure bases on data first presented in [13]).

It can be seen, that a positive power balance is reached at some points solely based on the electrical power generated by Earth albedo.

Upon entry into the second Sun, phase the solar path's voltage is yet again reduced to 12 V. As the −X solar array is aligned towards the Sun with the lowest offset

angle, it produces the largest amount of electrical power. As discussed already, the difference in current between the −X+Y and the −X−Y array can be attributed to the difference in Sun angle of both arrays.

Furthermore, a significant increase of current can be observed for the −X and the −X+Y solar array within the first 10 minutes of the second Sun period. It could be shown in Section 3.2.3 that the power generated by a solar cell will increase slightly at higher temperatures when operated at constant voltage[7]. However, when looking at Figure 4.14 it can be seen that the increase in temperature shows a similar profile for all three relevant panels (−X, −X+Y, and −X−Y), while the increase in generated power shows a significantly different profile for panel −X+Y and panel −X−Y.

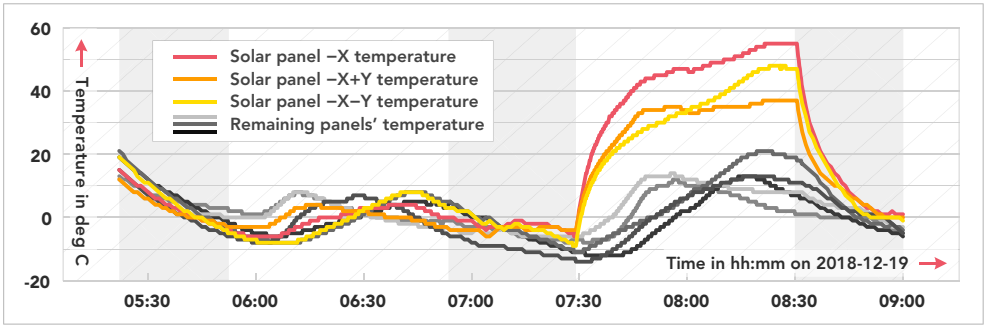

Figure 4.14: Solar panel temperatures throughout the Experiment. Here, the colour coding of the panels is the same as for the current in Figure 4.13 to allow for comparison. Grey coloured background indicates the eclipse periods (Figure bases on data first presented in [13]).

Another factor that may contribute to the electrical power generated by the solar cells is Earth albedo. In contrast to the Sun, that can be considered a point source as seen from the satellite, the Earth fills a significant part of the satellites field of view (FoV). The half angle of the Earth as seen from the satellite α_{Earth} can be calculated using the Earth's radius r_{Earth} and the orbit altitude h_{orbit}:

$$\alpha_{\mathrm{Earth}} = \arcsin \frac{r_{\mathrm{Earth}}}{r_{\mathrm{Earth}} + h_{\mathrm{orbit}}}. \tag{4.10}$$

[7] The opposite is true for a cell that is operated at the MPP, where the generated power decreases significantly at higher temperatures.

With its orbital altitude of 600 km a half angle of 66 degrees can be obtained for TechnoSat.

Figure 4.15 shows a comparison between the telemetry value for the current generated by the −X+Y panel and a simulation that takes into account the cell voltage, its temperature, the satellite's attitude relative to the Sun, and the season (cf. Section 4.1.4 for details on the simulation)[8]. For better clarity only the second Sun phase of the formerly considered period of time is shown here.

While telemetry and simulated values are in good agreement for the first half of the Sun period, significant deviations can be observed starting about half an hour into the Sun period. In the lower plot of the same figure, the angle between the normal of TechnoSat's −X+Y solar panel and the vector pointing from the spacecraft towards the centre of Earth is plotted. Furthermore, the amount of the Earth's surface that is in the FoV of the −X+Y solar panel is indicated by a coloured area. When comparing the two plots in the figure it becomes obvious that the mentioned deviation between simulation and telemetry values corresponds to the increasing fraction of Earth that is in the FoV of the solar panel. Here, it needs to be noted that the albedo's contribution to the generated power diminishes towards the end of the Sun phase albeit the fact that Earth is still in the solar panel's FoV due to the declining angle between the Sun vector and the Earth's surface below the spacecraft.

In order to confirm these observations, the same plot is presented for the −X+Y solar panel in Figure 4.16. Here, the deviation between telemetry data and simulation is most prominent at the beginning of the Sun phase, which again corresponds with the fraction of Earth that is in the FoV of the solar panel.

Figure 4.17 gives an overview of the overall power generation, storage and consumption within the TechnoSat spacecraft throughout the experiment. Here, the total power generated by the solar panels as well as the power consumed by the spacecraft throughout the experiment are plotted. Furthermore, the battery power is shown with values above zero denoting that the battery is charged while numbers below zero indicate that it is discharged to supply the spacecraft with power. The

[8] The solar cell model used in the simulation is very sensitive to variations in the voltage when the cell is operated at floating voltage. As the voltage of the solar path is measured centrally in the PCU and not locally on the panel, individual deviations of the different panels needed to be calibrated. For the −X−Y and the −X+Y solar panel, an offset of 0.12 V was compensated in the simulation at hand.

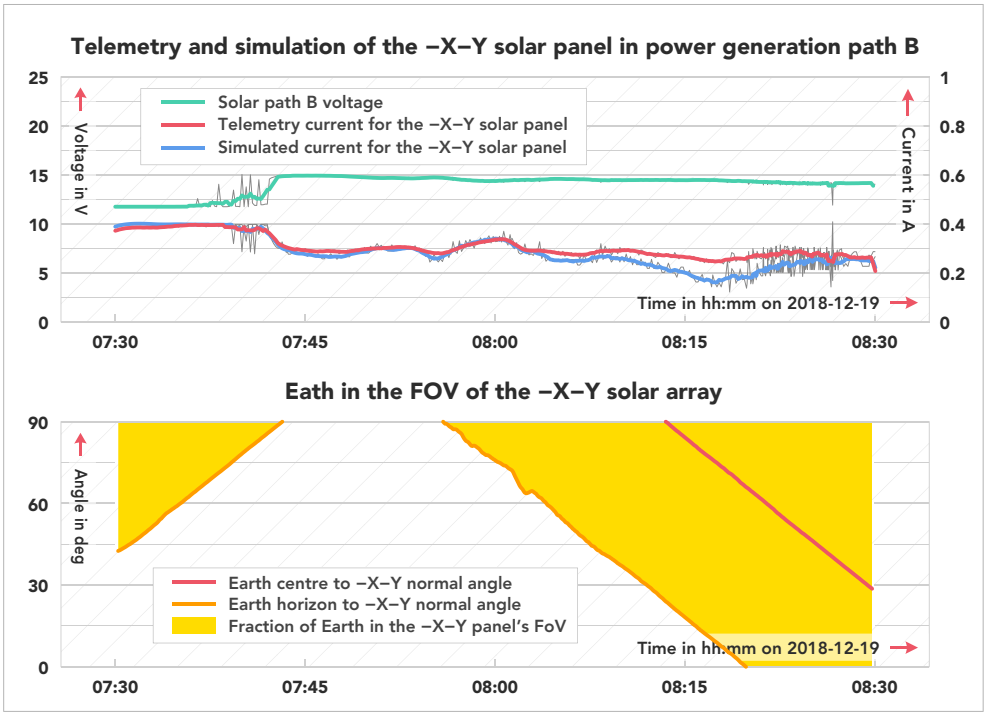

Figure 4.15: Impact of Earth albedo on the power generation. The upper plot shows a comparison between telemetry values for the current of the −X−Y solar panel of power generation path B and a simulation of the same parameter. The lower plot depicts the Angle between the direction vector from spacecraft to the centre of the Earth and the −X−Y solar array normal. Furthermore, the coloured sectors indicate the areas in which parts of the Earth are in the FoV of the solar panel (Figure bases on data first presented in [13]).

slightly elevated consumption at the end of the second Sun phase indicate UHF communications during a ground station pass.

Verification of the Power Generation Simulations

In the following, an orbit experiment is described that was conducted to verify the simulation that was developed in Section 3.2.3 for predicting the power generation capabilities for different platform configurations.

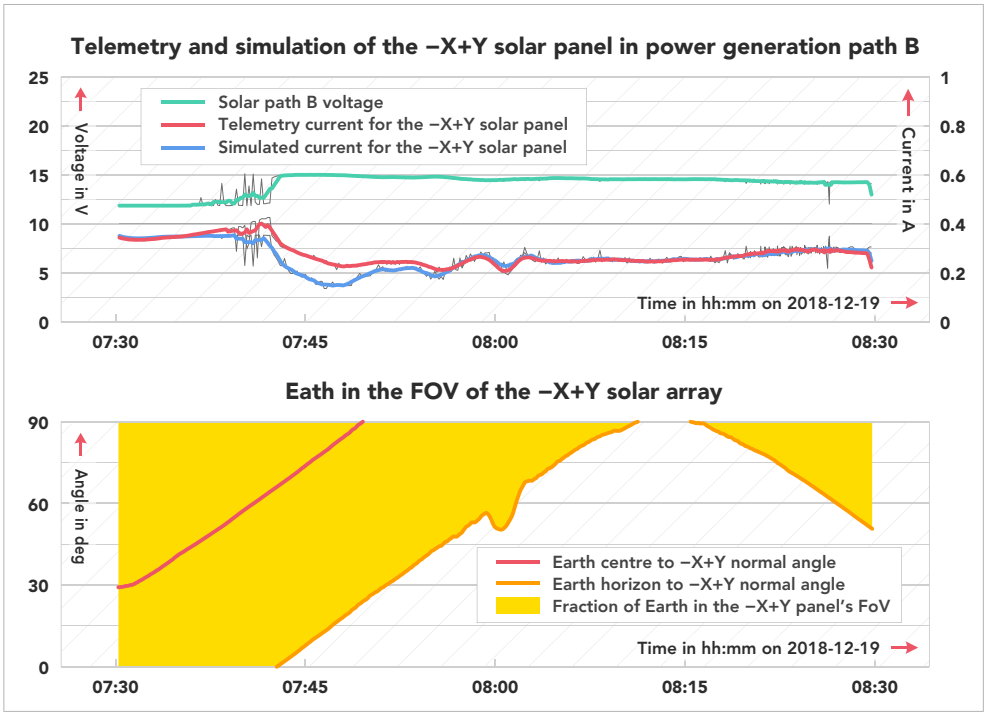

Figure 4.16: Impact of Earth albedo on the power generation. The upper plot shows a comparison between telemetry values for the current of the −X+Y solar panel of power generation path B and a simulation of the same parameter. The lower plot depicts the Angle between the direction vector from spacecraft to the centre of the Earth and the −X+Y solar array normal. Furthermore, the coloured sectors indicate the areas in which parts of the Earth are in the FoV of the solar panel (Figure bases on data first presented in [13]).

As discussed in Section 3.2.3, there is a number of factors that influence the current a solar cell may deliver. These include, among others, the temperature, the cell voltage, and the Sun illumination angle. In order to reduce the uncertainties within the experiment, it was designed such that the influence of most of these parameters was minimised.

The entire experiment took 45 minutes and generated over one million telemetry values. Within the experiment the satellite was performing Sun pointing with the +Z solar panels at the middle of the Sun phase, while it was configured such that more power was consumed than could be generated by the solar panels. Figure 4.18

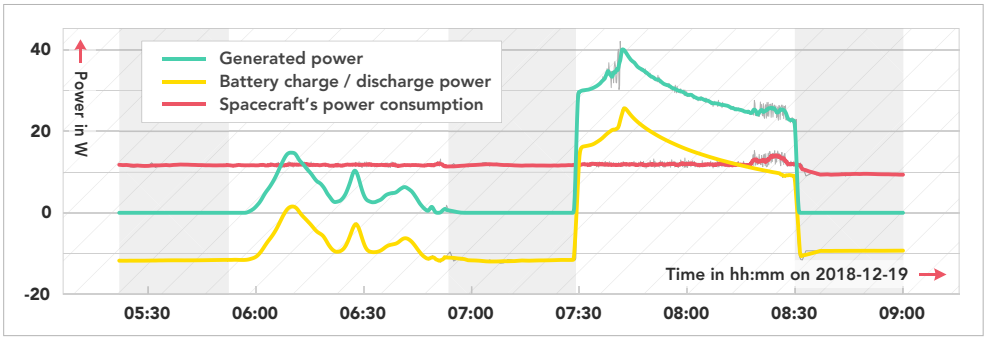

Figure 4.17: Telemetry data of the power generated by the solar panels, as well as power consumption of the spacecraft. Additionally, the battery power is shown with positive values represent battery charging and negative ones indicate discharging. For better visibility, the plotted lines are smoothed with a moving average that includes 10 data points (Figure bases on data first presented in [13]).

gives an overview of the development of the angle between the Sun vector and the solar panel normals within a selected fraction of the experiment. While the angle between Sun vector and the +Z side adjusts to the predefined 5 degrees at the beginning of the experiment, the respective angles of all other panels take values of above 85 degrees.

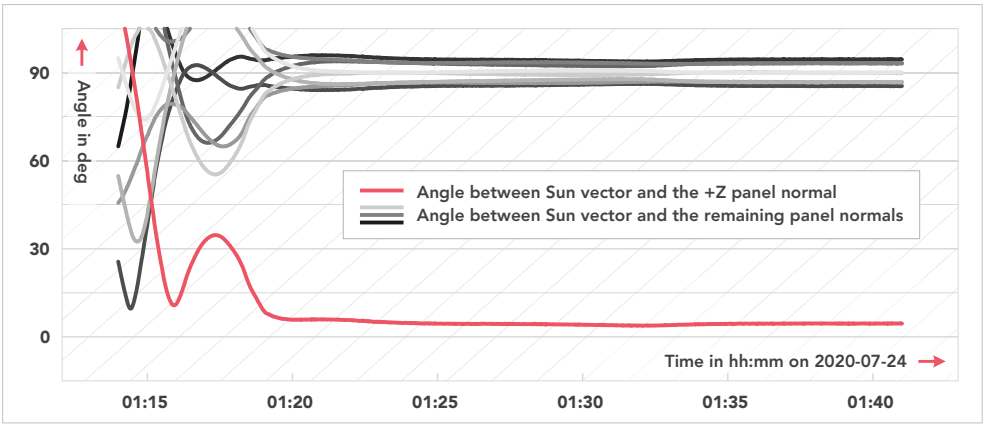

Figure 4.18: Telemetry showing the angle between TechnoSat's Sun vector and the spacecraft's solar panel normals throughout the experiment. At the beginning of the plot the spacecraft is still in the process of aligning its attitude for the experiment.

The experiment was timed such that it included the middle of the Sun phase, were the angle between the satellite's Earth and Sun vector is largest. This minimised the Earth albedo for the +Z solar panels. Figure 4.19 shows the minimal angle between Earth's horizon and the normal vectors of the solar panels. One can see that the angle raises to above 80 degrees for the +Z solar panel, at which point the albedo's influence is expected to be negligible for this panel (cf. the discussion of the Kelly cosine in Section 3.2.3).

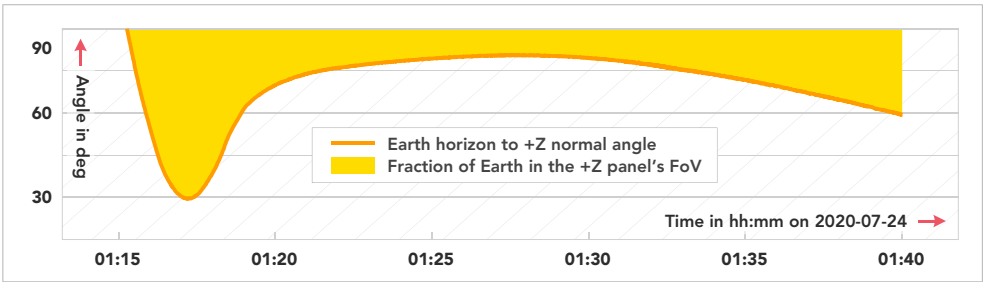

Figure 4.19: Minimal angle between Earth's horizon and +Z solar panel normal of the TechnoSat spacecraft calculated from telemetry.

Figure 4.20 gives an overview of the geometrical alignment of the satellite's +Z solar panel, Sun, and Earth when the Sun is highest above the spacecraft, i.e. when the albedo impact on the +Z solar panel is minimal. Here, the beta angle, i.e. the angle between the Sun vector and the Earth vector as seen from the satellite is 37 degrees. As a compromise between the solar panel's orientation towards the Sun and the objective to minimise the albedo seen by the panel, an angle of 5 degrees between the panel's normal and the Sun vector was chosen. This, in turn, results in a minimal angle between the solar panel normal and the vector towards the Earth's horizon of 82 degrees.

The current generated by each solar panel of the solar path A is shown in Figure 4.21. It can be seen that the +Z panel generated around 500 mA, while the values of all other currents remain below 100 mA.

As discussed before, the angle-power curve for solar cells deviates from the cosine for angles above 50 degrees, were the curve follows the Kelly cosine. For angles above 85 degrees the Kelly cosine predicts zero power generation (cf. [16] and Section 3.2.3). Based on the angles shown in Figure 4.18 it can therefore be concluded that all power shown in Figure 4.21 except from what is produced by the +Z panel is generated by albedo.

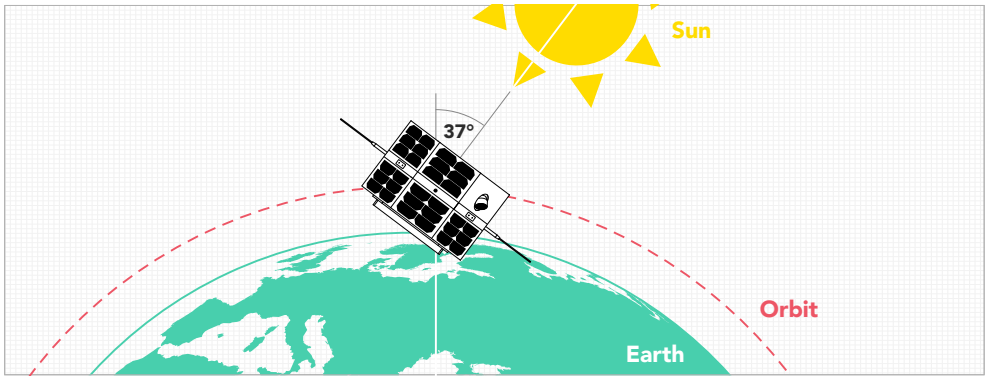

Figure 4.20: Illustration of the beta angle, i.e. the angle between the Earth vector and the Sun vector as seen from the satellite.

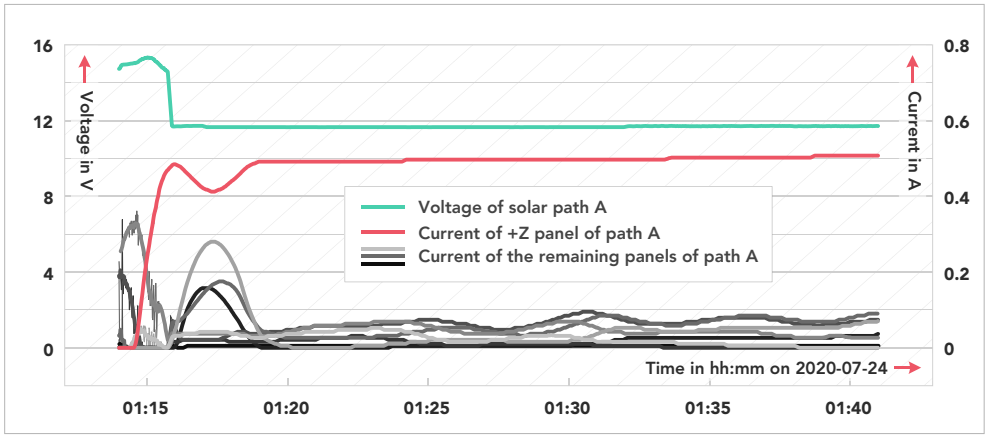

Figure 4.21: Currents generated by the solar panels of path A throughout the experiment according to telemetry. All currents except the ones generated by the +Z solar panel can be associated to Earth albedo.

In order to ensure that the solar cells are forced to operate at the minimum voltage that is permitted by the charge regulator, the power consumption of the spacecraft was increased above what could be generated by the solar cells. Figure 4.22 shows the power consumption of the spacecraft throughout the experiment. The increase of approximately 7 watts in power consumption that can be seen at the beginning of the experiment was realised by activating the satellites S-band transmitter for

15 minutes in which the total power consumed by the spacecraft increased to just below 20 watts.

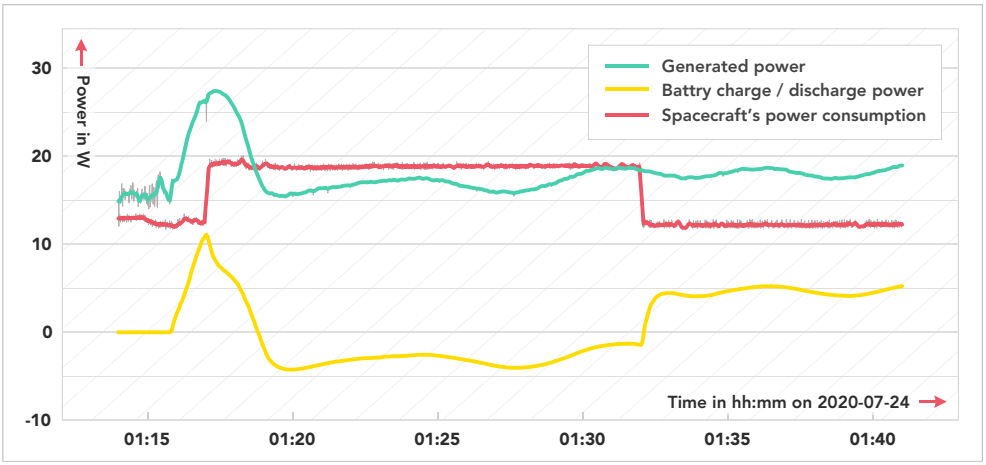

Figure 4.22: Power consumption and power generation of the TechnoSat spacecraft throughout the experiment according to telemetry. Furthermore, the charge and discharge power of the batteries is shown. For better visibility the plot is smoothed with a moving average involving 10 data points, while the original values are shown in grey in the background.

Furthermore, the figure shows the total power that is generated by the solar panels, as well as the charge and discharge power of the battery. The peak in power generation at about 1:17 hours Universal Time Coordinated (UTC) can be accounted to several panels that are illuminated during attitude alignment for the experiment, which do not generate any power in the experiment's final attitude. For the remainder of the experiment, the total generated power oscillates between values of 15 W to just below 20 W. Here, Figure 4.21 shows that the oscillations are due to albedo generated power.

The battery is charged for a short duration within the alignment phase and then discharged while the S-band transmitter is switched on. Here, battery discharge is indicated by negative values. As soon as the power consumption of the platform goes back to around 12 watts, the excess power of approximately 5 watts is used for battery charging.

Figure 4.23 gives an overview over the development the solar panels' temperatures throughout the experiment based on telemetry. While the temperature of all other

panels remains comparably stable at temperatures between zero and 20 degrees Celsius once the target attitude was reached, the temperature of the +Z panel increases constantly up to above 50 degrees.

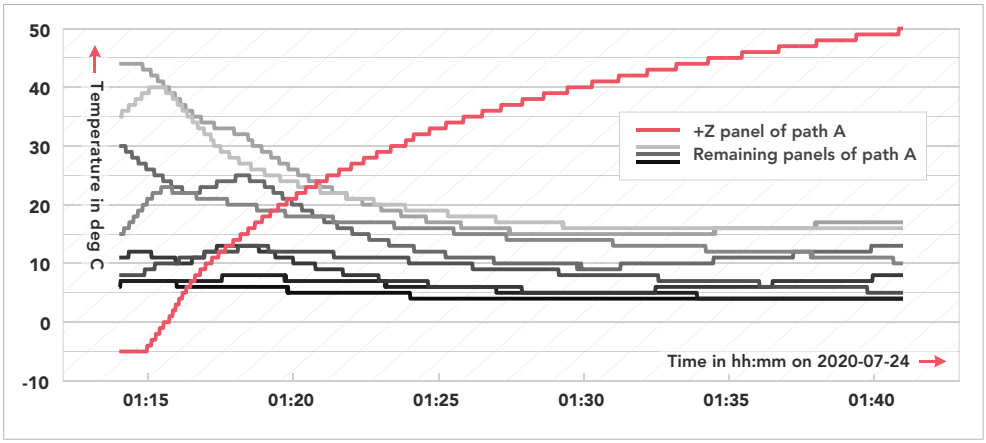

Figure 4.23: Telemetry for the temperature development of the solar panels of path A throughout the experiment. The +Z panel that is pointed towards Sun can clearly be identified by the raising panel temperature.

To parametrize the simulation presented in Section 3.2.3 to the orbit experiment the cells' temperature and voltage, the solar radiation, as well as the solar cells' individual performance needs to be taken into account.

As shown by Rai in [249] the solar radiant power density for a given day of the year can be calculated by:

$$P = P_{\text{avg}} \left[1 + 0.033 \cos \left(\frac{360(n-2)}{365} \right) \right] \tag{4.11}$$

with the day of the year n and the average solar radiant power density P_{avg} that was measured with $1\,360.8\,\text{W}\,\text{m}^{-2}$ according to Kopp and Lean [143].

The solar cells that were applied for the TechnoSat mission are part of a batch containing 420 cells. For the simulation of the panel average cell performance, values from this batch were used as reference.

Table 4.4 summarises the input parameters used for the simulation of the solar panel currents of the experiment.

Table 4.4: Input parameters used for the simulation of the solar panel currents performed for verification with telemetry values from orbit. The solar cell parameters assume a panel temperature of 28 °C and a perpendicular irradiation with 1 367 W m^{-2}.

Parameter	Value	Unit
Solar radiant power density	1 318.9	W
Average open-circuit solar cell voltage	2 600	mV
Average short-circuit solar cell current	512.3	mA
Solar cell voltage at maximum power point	2 304	mV
Solar cell current at maximum power point	476.6	mA

In the following, the uncertainties of the input parameters, as well as additional error sources for the current simulation of the solar panel are assessed and discussed regarding their impact on the simulation. For this analysis, a solar cell delivering 500 mA at 2 V and a temperature of 28 degrees Celsius being illuminated with 1 367 W m^{-2} is assumed as reference scenario.

- The voltage of the solar paths is measured on the PCU within the central avionics unit of the satellite. Here, the voltage drop between the solar panel and the PCU due to the resistance of the cable, the connectors and the components implemented into the power path needs to be considered. However, due to the selected experiment setup, the system is very robust against variations in the cell voltage. Here, a ten percent error of the cell voltage results in an 0.02 percent error in the simulated current.
- According to Kopp and Lean [143] the uncertainty on the solar radiation power is $\pm$0.5 watt. Here, a deviation of 0.5 watt for the solar radiated power results in an error of 0.04 percent in the simulated current.
- The 2σ pointing accuracy of TechnoSat was found to be 3.7 degrees in [151]. Such an misalignment would result in an error of 0.77 percent in the simulated current for errors that increase the angle to the panel normal and 0.35 percent for errors resulting in a lower incident angle.
- The panels temperature is measured by an IC with a maximum absolute error of 1.5 Kelvin. Furthermore, the IC is located on the opposite side of a 1 mm PCB, as seen from the solar cell. To account for this and also for potential gradients over the solar panel a maximum temperature error of

5 Kelvin is assumed. This in turn results in a maximum error of 0.33 percent in the simulated current.

– The maximum discretisation error introduced by the EPS software is minus 5.3 mA, which amounts to 1.06 percent. As the deviations in current are slow relative to the measurement period applied in the experiment these errors can be removed in post-processing almost completely.

– The current measurement error of the current measurement IC over the entire temperature range is 2.5 percent (including the tolerance of the shunt).

– The difference in performance between the best cell of the batch used for the TechnoSat flight model and the average of all cells is 2.50 percent, while the least efficient cell is 1.81 percent below the average.

Thus, the maximum positive deviation form the simulated nominal panel current under reference conditions is 15.2 mA (6.14 percent), while the maximum negative deviation is 17.8 mA (5.80 percent).

For the given experiment Figure 4.24 shows a comparison between the telemetry values gathered for the +Z solar panel of path A plotted in green, with the simulated nominal current that is depicted in red. Furthermore, the tolerance band of the simulation is plotted in yellow.

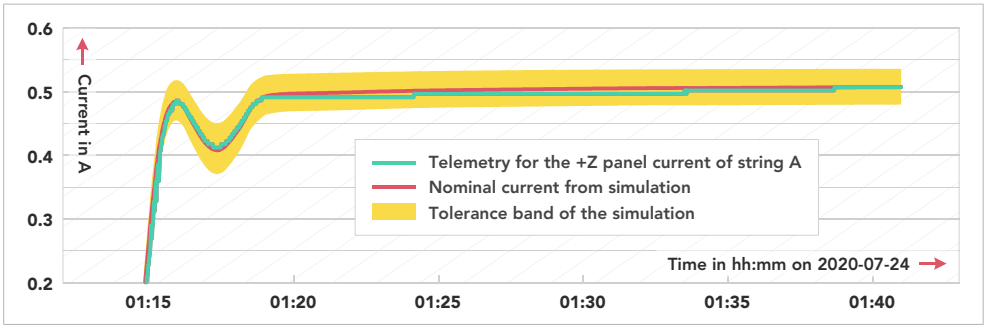

Figure 4.24: Currents generated by the +Z solar panel of path A throughout the experiment together with nominal simulation value and the simulation's tolerance band.

The average deviation between the simulation and the telemetry values for the part of the experiment where the angle between the Earth's horizon and the normal of the +Z side is above 70 degrees is 1.88 percent which equals to 9.32 mA.

Power Consumption

The power consumption of the satellite platform in different operational modes is an important parameter for evaluating the EPS. Table 4.5 gives an overview of the power consumption of the TechnoSat spacecraft in different modes of operation (cf. Figure 4.7) derived from telemetry. Here, each value represents an average over five minutes. The similar overall consumption of the imaging and the downlink mode can be explained by the fact that while the S-band transmitter is not operated in imaging mode, the FORs are powered, whose power consumption is in the same order. The maximum power consumption of the platform occurs when both the S-band transmitter and FORs are powered while the satellite performs active attitude pointing.

Table 4.5: Power consumption of the TechnoSat spacecraft in different satellite modes (cf. Figure 4.7) based on telemetry data. Each value represents an average over five minutes of data.

Satellite mode	Satellite's attitude	Power consumption W
Safe mode	Unconstrained	3.68
Suspend mode	Unconstrained	3.92
Imaging mode	Inertial pointing	12.12
Downlink mode	Target pointing	13.52
Maximum platform power[a]	Inertial pointing	18.35

[a] Same as the imaging mode, only that additionally the S-band transmitter is powered

4.1.5 Mission Operations

TechnoSat was brought to orbit on the 14th of July 2017 at 06:36:49 UTC with a Soyuz 2.1 launcher equipped with a Fregat upper stage. Within first pass over the ground station in Berlin at 09:54 UTC the satellite's first telemetry data was downloaded. Within the first two months of the mission platform and payloads could be commissioned successfully. Within the platform's commissioning phase, first performance improvements were realised for the Sun sensors by updating the software of the ADCS node [245][9].

[9] Peer reviewed journal publication with contributions from the author.

After the commissioning phase was concluded, the regular payload experimentation phase was initiated. Starting already from October 2017, experiments that combined the use of two or more payloads were conducted although this was originally only planned for a much later stage of the mission. This included, for example, imaging with the camera payload in parallel to S-band data downlink with reaction wheel actuated attitude control. Figure 4.25 shows a selection of images captured by the TechnoSat spacecraft during early experimentation.

As a result of the very successful testing that was conducted with the reaction wheels, the S-band transmitter, and the camera, these three components were declared regular platform components in January 2018.

Within a number of software updates, the platform's capabilities could continuously be upgraded. In the following, a selection of these improvements are described in more detail.

Because of the limited nominal data downlink capacity, only four images could be stored within the PDH upon launch of the spacecraft. The application of the S-band transmitter enabled the downlink of several hundred images per pass. Thereupon, the storage capability was increased to more than 1 000 pictures by means of software updates in order to effectively exploit the increase in downlink capability.

As the S-band transmitter was a declared payload on the TechnoSat mission, the experiments were originally planned such that all data could be downloaded via UHF. Thus, the limited data rate of the UHF communication system effectively restricted the potential for payload operation and platform characterisation. In order to enable more frequent experimentation and more data intensive scenarios, the software was updated to support telemetry downlink via S band.

One example for such a data intensive platform experiment is the recording temperatures on decks and solar panels, as well as the generated power in 10 second resolution for five consecutive orbits, which generated more than 820 000 telemetry values in total. Figure 4.26 exemplary shows the development of the temperature on the satellite's three decks. Here, deck A is the deck the separation system is mounted to, deck C is the side were camera is mounted to, and deck B is mounted in the middle between the decks A and C (cf. Figure 4.4). One can see that the temperatures of decks A and B stay within a range of approximately 20 degrees Celsius. Deck C, that is one of the outer two decks, which are exposed to direct sunlight are subject to higher temperature variation of around 30 degrees

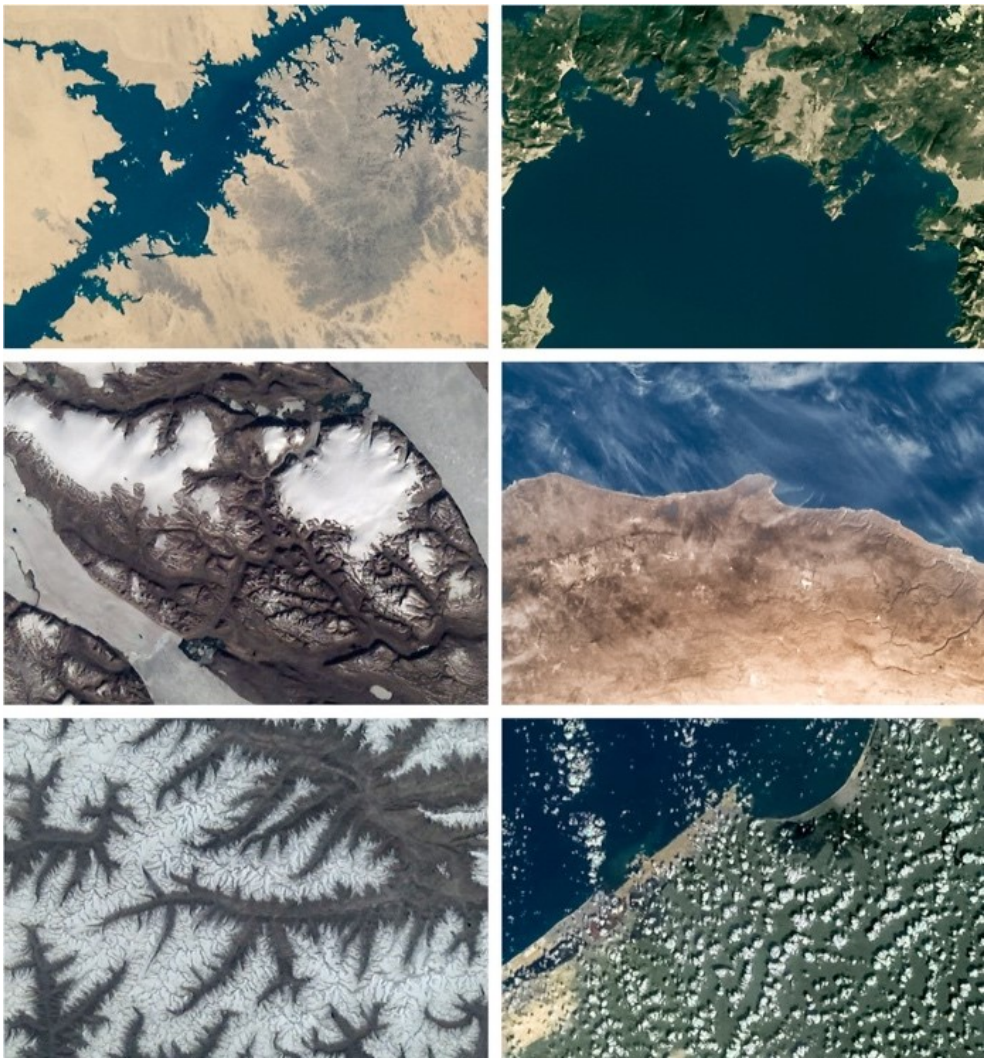

Figure 4.25: Selection of images that were captured by TechnoSat throughout payload commissioning and early operations [244].

Celsius. Here, difference of temperature variation between the decks A and C can be explained by the much larger heat capacity that is provided by the components mounted to deck A.

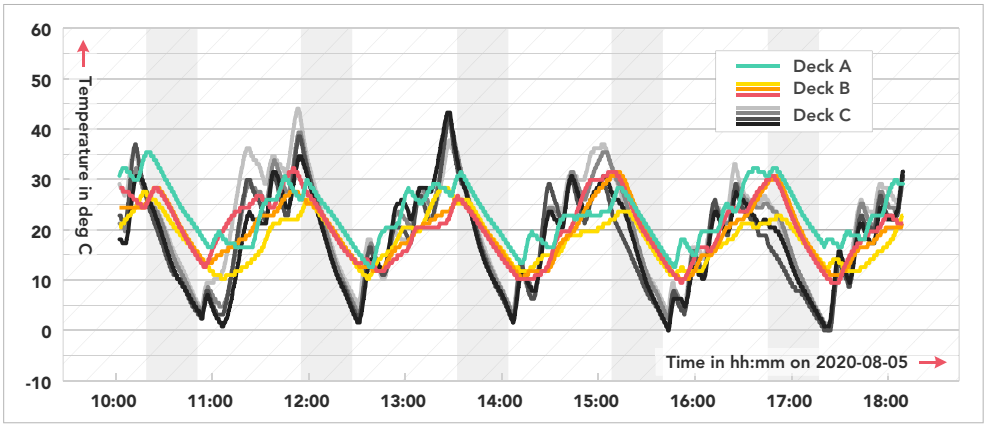

Figure 4.26: Telemetry data that show the development of the decks' temperatures throughout five consecutive orbits with unconstrained attitude. Grey coloured background indicates the eclipse periods.

The minimal time between two consecutive images of TechnoSat's camera is defined by the duration of the transfer of an image from the camera to the PDH. In order to image continuous swaths in nadir pointing, this time was reduced to 6.6 seconds, allowing for an overlap of one third image between two consecutive images.

This enabled to record many swaths to be combined in one scenery. Figure 4.27 shows a subset of a scene showing the Middle East region that was assembled using around 2 000 single images. The shown fraction comprises of approximately 170 pictures and depicts parts of Egypt and Israel.

In order to enable visual confirmation of the S-band antenna's pointing towards the ground station, a streaming mode was implemented for the camera that allows for directly sending images to the ground were they are imminently displayed without the need for on-board storage.

Furthermore, the spacecraft's ADCS software was improved by adding momentum management capabilities that helped to greatly reduce the zero-crossings in rotational rate that occur during active attitude pointing and thus improves its accuracy.

Figure 4.28 shows the angular error while acquiring nadir pointing for an experiment conducted on the 9th of March, 2019 [37]. One can see that from an initial error

Figure 4.27: Composite image showing parts of Egypt and Israel that combines approximately 170 pictures, which were captured by TechnoSat from orbit [37] (Image credit: Philipp Werner).

of more than 60 degrees, the satellites reaches the target attitude in less then 240 seconds. Generally, the momentum management feature is programmed to avoid high rotational rates for the reaction wheels as this may lead to saturation and increases mechanical abrasion [250].

In Figure 4.29 one can observe how the angular momentum of the individual reaction wheels is approaching and maintaining the target value of around 4 mN m s, which corresponds to approximately 400 rpm.

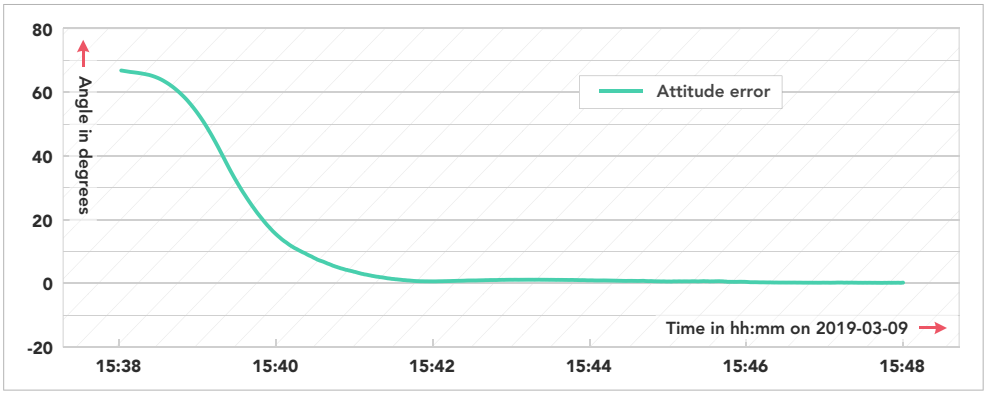

Figure 4.28: Telemetry for the development of the angular attitude error while acquiring nadir pointing (Figure bases on data first presented in [37]).

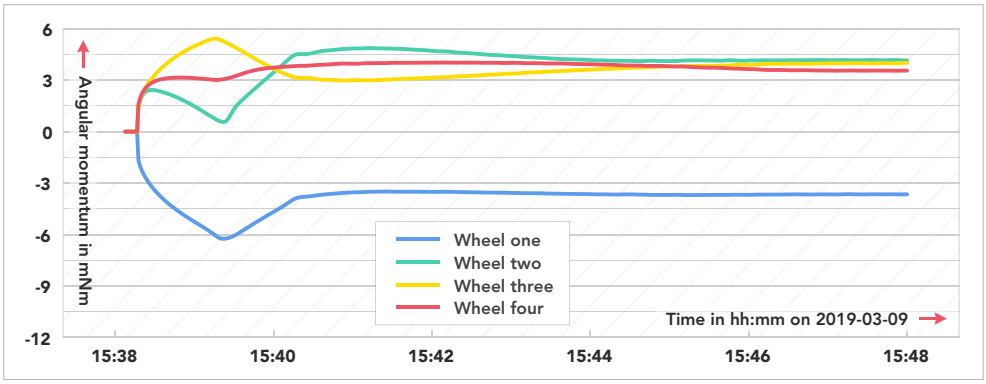

Figure 4.29: Telemetry for the development of the angular momentum of the reaction wheels that shows how angular momentum management is distributed between the four reaction wheels (Figure bases on data first presented in [37]).

On the 16th of July, 2018 a close encounter with the CORVUS BC-1[10] satellite allowed to demonstrate TechnoSat's improved pointing and imaging capabilities within an application scenario. CORVUS BC-1 is a 6 U CubeSat that was predicted to pass TechnoSat with a minimal distance of 235 meters. For the time were both satellites were between 3.5 and 17 kilometers apart the conditions were suitable for TechnoSat to capture images of CORVUS BC-1. Figure 4.30 shows three images on which the satellite can clearly be distinguished against the background.

[10]The satellite was was later renamed to *Landmapper BC-1*.

Figure 4.30: Three images of the 6 U CubeSat CORVUS BC-1 captured by TechnoSat in July 2018 at distances between 3.5 and 17 kilometres [244]. The images are cropped, the contrast is enhanced, and hot pixels of the camera were removed to improve visibility. The white circles were introduced to simplify the identification of the spacecraft on the images.

To assess the absolute attitude determination and control performance of TechnoSat images of Earth's surface were used to compare the recorded scene with the commanded target [150]. Here, the analysis of 14 individual images revealed a mean performance error of 2.0 degrees.

The aforementioned method for attitude control performance analyses involved the manual selection of ground control points (GCPs), which in turn limited the amount of data points that could be generated for a statistical analysis. To overcome this limitation, the Moon was selected as target to allow for automated processing of the images. Figure 4.31 shows selected images from one of the first series of Moon images recorded by TechnoSat in May 2018.

Results of the experiments performed to evaluate the pointing accuracy of the TechnoSat ADCS based on images of the Moon and other celestial bodies were presented by Jonglez et al. in [151][11]. Here, a series of more than 400 Moon images recorded in January 2019 revealed a mean performance error of 1.8 degrees and a standard deviation of 0.9 degrees, which is in agreement with the values derived from the Earth images.

Another software update that concerned all seven TUBiX20 nodes of the spacecraft upgraded the spacecraft's mode and FDIR architecture to the status that is

[11] Publication with contributions from the author.

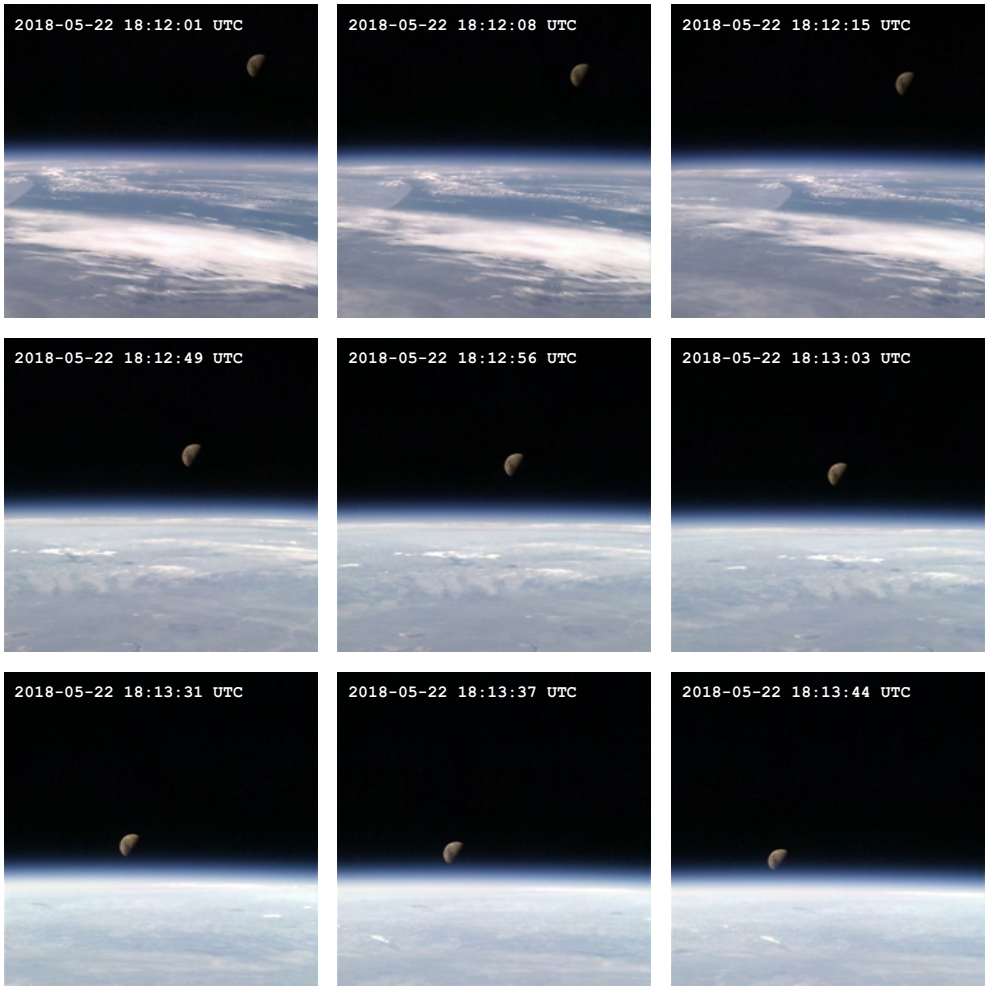

Figure 4.31: Selected images from a picture series showing a half Moon declining towards Earth's horizon over Chile recorded in May 2018. The images were cropped and enhanced for display.

described in this thesis (cf. Section 3.3.9 and Section 3.3.10) as this was not yet implemented when the satellite was launched.

In order to convey an impression of the operation that were conducted with the TechnoSat spacecraft in the first three years, an overview of different key figures is given in Table 4.6.

Table 4.6: Collection of key figures quantifying the TechnoSat operations that were performed within the first three years in orbit.

Parameter	Value	Unit
Number of orbits	16 325	-
Ground stations used for satellite operations	4	-
Number of passes in which operations were performed	3 631	-
Number of pictures downlinked by the spacecraft	98 522	-
Amount of telemetry that was downloaded	495	MiB
Amount of payload data that was downloaded	5 613	MiB
Number of software uploads that were performed	26	-

One can see that operations were conducted in 22 percent of all orbits with four different ground stations. However, for the majority of the operated passes, the primary ground station in Berlin was used. Nearly 100 000 images were downloaded accounting for the majority of the payload data. Furthermore, more than 25 software uploads were conducted, mainly to introduce new features for in-orbit testing. Here, each software upload denotes the update of one single node and a specific feature may require loading a new image on several nodes.

4.1.6 Conclusions

TechnoSat is an IOD mission that carries seven technology demonstration payloads. This includes a novel attitude actuator that is based on a magnetic fluid circulated in a ring-shaped tube to create an angular momentum, a set of newly developed reaction wheels and a new type of space debris detector. As the first spacecraft to be based on the TUBiX20 platform architecture, TechnoSat served as a proof-of-concept mission to validate the platform's key technologies, such as the distributed hardware design and the associated software architecture.

Besides verifying the platform concept in orbit, the TechnoSat mission generated a wealth of orbit data that is used to validate the platform's performance. Here, it could for example be shown that the simulations used to dimension the solar panels can accurately predict the generated power. Furthermore, images of the Earth's surface, the Moon and other celestial bodies captured with the satellite's camera payload were used to analyse the attitude determination and pointing

accuracies of the platforms coarse attitude control system configuration that was implemented for the TechnoSat mission. The retrieved data will furthermore be used to optimize the individual subsystems' capabilities for future implementations of the platform.

After three years in orbit nearly 100 000 pictures have been captured and sent to ground by TechnoSat and 26 software updates were performed to extend the satellite's range of functions. The spacecraft is still operated on a regular basis and is now also used as an in-orbit test bed for newly developed software features for upcoming missions.

4.2 The TUBIN Mission

The microsatellite mission TUBIN[12] has the primary objective to demonstrate wildfire detection by means of uncooled microbolometer arrays.

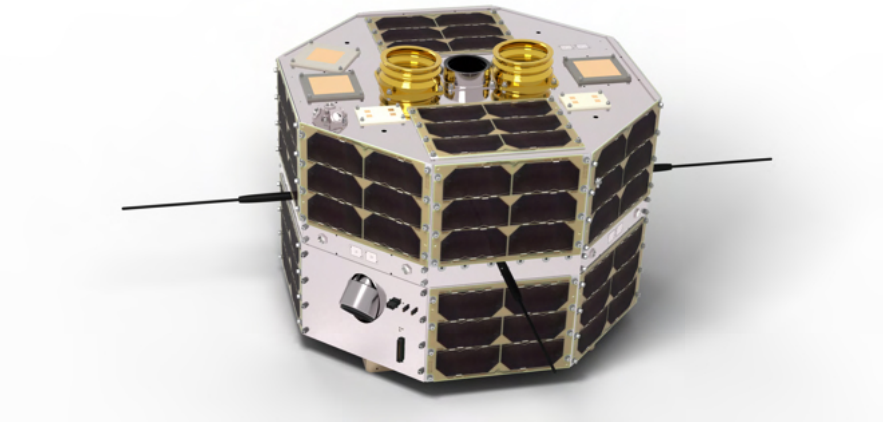

Figure 4.32: Digital rendering of the TUBIN spacecraft in operational configuration with the side that will be directed towards nadir for nominal imaging operations pointing upwards [251] (Image credit: Marc Lehmann).

[12]The TUBIN mission, as well as the IOD of XLink within the TUBIN mission are funded by the Federal Ministry for Federal Ministry for Economic Affairs and Energy (BMWi) through the German Aerospace Center (DLR) on the basis of a decision of the German Bundestag (grant no. 50RM1102 and 50RY2009).

Table 4.7: Main parameters of the TUBIN mission, as well as requirements and performance parameters of the satellite platform to support the mission.

Mission objective:	Detection of high-temperature events
Launch date:	30^{th} of June, 2021
Launcher:	Falcon 9
Orbit:	530 km SSO
Spacecraft launch mass:	22.57 kg
Spacecraft volume[a]:	$465 \times 465 \times 305\,\text{mm}^3$
Design lifetime:	1 year
Power generation capabilities:	37 W (peak power in Sun pointing)
Power storage capabilities:	117 W h
Required position knowledge:	1 km
Required attitude knowledge:	6 arcmin
Required attitude stability:	30 arcmin/s
Required pointing accuracy:	180 arcmin
Required pointing agility:	180 deg manoeuvre in 5 min
Data downlink rate:	$2\,\text{Mbit}\,\text{s}^{-1}$ (nominal S-band transmitters)
	$50\,\text{Mbit}\,\text{s}^{-1}$ (experimental X-band transceiver)

[a] Without antennas and payload baffles

An overview of the TUBIN mission was published in a peer reviewed journal article by Barschke et al. [32]. As a secondary objective, the mission shall demonstrate the capability of the TUBiX20 platform to support demanding Earth observation missions.

Late in the development, when most of the flight hardware was already produced, the X-band transceiver XLink was introduced into the mission as additional opportunity payload [252][13].

Figure 4.32 shows an digital rendering of the TUBIN spacecraft in operational configuration. At the top of the spacecraft, which is the side that will be directed towards nadir during nominal operations of the imagers, one can see the two

[13] Publication with contributions from the author.

golden baffles of the infrared microbolometers, with the smaller silver baffle of visible spectrum camera in between.

Table 4.7 gives an overview of the main parameters of the TUBIN spacecraft and mission. One can see that the experimental X-band transceiver that was added in a late development phase of the mission significantly increases the downlink capabilities of the spacecraft.

Besides adopting the satellite platform's capabilities to the needs of the mission's Earth observation payload, there were also a number of smaller updates and modifications that were made to the existing platform based on lessons leant from the TechnoSat mission. This included for example the introduction of a dedicated control node for the reaction wheels or the relocation of the MEMS rotation rate sensors from the sensor panels on the satellites outer structure to the ADCS node. A more detailed discussion of selected upgrades was presented in a peer reviewed journal contribution by Gordon, Barschke, and Werner in [253].

Figure 4.33 shows the engineering qualification model (EQM) of TUBIN while being integrated in the laboratory. The picture was taken just before the satellite is brought into an upright position to mount the solar panels as the last step of the integration process.

Figure 4.33: Integration of the engineering qualification model of TUBIN in a laminar flow box in the small satellite integration laboratory of Technische Universität Berlin. At this point only the solar panels on the sides of the spacecraft are missing for concluding the integration (Image credit: Philipp Werner).

Figure 4.34 shows the removal of the remove before flight (RBF) items at the bottom of the TUBIN spacecraft right before it is being integrated on the adapter to the EELV Secondary Payload Adapter (ESPA) ring of the Falcon 9 launcher.

Figure 4.34: Removal of the RBF items in the bottom of the spacecraft right before it is mounted to the adapter to the ESPA ring of the Falcon 9 launcher at Cape Canaveral (Image credit: Mario Starke).

In order to allow for referencing satellite orientations and the main elements of the spacecraft in the following sections, the satellite coordinate frame satellite is shown in Figure 4.35.

Launch and Commissioning

On the 30th of June, 2021 TUBIN was successfully launched from Cape Canaveral on a Falcon 9 rocket. At the time of writing, the commission phase of satellite platform and payloads is ongoing.

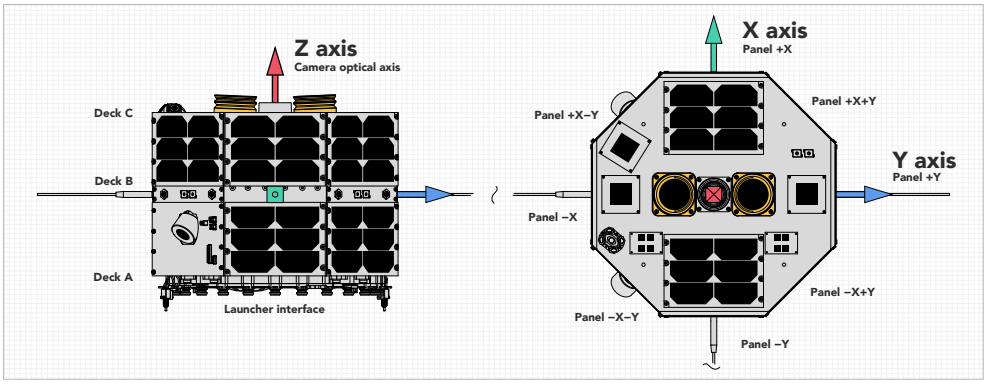

Figure 4.35: Satellite coordinate frame and solar panel naming conventions of the TUBIN spacecraft. The Z axis is aligned with the optical axis of the camera payload, the X axis points towards the satellite's EGSE panel and the Y axis completes the right-handed coordinate system.

All platform components required for the operation of the payload cameras and the downlink of the imagery were commissioned within the first eight days after launch and first light images of all three cameras were captured on the 9th of July 2021.

Only four days after the first light images fires were captured in Brazil, which were also successfully detected in the imagery by applying the TUBIN fire detection algorithm (cf. Section 4.2.2).

Figure 4.36 shows exemplary an infrared image of a number of fires that were captured Siberia on the 28th of July, 2021.

Among the many targets that were imaged within the commissioning phase of the TUBIN payload was also Las Vegas, that was captured on the 8th of August, 2021. Figure 4.37 shows an image of Las Vegas and the surrounding area captures by the visible spectrum camera.

Another high temperature event captured by TUBIN in infrared is the eruption of the Cumbre Vieja volcano on La Palma. the image that is shown in Figure 4.38 was captured on 2nd of October, 2021. Both the flowing lava, as well as a cloud of smoke are clearly visible in the image.

In the next sections the primary payload of the TUBIN mission is introduced and the late integration of the XLink payload into the mission is discussed. Following

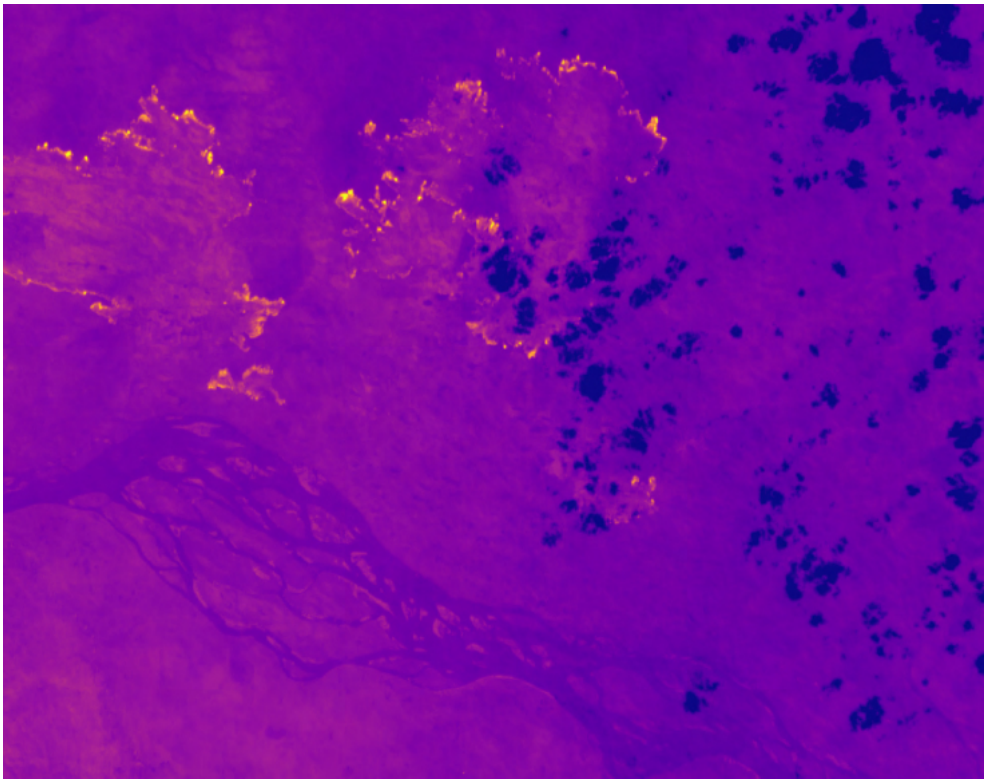

Figure 4.36: Infrared image from a series captured by TUBIN on the 28th of July, 2021 that shows vegetation fires in Siberia. The infrared image clearly reveals the fire fronts, the burned area, as well as a river in the lower part of the image and several clouds that exhibit the lowest temperatures on the image. The image was calibrated with calibration data produced on the ground before launch and with images taken in orbit.

Figure 4.37: Visible light spectrum image from a series captured by TUBIN on the 8th of August, 2021 that shows Las Vegas and surrounding area. The image was processed to enhance the colour.

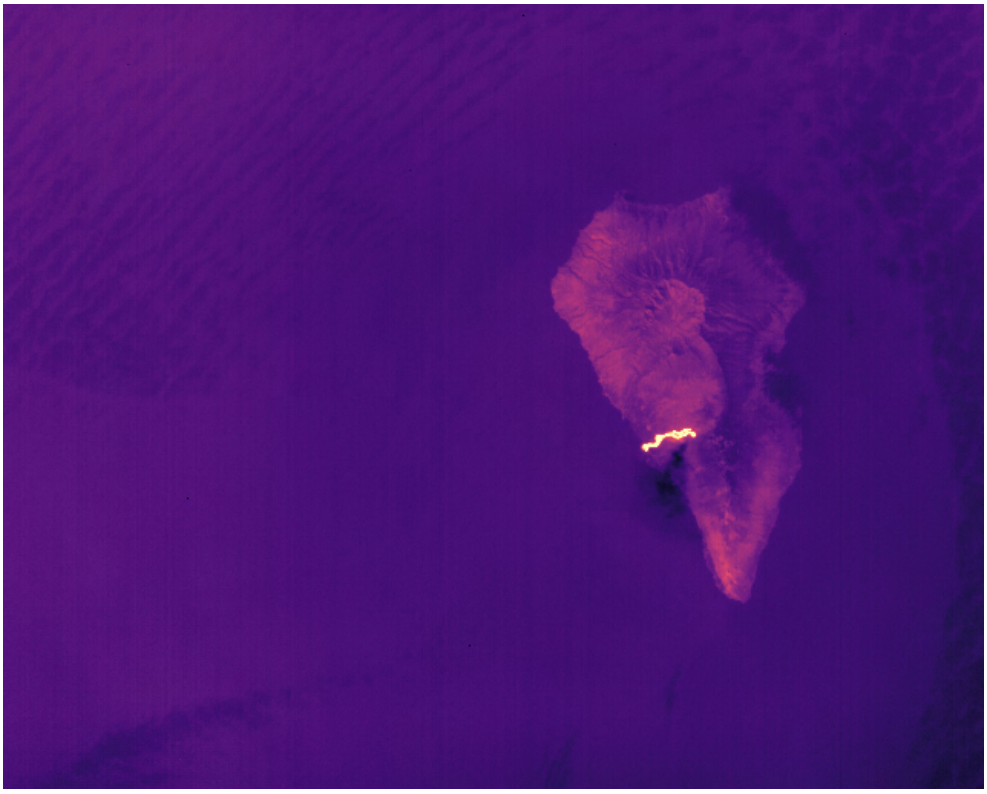

Figure 4.38: Infrared image captured on the 2nd of October, 2021 within a series of pictures of the Cumbre Vieja volcano on La Palma taken by the TUBIN spacecraft. The image was calibrated with calibration data produced on the ground before launch and with dark frames taken in orbit.

the introduction of the payloads, the systems design of the TUBIN satellite is presented and the an analysis of the power budget for different payload operation scenarios is detailed.

4.2.1 Wildfire Detection from Space

Fires play an important role in many ecosystems [254]. However, the last decades fire activity has been reported to increase dramatically in most parts of the world. The area burned from wildfires, for example, has nearly quadrupled within the last forty years in the United States according to Burke et al. [255] and 2020 has been called "the year of wildfire records" by Robinne et al. [256]. This development is due to a number of reasons including the legacy of fire suppression, natural climate variability, but also human-caused climate change [257]. The latter is for instance believed to have caused the forest fires responsible for half of the burnt area between 1984 and 2015 across the western Unites States [257].

The consequences of increasing wildfire activities include "substantial and irreversible alterations to permafrost landscapes" [258], a rising number of children affected by wildfire smoke [259], and a generally growing thread to people in fire prone areas [260].

Wildfire detection systems can generally be classified into ground-based, airborne, and spaceborne systems and can further be categorised regarding the used wavelength range across the electromagnetic spectrum (i.e. visible, infrared or multispectral systems) [261]. A review of how remote sensing is used to study fire ecology was published by Szpakowski and Jensen [262]. Hua and Shao presented the progress of operational forest fire monitoring with infrared remote sensing from space [263].

Spaceborne instruments that deliver fire products include the Moderate Resolution Imaging Spectroradiometer (MODIS) [264], the Advanced Spaceborne Thermal Emission and Reflection Radiometer (ASTER) [265], and the Advanced Very-High-Resolution Radiometer (AVHRR) [266]. Within the microsatellite mission BIRD of the DLR the first satellite specifically designed to detect and examine fires was launched in 2001 [267]. It was followed by the FireBird mission that comprises the small satellites TET-1 and BIROS launched in 2012 and 2016, respectively [268, 269].

A discussion of the TUBIN mission in the context of present and future satellite-based fire detection systems was presented by Bartholomäus, Barschke, and Lehmann in [251].

4.2.2 The Imaging Payload

In the following, the primary payload of the TUBIN mission is described in more detail to serve as an example for the requirements and constraints that are imposed to the satellite platform by an Earth observation payload. Equally to the TUBiX20 platform itself, the architecture of the TUBIN imaging payload is designed with modularity in mind, which opens up a wide-range of opportunities for synergies between payload and platform.

The section begins with a description of the microbolometer technology highlighting characteristics relevant for the application of this technology for Earth observation from space. Following this, the imaging payload for the TUBIN mission is presented. The section is concluded by a discussion of the fire detection algorithm that was developed for the mission.

Microbolometer Detectors

As indicated by the primary mission objective of TUBIN, the microbolometer technology is key to the project as it aims to demonstrate space-based remote sensing in the infrared without the need to cool the sensor to cryogenic temperatures. In the following, the functional principle of a microbolometer is briefly described taking the constraints of operating the imager on orbit into account.

The basic construction of an uncooled microbolometer is shown in Figure 4.39. Here, the left image depicts the fundamental construction of a single microbolometer pixel, whereas the right one shows a scanning electron microscope (SEM) image of several pixels of an exemplary microbolometer.

The core element of each microbolometer pixel is a thin membrane capable of absorbing infrared radiation (1). The membrane is located micrometers above a readout integrated circuit (ROIC) by means of long legs with small cross section to reduce heat exchange with the ROIC (2). Below the membrane, a reflector is located to direct light that passed through the membrane back and therefore to increase the fraction of absorbed light (3). The temperature of the membrane is

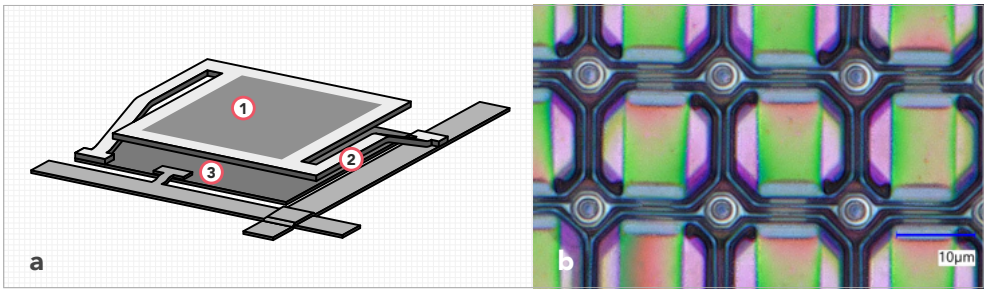

Figure 4.39: The right image (a) shows the basic construction of a single uncooled microbolometer pixel (Figure adapted from [270]) while the left image (b) depicts a microscope image showing several 17 µm microbolomenter pixels of the sensor implemented within payload of the mission TUBIN (Image credit: Vlad Dumitru Berlea).

measured by current pulses in a frequency of typically 30 and 60 Hz that are used to determine the resistance of the membrane. In order to maximise the signal range, the membrane is made by a material with high temperature coefficient of resistance [271]. Typical pixel pitches for a microbolometers are 50, 25, 17 and 12 µm, while the most advanced pixels today go down to 10 µm [272].

In contrast to photon counting sensors that measure the charge generated by incoming photons in a given period of time, a microbolometer does not support setting exposure times. Instead, the temperature membranes of the individual pixels are constantly following the observed scene with a time constant of typically 10 to 15 ms [273].

As a result of this, when recording objects or scenes that are moving fast compared to the microbolometer's time constant, a motion blur effect occurs. Oswald-Tranta, Sorger, and O'Leary [273] describe how an image recorded with a microbolometer that is subject to motion blur can be restored by deconvolution using the image's point spread function (PSF), while the noise in the restoration is suppressed by a Wiener filter.

Here, the decay constant of the PSF (τ_{image}) can be calculated with the time constant of the microbolometer τ_{camera}, the velocity of the moving target v_{ground} and the resolution of the camera (the inverse of the GSD) r [273]:

$$\tau_{\mathrm{image}} = \tau_{\mathrm{camera}} v_{\mathrm{ground}} r \tag{4.12}$$

The velocity of a satellite over ground can be calculated by the following formula for an SSO[14]:

$$v_{\text{ground}} = \sqrt{\frac{\mu}{r_{\text{Earth}} + h_{\text{orbit}}}} \tag{4.13}$$

If a 535 km SSO is assumed, the equivalent ground velocity of a pixel in nadir pointing is 7.01 km s^{-1}.

According to Table 4.8 TUBIN carries microbolometers with a 17 µm pixel pitch (p_{pixel}) that are equipped with lenses with 60 mm focal length (f). Based on this, the GSD can be calculated to be 152 meters using:

$$\text{GSD} = \frac{p_{\text{pixel}} h_{\text{orbit}}}{f} \tag{4.14}$$

With the microbolometer's time constant of 10 ms, this results in a decay constant of the PSF of 0.462. Now the bolometers response to a box function can be calculated as follows [273]:

$$\text{Output signal} = \begin{cases} 0, & \text{for } x < 0 \\ 1 - e^{-\frac{x}{\tau}}, & \text{for } 0 \leqslant x \leqslant a \\ e^{-\frac{x-a}{\tau}} - e^{-\frac{x}{\tau}}, & \text{for } a < x \end{cases} \tag{4.15}$$

Figure 4.40 shows the a microbolometers two dimensional response to three box functions of different lengths. Here, the box function input is plotted in yellow, while the sensors output is plotted in green. In the presented figure, the abscissa is counting the pixels, while the ordinate is indicating the normalised signal. For a one pixel wide input box function the signal only reaches about 90 percent of the input, while two pixels are already sufficient for the sensor to follow the input signal. Likewise, the signal's decrease requires two pixels until its aligned with the input again.

From this it can be derived that the discussed effect will affect the observation data generated by the thermal infrared (TIR) imagers of TUBIN and needs to be

[14] Here, the Earth's rotation is neglected as it contributes only marginally to the ground velocity in nearly polar orbits such as SSOs.

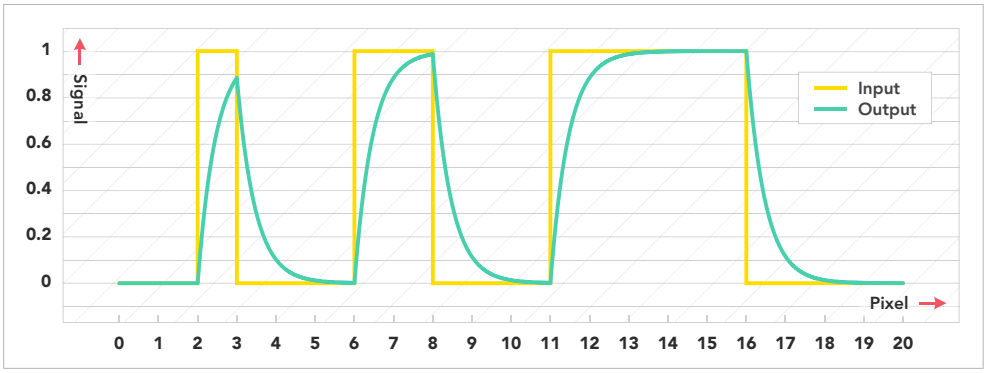

Figure 4.40: Impact of the microbolometer's operating principle on the recorded images when operated on an LEO satellite with 535 km orbital height.

corrected for. However, the impact for a given change in signal will be limited to two pixels.

Several satellite missions that carried microbolometer payloads for Earth remote sensing have been launched to date. The Japan Aerospace Exploration Agency (JAXA) developed Compact Infrared Camera (CIRC), a microbolometer that was launched aboard the ALOS-2 satellite in 2014 and was also installed on the ISS in 2015 [274, 275]. Other missions with microbolometer-based payloads include Aquarius SAC-D that launched in 2011 [276], UNIFORM that was brought to orbit in 2014 [277], and LAPAN-A3 that started to operate in 2016 [278].

Recently, there were a number of CubeSat missions launched that carried microbolometer-based payloads. This includes the ISARA CubeSat of the JPL that launched in 2018 and carried the CUMULOS payload developed by The Aerospace Corporation [279] and Phoenix of the Arizona State University that was deployed from the ISS in 2020 [280].

Design and Operation

The imaging payload of the TUBIN mission comprises of three cameras, namely two TIR microbolometers and one CMOS camera that is sensitive in the visible light spectrum.

Figure 4.41 shows picture of the TUBIN payload assembly in the laboratory, including the two infrared microbolometer arrays at the two sides of the assembly, as well as the camera for the visible light spectrum in between. The baffles for both infrared and visible spectrum camera that are also part of the assembly and can, for example, be seen in Figure 4.32.

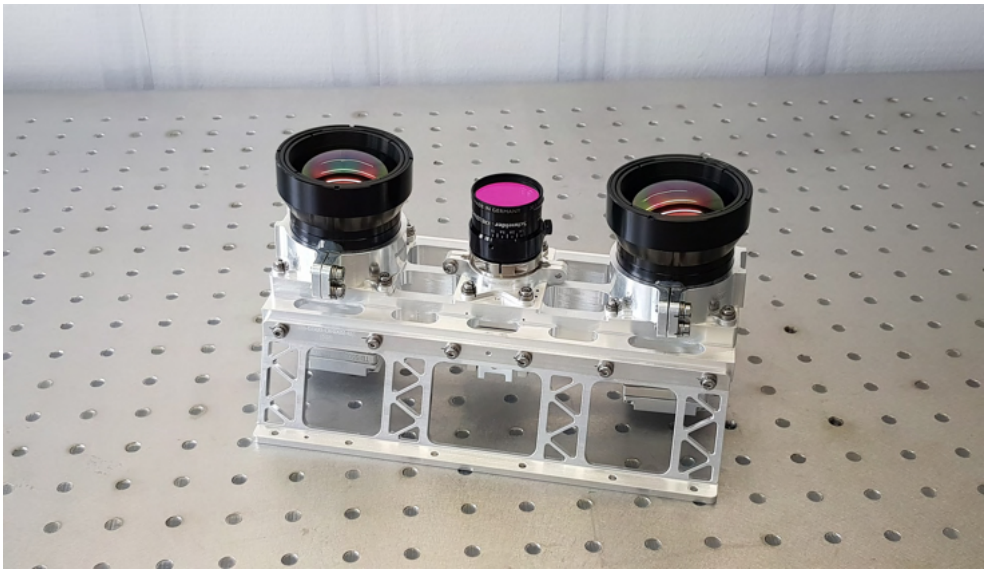

Figure 4.41: Flight model of the TUBIN payload assembly after integration in the clean room captured without baffles, as these are not mounted to the payload assembly but to the spaceraft's structure instead (Image credit: Julian Bartholomäus).

The main parameters of the two camera types the TUBIN payload assembly builds on are listed in Table 4.8 for the 535 km orbit. Here, the application of filters for tuning both imagers to individual bands is not considered as this is incompatible with the sensitivity provided by the bolometers. The camera for the visible spectrum complements TIR imagers to provide georeferencing capabilities and means for image registration.

The single cameras are integrated into an optical bench that is machined from one piece of aluminium to minimise the potential for misalignment between the imagers. Here, the three lenses, as well as the three sensors are directly mounted into the optical bench to simplify the alignment of the optical elements.

Table 4.8: Main parameters of the TUBIN infrared and visible light spectrum camera payloads for a 535 km orbit [32].

	Infrared cameras	Visible spectrum camera
Mass[a]:	450 g	240 g
Volume[a]:	$162 \times 83 \times 76\,\text{mm}^3$	$135 \times 64 \times 64\,\text{mm}^3$
Sensor technology:	VOx microbolometer	CMOS
Pixel pitch:	17 µm	1.67 µm
Bandwidth:	7 to 15 µm	400 to 800 nm
Pixel resolution:	640×512	$3\,664 \times 2\,748$
GSD:	152 m	39 m
Mounting angle:	$\pm 2.43°$	$0°$
Swath (combined swath):	97 km (143 km)	143 km
Optics:	GeAs lens	Lens with NIR filter
Focal Length:	60 mm	22.9 mm
f-number:	1.25	1.4
Detector NETD at 300 K:	0.05 K	n/a
Power consumption:	4.0 W	3.0 W
Operating system:	Linux	Linux
Processor clock:	696 MHz	696 MHz
Data interface[b]:	Ethernet	Ethernet
Data storage:	2.6 GB	2.6 GB

[a] Inclusive optics and baffles but without the optical bench the cameras are mounted into
[b] Used as both, command and telemetry interface and for image data downlink

While the camera sensitive to the visible light spectrum is integrated exactly perpendicular to the optical bench, both TIR imagers are mounted with an across-track off nadir angle of plus and minus 2.43 degrees, respectively. In this manner, the combined swath width of both microbolometers is the same as the swath width of the visible spectrum camera for a 535 km orbit. Furthermore, there is an overlap of approximately one third of the FoV of both cameras. This shall allow for studying potential improvements that can be made to the fire detection capabilities if two images of the same scene captured at exactly the same point in time. Furthermore, this simplifies the calibration of the cameras' mounting angles based on captured imagery and provides graceful degradation capabilities as many science goals of the mission can still be achieved with a single microbolometer.

Figure 4.42 indicates the mounting angles of all three cameras in the optical bench and illustrates their FoVs projected to Earth's surface for a 535 km orbit.

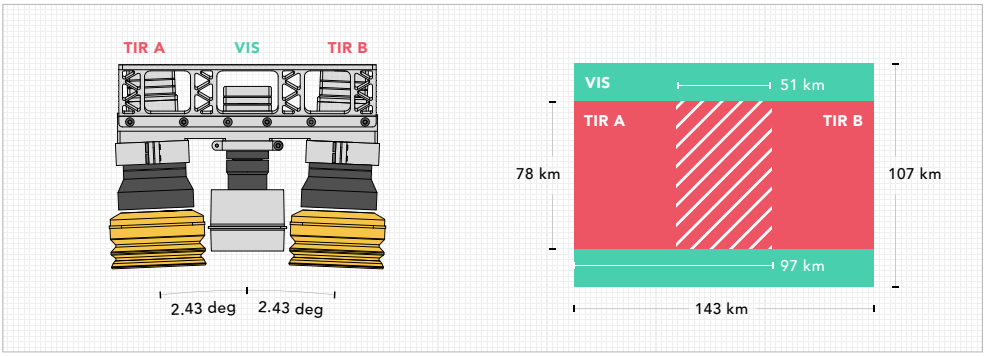

Figure 4.42: On the left side the mounting angle of the three cameras in the optical bench is shown. The right image depicts the cameras' FOVs projected to the Earth's surface for a 535 km orbit. Here, the FOV of the visible spectrum camera is depicted in green, the TIR FOVs are shown in red and the hatched area indicates the region in which both TIR FOVs overlap (Image adopted from [32]).

Similar to the platform, the overall architecture of the camera bases on a high level of modularity. Here, the electronics stack of each camera is build by four boards of which only one is specific to the individual camera.

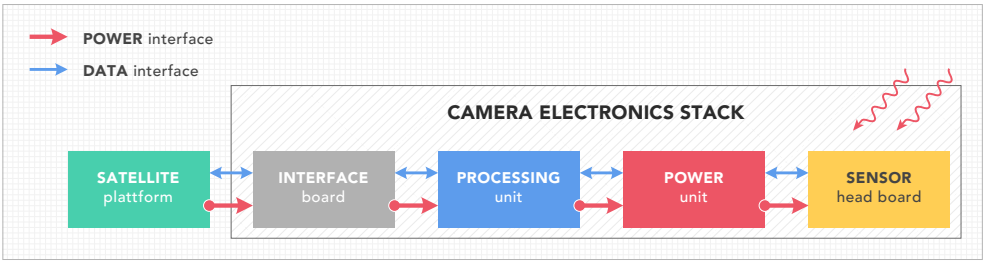

Figure 4.43: Block diagram of the electronics stack of the TUBIN payload cameras. Each block represents one PCB. The first two PCBs are identical in all three cameras while the power unit is customised to the type of sensor head board (image adopted from [32]).

An overview of the cameras' electronics stack is given in Figure 4.43. Here, the satellite platform is represented as a grey box that provides the power and data interface to the camera. The first PCB in the camera stack is the interface board that acts as bridge between the camera's connector and the board to board

connector of the stack. The power unit gathers all power converters required for the processing unit and the sensor. The penultimate PCB is the processing board that accommodates the cameras processor as well as its memory. Finally, the sensor head board carries the sensor of the camera. The use of a standardised connector between the different boards of the camera stack allows for customisation for a specific use case by exchanging specific boards without interference with the remainder of the system.

One of the most notable aspects of the payload's design in this context is the processing unit that is part of every single camera. The unit allows for performing image processing directly on the camera and provides sufficient memory to store the image products that are intended for downlink. As all cameras are part of the same Ethernet network, they can share image data among each other. If a downlink terminal is connected to the same switch as the cameras, as it is the case for XLink, the image data can be downlinked directly from the camera via the transmitter to the ground without requiring additional platform interaction (cf. Section 4.2.3).

Figure 4.44 gives an overview of the nominal acquisition sequence for both infrared and visible spectrum camera. While 10 dark frames in free space pointing are captured each before and after each image series for calibration with the TIR imagers, the visible spectrum camera is only operated in nadir pointing.

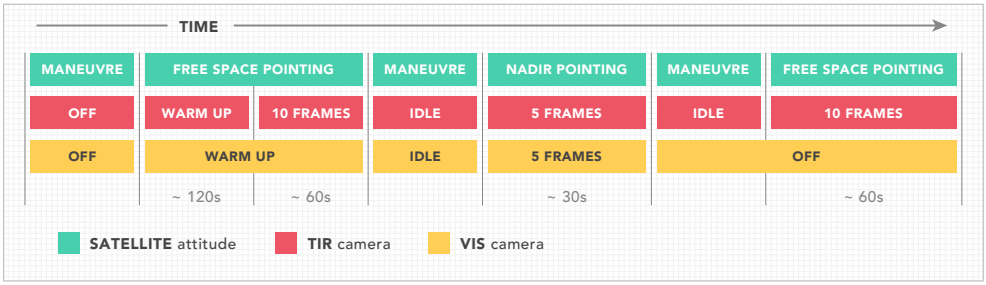

Figure 4.44: Image acquisition sequence detailing the operation of infrared and visible spectrum camera, as well as the satellite's attitude (Figure adopted from [32]).

Within the TechnoSat mission, pictures of the Moon and other celestial bodies, as well as images from Earth's surface captured with the satellite's camera have been used to assess the performance of the ADCS (cf. Section 4.1.5).

As discussed in Section 4.2.4 TUBIN will feature a much more capable attitude control system when being compared to the TechnoSat spacecraft, mainly due to the introduction of two star trackers. Furthermore, the camera suite of TUBIN will offer a much higher resolution when being compared to the imager on TechnoSat. This will allow to calibrate the relative mounting position of the cameras based on attitude data provided by the satellite as described in [151][15].

Fire Detection

As described in Section 4.2.2, the TUBIN imager payload provides a single infrared channel with a bandwidth from 7 to 15 µm. However, the sensitivity of the microbolometer varies across this bandwidth and the atmospheric transmission additionally impacts the signal as seen by the sensor. Figure 4.45 shows the spectral response curve of the TUBIN infrared imagers in red, an exemplary data set for the atmospheric transmission within the spectral range of 7 to 14 µm in yellow, as well as the product of both curves in green.

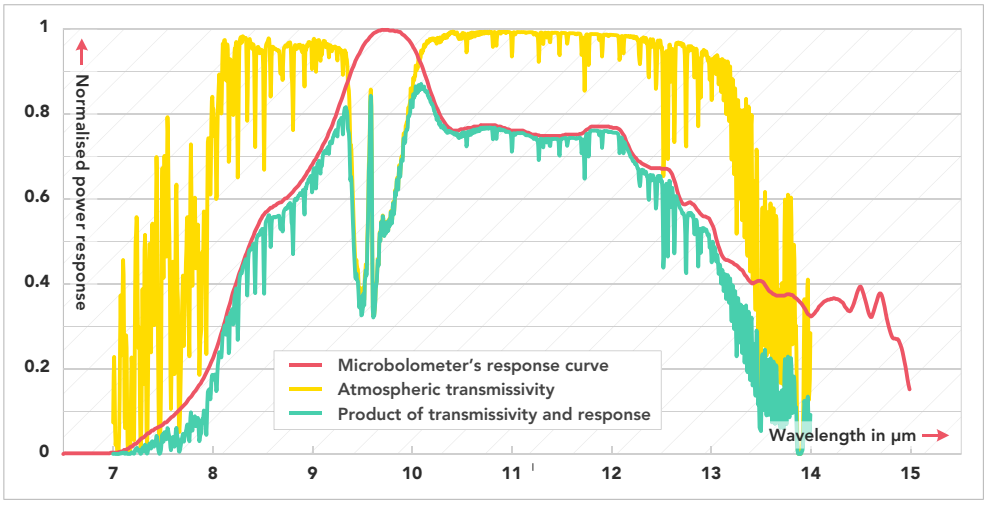

Figure 4.45: Spectral response curve of the TUBIN TIR microbolometer imagers (red) and exemplary atmospheric transmission (yellow). The green curve shows the product of both curves (Figure adapted from [281]).

[15] Publication with contributions of the author

In order to demonstrate fire detection capabilities based on the TIR imagery provided by the TUBIN mission a custom made fire detection algorithm was developed in a masters thesis supervised by the author [281] and was first published by Bartholomäus, Barschke, and Lehmann in [282].

The algorithm was developed based on data provided by the ASTER payload on the Terra spacecraft of NASA [283] and by the TET-1 spacecraft that is operated within the FireBird mission of DLR [269]. In order to be able to use the above mentioned data for algorithm development, they were adjusted to match the spatial resolution of the TUBIN imagers and adapted to the respective bandwidth.

The single channel fire detection algorithm for the TUBIN mission bases on four processing steps as illustrated in Figure 4.46.

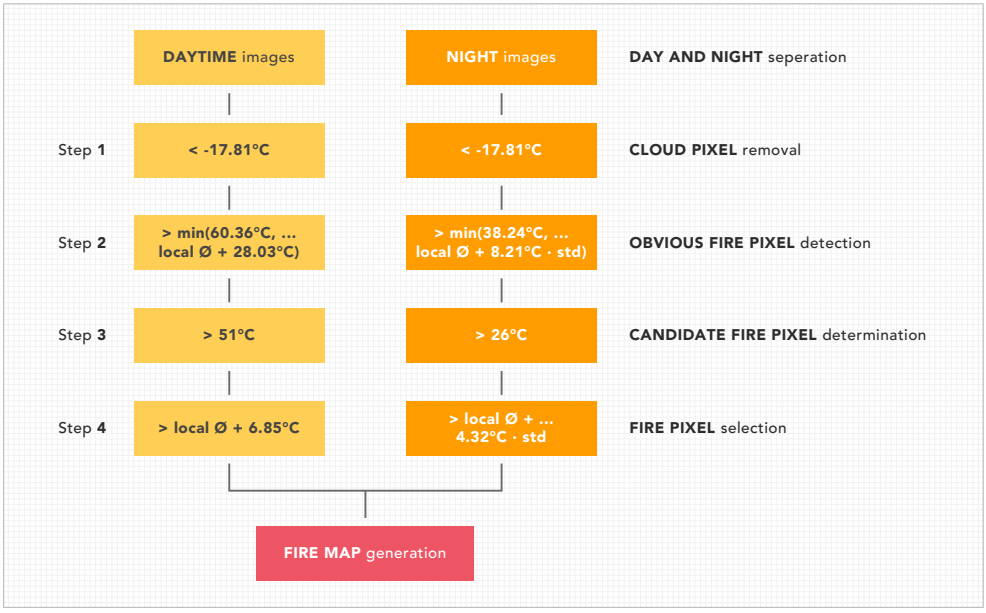

Figure 4.46: Flow chart detailing the four steps of the single channel TUBIN fire detection algorithm (Figure adapted from [282]).

As a first step, all pixels with a brightness temperature[16] below minus 17.81 °C are flagged as non-fire pixels as they are assumed to show clouds and would therefore

[16] The brightness temperature is the apparent temperature of a pixel, if an emissivity of one is assumed.

bias the following steps of the algorithm. After the cloud pixels were removed, all obvious fire pixels are identified in step two. For daytime images, all pixels that are above 60.36 °C or above the average of a 3×3 pixel patch around the pixel in question plus 28.03 °C in brightness temperature (whichever value is smaller) are classified as fire pixels. For night time images, the criteria are 38.24 °C and the average of a 21×21 pixel patch plus 8.21 times the standard deviation of the same patch. From all pixels that are not yet flagged as cloud or fire pixel, candidate fire pixels are now selected based on a simple threshold (51 °C for images taken during the day and 26 °C for images captured at night), while all other pixel are classified as non-fire pixels (step three). As a last step, candidate pixels are identified as fire pixels if their brightness temperature is above the local average plus 6.25 °C for the daytime and plus 4.32 times the standard deviation for images captured at night. All remaining pixels are now flagged as non-fire pixels.

Figure 4.47 shows an example for the fire detection based on the TUBIN single-channel detection algorithm and a comparison with a multi-channel algorithm based on data from the ASTER instrument [283]. Denoted with (a) is a false-colour representation of an original ASTER image of central Alaska captured on the 17^{th} of July, 2004 that contains a large vegetation fire. The image marked with (b) shows the same image cropped to show only the region that is affected by the fire (the cropped section is indicated in complete image). Image (c) now shows the same image section adjusted to match the capabilities of the TUBIN imager. Finally, the fire maps generated for the ASTER and the TUBIN imager are shown in (d). Here, all pixel that were identified as fire pixels by both algorithms are red, all pixels only identified by ASTER are yellow and all pixels that are only detected by TUBIN are black.

4.2.3 The XLink Payload

XLink is an SDR-based satellite transceiver that offers each two up and downlink channels that can be individually configured to S or X band. The transceiver was developed by IQ wireless GmbH in cooperation with Technische Universität Berlin and after concluding ground qualification it was decided to integrate it into the TUBIN mission for in-orbit demonstration despite the advanced status of the mission. Table 4.9 gives an overview of the XLink configuration that is demonstrated within the TUBIN mission.

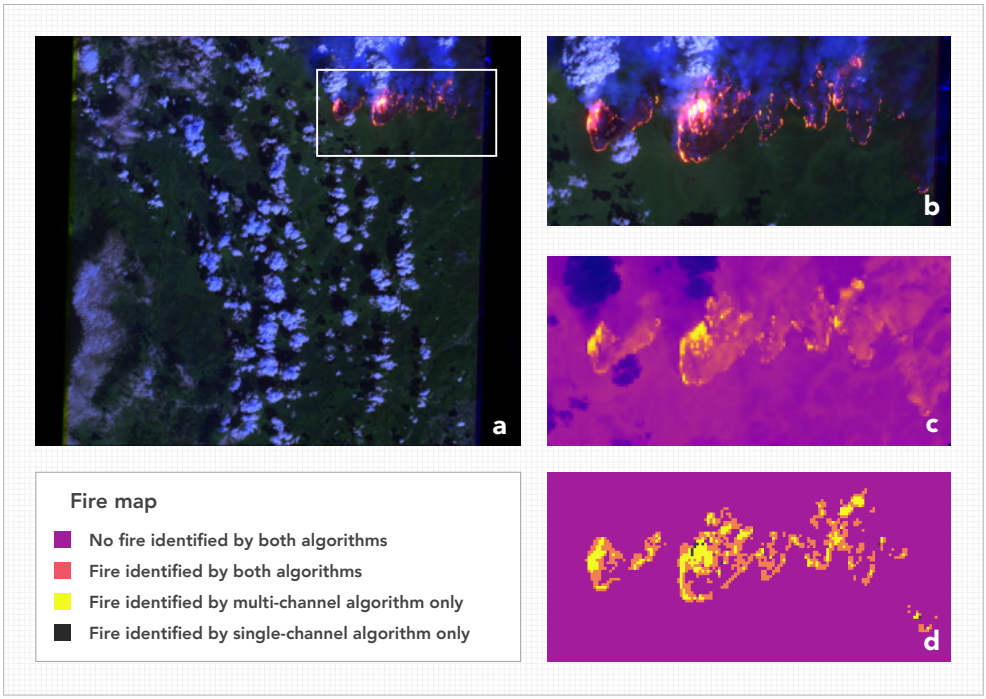

Figure 4.47: Comparison of the detection capabilities of the TUBIN single channel fire detection algorithm and a multi-channel algorithm based on data from the ASTER instrument [283]. Image (a) shows a false-colour representation of the analysed image and figure (b) shows a zoom of the region of the image affected by forest fires. Denoted with (c) is the same region of the image adjusted to match the performance of the TUBIN TIR imagers. The fire maps of both the ASTER and the TUBIN algorithm are shown in (d) (Figure adapted from [32]).

XLink was integrated into the TUBIN spacecraft by using existing interfaces only. However, the used interfaces partly needed to be adjusted in hardware for the needs of XLink. A block diagram detailing the integration of the XLink transceiver into the TUBIN spacecraft is shown in Figure 4.48.

At the top of the diagram, the PDH node is shown with its two MCUs. The PDH node interconnects to the Ethernet switch that is build by two Ethernet switch ICs. Here, each one of the two MCUs is connected to one of the two Ethernet switch ICs. Generally, Ethernet multiplexers are implemented to allow each externally provided Ethernet interface to connect to both switch ICs. However, as the switch

Table 4.9: Main parameters of the XLink transceiver in the configuration that is implemented into the TUBIN spacecraft [39, 252].

Downlink frequency (15 and 68 MHz bandwidth):	8 392.5 and 8 366.0 MHz
X-band uplink frequency:	7 210 MHz
S-band uplink frequency:	2 081.2 MHz
RF output power:	30 dBm
Downlink data rate:	Up to 100 Mbit s^{-1}
Uplink data rate:	64 Mbit s^{-1}
Data interface for payload data and telemetry:	Ethernet
Power consumption in transmit:	16.2 W
Power consumption in receive:	3.5 W
Dimensions:	$90 \times 65 \times 25$ mm^3
Mass:	280 g

ICs only provide four independent Ethernet interfaces, XLink and the EGSE share one interface in such way that each of them only connects to one of the switch ICs and can hence only be operated with one of the PDH's two MCUs. XLink is supplied directly by the unregulated power supply provided by the EPS. As the available interface does not support the use of both redundant power supply bus sides for a single unit, XLink will always be powered from power bus side A. In contrast, the cameras are supplied by the PDH node through the Ethernet switch and can thus be powered by both of the node's sides.

In order to support data uplink via S band as well as via X band, two distinct patch antennas are integrated onto deck C of the TUBIN spacecraft (cf. Figure 4.35). The two downlink channels are configured for transmission in X band and are connected to one single patch antenna via a combiner in order to maximise the RF output power.

An overview of the integration of XLink into the TUBIN mission was first presented by Bartholomäus et al. in [252][17].

[17] Publication with contributions from the author.

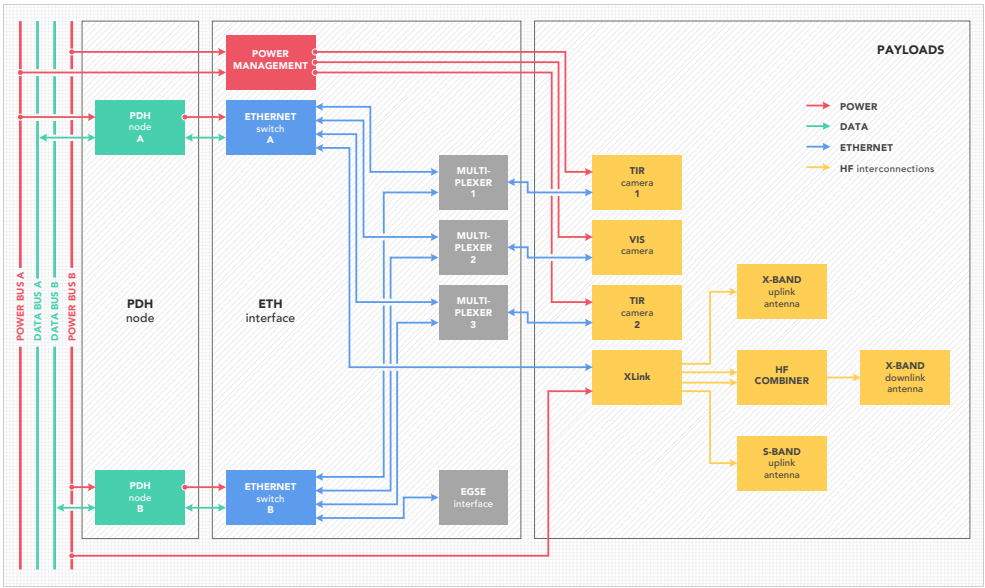

Figure 4.48: Block diagram showing the integration of the XLink transceiver into the TUBIN spacecraft. Ethernet interconnections are shown in blue, all other data interconnections are depicted in green. Further, HF links are drawn in yellow and the power lines are represented in red (Figure based on [210] and [252]).

4.2.4 Spacecraft Systems Overview

Figure 4.49 gives an overview over the systems design of the TUBIN spacecraft. Here, hatched grey boxes indicate the spacecraft's subsystems that contain the different components such as sensors or actuators, which are drawn in blue. Generally, the data flow is shown through green arrows, however, Ethernet interconnections are shown in blue. Power lines, as well as the PCUs are plotted in red. The different processing and interface nodes are depicted in green and the payloads are shown in yellow. The dashed line contains all units that are located in the platforms central avionics compartment.

The EPS of the TUBIN spacecraft is generally identical to what was implemented for TechnoSat. However, there were hardware updates performed due to discontinued components (e.g. a newer generation of battery cells), lessons learnt from the former mission (e.g. an improved voltage and current sensor topology for more accurate telemetry), and updated requirements from subsystems (e.g. updated

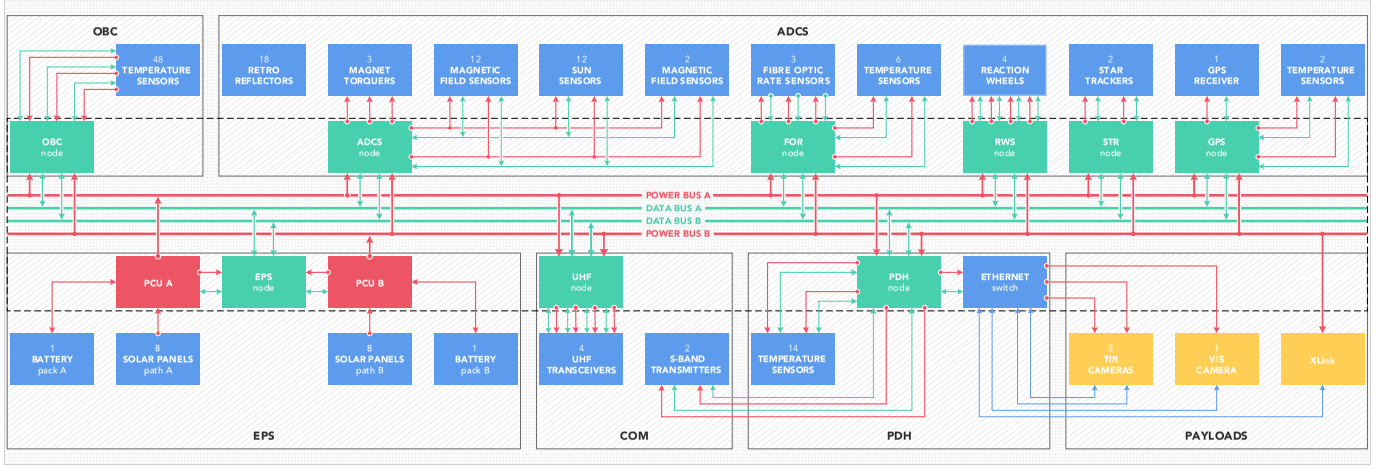

Figure 4.49: Systems design of the TUBIN spacecraft depicting the central power and data bus system, the processing nodes, as well as the components and payloads that are interfacing to these nodes (Figure adapted from [32]).

power converters for the 12 V power buses). Furthermore, the TUBIN satellite features one more star tracker than TechnoSat so that one additional solar panel had to be removed, leaving a total of eight panels for each of the two solar strings. As described before, the EPS node controls the power supply to all nodes of the system and is the time master and distributes the PPS synchronisation signal.

The OBC implemented for TUBIN is the same that was used for TechnoSat but the non-volatile memory was replaced with a different technology as a certain sensitivity to radiation was found with the model implemented for TechnoSat [253]. To achieve the required spatial resolution for the temperature sensing on the satellites structure, the number of sensors has been increased to a total of 45 sensors (each three sensors in 15 distinct positions) when being compared to TechnoSat.

The communication subsystem bases on the same four-channel UHF communications system that was already used within the TechnoSat mission. For payload data downlink, the UHF system is now complemented by two S-band transmitters. While these two transmitters shall nominally be operated in cold redundancy, they use two distinct downlink frequencies as the parallel operation of both transmitters shall be tested to increase the downlink rate to $2\,\mathrm{Mbit\,s^{-1}}$.

In order to allow to downlink payload data without transporting it on the central control data bus, the S-band transmitters interface directly with the PDH node. Additionally, the Ethernet switch is part of the PDH. It is controlled by the PDH node and provides interfaces for the three camera payloads the XLink transceiver and the PDH node. This allows the cameras to exchange data between each other and send imagery via PDH node and S-band transmitters to the ground. In addition, the cameras may send data to the S-band transceiver payload via the Ethernet switch for experimental transmission at much higher data rates of up to $50\,\mathrm{Mbit\,s^{-1}}$. While the XLink transceiver payload is supplied directly by the unregulated line of the central power bus system, the cameras are supplied with electrical power by the PDH node via the Ethernet switch (cf. Figure 4.48). In order to allow for capturing temperatures at various points of the camera payloads, the PDH node reads 14 temperature sensors (each two sensors at 7 distinct positions for redundancy).

The ADCS subsystem comprises of five TUBiX20 nodes. The ADCS core application that implements the higher-level subsystem functionality is running on the ADCS node that furthermore interfaces to a number of sensors, as well as to the magnetorquers. The sensors that are read out by the ADCS node include

a total of 16 MEMS gyroscopes (each four of two different types per node side) that are located directly on the node, 12 three-axis magnetometers and 12 Sun sensors located on the six outer surfaces of the spacecraft (all accessible from both node sides), as well as two fluxgate magnetometers. The FOR node reads three fibre optical rotation rate sensors with high frequency and publishes filtered rate data on the control data bus aligned to the ADCS control cycle. The FOR node additionally reads six temperature sensors (3 per node side) that monitor FORs for FDIR purposes. The four reaction wheels, the GPS receiver as well as the two star trackers are all controlled by individual nodes. Here, the GPS node reads two external temperature sensors to monitor the temperature of the low-noise amplifier (LNA). Finally, the ADCS subsystem includes 18 laser retro reflectors to support laser ranging from the ground.

4.2.5 Power Generation and Storage

The EPS of the TUBIN spacecraft builds on the flight-proven design that was already applied within the TechnoSat mission. However, TUBIN implements one solar panel less then TechnoSat to make room for an additional star tracker and a nearly 20 percent reduced battery capacity due to the implementation of a new generation of battery cells.

Table 4.10 lists the power consumption of platform and payloads of the TUBIN spacecraft for different operational modes. The underlying figures are either measured within the functional testing of the flight hardware production batch or are derived from TechnoSat flight data and include appropriate margins. Additional boundary conditions for the following simulations include an overall conversion efficiency of 0.85 between the solar panels and the consumers (i.e., satellite platform, payloads and battery) and operation at the day of the year with lowest radiated power from the Sun ($1\,315.9\,\mathrm{W\,m^{-1}}$).

Figure 4.50 gives an overview of the power balance for the nominal imaging scenario shown in Figure 4.44. The plot starts with the eclipse period where the spacecraft is idle performing coarse nadir pointing. Ten minutes into the Sun phase the camera is pointed to free space with the payload still switched off. This manoeuvre is expected to last five minutes. After the target attitude is reached, the three payload cameras are powered and 10 dark frames are recorded with the TIR cameras within 120 seconds. After another five minutes of reorientation each five images are taken with each camera. The imaging sequence is concluded with

Table 4.10: Power consumption of the TUBIN spacecraft in different satellite modes based on laboratory measurements or derived from TechnoSat flight data. All values include appropriate margins applied on component level.

Satellite mode	Platform power W	Payload power W	Total power W
Safe	4.64	-	4.64
Safe with UHF transmission	7.41	-	7.41
Coarse nadir pointing	9.57	-	9.57
Imaging (FORs powered)	21.57	13.20	34.77
Downlink	36.99	13.20	50.19
XLink downlink	21.57	29.70	51.27

recording another 10 calibration frames with both TIR cameras while pointing at free space. Within the same Sun period, 15 minutes of payload data downlink are foreseen. One can see that the discharge level of the battery is below 10 percent for the entire scenario and that the battery is fully charged again after about two thirds of the subsequent Sun period.

For the case that the charge level of the battery drops below a defined threshold, the satellite is set to safe mode where the power consumption is reduced to 4.12 watts (cf. Table 4.10). In order to analyse the recovery of the battery in such, a case a simulation was derived based on attitude and panel temperature data from the TechnoSat satellite recorded with unconstrained attitude.

For TUBIN, a maximum DoD of 30 percent is foreseen. Consequently, the starting condition for the battery recovery sequence shown in Figure 4.51 is a battery charge level of 70 percent at the end of the Sun period. In the subsequent eclipse period, a ground pass with operation of the UHF communications system is assumed (cf. Table 4.10). Within the eclipse period, the charge level of the battery drops another 1.8 percent before the batteries are charged again in the Sun phase. Here, the varying power generation level are caused by the rotation of the satellite. In each Sun phase approximately 10 percent overall battery capacity is recovered so that a fully charged battery is reached towards the end of the fourth Sun phase of the simulation.

Furthermore, it shall be evaluated if the power system would allow for an entire orbit of imaging. In this context, Figure 4.52 gives an overview of the power

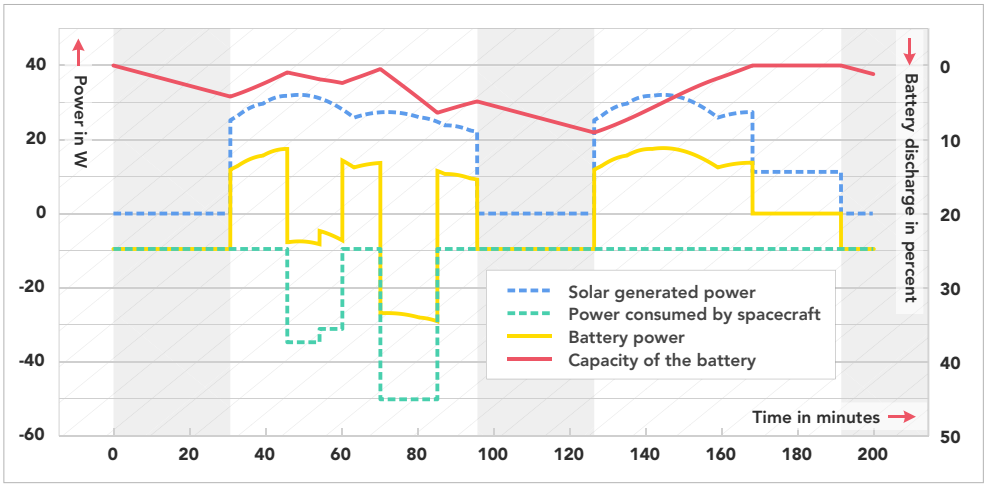

Figure 4.50: Power balance of the TUBIN satellite for a nominal image acquisition sequence showing the power generated by the solar panels and consumed by the spacecraft, the charge and discharge power of the battery, as well as the battery's capacity in percent.

balance for an experiment where imagery is collected for one orbit. Here, the infrared imagers are operated for the entire orbit while the visible spectrum camera is switched off during eclipse.

The plot starts with one orbit coarse nadir pointing mode in which 9.44 watts are consumed (cf. Table 4.10). Around one quarter into the first orbit's Sun period the battery is fully charged. Upon transition into eclipse of the second orbit the spacecraft is set into imaging mode with the visible spectrum camera still disabled. Once the spacecraft enters sunlight, the visible spectrum camera is activated as well leading to an overall power consumption of 34.77 watts. One can see that while imaging with all three cameras, the power balance is negative even in the Sun period. At the end of the Sun period the satellite is set to coarse Sun pointing mode (requiring 9.44 watts equally to the coarse nadir pointing) to recharge the batteries. After approximately 1.5 consecutive orbits in Sun pointing the batteries are fully charged again.

Within the given example, the DoD reaches a maximum of 28 percent and is thus maintained over the threshold of 30 percent set for the mission.

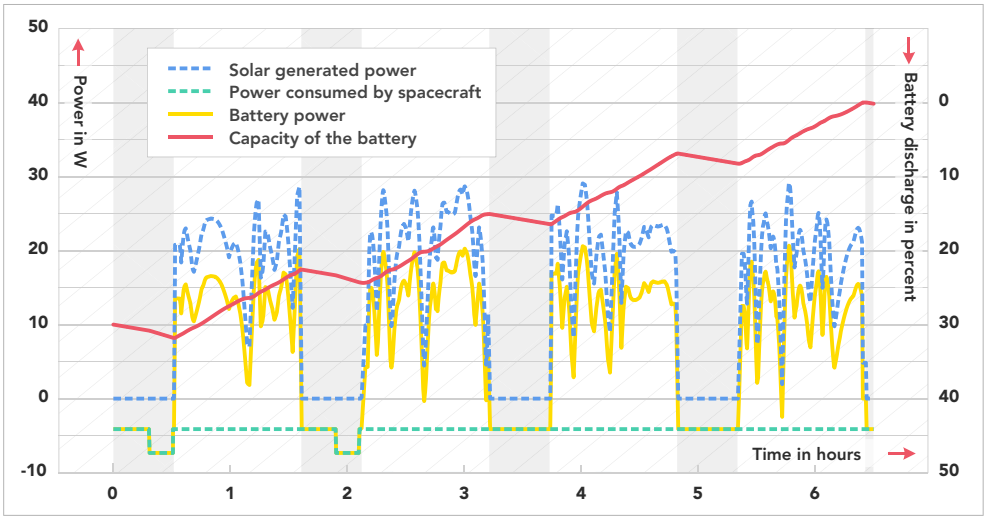

Figure 4.51: Recovery of the full battery capacity in safe mode after reaching the maximum DoD of 30 percent. The increased power consumption in the eclipse phase of the first two orbits is caused by the UHF communication system that transmits in operated ground station passes.

4.2.6 Conclusions

TUBIN is an Earth observation mission that shall demonstrate the detection of wildfires and other high-temperature events by means of uncooled TIR microbolometers. Furthermore, the mission's imaging payload includes a camera based on a CMOS sensor that is sensitive in the visible light spectrum.

While already in the flight hardware production phase, the X-band transceiver XLink was added as secondary payload into the mission. While the main objective here is demonstrating the transceiver in space, the mission itself would greatly benefit from the vastly increased data rates if the transceiver could be integrated into the operations of the imaging payload.

Similar to the platform, the imager payload of TUBIN bases on a modular design. Here, all three cameras are built on the same standardised electronics stack that includes a powerful processing unit that runs a Linux operating system and commands over a large flash memory for storage of the cameras' data products. In this manner, post-processing of the cameras' image products can be performed

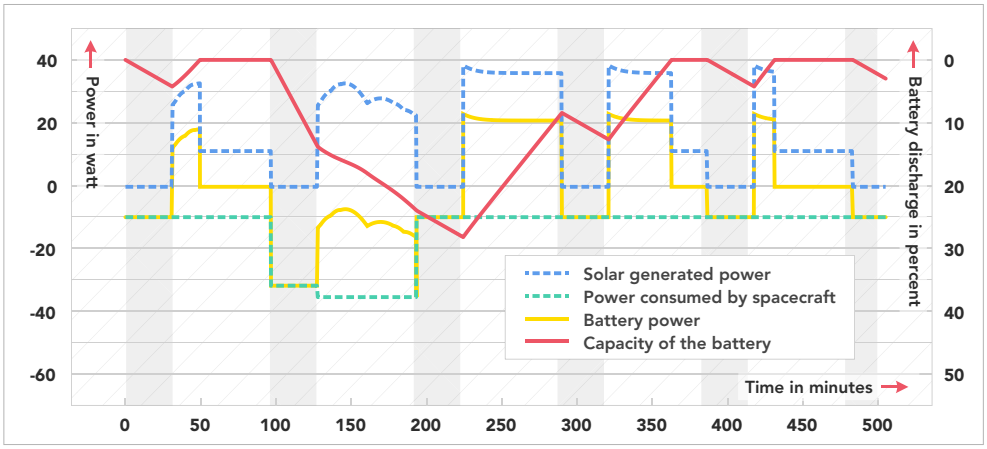

Figure 4.52: Power balance for an entire orbit of imaging. Here, both TIR imagers are operated for the entire orbit, while the visible spectrum camera is only powered in the Sun period. Eclipse periods are indicated with a grey background.

on the cameras and the images are sent to the payload data transmitter directly from the cameras' memory.

When being compared to the TechnoSat mission, notable modifications were implemented for the ADCS system of TUBIN in order to fulfil the more stringent requirements of an Earth observation mission. Here, it could be demonstrated how two star trackers, two fluxgate magnetic field sensors, as well as a GPS receiver could be introduced into the system without requiring to update the remainder of the platform. On the hardware side, this is made possible with the introduction of new interface nodes that abstract the proprietary interfaces of the different components from the platform. On the software side, an overall modular architecture allows for including new sensors and attitude determination algorithms based on applications and modules with standardised interfaces, whereby modifications of the existing code can largely be avoided.

TUBIN was launched into an 530 km SSO on the 30th of June, 2021. At the time of writing, the commission phase of satellite platform and payloads is ongoing and first fires could already be detected based on the imagery provided by the microbolometers.

4.3 The QUEEN Mission

QUEEN is a joint mission conducted by Humboldt-Universität zu Berlin, Technische Universität Berlin and the Ferdinand-Braun-Institut, Leibniz-Institut für Höchstfrequenztechnik[18]. The primary objective of mission is the demonstration of an optical frequency reference in orbit, which is an important bulding block for future quantum technology missions [20, 21]. Secondary objective is the demonstration of three additional in-orbit technology demonstration payloads.

Figure 4.53 shows a digital rendering of the QUEEN spacecraft in operational configuration.

Figure 4.53: Digital rendering of the QUEEN spacecraft in operational configuration with solar panels and UHF antennas deployed [21] (Image credit: Marc Lehmann).

This chapter briefly introduces the QUEEN mission and its payloads. Furthermore, the TUBiX20 platform implementation foreseen for the QUEEN mission is discussed focussing on the most relevant platform advancements that are realised for this mission. This includes a new structure design that supports significant improvements in the integration density of the platform, an extended EPS providing

[18]The project phases A and B of the QUEEN mission were funded by the Federal Ministry for Economic Affairs and Energy (BMWi) through the German Aerospace Center (DLR) on the basis of a decision of the German Bundestag (grant no. 50WM1753, 50WM1754, 50WM1755, 50RU1801, 50WM1857, and 50WM1857).

sufficient electrical power for continuous payload operations and an updated TCS that uses active elements to provide the thermal environment required by the payload.

Table 4.11 gives an overview over the most important parameters of the QUEEN mission and the subsystems performance of the QUEEN spacecraft.

Table 4.11: Main parameters of the QUEEN mission, as well as requirements and performance parameters of the satellite platform to support the mission (based on data first published in [21]).

Mission objective:	In-orbit technology demonstration
Orbit:	550 km to 620 km SSO
Launch mass:	35 kg
Payload mass:	17.5 kg
Spacecraft volume[a]:	$336 \times 339 \times 354\,\mathrm{mm}^3$
Design lifetime:	1 year
Power generation capabilities[b]:	102 W
Power storage capabilities:	154 W h
Required attitude knowledge:	0.05 deg
Required pointing accuracy:	0.1 deg
Required position knowledge:	50 m
Data downlink rate:	$6\,\mathrm{Mbit\,s}^{-1}$
Required thermal stability for the payload[c]:	± 5 K
Payload data storage:	5.25 GB

[a] Without deployable solar panels and antennas
[b] At 28 °C and $1\,367\,\mathrm{W\,m}^{-2}$ solar irradiation
[c] Required by the frequency reference payload

4.3.1 QUEEN Payloads

The QUEEN mission carries four different IOD payloads, which are described in more detail in the following.

Optical Frequency Reference

The primary payload of the mission is an optical vapour cell frequency reference based on rubidium developed by Humboldt-Universität zu Berlin and the Ferdinand-

Braun-Institut, Leibniz-Institut für Höchstfrequenztechnik. The payload bases on two extended cavity diode lasers (ECDLs) that are operated in a master-oscillator-power-amplifier configuration (MOPA) configuration and are individually stabilised in frequency to atomic transitions of rubidium. While generally only one laser would be required to built a frequency reference, the combination of two lasers allows to compare the output signals of both systems to assess the frequency stability. The objective of the experiment is to characterize the impact of the space environment on the frequency reference and to analyse the long-term stability of the system. A more detailed description of the payload has been published by Dinkelaker et al. in [20][19].

Optical Data Transmission Terminal

Another orbit demonstration payload on the QUEEN mission is the optical data transmission terminal OSIRIS that is developed by the German Aerospace Center (DLR). The terminal is an advancement of an existing design that offers a downlink data rate of $100\,\mathrm{Mbit\,s^{-1}}$ within a third of a CubeSat unit [18]. The enhanced system to be tested within the QUEEN mission will offer an improved data downlink rate of $1\,\mathrm{Gbit\,s^{-1}}$ and furthermore support ISL applications. To this end, the laser output power is increased to 1 W and a dedicated data management field programmable gate array (FPGA) is introduced which will increase the device's volume to one CubeSat unit with a mass of 750 g [21].

X-Band Transmitter

Furthermore, the QUEEN mission is aiming at demonstrating the modular SDR X-band transceiver XLink in orbit.[20] The transceiver was developed by IQ wireless GmbH together with Technische Universität Berlin and offers two uplink, as well as two downlink channels that can be configured based on the requirements of a specific mission [39]. For QUEEN, XLink will provide uplink capabilities in S band and in X band, while the two downlink paths are combined to provide data rates of up to $100\,\mathrm{Mbit\,s^{-1}}$ in X band.

[19] Peer-reviewed journal publication with contributions of the author.

[20] As the XLink transceiver was added as opportunity payload to the TUBIN mission and will, therefore, already be demonstrated in orbit before the launch of QUEEN the payload will be replaced by a different experiment in the next mission phase.

Camera System

The camera system that shall be demonstrated within the QUEEN mission comprises two cameras that are sensitive in the visible light spectrum. With a GSD of 10 m, the first camera is targeting a high ground resolution while the second camera provides an 80 degrees wide field of view. As analysed by Banatao et al. in [284], mounting both imagers in such a manner that there will be an angle between their line of sights (LoSs) allows to select targets for the high resolution camera based on frames received by the wide angle imager.

4.3.2 Spacecraft Systems Overview

The systems design of the TUBiX20 platform configuration that is implemented for the QUEEN mission, which is depicted in Figure 4.54, includes several advancements when being compared to configurations applied for former missions. In the following, the systems architecture of the QUEEN spacecraft is briefly described.

The EPS of the QUEEN spacecraft bases on the same architecture as the implementation for TechnoSat and TUBIN with the addition of MPPT capabilities for the solar panels in order to increase the power generation efficiency. The primary solar array is build by two deployable and one body-mounted solar panel that carry four strings with seven cells each. Additional panels with two strings each are mounted on four of the remaining five sides of the spacecraft to guarantee that sufficient power is generated while no attitude control is performed.

While some of the specific sensors that were applied within the TUBIN mission are exchanged against more current models with a better overall performance, the topology of the ADCS system for the QUEEN mission is similar to what is used on TUBIN. Here, the ADCS node interfaces to all baseline TUBiX20 ADCS sensors, as well as to the magnetorquers. Additional nodes are introduced to interface to the star trackers, the GNSS receivers and to the reaction wheels.

Given the requirement for active thermal control of parts of the payloads, a dedicated TCS node is introduced, which reads a number of temperature sensors and controls heaters to stabilise the temperature of the frequency reference payload.

The COM system comprises of two S-band transceivers that are operated in hot redundancy, as well as the four channel UHF transceiver that was already

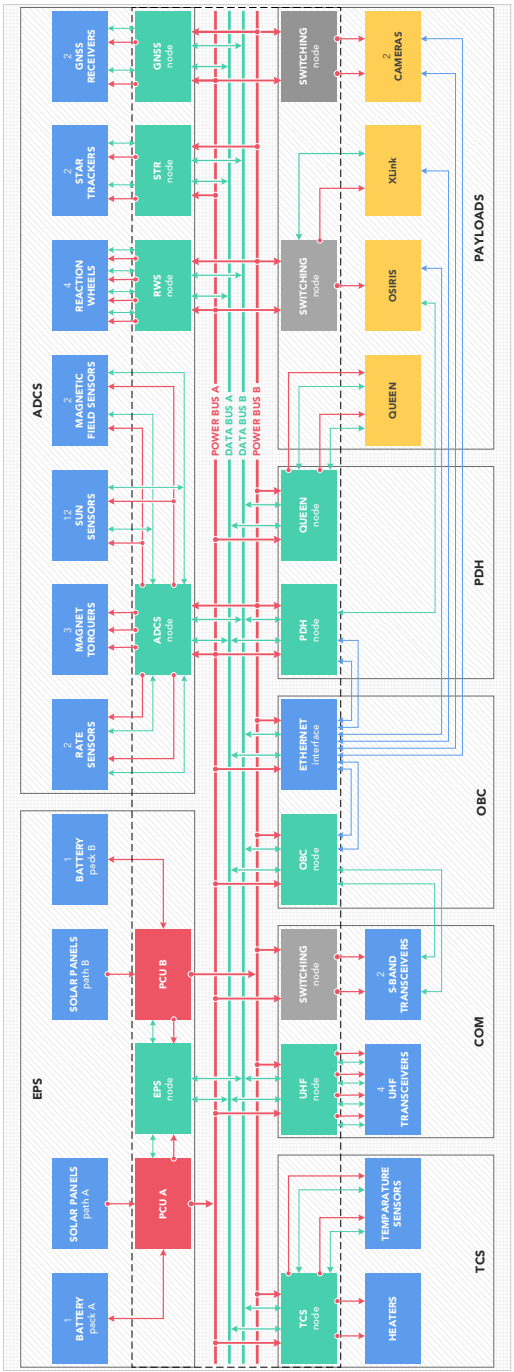

Figure 4.54: Systems design of the QUEEN spacecraft depicting the central power and data bus system, the nodes, as well as the interfacing components and payloads.

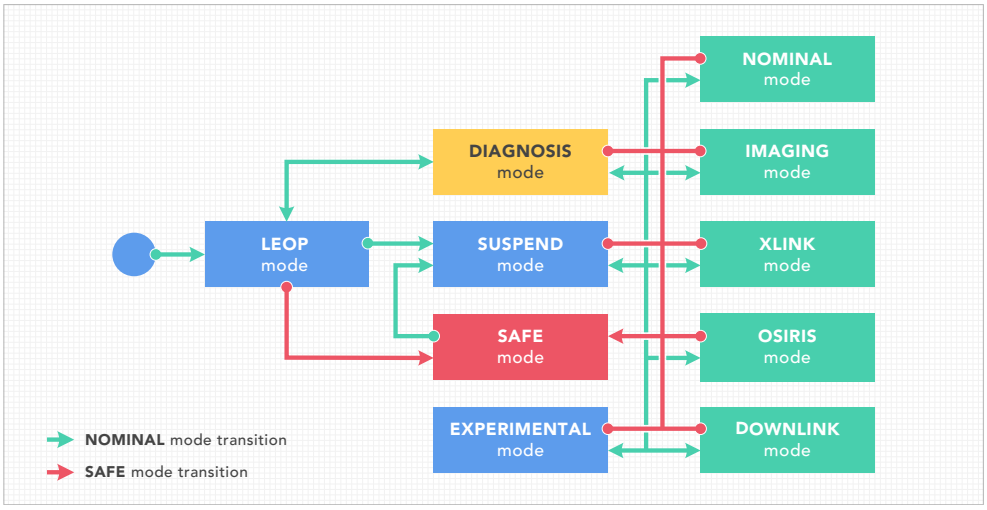

Figure 4.55: System modes of the QUEEN spacecraft. The five modes that are depicted in green are specific to the mission and serve to operate the various payloads, while all other modes are standard platform modes.

demonstrated in orbit within the TechnoSat mission as backup system. Here, the S-band transceivers' data interface is connected to the OBC.

Opposing to how it was designed for the TUBIN mission, the payload data bus is associated with the OBC, which itself comprises of a regular TUBiX20 node.

The PDH of the QUEEN platform comprises of a PDH node, as well as a dedicated control node for the optical frequency reference payload. Here, the PDH node provides the command interface for the optical communication terminal and hosts the software to control both the X-band transceiver and the camera payloads.

The system modes of the QUEEN spacecraft are shown in Figure 4.55. They comprise of the five standard TUBiX20 platform modes, namely the LEOP, safe, diagnosis, experimental, and the suspend mode (cf. Section 3.3.9), as well as five mission specific modes. Here, the nominal mode is the baseline for payload operations as the frequency reference is operated in this mode. Similarly, the imaging, XLink, and the OSIRIS modes are designed to operate the respective payloads. The downlink mode operates the two S-band transmitters and is the baseline for downlinking the data generated by the payloads.

Figure 4.56 illustrates how the satellite coordinate frame is oriented relative to the spacecraft's structure and therewith indicates the naming of the individual panels of the primary structure. The spacecraft is shown in operational configuration with both solar panels and UHF antennas deployed.

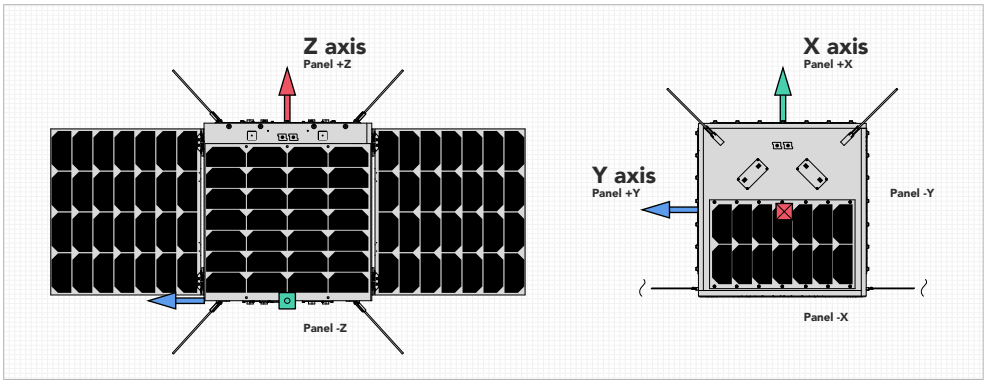

Figure 4.56: Satellite coordinate frame and structural panel naming conventions of the QUEEN spacecraft. The Z axis is aligned with the separation axis, the X axis points away from the primary solar panels and the Y axis completes the right-handed coordinate system. The satellite is shown in operational configuration with solar panels and antennas being deployed but without the part of the separation system that remains on the spacecraft.

In the following, the subsystems in which the most relevant updates were applied for the QUEEN mission in relation to TechnoSat and TUBIN, namely the structural design, the EPS and the TCS are discussed in more detail.

4.3.3 Structure Design

While the octagonal form factor implemented for TechnoSat and TUBIN was well suited for the specific requirements of these two proof-of-concept missions, potential for optimisation of the overall structure approach could be identified in order to facilitate a wider range of applications and simplify the launcher interface. Following the emerging trend of standardisation also for larger satellites like 12 and 16 U CubeSats and the fact that a definition of a 27 U CubeSat was released as well, the TUBiX20 structure concepts was aligned with these form factors (cf. Section 3.1.1).

The new form factor, together with the higher mass, leads to a much higher integration density for the QUEEN spacecraft when being compared to TechnoSat and TUBIN. While the latter mentioned missions had a mass ratio of 0.37 and 0.42 kg per volume unit, respectively, this value will be increased to 0.88 kg for QUEEN.

As described already in Section 3.2.1, the structure is based on six isogrid aluminium panels that form the sides of the cubic structure. Furthermore, a middle panel separates the platform compartment from the payload compartment. Here, the six outer panels are screwed together such that each panel but the +Z panel can be individually removed from the final assembly without the need to remove other elements of the spacecraft. All platform components that are not required to be placed on a specific panel (e.g. Sun sensors that need to cover all sides of the spacecraft) are gathered on the −Z panel that also accommodates the separation system for the launcher interface.

Within the missions TechnoSat and TUBIN the design of the wiring harness was restricted to the use of point-to-point connections to simplify implementation, documentation and integration. Nevertheless, tasks related to the wiring harness amounted for a large fraction of the time required for satellite integration. Furthermore, the challenges in the design and integration of the harness wiring for small satellite platforms were for example also discussed by Gwozdecky in [285].

In order to effectively reduce the time required to design and integrate the harness wiring for TUBiX20-based spacecraft, cables are replaced by distribution PCBs wherever possible.

The interconnections between the centralised electronics compartment and the individual components such as batteries, sensors, actuators, or transceivers are realised based on PCB distribution boards and board-to-board connectors are used to realise the transition to the other panels. To this end, the backplane of the avionics compartment connects to both the −Z panel and the middle panel's distribution board, while four side panels are, in turn, connecting to the middle panel. Finally, the +Z panel is interconnected to the avionics unit via the −Y and the middle panel.

Figure 4.57 shows the primary structure of the QUEEN satellite along with the distribution boards on the left side. Here, the −X panel is removed to show the avionics compartment carrying dummy electronic cards for illustration (1). The distribution board that is located on the middle panel (2) connects the avionics

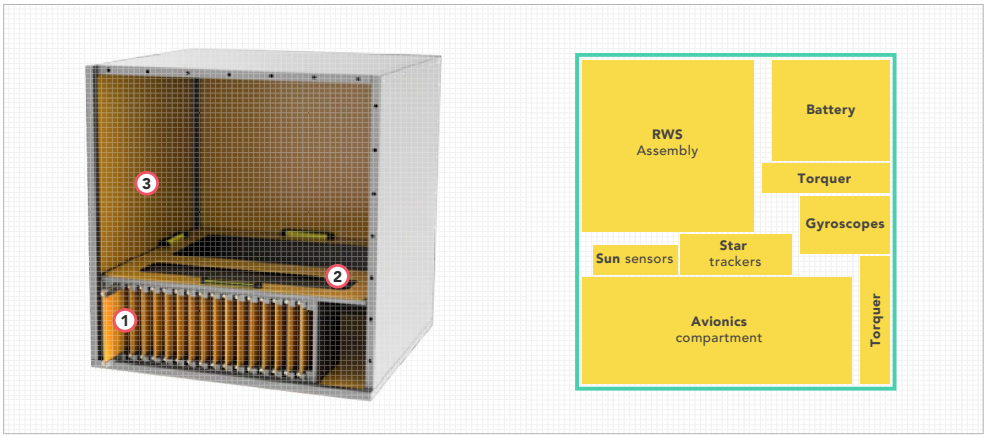

Figure 4.57: The left image shows the basic design of the primary structure along with location and interfaces of the distribution boards. Furthermore, the figure shows the central avionics compartment with one card slightly pulled out for illustration purposes. On the right side the arrangement of the platform components on the −Z panel is shown.

unit with the distribution boards on the side panels. While the distribution boards are generally shown as rectangular PCBs here (3), they are to be fractionated according to the needs of the respective components in the final structure design.

The right image in the same figure shows the arrangement of the platform components attached to the −Z panel. Here, the UHF transceivers are mounted from the outside onto the panel and are therefore not occupying space on the inner side.

Figure 4.58 gives an overview of the component accommodation on the different panels of the QUEEN satellite. Furthermore, the figure indicates the number of power and data interconnections that are required between the −Z panel and the adjacent panels. Here, the lines required for the components located on the +Z panel are routed through the −Y panel.

For satellite integration, first the individual components are mounted onto adapter structures that act as interface between the component and the primary structure and also carry the harness that translates between the individual connector of the component and the board-to-board connector of the respective distribution board. In this manner, the individual alignment for components such as reaction wheels or star trackers can be realised and the interface of the primary structure can

Figure 4.58: Distribution of equipment and payloads among the structural panels of the QUEEN satellite along with the number of power and signal lines between the panels.

largely be abstracted from the components, i.e. two reaction wheels from different manufacturers may be mounted onto the same interface on the primary structure.

An assembly of four RW3-0.06 reaction wheels of Sinclair Interplanetary [286] mounted onto the satellite's −Z panel is shown in Figure 4.59 to illustrate the approach. The left rendering shows three reaction wheel modules mounted onto an exemplary structure. Here one wheel is not shown to uncover the mounting points and the interface PCB used to replace the traditional harness. The module consist of the reaction wheel itself (1), the mounting structure (2), and the PCB (3) to bridge between the wheel's connector and the interface PCB (4). From where the

interface PCB ends in the shown cut out, it may be continued to the backplane either as PCB or as cable. Here, the interconnection of the distribution boards with cables would not significantly increase the complexity but would allow to further modularize the concept. The right rendering shows the same assembly with all four wheels from top to illustrate how compact the modules can be arranged. Here, the three screws that are exemplary marked for one module allow to remove the entire module from the assembly. Replacement of a module is further simplified by the use of NordLock wedge-locking washers [287] for screw lock.

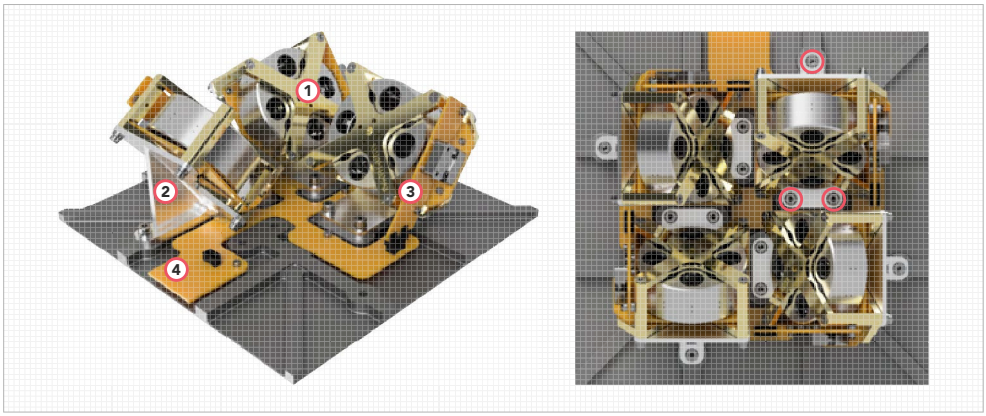

Figure 4.59: The left image shows three reaction wheel modules with the wheel itself (1), the mounting structure (2) and the PCB (3) that bridges between the wheel's connector and the on the interface PCB (4) mounted on an exemplary structure. Here, one wheel was removed to uncover the mounting structure and the interface PCB. The right image shows four reaction wheels mounted onto the satellite panel with the three screws that allow to remove the module circled in red for one of the modules.

The central avionics unit is generally representing a considerable part of the mass and volume occupied by the platform. Furthermore, the configuration of the avionics compartment that was implemented for TechnoSat and TUBIN is not suitable for a 6 U form factor. Following this, the existing design was optimised in mass and volume in the course of a masters thesis that was supervised by the author [217]. Here, the area of each individual card in the box could be reduced by 27 percent, which in turn results in a reduction of 40 percent in volume and 32 percent in mass for a representative unit. In order to ensure scalability towards missions with higher power demands the new design of the central avionics compartment allows for a power input of up to 300 W considering both electrical and thermal aspects.

In order to allow for straightforward access to the PCB cards of the avionics compartment is integrated into the primary structure such that it can be accessed by removing one of the spacecraft's side panels or by removing the entire −Z panel including the electronics compartment (cf. Figure 4.58).

Another upgrade of the QUEEN spacecraft in the structure domain is the addition of unfoldable solar arrays required to meet the payloads' electrical power demands. Here, a modular panel system that supports unfolding between one and six panels (each three on two sides) was designed within a masters thesis supervised by the author [126]. For the QUEEN mission two single panels can be unfolded, which are complemented by one body-mounted panel.

4.3.4 Power Generation and Storage

As already stated, the power demands of the QUEEN mission are significantly elevated when being compared to its predecessors TechnoSat and TUBIN. In this context, centrally implemented MPPT capabilities shall be added to the system in order to increase the power generation efficiency. Figure 4.60 gives an overview over the integration of the MPPT functionality into the flight-proven EPS used in the missions TechnoSat and TUBIN (cf. Figure 4.11 for the system without MPPT). Here, instead of programming a fixed solar panel voltage into the charge regulator like it was realised for TechnoSat and TUBIN, the MPPT continuously determines the MPP voltage and adjusts the charge regulator accordingly.

Generally, the power generation and storage capabilities of the QUEEN spacecraft are dimensioned following a graceful degradation approach. This means that while no single fault can completely disable the EPS, such fault may require a lower duty cycle of payload operation as the power generation and storage capabilities may be reduced.

In the following, the solar panels are dimensioned and the resulting power balance for both nominal operations and safe mode is analysed in more detail.

Nominal Power Balance

The platform configuration implemented for the QUEEN mission is required to support continuous operation of the optical frequency reference payload together with two data downlink sessions in consecutive orbits. As the frequency reference

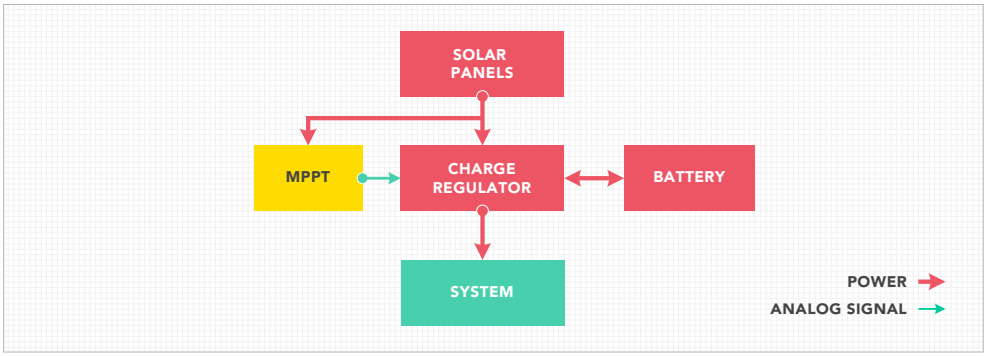

Figure 4.60: Schematic of the QUEEN EPS topology. While the majority of the system was already used for the missions TechnoSat and TUBIN, it is now complemented by a MPPT module that adjusts the charge regulator such that the solar panels are always operated at the MPP.

payload does not require a specific attitude to operate, Sun pointing can be performed at all times except during the ground station passes that are used for data downlink.

The operational scenario used for EPS dimensioning further requires that the batteries shall be fully charged after three orbits subsequent to the second data downlink session.

While operating the camera payload, the optical frequency reference is to be switched off, which will lead to considerably lower power consumption when being compared to the scenario used for EPS dimensioning. As both the X-band transceiver and the optical data downlink terminal consume less power than the nominal payload data downlink transmitters, experiments with both payloads can be conducted in parallel to operating the optical frequency reference.

Table 4.12 gives an overview over the power consumption of the QUEEN spacecraft in the operational modes that are relevant for dimensioning battery and solar array. Here the Safe mode is split into a state were two channels of the UHF communication system are ready to receive and a state were one channel is transmitting while the other is ready to receive.

An initial assessment of the average solar panel power required to support nominal operations of the QUEEN spacecraft can be performed with:

Table 4.12: Power consumption for operational modes relevant for dimensioning battery and solar arrays (based on data first published in [21]). The two modes relevant for the nominal dimensioning scenario are the QUEEN mode in which the optical frequency reference payload is operated as well as the downlink mode in which the two S-band transmitters are powered aditionally. All values include margins.

Subsystem	Safe mode[a] W	Safe mode[b] W	QUEEN mode W	Downlink mode W
TCS	-	-	4.7	4.7
EPS	3.0	3.5	3.8	4.7
ADCS	0.7	0.7	6.6	10.6
COM	0.4	3.2	0.4	29.0
OBC	0.2	0.2	0.2	2.5
PDH	-	-	0.4	1.0
Payloads	-	-	27.5	27.5
Sum	4.3	7.6	43.6	80.0

[a] Both channels of the UHF communication system in receive mode
[b] While transmitting with the one channel of the UHF communication system

$$P_{\text{panel}} = \frac{t_{\text{orbit}}}{t_{\text{Sun}}} P_{\text{satellite}} \cdot \eta_{\text{MPPT}} \cdot \eta_{\text{charge}} \tag{4.16}$$

With an orbit duration t_{orbit} of 90 minutes, an associated Sun period t_{Sun} of one hour, the satellites power consumption while operating the frequency reference payload $P_{\text{satellite}}$ of 48.4 watt (cf. Table 4.12), and an assumed MPPT efficiency η_{MPPT} of 0.9 the average power required to be generated by the primary solar array can be calculated with 83 watt.

From Figure 3.10 in Section 3.2.3 it can be found that a configuration with two deployable and one body-mounted solar panel is the most suitable option considering the initial power requirement.

A suitable battery size is found with 154.4 W h based on an estimated power storage capacity to be implemented and the requirement use the same two times four cells configuration as was implemented for TechnoSat and TUBIN. Furthermore, cells from the same family as used for the aforementioned missions were to be used.

As a next step, a simulation for the dimensioning scenario is performed, following the approach described in Section 3.2.3 and using the parameters that are listed in the following:

- a minimal solar irradiation is assumed (i.e., $1\,315.9\,\mathrm{W\,m^{-1}}$),
- the Sun period's duration is 60 min,
- the duration of the eclipse period is 30 min,
- the efficiency of the MPPT is assumed to be 0.9,
- the charging efficiency is assumed to be 0.95,
- the accuracy of the Sun pointing assumed with 5 degrees,
- the maximum allowed DoD is 30 percent,
- according to the findings of Section 3.2.3, solar cell degradation due to radiation is neglected.

The result of the simulation is shown in Figure 4.61. Here, the Sun periods are depicted with white background, while eclipse is indicated with a grey background. One can identify the two operated ground station passes by a significantly increased power consumption of the spacecraft. At the same time, the power income is reduced due to the fact that the satellite performs target pointing towards the ground station and can, thus, not align the solar array towards Sun. This, in turn, results in the fact that the battery is discharged during data downlink at a similar rate as in eclipse. However, as soon as no downlink is performed any more, the overall power balance is again positive and the batteries are fully charged again after two orbits. The maximum DoD that was reached during the simulation is 26 percent.

The small tips in the generated power at the beginning of the Sun periods are a result of the solar array's low temperature after eclipse. In the last two Sun phases one can furthermore observe how the generated power is reduced to match the satellite's overall consumption as soon the battery is fully charged. Here, the difference between generated power and consumed power can be explained by the efficiency of the MPPT.

Additionally to the graph for the nominal battery capacity (red), another one is plotted for a case in which one of the satellite's two batteries failed and only half of the capacity (i.e., 77.2 W h) is available (orange). As expected, the batteries

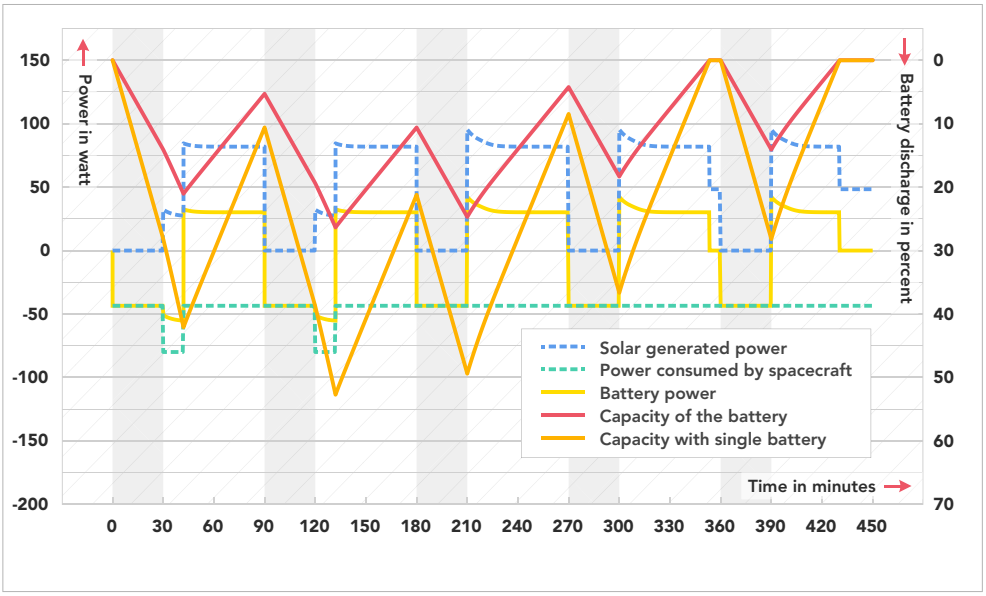

Figure 4.61: Simulated QUEEN power balance for five orbits during nominal operations. There are two 12 minute downlink periods in the first two orbits being conducted at the beginning of the Sun phase. The battery power is shown positive when charging and negative when the battery supplies the satellite.

are fully charged again at the same time for both cases, however the maximum DoD is 53 percent in the second case. Here, a graceful degradation approach is followed as the mission can still be continued if one of batteries failed but the lower discharge level may lead to faster battery degradation.

The solar panels are designed such that the solar path still generates power if one solar cell or even a string of 7 cells fails. However, if one entire solar path is disabled the power balance will not be positive any more for nominal operation of the QUEEN payload.

Safe Mode Power Balance

In addition to nominal operations, the safe mode power balance needs to be confirmed to ensure that sufficient power generation and storage capabilities are foreseen. Here, approximately eight hours (five orbits) of orbit data from the

TechnoSat spacecraft are used to generated input parameters for the illumination of the panels, as well as for the panels' temperatures. Furthermore, the following worst-case assumptions are made:

- the solar panels are not yet deployed,
- the spacecraft's attitude is unconstrained (as mentioned, TechnoSat attitude data were used),
- the panels' temperature is 10 degrees above the TechnoSat orbit data (worst case for MPPT),
- one solar path is disabled,
- minimal solar irradiation ($1\,315.9\,\mathrm{W\,m^{-1}}$),
- the MPPT efficiency is 0.8,
- the overall conversion efficiency between the solar panels and the consumers is 0.8,
- UHF radio operations are performed in two consecutive orbits,
- Earth albedo is not considered for power generation.

The consumption of the spacecraft in safe mode is listed in Table 4.12. The result of the safe mode power balance simulation is depicted in figure Figure 4.62. As for the nominal scenario, the eclipse periods are indicated with grey background. The generated power is plotted as the sum of the contribution by all panels. In this scenario, the highest battery discharge will occur if the operated ground station passes are assumed to be performed within the eclipse period, as power generation will not be significantly reduced as no pointing towards the ground station is performed as it is the case in the nominal scenario.

One can see that the largest fraction of the Sun period required to recharge the battery after eclipse is 52 percent within the second Sun phase. As in the nominal scenario, the solar generated power is reduced to match the present power consumption of the satellite after the battery is charged. Furthermore, it can be seen that the generated solar power is not sufficient to fully support the spacecraft's power demand at some points, which can be observed as short spikes of battery discharge, following by equally short charging spikes.

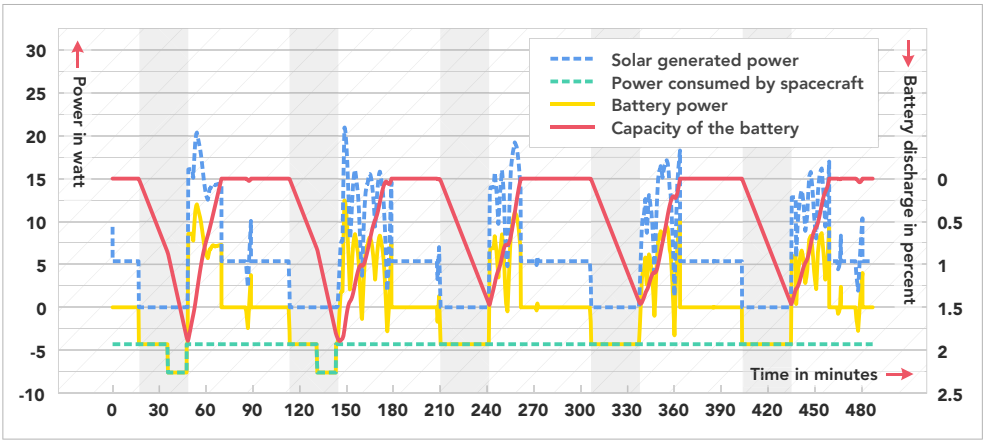

Figure 4.62: QUEEN safe mode power balance for five orbits simulated based on TechnoSat attitude data. Two UHF operated ground station passes are included in the first two eclipse times and safe mode power consumption is assumed for the rest of the scenario. The eclipse periods are marked with grey background.

With a maximum DoD of 1.9 percent, the batteries are much less stressed during safe mode when being compared to nominal operations.

4.3.5 Thermal Control System

The laser systems of the optical frequency reference payload of the QUEEN mission require a stable temperature with fluctuations below $\pm 5\,\mathrm{mK}$. By the implementation of Peltier elements for active temperature within the payload, this requirement is reduced to a $\pm 5\,\mathrm{K}$ window that needs to be within an absolute temperature between 15 and 30 K for the satellite platform [21].

Based on this, the driving requirement for the TCS design of the QUEEN spacecraft is to provide temperature stability of $\pm 5\,\mathrm{K}$ at the interface of the optical frequency reference payload throughout the mission. As preliminary simulations by Konaka et al. in [288][21] have shown, this cannot realistically be guaranteed using a purely passive TCS. Based on this, an active thermal control concept is foreseen for the QUEEN spacecraft. Here, the average power required for an electrical heater to compensate the temperature fluctuations over the year is estimated with 4.5 W,

[21] Publication with contributions of the author.

while the maximum consumption is expected to be 8 W. Alternatively, it is to be analysed if a larger overall efficiency can be achieved if the Peltier elements within the payload are enlarged to allow for higher temperature fluctuations at the interface to the satellite platform so that the spacecraft's TCS can be designed as passive system.

4.3.6 Conclusions

The QUEEN mission is a joined effort of Technische Universität Berlin, Humboldt-Universität zu Berlin and the Ferdinand-Braun-Institut, Leibniz-Institut für Höchstfrequenztechnik. The primary payload of the mission is an optical frequency reference based on rubidium, an important building block for future highly integrated quantum technology payloads. Secondary payloads include an optical data downlink terminal, an SDR-based X-band transceiver and a camera system comprising of two visible light imagers.

From the platform's perspective, the capabilities required to operate the mission's payloads exceed the capabilities demonstrated with the proof-of-concept missions TechnoSat and TUBIN, which allows to illustrate the platforms adaptability to specific payload requirements. The requirement to support continuous operation of the optical frequency reference payload necessitated the introduction of unfoldable solar arrays and the payload's comparatively stringent requirements regarding thermal stability led to the introduction of active thermal control elements. Furthermore, the requirements in attitude pointing and payload data downlink exceed the capabilities of the former missions. In addition to the modifications that were driven by the payloads' requirements, the TUBiX20 platform configuration to be applied for the QUEEN mission was also developed further based on the experiences made in the missions TechnoSat and TUBIN. Here, the most prominent update is the new structure design that follows the CubeSat form factor and allows for higher platform integration. Furthermore, the new structure configuration aims at drastically decreasing the time required for integration of TUBiX20-based spacecraft by fostering modularity and effectively removing the classical harness between components. As part of these updates, also the design of the avionics compartment has been updated to reduce the volume and enhance the integrability so that the same form factor of the slot-in cards can be used for all form factors of the platform family.

5 Summary and Conclusions

Within this thesis, the systems architecture of TUBiX20, a modular microsatellite platform targeting missions in the range of 10 to 50 kg is investigated. The development of TUBiX20, as well as the implementation of the first three missions based on the platform, namely TechnoSat (launched in 2017), TUBIN (launched in 2021), and QUEEN (under development) was led by the author of this thesis.

The research starts with a brief overview of the state of the art in technology for microsatellites in the considered mass range. After an introductory discussion of definitions and constraints such as the launcher interface, current and future missions in the field of Earth observation, communications, science, as well as robotics and close proximity are introduced. This includes listing a number of subsystem performance parameters for certain reference missions of each application area to gain an insight into the capabilities required for state-of-the-art applications. Furthermore, an introduction of terms and definitions for product platforms and an overview of microsatellite platforms in the 10 to 50 kg range available on the market is presented by the author.

As a next step, the research analyses the architecture of a modular small satellite platform, its subsystems and software and motivates central design decisions. Here, four different size variants are considered for the platform that generally follow the CubeSat form factor. Now, the most significant top level requirements for the platform are presented. Here, the central feature was found to be the ability of different platform implementations to serve mission scenarios with largely diverging requirements. This, in turn, raises the demand for scalability of performance parameters such as power generation, attitude pointing accuracy or data downlink capabilities. At the same time, the platform architecture is tasked to maximise the reuse potential across different missions as this is the prerequisite to facilitate short development times and to limit the overall costs. In order to identify relevant parameters and their scaling ranges, each subsystem is now analysed by the author and significant architecture and technology choices for the implementation are presented based on the findings.

Subsequently, this evolves into the presentation and motivation of the overall platform architecture chosen to implement the previously determined requirements. This architecture is based on a modular network of distributed computational nodes with a standardised interface to a central power and data bus system. Throughout the platform, fault tolerance is mainly implemented by means of redundancy. Here, the nodes and the data bus system are realised in cold redundancy, while the power bus system is operated in hot redundancy. As the node controlling the EPS is responsible for supervising the redundancy of all other nodes, as well as the data bus system, it is itself operated in warm redundancy. The nodes are gathered in a central avionics unit and interconnect external components, such as sensors and actuators, to the central data and power bus system. In addition to the software required to communicate with connected components, the nodes host the higher-level subsystem software. Here, the software is equally implemented a modular architecture to complement the scalability of the hardware and enable a similar level of reuse throughout different missions.

After the requirements for the platform were analysed and central architecture aspects are specified, three different missions that are based on the TUBiX20 platform, namely TechnoSat, TUBIN, and QUEEN are introduced. This allows the author to illustrate how the defined systems architecture can support diverging requirements for different missions. While TechnoSat and TUBIN can be seen as proof-of-concept missions for the modular TUBiX20 platform design, significant upgrades are foreseen for the platform design within the QUEEN mission. This is mainly reflected in the transition from the octagonal structure design towards a standardised 27 U form factor and the significant increase in launch mass and generated electrical power. Furthermore, the spacecraft will implement an active TCS to comply with the thermal requirements of the primary payload.

TechnoSat was launched in July 2017 and demonstrated newly developed small satellite technology in orbit. Within more than three years the satellite was operated so far, the overall concept of the TUBiX20 platform was validated in orbit and nearly 100 000 pictures downlinked. Furthermore, almost 0.5 GB of telemetry data were generated and used to analyse the platforms performance. In addition to that, TechnoSat is still used to test and demonstrate new software features for future missions in orbit.

In order to relate the shielding dependent TID values from the analysis of typical microsatellite orbits that was performed within the presented research to absolute values of a specific design, the author performed a sector analysis for the TechnoSat

spacecraft. This allowed to determine worst-case TID levels at relevant points within the satellites structure and may serve as a reference for future TUBiX20 missions.

Furthermore, TechnoSat orbit data from two experiments are used by the author to verify the simulations developed for power system dimensioning of TUBiX20-based spacecraft in the course of this research. Here, it could be shown that the deviation between simulation and orbit results is less than two percent for the conducted experiments. To showcase the different capabilities of the TechnoSat spacecraft, the author then presented a number of orbit experiments that have been conducted with the satellite in its first three years in orbit.

The second mission that implements the TUBiX20 platform is TUBIN, which will demonstrate wildfire detection based on microbolometer technology in orbit. Furthermore, the satellite carries an SDR-based X-band transmitter for in-orbit demonstration. TUBIN has a launch mass of 23 kg and bases on the same overall structure design as TechnoSat. The most significant evolution between TechnoSat and TUBIN concerns the ADCS. Here, the comparatively much higher pointing accuracy demanded by the mission is mainly realised by the addition of two star trackers and the associated software algorithms. At the time of writing the TUBIN flight model is being shipped to the launch site.

In this thesis the overall systems design of the TUBIN spacecraft is presented and the interfaces between platform, camera payloads and experimental X-band transmitter are discussed. Furthermore, the microbolometer payload along with the wildfire detection algorithm are described in more detail to serve as an example for an Earth observation payload to be supported by the platform. In this context, also the platform's power generation and storage capabilities are analysed regarding their ability to support the different operational modes that are foreseen for the mission.

In order to meet the payloads' requirements, three substantial platform upgrades are realised within the QUEEN mission. Firstly, the structural design is changed to a cubic, 27 U CubeSat compatible, form factor to support a higher payload mass within smaller envelope. Further, the power generation and storage capabilities of the spacecraft are raised significantly. This is mainly reflected in the two deployable solar panels and the implementation of MPPT to increase the power generation efficiency. In order to reduce the temperature fluctuations to the magnitude requested by the payload, active thermal control elements are introduced.

Furthermore, the author presents a new structure concept to drastically reduce the time required for spacecraft integration. This concept modularizes the platform hardware by implementing a harness approach that exchanges cables with distribution PCBs routed on side and middle panels of the primary structure. Platform components such as reaction wheels or attitude sensors are pre-assembled on small and lightweight interface structures that also serve as adapter between the component specific electrical connector and a unified connector type that can directly be plugged into the distribution board. In this manner, all components can be exchanged solely by removing a number of screws that use a reusable mechanical locking system and no installing or locking of cables is required. This approach is combined with an integration approach of the primary structure that allows to remove any of the six primary panels of the satellite but the top panel without interfering with the other panels. In this manner, any platform component may be added or removed to the satellite with only two integration steps.

In general, the research presented in this thesis represents an important contribution to the development of the TUBiX20 platform which enables Technische Universität Berlin to support microsatellite missions with strongly diverging requirements. To date, more than 45 papers on the TUBiX20 platform and supported missions have been published with contributions of the author.

Bibliography

[1] J.-C. Laprie. "Dependable computing and fault-tolerance: Concepts and terminology". In: *Proceedings of the 25th International Symposium on Fault-Tolerant Computing*. Pasadena, USA, 1985.

[2] K. Brieß. "Present and future picosatellite missions at TU Berlin". In: *Proceedings of the 8th IAA Symposium on Small Satellites for Earth Observation*. 2011, pp. 49–52.

[3] G. N. Sharma. "Hot redundant versus cold redundant systems". In: *Reliability Engineering* 2.3 (1981), pp. 193–197.

[4] Robert Bosch GmbH. *CAN specification*. Specification. Version 2.0. 1991.

[5] The CubeSat Program. *CubeSat design specification*. Specification. Version 13. 2014.

[6] The CubeSat Program. *6U CubeSat design specification*. Specification. Version 1.0. 2018.

[7] G. Dakermanji and R. Sullivan. "Space power systems". In: *Fundamentals of space systems*. Ed. by V. L. Pisacane. 2nd ed. New York, USA: Oxford University Press, 2005. Chap. 6, pp. 326–422.

[8] Y.-L. Mok, C.-H. Goh, and R. C. Segaran. "Redundancy modeling for the X-Sat microsatellite system". In: *Proceedings of the Annual Reliability and Maintainability Symposium*. Orlando, USA, 2013.

[9] D. Noack and K. Brieß. "Laboratory investigation of a fluid-dynamic actuator designed for CubeSats". In: *Acta Astronautica* 96 (2014), pp. 78–82.

[10] D. Noack et al. "FDA-A6 – A fluid-dynamic attitude control system for TechnoSat". In: *Proceedings of the Nano-Satellite Symposium*. Matsuyama-Ehime, Japan, 2017.

[11] D. Noack et al. "FDA in space – First in-orbit results of a fluid dynamic attitude control system". In: *Proceedings of the Small Satellites Systems and Services Symposium*. Sorrento, Italy, 2018.

[12] K. Brieß et al. "S-Band communication for nano- and pico satellites for cross platform compatibility". In: *Proceedings of the 59th International Astronautical Congress*. Glasgow, Scotland, 2008.

[13] M. F. Barschke et al. "Initial results from the TechnoSat in-orbit demonstration mission". In: *Proceedings of the 32nd AIAA / USU Conference on Small Satellites*. Logan, USA, 2018.

[14] NXP Semiconductors N.V. *I2C-bus specification and user manual*. Specification. Version 6. 2014.

[15] IEEE Aerospace and Electronic Systems Society. *IEEE Standard letter designations for radar-frequency bands*. Standard IEEE Std 521-2002. New York, USA: The Institute of Electrical and Electronics Engineers, Inc., 2003.

[16] M. R. Patel, ed. *Spacecraft power systems*. 2nd ed. Boca Raton, USA: CRC Press, 2005.

[17] M. N. Sweeting. "UoSAT microsatellite missions". In: *Electronics and Communication Engineering Journal* 4.3 (1992), pp. 141–150.

[18] C. Fuchs and C. Schmidt. "Update on DLR's OSIRIS program". In: *Proceedings of the International Conference on Space Optics*. Chania, Greece, 2018.

[19] M. H. Meyer and A. P. Lehnerd. *The power of product platforms*. 1st ed. New York, USA: The Free Press, 1997.

[20] A. N. Dinkelaker et al. "Optical quantum technologies for compact rubidium vapor-cell frequency standards in space using small satellites". In: *Journal of the British Interplanetary Society* 72.3 (2019), pp. 74–82.

[21] M. F. Barschke et al. "The QUEEN mission to demonstrate an optical Rb frequency reference payload and advanced small satellite platform technology". In: *Proceedings of the 70th International Astronautical Congress*. Washington D.C., USA, 2019.

[22] D. Sinclair and J. Dyer. "Radiation Effects and COTS Parts in SmallSats". In: *Proceedings of the 27th Annual AIAA / USU Conference on Small Satellites*. Logan, USA, 2013.

[23] W. Bauer et al. "In orbit debris-detection based on solar panels". In: *CEAS Space Journal* 5 (2013), pp. 49–56.

[24] W. Bauer et al. "Development of in-situ space debris detector". In: *Advances in Space Research* 54.9 (2014), pp. 1858–1869.

[25] W. Bauer, O. Romberg, and M. F. Barschke. "Space environment characterisation by applying an innovative debris detector". In: *Proceedings of the Advanced Maui Optical and Space Surveillance Technologies Conference*. Maui, Hawaii, 2015.

[26] O. Balagurin, H. Kayal, and H. Wojtkowiak. "Test and performance analysis of the new star tracker STELLA". In: *Proceedings of the 60th German Aerospace Congress*. Bremen, Germany, 2011.

[27] O. Balagurin, H. Kayal, and H. Wojtkowiak. "Validation and qualification of a CMOS based miniature star tracker for small satellites". In: *Proceedings of the Small Satellites Systems and Services Symposium*. Portorož, Slovenia, 2012.

[28] M. F. Barschke et al. "The TechnoSat mission for on-orbit technology demonstration". In: *Proceedings of the 65th German Aerospace Congress*. Braunschweig, Germany, 2016.

[29] The International Organization for Standardization. *Road vehicles — Controller area network (CAN) — Part 4: Time-triggered communication*. Standard ISO 11898-4. Geneva, Switzerland, Aug. 2004.

[30] R. E. Kuehn. "Computer redundancy: Design, performance, and future". In: *IEEE Transactions on Reliability* R-18.1 (1969), pp. 3–11.

[31] J. F. Wakerly. "Microcomputer reliability improvement using triple-modular redundancy". In: *Proceedings of the IEEE* 64.6 (1976), pp. 889–895.

[32] M. F. Barschke et al. "The TUBIN mission for wildfire detection using nanosatellites". In: *CEAS Space Journal* 9.2 (2017), pp. 183–194.

[33] M. F. Barschke, Z. Yoon, and K. Brieß. "TUBiX - The TU Berlin innovative next generation nanosatellite bus". In: *Proceedings of the 64th International Astronautical Congress*. Beijing, China, 2013.

[34] W. Frese et al. "TUBiX-10 - Design and flight experience of a nanosatellite bus for distributed missions". In: *Proceedings of the 70th International Astronautical Congress*. Washington D.C., USA, 2019.

[35] M. F. Barschke et al. "TUBiX20 - The novel nanosatellite bus of TU Berlin". In: *Proceedings of the 9th IAA Symposium on Small Satellites for Earth Observation*. 2013, pp. 93–96.

[36] M. F. Barschke et al. "Microsatellite development at Technische Universität Berlin: Status and perspective". In: *Proceedings of the German Aerospace Congress*. Darmstadt, Germany, 2019.

[37] M. F. Barschke et al. “Initial orbit results from the TUBiX20 platform”. In: *Acta Astronautica* 167 (2020), pp. 108–116.

[38] M. Buhl. “TUBSAT: The Technical University of Berlin satellite program”. In: *Small satellites: past, present, and future*. Ed. by H. Helvajian and S. W. Janson. 1st ed. El Segundo, USA: The Aerospace Press, 2008. Chap. 12, pp. 349–383.

[39] M. Reibe et al. “A modular family of high data rate SDR transceivers”. In: *Proceedings of the 33st AIAA / USU Conference on Small Satellites*. Logan, USA, 2019.

[40] M. Sweeting. “Modern small satellites - Changing the economics of space”. In: *Proceedings of the IEEE* 106.3 (2018), pp. 343–361.

[41] M. Swartwout. “You say "picosat", I say "CubeSat": Developing a better taxonomy for secondary spacecraft”. In: *Proceedings of the IEEE Aerospace Conference*. Big Sky, USA, 2018.

[42] T. Villela et al. “Towards the thousandth CubeSat: A statistical overview”. In: *International Journal of Aerospace Engineering* 2019 (2019).

[43] H. Heidt et al. “CubeSat: A new generation of picosatellite for education and industry low-cost space experimentation”. In: *Proceedings of the 14th Annual AIAA / USU Conference on Small Satellites*. Logan, USA, 2000.

[44] C. M. Pong. “On-orbit performance & operation of the attitude & pointing control subsystems on ASTERIA”. In: *Proceedings of the 32nd Annual AIAA / USU Conference on Small Satellites*. Logan, USA, 2018.

[45] K. Devarajy et al. “Planet high speed radio: Crossing Gbps from a 3 U CubeSat”. In: *Proceedings of the 33st AIAA / USU Conference on Small Satellites*. Logan, USA, 2019.

[46] A. T. Klesh. “MarCO: Flight results from the first interplanetary CubeSat mission”. In: *Proceedings of the 70th International Astronautical Congress*. Washington D.C., USA, 2019.

[47] SpaceWorks Enterprises, Inc. *Nano/microsatellite market forecast, 9th edition*. Report. 2018.

[48] R. Hevner et al. “An advanced standard for CubeSats”. In: *Proceedings of the 25th Annual AIAA / USU Conference on Small Satellites*. Logan, USA, 2011.

[49] D. J. Barnhart and M. N. Sweeting. "Right-sizing small satellites". In: *Proceedings of the 28th AIAA / USU Conference on Small Satellites*. Logan, USA, 2014.

[50] C. G. Niederstrasser. "A 2019 view of the impending small launch vehicle boom". In: *Proceedings of the 70th International Astronautical Congress*. Washington D.C., USA, 2019.

[51] J. Kingston. "Modular architecture and product platform concepts applied to multipurpose small spacecraft". In: *Proceedings of the 19th Annual AIAA / USU Conference on Small Satellites*. Logan, USA, 2005.

[52] F. Dannemann and M. Jetzschmann. "Technology-driven design of a scalable small satellite platform". In: *Proceedings of the Small Satellites Systems and Services Symposium*. Valetta, Malta, 2016.

[53] S. Song, H. Kim, and Y.-K. Chang. "Design and implementation of 3U CubeSat platform architecture". In: *International Journal of Aerospace Engineering* (2018).

[54] S. Grau. "Contributions to the advance of the integration density of CubeSats". PhD thesis. Straße des 17. Juni 135, 10623 Berlin, Germany: Technische Universität Berlin, 2019.

[55] F. Erens and K. Verhulst. "Architectures for product families". In: *Computers in Industry* 33.2 (1997), pp. 165–178.

[56] M. Jetzschmann et al. "Scalability and modularity as dimensions of flexibility of a microsatellite platform". In: *Proceedings of the 68th International Astronautical Congress*. Adelaide, Australia, 2017.

[57] E. Falkenhayn. "Multimission modular spacecraft (MMS)". In: *Proceedings of the AIAA Space Programs and Technologies Conference*. Houston, USA, 1988.

[58] F. Nohka, M. Drobczyk, and A. Heidecker. "Experiences in combining CubeSat hardware and commercial components from different manufacturers in order to build the nano satellite AISat/Clavis-1". In: *Proceedings of the 26st AIAA / USU Conference on Small Satellites*. Logan, USA, 2012.

[59] C. Horch, M. Schimmerohn, and F. Schäfer. "Integrating a large nanosatellite from CubeSat components – Challenges and solutions". In: *Proceedings of the 68th International Astronautical Congress*. Adelaide, Australia, 2017.

[60] M. F. Barschke, K. Brieß, and U. Renner. "Twenty-five years of satellite development at Technische Universität Berlin". In: *Proceedings of the Small Satellites Systems and Services Symposium*. Valletta, Malta, 2016.

[61] S. Schulz and U. Renner. "DLR-TUBSAT: a microsatellite for interactive earth observation". In: *Proceedings of the 3th IAA Symposium Small Satellites for Earth Observation*. 2001, pp. 75–78.

[62] H. Kayal et al. "BEESAT: A pico satellite for the on orbit verification of micro wheels". In: *Proceedings of the 3nd International Conference on Recent Advances in Space Technologies*. Istanbul, Turkey, 2007.

[63] Z. Yoon et al. "System design of an S-band network of distributed nanosatellites". In: *CEAS Space Journal* 6.1 (2014), pp. 61–71.

[64] W. Frese et al. "Communication network in LEO: In-orbit verification of intersatellite link by nanosatellite cluster S-Net". In: *Proceedings of the 69th International Astronautical Congress*. Bremen, Germany, 2018.

[65] J. Großhans et al. "SALSAT - An innovative nanosatellite for spectrum analysis based on SDR technology". In: *Proceedings of the 69th International Astronautical Congress*. Bremen, Germany, 2018.

[66] J. Louet and S. Bruzzi. "ENVISAT Mission and System". In: *Proceedings of the International Geoscience and Remote Sensing Symposium*. Hamburg, Germany, 1999.

[67] T.Parrinello et al. "CryoSat: ESA's ice mission – Eight years in space". In: *Advances in Space Research* 62.6 (2018), pp. 1178–1190.

[68] S. Föckersperger et al. "TET-1 – A German microsatellite for technology on-orbit verification". In: *Proceedings of the Small Satellites Systems and Services Symposium*. Sorrento, Italy, 2018.

[69] D. Gerhardt et al. "GOMX-3: Mission results from the inaugural ESA in-orbit demonstration CubeSat". In: *Proceedings of the 30th AIAA / USU Conference on Small Satellites*. Logan, USA, 2016.

[70] S. Radu et al. "Delfi-PQ: The first pocketqube of Delft University of Technology". In: *Proceedings of the 69th International Astronautical Congress*. Bremen, Germany, 2018.

[71] L. Yang et al. "The design and experiment of Stardust femto-satellite". In: *Acta Astronautica* 174 (2020), pp. 72–81.

[72] A. R. Aslan, C. Bernal, and J. Puig-Suari. "Deployment systems". In: *Nanosatellites: Space and ground technologies, operations and economics*. Ed. by R. A. de Carvalho, J. Estela, and M. Langer. 1st ed. London, UK: Wiley & Sons, 2020. Chap. 18, pp. 375–397.

[73] F. Caramelli et al. "Status of Small Spacecraft Mission Service (SSMS) development for VEGA". In: *Proceedings of the 33st AIAA / USU Conference on Small Satellites*. Logan, USA, 2017.

[74] D. Selva and D. Krejci. "A survey and assessment of the capabilities of Cubesats for Earth observation". In: *Acta Astronautica* 74 (2012), pp. 50–68.

[75] A. Freeman. "Deep space nanosats – Positioned for exponential growth". In: *Proceedings of the Small Satellites Systems and Services Symposium*. Valetta, Malta, 2016.

[76] A. Shao, E. A. Koltz, and J. R. Wertz. "Performance based cost modeling: Quantifying the cost reduction potential of small observation satellites". In: *Proceedings of the Reinventing Space Conference*. Los Angeles, USA, 2013.

[77] N. Crisp et al. "The benefits of very low Earth orbit for Earth observation missions". In: *Progress in Aerospace Sciences* 117 (2020), p. 100619.

[78] E. Peral et al. "RainCube, a Ka-band precipitation radar in a 6U CubeSat". In: *Proceedings of the 31st AIAA / USU Conference on Small Satellites*. Logan, USA, 2017.

[79] E. Peral et al. "RainCube: the first ever radar measurements from a CubeSat in space". In: *Journal of Applied Remote Sensing* 13 (2019).

[80] D. J. Varon et al. "Quantifying time-averaged methane emissions from individual coal mine vents with GHGSat-D satellite observations". In: *Environmental Science and Technology* 54.16 (2020), pp. 10246–10253.

[81] D. J. Varon et al. "Satellite discovery of anomalously large methane point sources from oil/gas production". In: *Geophysical Research Letters* 46.22 (2019), pp. 13507–13516.

[82] M. Ligori et al. "GHGSat constellation: The future of monitoring greenhouse gas emissions". In: *Proceedings of the 33st AIAA / USU Conference on Small Satellites*. Logan, USA, 2019.

[83] M. Chen et al. "Developing and In-orbit test of the ultra-lightweight and high resolution microsatellite Jilin-1gf03A for commercial service". In: *Proceedings of the 71st International Astronautical Congress*. Online, 2020.

[84] R. Guzmán et al. "A compact multispectral imager for the MANTIS mission 12 U CubeSat". In: *Proceedings of SPIE* 11505 (2020).

[85] D. Weidmann et al. "CubeSats for Monitoring Atmospheric Processes (CubeMAP): A constellation mission to study the middle atmosphere". In: *Sensors, Systems, and Next-Generation Satellites XXIV*. Ed. by S. P. Neeck, A. Hélière, and T. Kimura. Vol. 11530. International Society for Optics and Photonics. SPIE, 2020, pp. 141–159.

[86] D.-H. Cho et al. "High-resolution image and video CubeSat (HiREV): Development of space technology test platform using a low-cost CubeSat platform". In: *International Journal of Aerospace Engineering* 2019 (2019).

[87] N. Saeed et al. "CubeSat communications: Recent advances and future challenges". In: *IEEE Communications Surveys and Tutorials* 22.3 (2020), pp. 1839–1862.

[88] S. C. Burleigh et al. "From connectivity to advanced internet services: A comprehensive review of small satellites communications and networks". In: *Wireless Communications and Mobile Computing* 2019 (2019).

[89] M. Buscher. "Investigations on the current and future use of radio frequency allocations for small satellite operations". PhD thesis. Straße des 17. Juni 135, 10623 Berlin, Germany: Technische Universität Berlin, 2019.

[90] M. Toyoshima. "Recent trends in space laser communications for small satellites and constellations". In: *Proceedings of the IEEE International Conference on Space Optical Systems and Applications (ICSOS)*. Portland, USA, 2019.

[91] R. Bedington, J. M. Arrazola, and A. Ling. "Progress in satellite quantum key distribution". In: *npj Quantum Information* 3.30 (2017).

[92] R. Birkeland and D. Palma. "An assessment of IoT via satellite: Technologies, services and possibilities". In: *Proceedings of the 70th International Astronautical Congress*. Washington D.C., USA, 2019.

[93] I. F. Akyildiz and A. Kak. "The internet of space things/CubeSats". In: *IEEE Network* 33.5 (2019), pp. 212–218.

[94] I. U. Zaman et al. "A comparative study of inter CubeSat high speed links: RF, mmWave and optical". In: *Proceedings of the IEEE International Conference on Space Optical Systems and Applications (ICSOS)*. Portland, USA, 2019.

[95] H. Takenaka et al. "Satellite-to-ground quantum-limited communication using a 50-kg-class microsatellite". In: *Nature Photonics* 11 (2017), pp. 502–509.

[96] E. Kerstel et al. "Nanobob: a CubeSat mission concept for quantum communication experiments in an uplink configuration". In: *EPJ Quantum Technology* 5.6 (2018).

[97] L. Mazzarella et al. "QUARC: Quantum Research Cubesat — A constellation for quantum communication". In: *Cryptography* 4.1 (2020).

[98] J. E. Velazco and J. S. de la Vega. "Q4 – A CubeSat mission to demonstrate omnidirectional optical communications". In: *Proceedings of the IEEE Aerospace Conference*. Big Sky, USA, 2020.

[99] C. Schieler et al. "NASA's Terabyte Infrared Delivery (TBIRD) program: Large-volume data transfer from LEO". In: *Proceedings of the 33st AIAA / USU Conference on Small Satellites*. Logan, USA, 2019.

[100] A. Freeman. "Exploring our solar system with CubeSats and SmallSats: The dawn of a new era". In: *CEAS Space Journal* 12 (2020), pp. 491–502.

[101] K. V. Mani et al. "Systems design of MARIO: Stand-alone 16U CubeSat from Earth to Mars". In: *Proceedings of the 70th International Astronautical Congress*. Washington D.C., USA, 2019.

[102] M. W. Smith et al. "On-orbit results and lessons learned from the ASTERIA space telescope mission". In: *Proceedings of the 32nd AIAA / USU Conference on Small Satellites*. Logan, USA, 2018.

[103] J. Racusin et al. "BurstCube: A CubeSat for gravitational wave counterparts". In: *Proceedings of the 35th International Cosmic Ray Conference*. Busan, Korea, 2017.

[104] T. Enoto et al. "NinjaSat: An agile CubeSat approach for monitoring of bright X-ray compact objects". In: *Space Telescopes and Instrumentation*. Vol. 11444. International Society for Optics and Photonics. SPIE, 2020.

[105] D. K. L. Oi et al. "Nanosatellites for quantum science and technology". In: *Contemporary Physics* 58 (2017), pp. 25–52.

[106] D. Devani et al. "Gravity sensing: cold atom trap onboard a 6U CubeSat". In: *CEAS Space Journal* 12 (2020), pp. 539–549.

[107] C. Underwood et al. "AAReST autonomous assembly reconfigurable space telescope flight demonstrator". In: *Proceedings of the 69th International Astronautical Congress*. Bremen, Germany, 2018.

[108] J. Bowen et al. "CubeSat Proximity Operations Demonstration (CPOD) mission update". In: *Proceedings of the IEEE Aerospace Conference*. Big Sky, USA, 2015.

[109] C. P. Mark and S. Kamath. "Review of active space debris removal methods". In: *Space Policy* 41 (2019), pp. 194–206.

[110] H. Hakima and M. R. Emami. "Deorbiter CubeSat system engineering". In: *The Journal of the Astronautical Sciences* (2020).

[111] J. P. Gonzalez-Zugasti, K. N. Otto, and J. D. Baker. "A method for architecting product platforms". In: *Research in Engineering Design* 12.2 (2000), pp. 61–72.

[112] R. Caffrey et al. "Product platform concepts applied to small satellites: A new multipurpose radio concept by AeroAstro Inc." In: *Proceedings of the 16th AIAA / USU Conference on Small Satellites*. Logan, USA, 2002.

[113] J. Kingston. "Modularity as an enabler for a more efficient commercial small satellite program". In: *Proceedings of the 17th Annual AIAA / USU Conference on Small Satellites*. Logan, USA, 2003.

[114] J. Kingston. "A modular, reconfigurable approach for a commercial small spacecraft programme". PhD thesis. College Road, Cranfield, MK43 0AL, UK: Cranfield University, 2003.

[115] J. R. Jiao, T. W. Simpson, and Z. Siddique. "Product family design and platform-based product development: A state-of-the-art review". In: *Journal of Intelligent Manufacturing* 18 (2007), pp. 5–29.

[116] M. F. Barschke. "A modular platform architecture to enable system level scalability". In: *Proceedings of the 12th IAA Symposium on Small Satellites for Earth Observation*. Berlin, Germany, 2019.

[117] S. Shirasaka and S. Nakasuka. "Realization of the concept of reasonably reliable systems engineering in the design of nano-satellites". In: *Transactions of the Japan Society for Aeronautical and Space Sciences* 10 (2012), pp. 7–12.

[118] B. Jackson. "A robust fault protection architecture for low-cost nanosatellites". In: *Proceedings of the IEEE Aerospace Conference*. Big Sky, USA, 2014.

[119] S. V. Amari and G. Dill. "Redundancy optimization problem with warm-standby redundancy". In: *Proceedings of the Annual Reliability and Maintainability Symposium*. San Jose, USA, 2010.

[120] H. Hecht. "Fault-tolerant computers for spacecraft". In: *Journal of Spacecraft and Rockets* 14.10 (1977), pp. 579–586.

[121] S. V. Amari and G. Dill. "A new method for reliability analysis of standby systems". In: *Proceedings of the Annual Reliability and Maintainability Symposium*. Fort Worth, USA, 2009.

[122] B. W. Johnson. "Fault-tolerant microprocessor-based systems". In: *IEEE Micro* 4.6 (1984), pp. 6–21.

[123] V. V. Pascual. "Design of a modular 12 U/16 U structure concept for the TUBiX20 nanosatellite platform". MA thesis. Straße des 17. Juni 135, 10623 Berlin, Germany: Technische Universiät Berlin, 2017.

[124] D. Heynderickx et al. "ESA's Space ENVironment Information System (SPENVIS): a web-based tool for assessing radiation doses and effects in spacecraft systems". In: *Proceedings of the Space Nuclear Conference*. 2005, pp. 548–552.

[125] F. Labonville, P. Charbonneau, and A. Lemerle. "A dynamo-based forecast of solar cycle 25". In: *Solar Physics* 294.6 (2019).

[126] F. Bartels. "Auslegung entfaltbarer und modularer Solarpaneele für die Mikrosatellitenplattform TUBiX20". MA thesis. Straße des 17. Juni 135, 10623 Berlin, Germany: Technische Universiät Berlin, 2020.

[127] D. G. Gilmore et al. "Thermal". In: *Space mission analysis and design*. Ed. by W. J. Larson and J. R. Wertz. 3rd ed. Torrance, USA: Microcosm Press, 1999, pp. 428–458.

[128] D. G. Gilmore, ed. *Spacecraft Thermal Control Handbook*. 2nd ed. El Segundo, USA: The Aerospace Press, 2002.

[129] J. M. Elliott. "The thermal design of the CanX-4/-5 and NEMO-AM nanosatellites". MA thesis. 27 King's College Circle, Toronto, Ontario M5S 1A1, Canada: University of Toronto, 2014.

[130] J. Rotteveel and A. Bonnema. "Thermal control issues for nano- and picosatellites". In: *Proceedings of the 57th International Astronautical Congress*. Valencia, Spain, 2006.

[131] F. Lura et al. "Experience of passive thermal control of long-term near-Earth small satellite mission". In: *Proceedings of the 9th IAA Symposium on Small Satellites for Earth Observation*. 2013, pp. 367–370.

[132] S. L. Tuttle, S. M. Barraclough, and R. Dudziak. "Advanced thermal control technologies for nano-satellites". In: *Proceedings of the 47th International Conference on Environmental Systems*. Charleston, USA, 2017.

[133] L. Yang et al. "Quasi-all-passive thermal control system design and on-orbit validation of Luojia 1-01 satellite". In: *Sensors* 19.4 (2019).

[134] J. Kühn. "Implementierung und Validierung einer thermalen Simulation für den Nanosatellitenbus TUBiX20". MA thesis. Technische Universiät Berlin, 2016.

[135] J. Kühn, M. F. Barschke, and D. Költzsch. "Development of a thermal simulation tool for nanosatellites based on commercial Finite Element Analysis software". In: *11th IAA Symposium on Small Satellites for Earth Observation*. Berlin, Germany, 2017, pp. 385–388.

[136] R. V. White and F. M. Miles. "Principles of fault tolerance". In: *Proceedings of the Applied Power Electronics Conference*. Vol. 1. 1996, pp. 18–25.

[137] AZUR SPACE Solar Power GmbH. *30% triple junction GaAs solar cell (40 mm x 80 mm)*. Data sheet. 0003429-01-01. 2016.

[138] J. K. McDermott. "Power". In: *Space mission analysis and design*. Ed. by W. J. Larson and J. R. Wertz. 3rd ed. Torrance, USA: Microcosm Press, 1999, pp. 407–427.

[139] G. Bonin, D. Sinclair, and R. E. Zee. "Peak power tracking on a nanosatellite scale: The design and implementation of digital power electronics on the SFL Generic Nanosatellite Bus". In: *Proceedings of the 23rd AIAA / USU Conference on Small Satellites*. Logan, USA, 2009.

[140] C. S. Clark and A. L. Mazarias. "Power system challenges for small satellite missions". In: *Proceedings of the Small Satellites Systems and Services Symposium*. Chia Laguna, Italy, 2006.

[141] C. J. Savage. "Thermal control of spacecraft". In: *Spacecraft systems engineering*. Ed. by P. W. Fortescue, G. G. Swinerd, and J. P. W. Stark. 4th ed. Chichester, UK: John Wiley and Sons, 2011, pp. 357–395.

[142] C. Weidner. *Materialverbund am Beispiel von FR4 und CU*. Lecture notes. July 2012.

[143] G. Kopp and J. L. Lean. "A new, lower value of total solar irradiance: Evidence and climate significance". In: *Geophysical Research Letters* 38 (2011).

[144] O. Shekoofa and E. Kosari. "Comparing the topologies of satellite electrical power subsystem based on system level specifications". In: *Proceedings of the 6th International Conference on Recent Advances in Space Technologies*. 2013, pp. 671–675.

[145] T. Esram and P. L. Chapman. "Comparison of photovoltaic array maximum power point tracking techniques". In: *IEEE Transactions on Energy Conversion* 22.2 (2007), pp. 439–449.

[146] T. Nahak and Y. Pal. "Comparison between conventional and advance maximum power point tracking techniques for photovoltaic power system". In: *Proceedings of the 7th Power India International Conference*. Bikaner, India, 2016.

[147] K. B. Chin et al. "Energy storage technologies for small satellite applications". In: *Proceedings of the IEEE* 106.3 (2018), pp. 419–428.

[148] H. Croft et al. "Cycling and low temperature performance of Li-ion cells". In: *Proceedings of the 35th Intersociety Energy Conversion Engineering Conference*. Las Vegas, USA, 2000.

[149] A. Slavinskis et al. "Flight results of ESTCube-1 attitude determination system". In: *Journal of Aerospace Engineering* 29.1 (2016).

[150] M. F. Barschke et al. "TechnoSat - Results from the first 18 months of operation". In: *Proceedings of the 12th IAA Symposium on Small Satellites for Earth Observation*. Berlin, Germany, 2019.

[151] C. Jonglez et al. "ADCS performance assessment using payload camera: lessons learned on a small satellite mission and future applications". In: *Proceedings of the 16th International Conference on Space Operations*. Online, 2021.

[152] B. Johnston-Lemke et al. "Arc-minute attitude stability on a nanosatellite: Enabling stellar photometry on the smallest scale". In: *Proceedings of the 25th Annual AIAA / USU Conference on Small Satellites*. Logan, USA, 2011.

[153] A. O. Erlank and W. H. Steyn. "Arcminute attitude estimation for CubeSats with a novel nano star tracker". In: *IFAC Proceedings Volumes* 47.3 (2014), pp. 9679–9684.

[154] T. Nguyen, K. Cahoy, and A. Marinan. "Attitude determination for small satellites with infrared Earth horizon sensors". In: *Journal of Spacecraft and Rockets* 55.6 (2018), pp. 1466–1475.

[155] S. A. Rawashdeh et al. "A stellar gyroscope for small satellite attitude determination". In: *Proceedings of the 25st AIAA / USU Conference on Small Satellites*. Logan, USA, 2012.

[156] H. C. Polat, J. Virgili-Llop, and M. Romano. "Survey, statistical analysis and classification of launched CubeSat missions with emphasis on the attitude control method". In: *Journal of Small Satellites* 5 (3 2016), pp. 513–530.

[157] A. R. Khuller et al. "Pulsed plasma thruster for multi-axis CubeSat attitude control applications". In: *Proceedings of the Joint Propulsion Conference*. Cincinnati, USA, 2018.

[158] E. G. Lightsey, T. Stevenson, and M. Sorgenfrei. "Development and testing of a 3D-printed cold gas thruster for an interplanetary CubeSat". In: *Proceedings of the IEEE* 106.3 (2018), pp. 379–390.

[159] S. Romero-Diez et al. "A single-use microthruster concept for small satellite attitude control in formation-flying applications". In: *Aerospace* 5.4 (2018).

[160] S. Grau et al. "Control of an over-actuated spacecraft using a combination of a fluid actuator and reaction wheels". In: *Proceedings of the 70th International Astronautical Congress*. Washington D.C., USA, 2019.

[161] V. Lappas, W. H. Steyn, and C. Underwood. "Design and testing of a control moment gyroscope cluster for small satellites". In: *Journal of Spacecraft and Rockets* 42.4 (2005), pp. 729–739.

[162] R. Votel and D. Sinclair. "Comparison of control moment gyros and reaction wheels for small Earth-observing satellites". In: *Proceedings of the 26th Annual AIAA / USU Conference on Small Satellites*. Logan, USA, 2012.

[163] M. Ovchinnikov et al. "Attitude control for the first Swedish nanosatellite MUNIN". In: *Acta Astronautica* 46 (2000), pp. 319–326.

[164] M. F. Barschke, F. Baumann, and K. Brieß. "BEESAT-3: Passive attitude control for directed radio transmission on a single-unit CubeSat". In: *Proceedings of the Nano-Satellite Symposium*. Nagoya, Japan, 2012.

[165] G. Falbel, J. Puig-Suari, and A. Peczalski. "Sun oriented and powered, 3 axis and spin stabilized CubeSats". In: *Proceedings of the IEEE Aerospace Conference*. Big Sky, USA, 2002.

[166] T. Neilsen et al. "DICE: challenges of spinning CubeSats". In: *Proceedings of the 37th Annual AAS Guidance and Control Conference*. Breckenridge, USA, 2014.

[167] K. Gordon and M. F. Barschke. "A new concept of software architecture for a flexible attitude determination and control of nanosatellites". In: *Proceedings of the 65th International Astronautical Congress*. Jerusalem, Israel, 2015.

[168] K. Gordon. "A flexible attitude control system for three-axis stabilized nanosatellites". PhD thesis. Straße des 17. Juni 135, 10623 Berlin, Germany: Technische Universität Berlin, 2018.

[169] J. Bos et al. "ACMS FDIR system for the Herschel / Planck satellites". In: *Proceedings of the 6th International ESA Conference on Guidance, Navigation and Control Systems*. Loutraki, Greece, 2005.

[170] Z. Ismail and R. Varatharajoo. "A study of reaction wheel configurations for a 3-axis satelliteattitude control". In: *Advances in Space Research* 45.6 (2010), pp. 750–759.

[171] Zarm Technik AG. *Magnetic Torquers for Spacecraft Attitude Control*. Data sheet. 2010.

[172] J. Bouwmeester and J. Guo. "Survey of world wide pico- and nanosatellite missions, distributions and subsystem technology". In: *Acta Astronautica* 67.7-8 (2010), pp. 854–862.

[173] Consultative Committee for Space Data Systems. *TM space data link protocol*. Standard CCSDS 132.0-B-3. Washington, DC, USA, 2021.

[174] L. M. Bradbury et al. "NORSAT-2: Enabling advanced maritime communication with VDES". In: *Proceedings of the 31st AIAA / USU Conference on Small Satellites*. Logan, USA, 2017.

[175] M. A. Fernandez et al. "A game-changing radio communication architecture for cube/nano-satellites". In: *Proceedings of the 65th International Astronautical Congress*. Jerusalem, Israel, 2015.

[176] T. S. Rose et al. "Optical communications downlink from a 1.5U CubeSat: OCSD program". In: *Proceedings of the International Conference on Space Optics*. Chania, Greece, 2018.

[177] B. Jackson. "A robust fault protection strategy for a COTS-based spacecraft". In: *Proceedings of the IEEE Aerospace Conference*. Big Sky, USA, 2007.

[178] J. Eickhoff. *Onboard computers, onboard software and satellite operations*. 1st ed. Heidelberg, Germany: Springer International Publishing, 2012.

[179] M. F. Barschke and K. Gordon. "Enabling flexible payload management through modularity". In: *Proceedings of the 65th International Astronautical Congress*. Jerusalem, Israel, 2015.

[180] J. Arlas and S. Spangelo. "GPS results for the Radio Aurora Explorer II CubeSat Mission". In: *Proceedings of the 51st AIAA Aerospace Sciences Meeting*. Grapevine, USA, 2013.

[181] J. W. Gangestad, B. S. Hardy, and D. A. Hinkley. "Operations, orbit determination, and formation control of the AeroCube-4 CubeSats". In: *Proceedings of the 27th Annual AIAA / USU Conference on Small Satellites*. Logan, USA, 2013.

[182] G. Kirchner et al. "Laser ranging to nano-satellites". In: *Proceedings of the 18th International Workshop on Laser Ranging*. Fujiyoshida, Japan, 2013.

[183] P. Wang et al. "kHz SLR application on the attitude analysis of TechnoSat". In: *Proceedings of the 21st International Workshop on Laser Ranging*. Canberra, Australia, 2018.

[184] C. Foster, H. Hallam, and J. Mason. "Orbit determination and differential-drag control of Planet Labs CubeSat constellations". In: *Proceedings of the AIAA Astrodynamics Specialist Conference*. Vale, USA, 2015.

[185] N. H. Roth et al. "Fight results from the CanX-4 and CanX-5 formation flying mission". In: *Proceedings of the Small Satellites Systems and Services Symposium*. Valetta, Malta, 2016.

[186] D. Krejci and P. Lozano. "Space propulsion technology for small spacecraft". In: *Proceedings of the IEEE* 106.3 (2018), pp. 362–378.

[187] J. C. Pascoa, O. Teixeira, and G. Filipe. "A review of propulsion systems for CubeSats". In: *Proceedings of the ASME 2018 International Mechanical Engineering Congress*. Pittsburgh, USA, 2018.

[188] P. E. Skanke and R. Birkeland. "CubeSat propulsion-expanding the possibilities of the affordable space platform". In: *Proceedings of the Small Satellites Systems and Services Symposium*. Sorrento, Italy, 2018.

[189] D. C. Sharp et al. “Challenges and solutions for embedded and networked aerospace software systems”. In: *Proceedings of the IEEE* 98.4 (2010), pp. 621–634.

[190] K. Gordon et al. “Multi-mission software development for small spacecraft”. In: *Proceedings of the 12th IAA Symposium on Small Satellites for Earth Observation*. Berlin, Germany, 2019.

[191] A. Ferrari and A. Sangiovanni-Vincentelli. “System design: traditional concepts and new paradigms”. In: *Proceedings of the IEEE International Conference on Computer Design: VLSI in Computers and Processors*. Austin, USA, 1999.

[192] D. McComas, J. Wilmot, and A. Cudmore. “The Core Flight System (cFS) community: Providing low cost solutions for small spacecraft”. In: *Proceedings of the 30th AIAA / USU Conference on Small Satellites*. Logan, USA, 2016.

[193] F. Dannemann and F. Greif. “Software platform of the DLR Compact Satellite series”. In: *Proceedings of the Small Satellites Systems and Services Symposium*. Mallorca, Spain, 2014.

[194] B. Bätz. “Design and implementation of a spacecraft flight software framework”. PhD thesis. Pfaffenwaldring 29, 70569 Stuttgart, Germany: University of Stuttgart, 2020.

[195] S. Gaisser et al. “In-flight experience with an object-oriented flight software”. In: *Proceedings of the Small Satellites Systems and Services Symposium*. Sorrento, Italy, 2018.

[196] S. Kobayashi et al. “Software development framework for small satellite onboard computers”. In: *Transactions of the Japan Society for Aeronautical and Space Sciences* 12.29 (2014), pp. 1–6.

[197] F. Baumann et al. “Flight experience with the picosatellite BEESAT”. In: *Proceedings of the 59th German Aerospace Congress*. Hamburg, Germany, 2010.

[198] F. Baumann et al. “TUBIN – a nanosatellite mission with infrared imager payload”. In: *Proceedings of the Small Satellites Systems and Services Symposium*. Portorož, Slovenia, 2012.

[199] L. J. Hansen, R. W. Hosken, and C. H. Pollock. “Spacecraft computer systems”. In: *Space mission analysis and design*. Ed. by W. J. Larson and J. R. Wertz. 3rd ed. Torrance, USA: Microcosm Press, 1999, pp. 645–684.

[200] B. Palmintier et al. "A distributed computing architecture for small satelliteand multi-spacecraft missions". In: *Proceedings of the 16th Annual AIAA / USU Conference on Small Satellites*. Logan, USA, 2002.

[201] T. Pitterá and M. D'Errico. "Multi-purpose modular plug and play architecture for space systems: Design, integration and testing". In: *Acta Astronautica* 69 (2011), pp. 629–643.

[202] N. Navarathinam et al. "X50: Reducing cost and schedule while being modular and adaptable for RemoveDEBRIS". In: *Proceedings of the 66th International Astronautical Congress*. Jerusalem, Israel, 2015.

[203] J. Bouwmeester, M. Langer, and E. Gill. "Survey on the implementation and reliability of CubeSat electrical bus interfaces". In: *CEAS Space Journal* 9.2 (2017), pp. 163–173.

[204] K. Janschek and A. Braun. "Application of industrial CAN bus technology for LEO-satellites". In: *Acta Astronautica* 46.2-6 (2000), pp. 313–317.

[205] G. Casarosa et al. "Characterization of the EMC performances of the CAN bus in a typical system bus architecture for small satellites". In: *Proceedings of the 9th EUROMICRO Conference on Digital System Design*. Dubrovnik, Croatia, 2006.

[206] A. M. Woodroffe and P. Madle. "Application and experience of CAN as a low cost OBDH bus system". In: *Proceedings of Data Systems in Aeropspace*. Nice, France, 2004.

[207] P. Rathsman et al. "SMART-1: Development and lessons learnt". In: *Acta Astronautica* 57 (2005), pp. 455–468.

[208] M. Khurram, S. Muhammad, and Y. Zaidi. "CAN as a spacecraft communication bus in LEO satellite mission". In: *Proceedings of 2nd International Conference on Recent Advances in Space Technologies*. Istanbul, Turkey, 2005.

[209] T. Bretschneider. "Singapore's Satellite Mission X-Sat". In: *Proceedings of the 4th IAA Symposium on Small Satellites for Earth Observation*. Berlin, Germany, 2003.

[210] M. Lehmann. "Eine Highspeed-Datenschnittstelle zur Anbindung optischer Nutzlasten an den TUBiX20 Nanosatellitenbus". MA thesis. Straße des 17. Juni 135, 10623 Berlin, Germany: Technische Universiät Berlin, 2015.

[211] E. Webb. "Ethernet for space flight applications". In: *Proceedings of the Aerospace Conference*. Vol. 4. 2002, pp. 1927–1934.

[212] J. Arrigo et al. “Overcoming design challenges for a radiation-tolerant, radiation-hardened fast Ethernet interface”. In: *Proceedings of the IEEE Aerospace Conference*. Big Sky, USA, 2013.

[213] A. T. Loveless. “On TTEthernet for integrated fault-tolerant spacecraft networks”. In: *Proceedings of the AIAA SPACE Conference*. Pasadena, USA, 2015.

[214] R. Burt. “Distributed electrical power system in CubeSat applications”. MA thesis. Logan, UT 84322, USA: Utah State University, 2011.

[215] N. Ivkovic et al. “Verifying worst case delays in controller area network”. In: *Proceedings of the International GI/ITG Conference on Measurement, Modelling, and Evaluation of Computing Systems and Dependability and Fault Tolerance*. 2012, pp. 91–105.

[216] G. Leen and D. Heffernan. “Time-triggered controller area network”. In: *Computing Control Engineering Journal* 12.6 (2001), pp. 245–256.

[217] L. Zander. “Entwicklung der zentralen Avionik-Einheit für die skalierbare Satellitenfamilie TUBiX20”. MA thesis. Straße des 17. Juni 135, 10623 Berlin, Germany: Technische Universiät Berlin, 2019.

[218] B. Johnston-Lemke et al. “Modular power system: Enabling scalable missions for the 1 W to 1 kW range”. In: *Proceedings of the 27th Annual AIAA / USU Conference on Small Satellites*. Logan, USA, 2013.

[219] S. Notani and S. Bhattacharya. “Flexible electrical power system controller design and battery integration for 1 U to 12 U CubeSats”. In: *Proceedings of the IEEE Energy Conversion Congress and Exposition*. Phoenix, USA, 2011.

[220] M. F. Barschke et al. “FDIR approach of a modular satellite platform architecture”. In: *Proceedings of the 66th International Astronautical Congress*. Guadalajara, Mexico, 2016.

[221] F. Buschmann et al. “Design patters”. In: *Pattern-oriented software architecture - A system of patters*. 1st ed. Chichester, UK: John Wiley and Sons, 1995. Chap. 3, pp. 221–343.

[222] M. F. Barschke, K. Großekatthöfer, and S. Montenegro. “Implementation of a nanosatellite on-board software based on building blocks”. In: *Proceedings of the Small Satellites Systems and Services Symposium*. Porto Petro, Spain, 2014.

[223] K. Gordon, M. Lehmann, and M. F. Barschke. "Flexible low-cost verification of attitude determination and control systems". In: *Proceedings of the 11th IAA Symposium on Small Satellites for Earth Observation*. 2017, pp. 405–408.

[224] K. Gordon, A. Graf, and M. F. Barschke. "Practical experience in using continuous integration within the development of nanosatellite software". In: *Proceedings of the 10th IAA Symposium on Small Satellites for Earth Observation*. 2015, pp. 191–194.

[225] K.-S. Klemich and J. Eickhoff. "The FLP platform operability". In: *The FLP microsatellite platform: Flight operations manual*. Ed. by J. Eickhoff. 1st ed. Heidelberg, Germany: Springer International Publishing, 2015.

[226] M. Tipaldi and B. Bruenjes. "Spacecraft health monitoring and management systems". In: *Proceedings of the IEEE Workshop an Metrology for Aerospace*. Benevento, Italy, 2014.

[227] X. Olive. "FDI(R) for satellite at Thales Alenia Space how to deal with high availability and robustness in space domain?" In: *Proceedings of the Conference on Control and Fault-Tolerant Systems*. 2010, pp. 837–842.

[228] A. Zolghadri. "Advanced model-based FDIR techniques for aerospace systems: Today challenges and opportunities". In: *Progress in Aerospace Sciences* 53 (2012), pp. 18–29.

[229] A. Wander and R. Förstner. "Innovative fault detection, isolation and recovery strategies on-board spacecraft: State of the art and research challanges". In: *Proceedings of the 61st German Aerospace Congress*. Berlin, Germany, 2012.

[230] J.-G. Meß, F. Dannemann, and F. Greif. "Techniques of artificial intelligence for space applications - A survey". In: *Proceedings of the European Workshop on On-Board Data Processing*. Noordwijk, The Netherlands, 2019.

[231] J. Lian-Xiang, X. Ming-Rui, and C. Zhan-Guo. "A fault detection method based on BIT for satellite avionics". In: *Applied Mechanics and Mechatronics Automation* 182 (2012), pp. 431–435.

[232] J. Lian-Xiang et al. "Fault Detection, isolation and recovery design for micro-satellites". In: *Proceedings of the 6th International Conference on Instrumentation and Measurement, Computer, Communication and Control*. 2016, pp. 380–383.

[233] P. von Keiser. "Entwurf und Implementierung der Software des Energieversorgungssystems eines einfehlertoleranten Nanosatellitenbusses". MA thesis. Straße des 17. Juni 135, 10623 Berlin, Germany: Technische Universiät Berlin, 2016.

[234] M. F. Barschke and K. Gordon. "A generic systems architecture for a single-failure tolerant nanosatellite platform". In: *Proceedings of the 64th International Astronautical Congress*. Toronto, Canada, 2014.

[235] J. A. Townsend et al. "Effects of a distributed computing architecture on the Emerald Nanosatellite development process". In: *Proceedings of the 14th Annual AIAA / USU Conference on Small Satellites*. Logan, USA, 2000.

[236] N. Peccia et al. "Common EGSE (Electrical Ground Support Equipment) and MCS (Mission Control System) for ESA Herschel / Planck missions". In: *Proceedings of the 7th International Conference on Space Operations*. Houston, USA, 2002.

[237] H. Wiegmann, J. Consiglio, and B. Destrez. "Use of a common solution for EGSE and satellite operations". In: *Proceedings of the 10th International Conference on Space Operations*. Heidelberg, Germany, 2008.

[238] Y. Huh and J.-Y. Choi. "The Common Ground System for both satellite ground test and on-orbit operations". In: *Proceedings of the 13th International Conference on Space Operations*. Pasadena, USA, 2014.

[239] M. Niézette, N. Mecredy, and M. Götzelmann. "Reducing the gap from satellite AIT to operations". In: *Proceedings of the 14th International Conference on Space Operations*. Daejeon, Korea, 2016.

[240] M. Battelino and C. Svärd. "RAMSES - A modern and flexible checkout and operational ground system for small satellite projects". In: *Proceedings of the 12th International Conference on Space Operations*. Stockholm, Sweden, 2012.

[241] P. Werner et al. "Modular support software for nanosatellites". In: *Proceedings of the 10th IAA Symposium on Small Satellites for Earth Observation*. 2015, pp. 211–214.

[242] M. Starke. "Entwurf und Implementierung eines Selbstdiagnosesystems für die Nanosatelliten-Plattform TUBiX20". MA thesis. Straße des 17. Juni 135, 10623 Berlin, Germany: Technische Universiät Berlin, 2016.

[243] M. Starke, M. F. Barschke, and P. von Keiser. "A modular hardware diagnosis framework for small spacecraft". In: *Proceedings of the 69th International Astronautical Congress*. Bremen, Germany, 2018.

[244] M. F. Barschke et al. "Initial orbit results from the TUBiX20 platform". In: *Proceedings of the 69th International Astronautical Congress*. Bremen, Germany, 2018.

[245] K. Gordon, M. F. Barschke, and P. Werner. "Upgrading TUBiX20 - bringing TechnoSat flight experience into the TUBIN mission". In: *Proceedings of the Small Satellites Systems and Services Symposium*. Sorrento, Italy, 2018.

[246] L. Grunwaldt, R. Neubert, and M. F. Barschke. "Optical tests of a large number of small COTS cubes". In: *Proceedings of the 20th International Workshop on Laser Ranging*. Potsdam, Germany, 2016.

[247] W. Frese et al. "Design and on-orbit experience of reaction wheels for small satellites". In: *Proceedings of the 33st AIAA / USU Conference on Small Satellites*. Logan, USA, 2019.

[248] G. B. Palmerini and F. Pizzirani. "Design of the radiation shielding for a microsatellite". In: *Acta Astronautica* 50 (2002), pp. 159–166.

[249] G. D. Rai. *Solar Energy Utilisation*. 1st ed. Delhi, India: Khanna Publishers, 1995.

[250] Z. Yoon et al. "Fault tolerant attitude control system of OOV-TET satellite – Design and test results". In: *Proceedings of the Small Satellites Systems and Services Symposium*. Madeira, Portugal, 2010.

[251] J. Bartholomäus, M. F. Barschke, and M. Lehmann. "The TUBIN mission within the context of present and future satellite-based fire detection systems". In: *Proceedings of the 12th IAA Symposium on Small Satellites for Earth Observation*. Berlin, Germany, 2019.

[252] J. Bartholomäus et al. "A last-minute upgrade: Rapid integration of an opportunity payload into the TUBIN mission". In: *Proceedings of the 34th AIAA / USU Conference on Small Satellites*. Online, 2020.

[253] K. Gordon, M. F. Barschke, and P. Werner. "From TechnoSat to TUBIN – performance upgrade for the TUBiX20 microsatellite platform based on flight experience". In: *CEAS Space Journal* 12 (2020), pp. 515–525.

[254] J. G. Pausas and V. R. Vallejo. "The role of fire in European Mediterranean ecosystems". In: *Remote sensing of large wildfires in the European Mediterranean basin*. Ed. by E. Chuvieco. Berlin, Germany: Springer, 1999. Chap. 2, pp. 3–15.

[255] M. Burke et al. "The changing risk and burden of wildfire in the United States". In: *Proceedings of the National Academy of Sciences* 118.2 (2021).

[256] F. Robinne et al. "Scientists' warning on extreme wildfire risks to water supply". In: *Hydrological Processes* (2021).

[257] J. T. Abatzogloua and A. P. Williams. "Impact of anthropogenic climate change on wildfire across western US forests". In: *Proceedings of the National Academy of Sciences* 113.42 (2016), pp. 11770–11775.

[258] J. E. Holloway et al. "Impact of wildfire on permafrost landscapes: A review of recent advances and future prospects". In: *Permafrost and Periglacial Processes* 31 (2020), pp. 371–382.

[259] S. M. Holm, M. D. Miller, and J. R. Balmes. "Health effects of wildfire smoke in children and public health tools: a narrative review". In: *Journal of Exposure Science and Environmental Epidemiology* 31 (2021), pp. 1–20.

[260] N. Mietkiewicz et al. "In the line of fire: Consequences of human-ignited wildfires to homes in the U.S. (1992–2015)". In: *Fire* 3.3 (2020), pp. 629–643.

[261] P. Barmpoutis et al. "A review on early forest fire detection systems using optical remote sensing". In: *Sensors* 20.22 (2020).

[262] D. M. Szpakowski and J. L. R. Jensen. "A review of the applications of remote sensing in fire ecology". In: *Remote Sensing* 11.22 (2019).

[263] L. Hua and G. Shao. "The progress of operational forest fire monitoring with infrared remote sensing". In: *Journal of Forestry Research* 28 (2017), pp. 215–229.

[264] C. Justice et al. "The MODIS fire products". In: *Remote Sensing of Environmen* 83.1-2 (2002), pp. 244–262.

[265] L. Giglio et al. "Active fire detection and characterization with the advanced spaceborne thermal emission and reflection radiometer (ASTER)". In: *Remote Sensing of Environmen* 112.6 (2008), pp. 3055–3063.

[266] D. Stroppiana, S. Pinnock, and J.-M. Gregoire. "The global fire product: Daily fire occurrence from April 1992 to December 1993 derived from NOAA AVHRR data". In: *International Journal of Remote Sensing* 21.6-7 (2000), pp. 1279–1288.

[267] B. Zhukov et al. "Detection and analysis of high-temperature events in the BIRD mission". In: *Acta Astronautica* 56.1-2 (2005), pp. 65–71.

[268] E. Lorenz. "Thermal remote sensing with small satellites: BIRD, TET and the next generation BIROS". In: *Thermal infrared remote sensing*. Ed. by C. Kuenzer and S. Dech. 1st ed. Dordrecht, Netherlands: Springer, 2013. Chap. 8, pp. 149–176.

[269] E. Lorenz et al. "Remote sensing of high temperature events by the FireBird mission". In: *The International Archives of the Photogrammetry, Remote Sensing and Spatial Information Sciences* XL-7/W3 (2015), pp. 461–467.

[270] P. W. Kruse. "Principles of uncooled infrared focal plane arrays". In: *Uncooled infrared imaging arrays and systems*. Ed. by P. W. Kruse and D. D. Skatrud. San Diego, USA: Academic Press, 1997. Chap. 2, pp. 17–44.

[271] M. Kohin and N. R. Butler. "Performance limits of uncooled VOx microbolometer focal plane arrays". In: *Infrared Technology and Applications XXX*. Ed. by B. F. Andresen and G. F. Fulop. Vol. 5404. SPIE, 2004, pp. 447–453.

[272] M. Kimata. "Uncooled infrared focal plane arrays". In: *Transactions on Electrical and Electronic Engineering* 13.1 (2018), pp. 4–12.

[273] B. Oswald-Tranta, M. Sorger, and P. O'Leary. "Motion deblurring of infrared images from a microbolometer camera". In: *Infrared Physics and Technology* 53 (2010), pp. 274–279.

[274] M. Sakai et al. "On-orbit performance of the Compact Infrared Camera (CIRC) onboard ALOS-2". In: *Proceedings of SPIE Remote Sensing*. Toulouse, France, 2015.

[275] H. Tonooka et al. "In-flight radiometric calibration of Compact Infrared Camera (CIRC) instruments onboard ALOS-2 satellite and International Space Station". In: *Remote Sensing* 12.1 (2020).

[276] L. N. Phong et al. "Spaceborne linear arrays of 512x3 microbolometers". In: *Reliability, Packaging, Testing, and Characterization of MOEMS/MEMS and Nanodevices XII*. Ed. by R. Ramesham and H. R. Shea. Vol. 8614. SPIE, 2013.

[277] T. Fukuhara et al. "Detection of small wildfire by thermal infrared camera with the uncooled microbolometer array for 50-kg class satellite". In: *IEEE Transactions on Geoscience and Remote Sensing* 55.8 (2017), pp. 4314–4324.

[278] R. Hartono et al. "Performance of thermal imager on LAPAN-A3/IPB satellite compare with thermal band Landsat imager". In: *IOP Conference Series: Earth and Environmental Science* 284 (2018).

[279] D. W. Pack, C. M. Coffman, and J. R. Santiago. "A year in space for the CUbesat MULtispectral Observing System: CUMULOS". In: *Proceedings of the 33st AIAA / USU Conference on Small Satellites*. Logan, USA, 2019.

[280] S. Rogers et al. "Phoenix: A CubeSat mission to study the impact of urban heat islands within the U.S." In: *Proceedings of the 34th AIAA / USU Conference on Small Satellites*. Online, 2020.

[281] J. Bartholomäus. "Development of a single-channel fire detection algorithm for the nanosatellite mission TUBIN". MA thesis. Straße des 17. Juni 135, 10623 Berlin, Germany: Technische Universiät Berlin, 2017.

[282] J. Bartholomäus, M. F. Barschke, and M. Lehmann. "Development of a single-channel wildfire detection algorithm for the TUBIN mission". In: *Proceedings of the 69th International Astronautical Congress*. Bremen, Germany, 2018.

[283] M. Abrams. "The Advanced Spaceborne Thermal Emission and Reflection Radiometer (ASTER): Data products for the high spatial resolution imager on NASA's Terra platform". In: *International Journal of Remote Sensing* 21.5 (2000), pp. 847–859.

[284] J. A. Banatao et al. "Realtime dynamic target pointing using onboard image processing of cloud cover for Earth observation microsatellites". In: *Proceedings of the 12th IAA Symposium on Small Satellites for Earth Observation*. Berlin, Germany, 2019.

[285] K. Gwozdecky. "Methodologies for development of a modular wiring harness for use in small satellite constellations". In: *Proceedings of the 34th AIAA / USU Conference on Small Satellites*. Online, 2020.

[286] Sinclair Interplanetary. *Microsatellite reaction wheels (RW3-0.06)*. Data sheet. Version Rev 2019a. 2019.

[287] Nord-Lock Group. *Nord-Lock wedge-locking washers*. Data sheet. 2020.

[288] M. Konaka et al. "Preliminary thermal design for the small satellite mission QUEEN, carrying an optical atomic frequency reference". In: *Proceedings of the 9th Nano-Satellite Symposium*. Fukui, Japan, 2019.

[289] U. Renner. "Flight Results of TUBSAT-A". In: *Proceedings of the 42nd International Astronautical Congress*. Montreal, Canada, 1991.

[290] U. Renner, B. Lübke-Ossenbeck, and P. Butz. "TUBSAT, low cost access to space technology". In: *Proceedings of the 7th Annual AIAA / USU Conference on Small Satellites*. Logan, USA, 1993.

[291] R. Schulte. "TUBSAT-N, an ultra low cost global communication nanosatellite system". In: *Air and Space* 2.5 (2000), pp. 80–83.

[292] S. Roemer and U. Renner. "Flight experience with the micro satellite MAROC-TUBSAT". In: *Proceedings of the 54th International Astronautical Congress*. Bremen, Germany, 2003.

[293] R. Triharjanto et al. "LAPAN-TUBSAT: Micro-satellite platform for surveillance & remote sensing". In: *Proceedings of the Small Satellites Systems and Services Symposium*. La Rochelle, France, 2004.

[294] S. Trowitzsch, F. Baumann, and K. Brieß. "BEESAT-2 – A picosatellite demonstrating three-axis attitude control using reaction wheels". In: *Proceedings of the 65th International Astronautical Congress*. Toronto, Canada, 2014.

[295] M. F. Barschke, F. Baumann, and K. Brieß. "BEESAT-3: A picosatellite developed by students". In: *Proceedings of the 61st German Aerospace Congress*. Berlin, Germany, 2012.

[296] M. F. Barschke, P. Werner, and S. Kapitola. "BEESAT-3 commissioning – better late than never". In: *Proceedings of the 69th International Astronautical Congress*. Bremen, Germany, 2018.

[297] S. Kapitola, S. Weiß, and K. Brieß. "Flight Experience and Operations with the CubeSat BEESAT-4". In: *Proceedings of the 11th IAA Symposium on Small Satellites for Earth Observation*. Berlin, Germany, 2017.

[298] S. Kapitola, S. Grau, and S. Weiß. "Automated operations of BEESAT-9: A CubeSat with a fluid-dynamic actuator and GPS receiver". In: *Proceedings of the 12th IAA Symposium on Small Satellites for Earth Observation*. Berlin, Germany, 2019.

[299] F. Baumann et al. "A Picosatellite Swarm for Technology Demonstration". In: *Proceedings of the 69th International Astronautical Congress*. Adelaide, Australia, 2017.

[300] S. Weiß et al. "NanoFF: A 2 U-CubeSat formation flight mission". In: *Proceedings of the 70th International Astronautical Congress*. Washington D.C., USA, 2019.

[301] *CubeSat platforms*. www.endurosat.com/products/#cubesat-platforms. Accessed: 2021-01-02.

[302] *CubeSat platforms*. www.isispace.nl/cubesat-platforms. Accessed: 2020-12-31.

[303] *A revolution in space technology*. www.open-cosmos.com/satellites. Accessed: 2021-01-02.

[304] *6U platform*. gomspace.com/6u-platform.aspx. Accessed: 2021-01-02.

[305] *CubeSat platforms*. www.adcolemai.com/small-satellites. Accessed: 2021-01-02.

[306] *Nanosatellite*. www.hemeria-group.com/en/nanosatellite. Accessed: 2021-01-02.

[307] *Apogee Small Satellite Bus*. www.inovor.com.au/space-technology/bus-platform. Accessed: 2020-12-31.

[308] *Microsatellite Platform Auriga*. eng.dauria.ru/category/products/platforms. Accessed: 2020-12-31.

[309] *Chameleon 6U to 27U OMSR Bus*. www.spaceinformationlabs.com/products/chameleon. Accessed: 2020-12-31.

[310] *Satellite Platforms*. www.utias-sfl.net/?page_id=89. Accessed: 2020-12-31.

[311] *EPIC spacecraft*. www.aac-clyde.space/epic-spacecraft. Accessed: 2020-12-31.

[312] *What We Sell*. www.argotec.it/online/what-we-sell. Accessed: 2020-12-31.

[313] *Space products*. www.ohb-sweden.se/space-products. Accessed: 2020-12-31.

[314] *Small sats. Big missions*. www.lockheedmartin.com/en-us/products/satellite.html. Accessed: 2020-12-31.

[315] *Small sats. Big missions.* nanoavionics.com/nanosatellite-buses. Accessed: 2021-01-01.

[316] *MinoSpace*. satsearch.co/suppliers/minospace/product. Accessed: 2021-01-01.

[317] *Nadir Platform*. www.imtsrl.it/nadir.html. Accessed: 2021-01-01.

[318] *Spacecraft*. www.spacequest.com/spacecraft. Accessed: 2021-01-01.

[319] *Spacecraft*. sputnix.ru/en/satellites/cubesat-platforms. Accessed: 2021-01-02.

[320] *Microsatellite Platform Auriga*. www.orbitalsystems.de/cubesat-missions. Accessed: 2021-01-02.

[321] *Small satellites*. www.sitael.com/space/small-satellites/systems. Accessed: 2021-01-02.

[322] *SAT12U*. hyperiontechnologies.nl/products/sat12u. Accessed: 2021-01-02.

[323] *SAT12U*. www.sncorp.com/what-we-do/satellite-solutions-space-mission-systems. Accessed: 2021-01-02.

[324] *Satellite Platforms*. www.sstl.co.uk/what-we-do/satellite-platforms. Accessed: 2021-01-02.

[325] *Platforms*. www.tyvak.com/platforms. Accessed: 2021-01-02.

[326] *Spacecraft*. www.bluecanyontech.com/spacecraft. Accessed: 2020-12-31.

[327] AZUR SPACE Solar Power GmbH. *28% triple junction GaAs solar cell (40 mm x 80 mm)*. Data sheet. 00002490-00-03. 2016.

[328] AZUR SPACE Solar Power GmbH. *30% triple junction GaAs solar cell (40 mm x 70 mm)*. Data sheet. 0006050-01-00. 2019.

[329] AZUR SPACE Solar Power GmbH. *30% triple junction GaAs solar cell (60 mm x 120 mm)*. Data sheet. 0003422-02-02. 2016.

[330] AZUR SPACE Solar Power GmbH. *30% triple junction GaAs solar cell (80 mm x 80 mm)*. Data sheet. 0003421-01-02. 2016.

[331] AZUR SPACE Solar Power GmbH. *32% triple junction GaAs solar cell (40 mm x 80 mm)*. Data sheet. 0005979-01-00. 2019.

[332] CESI S.p.A. *Triple-junction solar cell for space applications (CTJ30)*. Data sheet. 2020.

[333] CESI S.p.A. *Low cost triple-junction solar cell for space applications (CTJ–LC)*. Data sheet. 2020.

[334] CESI S.p.A. *Thin triple-junction solar cell for space applications (CTJ30 – Thin)*. Data sheet. 2020.

[335] SolAero Technologies Corp. *IMM-α space solar cell*. Data sheet. 2018.

[336] Shanghai Institute of Space Power-sources. *30% triple junction GaAs solar cell assembly*. Data sheet. 2018.

[337] Shanghai Institute of Space Power-sources. *32% triple junction GaAs solar cell assembly*. Data sheet. 2018.

[338] Spectrolab, Inc. *Ultra Triple Junction (UTJ)*. Data sheet. 2018.

[339] Spectrolab, Inc. *XTE-SF (standard fluence) space qualified triple junction solar cell*. Data sheet. 2019.

[340] Spectrolab, Inc. *30.7% XTJ Prime space qualified triple junction solar cell*. Data sheet. 2018.

[341] SolAero Technologies Corp. *ZTJ space solar cell*. Data sheet. 2018.

[342] SolAero Technologies Corp. *ZTJ-Ω space solar cell*. Data sheet. 2018.

[343] SolAero Technologies Corp. *Z4J space solar cell*. Data sheet. 2019.

[344] Sodern. *Auriga last innovative star tracker*. Data sheet. Version 10/2017. 2017.

[345] EICAS Automazione S.p.A. *ARGO 1.0 multicamera star tracker*. Data sheet. 2019.

[346] CubeSpace. *Star trackers*. Data sheet. 2019.

[347] KU Leuven. *KU Leuven star tracker*. Data sheet. 2019.

[348] Adcole Maryland Aerospace, LLC. *MAI-SS space sextant*. Data sheet. 2018.

[349] Space Micro Inc. *MIST miniature integrated star tracker*. Data sheet. Version Rev 5. 2021.

[350] Blue Canyon Technologies. *Star trackers*. Data sheet. 2019.

[351] TY-Space Technology Ltd. *Nano star tracker NST-3*. Data sheet. 2019.

[352] TY-Space Technology Ltd. *Nano star tracker NST-4*. Data sheet. 2019.

[353] TY-Space Technology Ltd. *Pico star tracker*. Data sheet. 2019.

[354] Hyperion Technologies B.V. *ST200 star tracker*. Data sheet. Version V2.0. 2019.

[355] Hyperion Technologies B.V. *ST400 star tracker*. Data sheet. Version V2.0. 2019.

[356] Space Inventor. *STAR-T3 accurate star-tracker unit*. Data sheet. 2018.

[357] Sinclair Interplanetary. *Second generation star tracker (ST-16RT2)*. Data sheet. Version Rev 2019a. 2019.

[358] VECTRONIC Aerospace GmbH. *Star tracker VST-68M*. Data sheet. 2019.

[359] Lens Research & Development. *BiSon64-ET sunsensor product specification document*. Data sheet. 2018.

[360] GomSpace A/S. *NanoSense fine sun sensor*. Data sheet. Version 2.5. DS 1018157. 2019.

[361] Bradford Space B.V. *Mini fine Sun sensor*. Data sheet. Version JAN.2017. 2017.

[362] Solar MEMS Technologies S.L. *nanoSSOC-A60 Sun sensor for nano-satellites analog interface*. Data sheet. 2017.

[363] Solar MEMS Technologies S.L. *nanoSSOC-D60 Sun sensor for nano-satellites digital interface*. Data sheet. 2017.

[364] NewSpace Systems (Pty) Ltd. *Sun sensor*. Data sheet. Version 8a. 2018.

[365] Hyperion Technologies B.V. *SS200 Sun sensor*. Data sheet. Version V2.0. 2019.

[366] Sinclair Interplanetary. *SS-411 two-axis digital Sun sensors*. Data sheet. Version Rev 2011a. 2011.

[367] Solar MEMS Technologies S.L. *SSOC-A60 Sun sensor for nano-satellites with analog interface*. Data sheet. 2017.

[368] Solar MEMS Technologies S.L. *SSOC-D60 Sun sensor for nano-satellites with digital interface*. Data sheet. 2016.

[369] German Orbital Systems GmbH. *Sun sensor*. Data sheet. 2017.

[370] Meisei Electric Co., Ltd. *3-axis magnetometer for small satellite*. Data sheet. Version June 2018. MSPA4-047. 2018.

[371] Zarm Technik AG. *Magnetometer AMR-RS422-LV*. User's manual. Version 4. GEN-TN-ZAR-AMR-01. 2015.

[372] Texas Instruments. *DRV425 fluxgate magnetic-field sensor*. Data sheet. SBOS729A. 2016.

[373] Stefan Mayer Instruments. *Magnetic field sensor FLC3-70*. Data sheet. 2019.

[374] Honeywell. *3-axis digital compass IC HMC5983*. Data sheet. PDS-42008. 2019.

[375] Honeywell. *Smart digital magnetometer HMR2300*. Data sheet. PDS-42008. 2019.

[376] GomSpace A/S. *NanoSense M315*. Data sheet. Version 1.2. DS 1018558. 2019.

[377] SpaceQuest, Ltd. *MAG-3 satellite magnetometer*. Data sheet. Version 2016-06-21. 2016.

[378] NewSpace Systems (Pty) Ltd. *Magnetometer*. Data sheet. Version 8b. 2018.

[379] Analog Devices, Inc. *Low Profile, six degrees of freedom inertial sensor*. Data sheet. Version D. D09362-0-4/19(D). 2019.

[380] Analog Devices, Inc. *Tactical grade, six degrees of freedom inertial sensor*. Data sheet. Version H. D10666-0-2/19(H). 2019.

[381] Astro- und Feinwerktechnik Adlershof GmbH. *Gyro-system AGS-1 for small satellites*. Data sheet. 2019.

[382] Silicon Sensing Systems Limited. *CRH02 analogue angular rate sensor high performance MEMS gyroscope*. Data sheet. Version Rev 2. CRH02-00-0100-132. 2019.

[383] Honeywell Aerospace. *HG1120 MEMS inertial measurement unit*. Data sheet. Version 10/19. N61-1524-000-005. 2019.

[384] Honeywell Aerospace. *HG4930 MEMS inertial measurement unit*. Data sheet. Version 03/18. N61-1523-000-005. 2018.

[385] Honeywell Aerospace. *HGuide i300 MEMS inertial measurement unit*. Data sheet. Version 09/19. N61-2009-000-003. 2019.

[386] Inertial Labs. *High performance advanced MEMS industrial & tactical grade inertial measurement units IMU-P*. Data sheet. Version 2.8. 2019.

[387] EMCORE Corporation. *SDD3000-A01 MEMS quartz digital single axis rate sensor*. Data sheet. Version B. 966238. 2019.

[388] EMCORE Corporation. *EMCORE-Hawkeye series EG-120 fiber optic gyroscope (FOG)*. Data sheet. Version REV 2019.06. 2019.

[389] EMCORE Corporation. *EMCORE-Hawkeye EG-1300 lithium-niobate fiber optic gyroscope (FOG)*. Data sheet. Version REV 2018.07. 2018.

[390] Gladiator Technologies. *G150Z gyroscope low noise analog MEMS gyro*. Data sheet. 2019.

[391] Gladiator Technologies. *G300D digital triaxial MEMS gyroscope*. Data sheet. 2019.

[392] Tronic's Microsystems S.A. *GYPRO2300 datasheet MCD001-E*. Data sheet. 2019.

[393] Xsens Technologies B.V. *MTi 10-series*. Data sheet. 2018.

[394] Sensonor AS. *STIM210 multi-axis gyro module*. Data sheet. Version 18. TS1545. 2018.

[395] Northrop Grumman LITEF GmbH. *High performance fiber optic rate gyros*. Data sheet. 2012.

[396] TAMAGAWA TRADING CO., LTD. *3-axis FOG/IRU for micro-satellite*. Data sheet. Version 18.08. T12-1706N2. 2018.

[397] Hyperion Technologies B.V. *GNSS200 GNSS receiver*. Data sheet. Version V2.1. 2019.

[398] SpaceQuest, Ltd. *GPS-601 satellite GNSS receiver*. Data sheet. 2016.

[399] Pumpkin, Inc. *CubeSat Kit GPSRM 1 GPS receiver module*. Data sheet. Version A. 2018.

[400] China Great Wall Industry Corporation. *GW-CMS-V/X20 series GNSS receiver module product specification*. Data sheet. 2020.

[401] GomSpace A/S. *NanoSense GPS kits*. Data sheet. Version 2.3. 1015610. 2019.

[402] NewSpace Systems (Pty) Ltd. *GPS receiver*. Data sheet. Version 9a. 2018.

[403] German Aerospace Center (DLR). *Phoenix GPS data sheet*. Data sheet. Version 1.1. 2007.

[404] German Aerospace Center (DLR). *User's manual for the Phoenix GPS receiver*. User's manual. Version 1.9. GTN-MAN-0120. 2008.

[405] SkyTraq Technology, Inc. *Venus838FLPx GPS receiver for CubeSat application*. Data sheet. Version 4. 2019.

[406] NovAtel Inc. *Receivers OEM719*. Data sheet. Version 5. D21049. 2019.

[407] CubeSpace. *Reaction wheels*. Data sheet. 2019.

[408] GomSpace A/S. *NanoTorque GSW-600*. Data sheet. Version 2.0. DS 1013128. 2018.

[409] Maryland Aerospace, Inc. *MAI-400 single axis reaction wheel assembly*. Data sheet. 410-451-2505. 2015.

[410] Space Inventor. *WHL-50 50mm high performance reaction wheel*. Data sheet. Version v2.4. 2021.

[411] Sinclair Interplanetary. *Nanosatellite reaction wheels (RW-0.03)*. Data sheet. Version Rev 2019a. 2019.

[412] NanoAvionics, LLC. *Reaction wheels*. Data sheet. Version R9. NA-4RW0-G0-R9. 2019.

[413] Astro- und Feinwerktechnik Adlershof GmbH. *Reaction wheel RW35 for nano and micro satellites*. Data sheet. 2021.

[414] Blue Canyon Technologies. *Reaction wheels*. Data sheet. 2019.

[415] Hyperion Technologies B.V. *RW400 reaction wheel*. Data sheet. Version V2.0. 2019.

[416] CubeSpace. *Magnetorquers*. Data sheet. 2019.

[417] GomSpace A/S. *NanoTorque GST-600*. Data sheet. Version 1.3. DS 1013874. 2018.

[418] ISIS - Innovative Solutions In Space B.V. *Magnetorquer board (iMTQ)*. Data sheet. 2016.

[419] Agencia Espacial Civil Ecuatoriana. *Magnetorquer board (iMTQ)*. Data sheet. 2016.

[420] Zarm Technik AG. *Magnetic torquers for micro-satellites*. Data sheet. Version CST_07-2010. 2010.

[421] Zarm Technik AG. *MT2-1-02 technical performance data sheet*. Data sheet. Version 1. MT2-1-02-TN-ZAR-MTR-01. 2017.

[422] NewSpace Systems (Pty) Ltd. *Magnetorquer rod*. Data sheet. Version 8a. 2018.

[423] GomSpace A/S. *NanoTorque z-axis internal*. Data sheet. Version 1.0. 2016.

[424] NanoAvionics, LLC. *Magnetorquers MTQ3X*. Data sheet. Version R0. NA-MTQ3X-G1-R0. 2019.

[425] Tesat-Spacecom GmbH & Co. KG. *CUBE-LCT smallest laser communication transceiver worldwide*. Data sheet. 2018.

[426] IQ wireless GmbH. *HiSPiCO S band transmitter SDR for small satellites*. Data sheet. Version 08-19. 2019.

[427] Sinclair Interplanetary. *Laser downlink plus star tracker*. Data sheet. Version Rev 2017b. 2017.

[428] AAC Clyde Space. *PULSAR-DATA*. Data sheet. 205396. 2019.

[429] Augustus Aerospace Company. *S2DR HRTX high-rate software defined DVB-S2 transmitter*. Data sheet. Version v0.3. 2020.

[430] EnduroSat. *S-band receiver*. Data sheet. Version 1. 2019.

[431] EnduroSat. *S-band transmitter*. Data sheet. Version 1. 2019.

[432] ISIS - Innovative Solutions In Space B.V. *TXS S-band transmitter datasheet*. Data sheet. Version 1.0. ISIS.TXS.DS.001. 2019.

[433] EnduroSat. *X-band transmitter*. Data sheet. Version 1.2. 2019.

[434] Hyperion Technologies B.V. *CUBECAT laser communication terminal*. Data sheet. Version V2.0. 2019.

[435] AAC Clyde Space. *PULSAR-TMTC*. Data sheet. 205396. 2019.

[436] NanoAvionics, LLC. *UHF Radio SAT2RF1-1D*. Data sheet. Version R3. NA-UHF-G1-R3. 2020.

[437] Innoflight Inc. *Innoflight compact S-band transceiver (SCR-100)*. Data sheet. 2019.

[438] Innoflight Inc. *Innoflight compact (L+S)/S radio (SCR-104)*. Data sheet. 2019.

[439] Innoflight Inc. *Innoflight compact X-band transceiver (SCR-106)*. Data sheet. 2019.

[440] Innoflight Inc. *Innoflight compact K-band transceiver (SCR-108)*. Data sheet. 2019.

[441] IQ wireless GmbH. *SLink / SLink-Phy S band transceiver for small satellites*. Data sheet. Version 06-19. 2019.

[442] Satlab ApS. *Full-duplex low-power S-band transceiver*. Data sheet. Version 1.1. 2018.

[443] Augustus Aerospace Company. *S2DR 1000 dual-transceiver space SDR*. Data sheet. Version v0.3. 2020.

[444] EnduroSat. *UHF transceiver type II*. Data sheet. Version 1.6. 2019.

[445] ISIS - Innovative Solutions In Space B.V. *VHF/UHF duplex transceiver*. Data sheet. 2016.

[446] IQ wireless GmbH. *XLink X band transceiver SDR for small satellites*. Data sheet. Version 06-19. 2019.

[447] Busek Co. Inc. *BmP-220 micro-pulsed plasma thruster*. Data sheet. 70008502G. 2019.

[448] Busek Co. Inc. *BIT-3 RF ion thruster*. Data sheet. 70010819F. 2019.

[449] VACCO Industries. *NEA Scout propulsion system*. Data sheet. Version Rev 7/17. 2017.

[450] Bradford Space. *Comet water-based propulsion for small satellites*. Data sheet. Version OCT.2019. 2019.

[451] NanoAvionics, LLC. *Propulsion system EPSS C1*. Data sheet. Version R0. NA-EPSS1-G0-R0-TO. 2019.

[452] VACCO Industries. *Green Propulsion System X19041000*. Data sheet. Version Rev 7/19. 2019.

[453] VACCO Industries. *ArgoMoon propulsion system*. Data sheet. Version Rev 7/17. 2017.

[454] ENPULSION GmbH. *IFM nano thruster*. Data sheet. Version F.1. ENP2018-001. 2018.

[455] ENPULSION GmbH. *IFM micro thruster*. Data sheet. Version E.1. ENP2018-002. 2018.

[456] VACCO Industries. *Integrated Propulsion System*. Data sheet. Version Rev 8/19. 2019.

[457] VACCO Industries. *JPL MarCO - Micro CubeSat propulsion system*. Data sheet. Version Rev 9/19. 2019.

[458] Aerojet Rocketdyne. *MPS-130 innovative propulsion solutions for SmallSats*. Data sheet. 2020.

[459] Aerojet Rocketdyne. *MPS-130 innovative propulsion solutions for SmallSats*. Data sheet. 2020.

[460] GomSpace A/S. *NanoProp CGP3*. Data sheet. 2019.

[461] GomSpace A/S. *NanoProp 6U*. Data sheet. 2019.

[462] Hyperion Technologies B.V. *PM200 propulsion module*. Data sheet. Version V2.0. 2019.

[463] VACCO Industries. *Standard Propulsion System*. Data sheet. Version Rev 8/19. 2019.

List of Publications

[1] A. Asif, M. F. **Barschke**, B. Bastian-Querner, D. Berge, R. Bühler, N. D. Simone, G. Giavitto, J. M. H. Crespo, N. Kaipachery, M. Kowalski, S. R. Kulkarni, D. Küsters, S. Philipp, H. Prokoph, J. Schliwinski, M. Vasilev, J. J. Watson, S. Worm, F. Zappon, S. Alfassi, S. Ben-Ami, A. Birman, K. Boggs, G. Bredthauer, A. Fenigstein, A. Gel-Yam, D. Ivanov, O. Katz, O. Lapid, T. Liran, E. Netzer, E. O. Ofek, S. Regev, Y. Shvartzvald, J. Tufts, D. Veinger, and E. Waxman. "Design of the ULTRASAT UV Camera". In: *Proceedings of SPIE Optical Engineering and Applications*. San Diego, USA, 2021.

[2] B. Bastian-Querner, N. Kaipachery, D. Küsters, J. Schliwinski, S. Alfassi, A. Asif, M. F. **Barschke**, S. Ben-Ami, D. Berge, V. D. Berlea, A. Birman, R. Bühler, N. D. Simone, A. Fenigstein, A. Gel-Yam, G. Giavitto, J. M. H. Crespo, D. Ivanov, O. Katz, M. Kowalski, S. R. Kulkarni, O. Lapid, T. Liran, E. O. Ofek, S. Philipp, H. Prokoph, S. Regev, Y. Shvartzvald, M. Vasilev, D. Veinger, J. J. Watson, E. Waxman, S. Worm, and F. Zappon. "Sensor characterization for the ULTRASAT space telescope". In: *Proceedings of SPIE Optical Engineering and Applications*. San Diego, USA, 2021.

[3] C. Jonglez, K. Gordon, P. Werner, J. Bartholomäus, and M. F. **Barschke**. "ADCS performance assessment using payload camera: lessons learned on a small satellite mission and future applications". In: *Proceedings of the 16th International Conference on Space Operations*. Online, 2021.

[4] M. F. **Barschke**. "Nanosatellites as educational projects". In: *Nanosatellites: Space and ground technologies, operations and economics*. Ed. by R. A. de Carvalho, J. Estela, and M. Langer. 1st ed. London, United Kingdom: Wiley & Sons, 2020. Chap. 14, pp. 309–325.

[5] M. F. **Barschke**. "Launch costs". In: *Nanosatellites: Space and ground technologies, operations and economics*. Ed. by R. A. de Carvalho, J. Estela, and M. Langer. 1st ed. London, United Kingdom: Wiley & Sons, 2020. Chap. 26, pp. 533–543.

[6] K. Gordon, M. F. **Barschke**, and P. Werner. "From TechnoSat to TUBIN – performance upgrade for the TUBiX20 microsatellite platform based on flight experience". In: *CEAS Space Journal* 12 (2020), pp. 515–525.

[7] M. F. **Barschke**, C. Jonglez, P. Werner, K. Gordon, P. von Keiser, M. Starke, and M. Lehmann. "Initial orbit results from the TUBiX20 platform". In: *Acta Astronautica* 167 (2020), pp. 108–116.

[8] J. Bartholomäus, C. Jonglez, P. von Keiser, J. Léglise, M. Lehmann, P. Werner, M. F. **Barschke**, M. Reibe, and K. Jäckel. "A last-minute upgrade: Rapid integration of an opportunity payload into the TUBIN mission". In: *Proceedings of the 34th AIAA/USU Conference on Small Satellites*. Online, 2020.

[9] D. Ivanov, M. F. **Barschke**, M. Ovchinnikov, and K. Brieß. "Flight results from a passively magnetic stabilised single unit CubeSat". In: *Proceedings of the 3rd IAA Conference on University Satellite Missions*. Rome, Italy, 2020.

[10] A. N. Dinkelaker, A. Kaparthy, S. E. Reher, A. Bawamia, C. Kürbis, R. Smol, H. Christopher, A. Wicht, P. Werner, J. Bartholomäus, S. Rotter, R. Jördens, M. F. **Barschke**, and M. Krutzik. "Optical quantum technologies for compact rubidium vapor-cell frequency standards in space using small satellites". In: *Journal of the British Interplanetary Society* 72.3 (2019), pp. 74–82.

[11] M. F. **Barschke**, A. N. Dinkelaker, A. Bawamia, J. Bartholomäus, A. Kaparthy, S. Rotter, P. Werner, E. Klioner, C. Jonglez, J. M. H. Crespo, M. Krutzik, C. Schmidt, C. Fuchs, K. Jäckel, and M. Reibe. "The QUEEN mission to demonstrate an optical Rb frequency reference payload and advanced small satellite platform technology". In: *Proceedings of the 70th International Astronautical Congress*. Washington D.C., USA, 2019.

[12] M. F. **Barschke**, P. Werner, J. Bartholomäus, C. Meumann, and K. Brieß. "Microsatellite development at Technische Universität Berlin: Status and perspective". In: *Proceedings of the German Aerospace Congress*. Darmstadt, Germany, 2019.

[13] M. Reibe, K. Jäckel, M. F. **Barschke**, and C. Jonglez. "A modular family of high data rate SDR transceivers". In: *Proceedings of the 33rd AIAA / USU Conference on Small Satellites*. Logan, United States of America, 2019.

[14] M. Konaka, J. M. Haces Crespo, J. Bartholomäus, A. N. Dinkelaker, A. Bawamia, M. Krutzik, and M. F. **Barschke**. "Preliminary thermal design for the small satellite mission QUEEN, carrying an optical atomic frequency reference". In: *Proceedings of the 9th Nano-Satellite Symposium*. Fukui, Japan, 2019.

[15] D. Noack, M. F. **Barschke**, J. Großhans, B. G. Ungermann, H. Q. Vu, P. Werner, and K. Brieß. "In-orbit verification of a fluid-dynamic attitude control system". In: *Proceedings of the 9th Nano-Satellite Symposium*. Fukui, Japan, 2019.

[16] M. F. **Barschke**, J. Bartholomäus, J. M. H. Crespo, K. Gordon, C. Jonglez, P. von Keiser, D. Költzsch, J. Leglise, M. Lehmann, C. Meumann, S. Reinert, S. Rotter, M. Starke, P. Werner, and L. Zander. "TechnoSat – Results from the first 18 months of operation". In: *Proceedings of the 12th IAA Symposium on Small Satellites for Earth Observation*. Berlin, Germany, 2019.

[17] J. Bartholomäus, M. F. **Barschke**, and M. Lehmann. "The TUBIN mission within the context of present and future satellite-based fire detection systems". In: *Proceedings of the 12th IAA Symposium on Small Satellites for Earth Observation*. Berlin, Germany, 2019.

[18] M. F. **Barschke**. "A modular platform architecture to enable system level scalability". In: *Proceedings of the 12th IAA Symposium on Small Satellites for Earth Observation*. Berlin, Germany, 2019.

[19] K. Gordon, M. Starke, P. von Keiser, and M. F. **Barschke**. "Multi-mission software development for small spacecraft". In: *Proceedings of the 12th IAA Symposium on Small Satellites for Earth Observation*. Berlin, Germany, 2019.

[20] P. Wang, H. Almer, G. Kirchner, F. Koidl, M. Steindorfer, M. F. **Barschke**, P. Werner, and M. Starke. "kHz SLR application on the attitude analysis of TechnoSat". In: *Proceedings of the 21st International Workshop on Laser Ranging*. Canberra, Australia, 2018.

[21] A. N. Dinkelaker, A. Kaparthy, S. Reher, A. Bawamia, C. Kürbis, R. Smol, H. Christopher, A. Wicht, P. Werner, J. Bartholomäus, S. Rotter, R. Jördens, M. F. **Barschke**, and M. Krutzik. "Optical quantum technologies for compact rubidium vapor-cell frequency standards in space using small satellites". In: *Proceedings of the 6th Reinventing Space conference*. London, United Kingdom, 2018.

[22] J. Bartholomäus, M. F. **Barschke**, and M. Lehmann. "Development of a single-channel wildfire detection algorithm for the TUBIN mission". In: *Proceedings of the 69th International Astronautical Congress*. Bremen, Germany, 2018.

[23] M. F. **Barschke**, K. Gordon, P. von Keiser, M. Lehmann, M. Starke, and P. Werner. "Initial orbit results from the TUBiX20 platform". In: *Proceedings of the 69th International Astronautical Congress*. Bremen, Germany, 2018.

[24] M. F. **Barschke**, P. Werner, and S. Kapitola. "BEESAT-3 commissioning – Better late than never". In: *Proceedings of the 69th International Astronautical Congress*. Bremen, Germany, 2018.

[25] M. Starke, M. F. **Barschke**, and P. von Keiser. "A modular hardware diagnosis framework for small spacecraft". In: *Proceedings of the 69th International Astronautical Congress*. Bremen, Germany, 2018.

[26] M. F. **Barschke**, P. Werner, K. Gordon, M. Lehmann, W. Frese, D. Noack, L. Grunwaldt, G. Kirchner, P. Wang, and B. Schlepp. "Initial results from the TechnoSat in-orbit demonstration mission". In: *Proceedings of the 32nd AIAA/USU Conference on Small Satellites*. Logan, United States of America, 2018.

[27] D. Noack, M. F. **Barschke**, P. Werner, and K. Brieß. "FDA in space – First in-orbit results of a fluid dynamic attitude control system". In: *Proceedings of the Small Satellites Systems and Services Symposium*. Sorrento, Italy, 2018.

[28] F. Hufgard, M. Lengowski, M. F. **Barschke**, N. Harmansa, S. Klinkner, and K. Brieß. "Preliminary study of an academic micro-satellite formation mission for meteoroid trajectories determination and dust mass flow measurement". In: *Proceedings of the Small Satellites Systems and Services Symposium*. Sorrento, Italy, 2018.

[29] K. Gordon, M. F. **Barschke**, and P. Werner. "Upgrading TUBiX20 – Bringing TechnoSat flight experience into the TUBIN mission". In: *Proceedings of the Small Satellites Systems and Services Symposium*. Sorrento, Italy, 2018.

[30] R. Gerlich, R. Gerlich, S. Montenegro, E. Dilger, F. Flederer, K. Gordon, and M. F. **Barschke**. "Verification of the C++-operating system RODOS in context of a small-satellite". In: *Proceedings of the 2nd Workshop on Computer Architectures in Space*. Braunschweig, Germany, 2018.

[31] M. F. **Barschke**, J. Bartholomäus, K. Gordon, M. Lehmann, and K. Brieß. "The TUBIN mission for wildfire detection using nanosatellites". In: *CEAS Space Journal* 9.2 (2017), pp. 183–194.

[32] M. F. **Barschke**, A. N. Dinkelaker, J. Bartholomäus, P. Werner, H. Christopher, and M. Krutzik. "Optical quantum technology in space using small satellites". In: *Proceedings of the 68th International Astronautical Congress*. Adelaide, Australia, 2017.

[33] S. Junk, M. Lehmann, M. F. **Barschke**, and S. Rotter. "Lean hardware update process for a modular satellite platform". In: *Proceedings of the 68th International Astronautical Congress*. Adelaide, Australia, 2017.

[34] J. Grosshans and M. F. **Barschke**. "Mission concept of a satellite constellation for global wildfire monitoring". In: *Proceedings of the AIAA SPACE and Astronautics Forum*. Orlando, United States of America, 2017.

[35] D. Noack, J. Ludwig, P. Werner, M. F. **Barschke**, and K. Brieß. "FDA-A6 – A fluid-dynamic attitude control system for TechnoSat". In: *Proceedings of the Nano-Satellite Symposium*. Matsuyama-Ehime, Japan, 2017.

[36] W. Bauer, A. Braukhane, J. T. Grundmann, O. Romberg, F. Dannemann, and M. F. **Barschke**. "Step by step realization of an operational on orbit detection network". In: *Proceedings of the 7th European Conference on Space Debris*. Darmstadt, Germany, 2017.

[37] J. Kühn, M. F. **Barschke**, and D. Költzsch. "Development of a thermal simulation tool for nanosatellites based on commercial finite element analysis software". In: *Proceedings of the 11th IAA Symposium on Small Satellites for Earth Observation*. Berlin, Germany, 2017, pp. 385–388.

[38] K. Gordon, M. Lehmann, and M. F. **Barschke**. "Flexible low-cost verification of attitude determination and control systems". In: *Proceedings of the 11th IAA Symposium on Small Satellites for Earth Observation*. Berlin, Germany, 2017, pp. 405–408.

[39] D. Költzsch and M. F. **Barschke**. "Finite element analysis aided structure design for a modular nanosatellite platform". In: *Proceedings of the 11th IAA Symposium on Small Satellites for Earth Observation*. Berlin, Germany, 2017, pp. 351–354.

[40] M. F. **Barschke**, K. Gordon, and S. Junk. "Modular architecture and rapid technology update for a flexible nanosatellite platform". In: *Proceedings of the 11th IAA Symposium on Small Satellites for Earth Observation*. Berlin, Germany, 2017, pp. 289–292.

[41] L. Grunwaldt, R. Neubert, and M. F. **Barschke**. "Optical tests of a large number of small COTS cubes". In: *Proceedings of the 20th International Workshop on Laser Ranging*. Potsdam, Germany, 2016.

[42] M. F. **Barschke**, K. Gordon, M. Lehmann, and K. Brieß. "The TechnoSat mission for on-orbit technology demonstration". In: *Proceedings of the 65th German Aerospace Congress*. Braunschweig, Germany, 2016.

[43] M. F. **Barschke**, K. Gordon, P. von Keiser, and M. Starke. "FDIR approach of a modular satellite platform architecture". In: *Proceedings of the 66th International Astronautical Congress*. Guadalajara, Mexico, 2016.

[44] W. Bauer, O. Romberg, H. Krag, G. H. Visser, D. Digirolamo, M. F. **Barschke**, and S. Montenegro. "Debris in-situ impact detection by utilization of CubeSat solar panels". In: *Proceedings of the Small Satellites Systems and Services Symposium*. Valletta, Malta, 2016.

[45] M. F. **Barschke**, K. Brieß, and U. Renner. "Twenty-five years of satellite development at Technische Universität Berlin". In: *Proceedings of the Small Satellites Systems and Services Symposium*. Valletta, Malta, 2016.

[46] M. F. **Barschke**, W. Ballheimer, K. Gordon, and K. Brieß. "The TUBIN mission – Wildfire detection using nanosatellites". In: *Proceedings of the 64th German Aerospace Congress*. Rostock, Germany, 2015.

[47] W. Bauer, O. Romberg, and M. F. **Barschke**. "Space environment characterisation by applying an innovative debris detector". In: *Proceedings of the Advanced Maui Optical and Space Surveillance Technologies*. Maui, Hawaii, 2015.

[48] K. Gordon and M. F. **Barschke**. "A new concept of software architecture for a flexible attitude determination and control of nanosatellites". In: *Proceedings of the 65th International Astronautical Congress*. Jerusalem, Israel, 2015.

[49] M. F. Barschke and K. Gordon. "Enabling flexible payload management through modularity". In: *Proceedings of the 65th International Astronautical Congress*. Jerusalem, Israel, 2015.

[50] K. Gordon, A. Graf, and M. F. **Barschke**. "Practical experience in using continuous integration within the development of nanosatellite software". In: *Proceedings of the 10th IAA Symposium on Small Satellites for Earth Observation*. Berlin, Germany, 2015.

[51] P. Werner, M. Starke, A. Graf, K. Gordon, and M. F. **Barschke**. "Modular support software for nanosatellites". In: *Proceedings of the 10th IAA Symposium on Small Satellites for Earth Observation*. 2015, pp. 211–214.

[52] M. F. **Barschke**, J. Levenhagen, D. Reggio, and P. C. E. Roberts. "ASSET: a software tool for the evaluation of manoeuvre capabilities of highly agile satellites". In: *CEAS Space Journal* 6 (2014), pp. 37–45.

[53] M. F. **Barschke** and K. Gordon. "A generic systems architecture for a single-failure tolerant nanosatellite platform". In: *Proceedings of the 64th International Astronautical Congress*. Toronto, Canada, 2014.

[54] D. Költzsch and M. F. **Barschke**. "Development and verification of a lightweight and modular structure for a novel nanosatellite platform". In: *Proceedings of the 63th German Aerospace Congress*. Augsburg, Germany, 2014.

[55] M. F. **Barschke**, K. Großekatthöfer, and S. Montenegro. "Implementation of a nanosatellite on-board software based on building-blocks". In: *Proceedings of the Small Satellites Systems and Services Symposium*. Porto Pedro, Spain, 2014.

[56] G. Kirchner, L. Grunwaldt, R. Neubert, F. Koidl, M. F. **Barschke**, Z. Yoon, and H. Fiedler. "Laser ranging to nano-satellites in LEO orbits: plans, issues, simulations". In: *Proceedings of the 18th International Workshop on Laser Ranging*. Fujiyoshida, Japan, 2013.

[57] M. F. **Barschke**, Z. Yoon, and K. Brieß. "TUBiX - The TU Berlin innovative next generation nanosatellite bus". In: *Proceedings of the 64th International Astronautical Congress*. Beijing, China, 2013.

[58] M. F. **Barschke**, H. Adirim, O. Balagurin, W. Ballheimer, L. Dornburg, H. Kayal, D. Noak, C. Nitzschke, N. A. Pilz, H. Wojtkowiak, and K. Brieß. "TechnoSat - A nanosatellite mission for on-orbit technology demonstration". In: *Proceedings of the 27th AIAA/USU Conference on Samll Satellites*. Logan, United States of America, 2013.

[59] M. F. **Barschke**, F. Baumann, W. Ballheimer, K. Großekatthöfer, C. Nitzschke, and K. Brieß. "TUBiX20 - The novel nanosatellite bus of TU Berlin". In: *Proceedings of the 9th IAA Symposium on Small Satellites for Earth Observation*. 2013, pp. 93–96.

[60] S. Trowitzsch, F. Baumann, M. **Barschke**, and K. Brieß. "Lessons learned from picosatellite development at TU Berlin". In: *Proceedings of the 2nd IAA Conference on University Satellites Missions*. Rome, Italy, 2013.

[61] M. F. **Barschke**, F. Baumann, and K. Brieß. "BEESAT-3: Passive attitude control for directed radio transmission on a single-unit CubeSat". In: *Proceedings of the Nano-Satellite Symposium*. Nagoya, Japan, 2012.

[62] M. F. **Barschke**, R. Badsi, B. Soyer, and J. Marx. "OpenCube-alpha: A plug & play nanosatellite demonstrator". In: *Proceedings of the Nano-Satellite Symposium*. Nagoya, Japan, 2012.

[63] M. F. **Barschke**, J. Levenhagen, D. Reggio, and P. C. E. Roberts. "Design and analysis of manoeuvre scenarios for highly agile satellites". In: *Proceedings of the 61th German Aerospace Congress*. Berlin, Germany, 2012.

[64] M. F. **Barschke**, F. Baumann, and K. Brieß. "BEESAT-3: A picosatellite developed by students". In: *Proceedings of the 61th German Aerospace Congress*. Berlin, Germany, 2012.

[65] M. F. **Barschke**, S. Özkan, and M. J. Johnson. "Mission control for citizen space exploration". In: *Proceedings of the 12th International Conference on Space Operations*. Stockholm, Sweden, 2012.

[66] R. Badsi, M. F. **Barschke**, B. Soyer, C. Engeldrum, and J. Marx. "Operations of a self-reconfigurable CubeSat". In: *Proceedings of the 12th International Conference on Space Operations*. Stockholm, Sweden, 2012.

[67] M. F. **Barschke**, S. Özkan, and M. J. Johnson. "Open source mission control software for small space projects". In: *Proceedings of the 60th German Aerospace Congress*. 2011, pp. 1647–1652.

[68] M. **Barschke**, G.-J. Menken, and O. Hasemann. "Development of a simulation based control unit design tool for MEWAS". In: *Development in Mechanical Engineering* 4 (2010), pp. 187–196.

[69] M. **Barschke**, D. Uribe, O. Ruiz, J. Jensen, and C. Lopez. "Finite Element Modelling of Composite Materials using Kinematic Constraints". In: *Journal of Engineering and Science* 5 (2010), pp. 133–153.

[70] M. **Barschke**, G.-J. Menken, and O. Hasemann. "Development of a simulation based control unit design tool for MEWAS". In: *Proceedings of the 19th International Symposium on Research, Education and Technology*. Bremen, Germany, 2010.

A Satellite Missions of Technische Universität Berlin

Since 1991 Technische Universität Berlin successfully designed, launched and operated 26 satellites within a mass range of 0.375 to 56 kg, while four additional spacecraft are currently being developed. Table A.1 gives an overview over launched and planned missions of the university.

Table A.1: Satellite missions launched by Technische Universität Berlin to date.

Number	Mission	Mission objectives	Launch mass kg	Launch date	References
1	TUBSAT-A	Communications	35	1991	[289]
2	TUBSAT-B	Earth observation	45	1994	[290]
3, 4	TUBSAT-N and N1	Communications	3 and 8	1998	[291]
5	DLR-TUBSAT	Earth observation	45	1999	[61]
6	MAROC-TUBSAT	Earth observation	47	2001	[292]
7	LAPAN-TUBSAT	Earth observation	56	2007	[293]
8	BEESAT-1	Technology demonstration	1	2009	[62, 197]
9	BEESAT-2	Technology demonstration	1	2013	[294]
10	BEESAT-3	Education and technology demonstration	1	2013	[164, 295, 296]
11	BEESAT-4	Technology demonstration	1	2016	[297]
12	TechnoSat	Technology demonstration	20	2017	[28, 37, 150]
13 ... 16	S-Net	Inter-satellite communications	4 x 8.7	2018	[63, 64]
17	BEESAT-9	Technology demonstration	1	2019	[298]
18 ... 21	BEESAT-10 to 13	Technology demonstration	4 x 0.375	2019	[299]
22	SALSAT	Frequency spectrum analysis	12	2020	[65]
23 ... 26	BEESAT-5 to 8	Technology demonstration	4 x 0.375	2021	[299]
27	TUBIN	Earth observation in TIR	23	2021	[32, 251]
28, 29	NanoFF	Formation flight	2 x 2.7	TBC	[300]
30	QUEEN	Quantum technology demonstration	35	TBC	[20, 21, 32]

B Commercial Small Satellite Platforms

There are a number of microsatellite platforms for missions with launch masses between 10 and 50 kg available on the market. Appendix B lists 51 commercially available microsatellite platforms offered by 26 different vendors. The list makes no claim to being complete and for some platforms the development status could not be confirmed conclusively.

Table B.1: Selection of commercially available small satellite platforms with a launch masses between 10 and 50 kg.

Platform	Manufacturer	Launch mass[a]	References
6 U CubeSat platform	Endurosat	6 U	[301]
6 U CubeSat platform	Innovative Solutions In Space	6 U	[302]
6 U platform	Open Cosmos	6 U	[303]
6 U platform	GomSpace	6 U	[304]
12 U CubeSat spacecraft	Adcole Maryland Aerospace	12 U	[305]
12 U CubeSat platform	Endurosat	12 U	[301]
12 U CubeSat platform	Innovative Solutions In Space	12 U	[302]
12 U platform	Open Cosmos	12 U	[303]
16 U CubeSat platform	Innovative Solutions In Space	16 U	[302]
Advanced platform	HEMERIA	8 U	[306]
Apogee	Inovor Technologies	12 U	[307]
Auriga	Dauria Aerospace	16 U	[308]
Chameleon 6 U	Space Information Labs	6 U	[309]
Chameleon 12 U	Space Information Labs	12 U	[309]
Chameleon 27 U	Space Information Labs	27 U	[309]
DEFIANT	Space Flight Laboratory	20 to 50 kg	[310]
DX	Dauria Aerospace	10 kg	[308]
EPIC 6 U	AAC Clyde Space	6 U	[311]
EPIC 12 U	AAC Clyde Space	12 U	[311]
HAWK-6	Argotec	6 U	[312]
HAWK-12	Argotec	12 U	[312]
InnoSat	OHB Sweden	50 to 60 kg	[313]

Table B.1: Selection of commercially available small satellite platforms with a launch masses between 10 and 50 kg (continued from last page).

Platform	Manufacturer	Launch mass[a]	References
Intermediate platform	HEMERIA	8 U	[306]
JAEGER 12 U	Space Flight Laboratory	12 U	[310]
JAEGER 16 U	Space Flight Laboratory	16 U	[310]
LM-50	Lockheed Martin	6 U	[314]
M6P	NanoAvionics	6 U	[315]
M12P	NanoAvionics	12 U	[315]
M16P	NanoAvionics	16 U	[315]
MN6 U	MinoSpace	6 U	[316]
MN10	MinoSpace	10 kg	[316]
MN10A	MinoSpace	15 to 20 kg	[316]
Nadir	IMT	30 kg	[317]
Nanosatellite Bus	SpaceQuest	13 kg	[318]
NEMO	Space Flight Laboratory	15 to 20 kg	[310]
OrbiCraft-Pro 6 U	Sputnix	6 U	[319]
Perseus	Dauria Aerospace	16 U	[308]
RAVEN 6 U	German Orbital Systems	6 U	[320]
RAVEN 8 U	German Orbital Systems	8 U	[320]
RAVEN 12 U	German Orbital Systems	12 U	[320]
RAVEN 16 U	German Orbital Systems	16 U	[320]
S-50	SITAEL	50 kg	[321]
SAT12 U	Hyperion Technologies	12 U	[322]
SN-30L	Sierra Nevada Corporation	22 kg	[323]
SPARTAN	Space Flight Laboratory	6 U	[310]
SSTL-CUBE	Surrey Satellite Technology	12 U	[324]
Standard platform	HEMERIA	8 U	[306]
TRESTLES 6 U	Tyvak	6 U	[325]
TRESTLES 12 U	Tyvak	12 U	[325]
XB6	Blue Canyon Technologies	6 U	[326]
XB12	Blue Canyon Technologies	12 U	[326]

[a] If the platform adheres to the CubeSat standard, the launch mass is given in CubeSat units

C Commercial Small Satellite Components

In this appendix commercially available components that are suitable for the implementation within the TUBiX20 platform are presented. This includes:

- 18 types of solar cells from 5 different manufacturers (Table C.1)
- 15 star trackers from 12 different vendors (Table C.2)
- 11 Sun sensors from 9 different vendors (Table C.3)
- 10 magnetometers from 8 different vendors (Table C.4)
- 18 gyroscopes from 12 different vendors (Table C.5)
- 8 GNSS receivers from 7 different vendors (Table C.6)
- 16 reaction wheels from 8 different vendors (Table C.7)
- 16 magnetorquers from 7 different vendors (Table C.8)
- 10 data transmitters from 7 different vendors (Table C.9)
- 13 radio transceivers from 9 different vendors (Table C.10)
- 20 propulsion systems from 9 different vendors (Table C.11)

Table C.1: Selection of solar cells specifically developed for space appllications.

Device	Manufacturer	Efficiency %	Voltage[a] V	Current per area[a] mA cm^{-2}	Reference
3G28C - 40 x 80 mm	AZUR SPACE	28.0	2.371	16.14	[327]
3G30C - 40 x 70 mm	AZUR SPACE	30.0	2.411	16.70	[328]
3G30C - 40 x 80 mm	AZUR SPACE	30.0	2.411	16.71	[137]
3G30C - 60 x 120 mm	AZUR SPACE	30.0	2.411	16.68	[329]
3G30C - 80 x 80 mm	AZUR SPACE	30.0	2.411	16.68	[330]
4G32C - 40 x 80 mm	AZUR SPACE	30.0	3.025	14.36	[331]
CTJ30	CESI	29.5	2.32[b]	17.17[b]	[332]
CTJ-LC	CESI	28.0	2.32[b]	16.45[b]	[333]
CTJ30 - Thin	CESI	29	2.31	17.13	[334]
IMM-α	SolAero	32.0	4.28	10.12	[335]
SC-3GA-3	SISP	30	2.43	16.7	[336]
SC-3GA-4	SISP	32	2.34	18.5	[337]
UTJ	Spectrolab	28.4[c]	2.350[c]	16.38[c]	[338]
XTE-SF	Spectrolab	32.2	2.435	17.8	[339]
XTJ Prime	Spectrolab	30.7	2.406	17.5	[340]
ZTJ	SolAero	29.5	2.41	16.5	[341]
ZTJ-Ω	SolAero	30.2	2.43	16.8	[342]
Z4J	SolAero	30.0	3.54	11.5	[343]

[a] At maximum power
[b] Applicable for cells with an area of 26.5 mm^2
[c] Applicable for cells with an area below 32 mm^2

Table C.2: Selection of commercially available star trackers suitable for the TUBiX20 platform.

Device	Manufacturer	Mass g	Supply voltage V	Power consumption[a] W	Accuracy[b] arcsec	Reference
Auriga[c]	Sodern	210	5	1	6 / 40	[344]
ARGO 1.0[c]	EICAS Automazione	385	9 to 60	2.7	15 / 15	[345]
CubeStar	CubeSpace	55	3.3	0.3	55.4 / 77.4	[346]
KULST	KU Leuven	350[d]	3.3	1	2 / 10	[347]
MAI-SS	Adcole Maryland Aerospace	282	5	1.5	6 / 27	[348]
MIST[e]	Space Micro	520	unspecified	4	5 / 5	[349]
NST	Blue Canyon Technologies	350[f]	5 to 28[d]	1.5	6 / 40	[350]
NST-3	TY-Space Technology	165	5	0.6	3 / 50	[351]
NST-4	TY-Space Technology	360	5	0.6	3 / 50	[352]
PST3	TY-Space Technology	95	5	0.6	5 / 50	[353]
ST200	Hyperion Technologies[g]	42[h]	3.6 to 5	1	30 / 200	[354]
ST400	Hyperion Technologies[g]	280[h]	3.6 to 34	1	10 / 120	[355]
STAR-T3	Space Inventor	350	5 to 12	1	5 / 30	[356]
ST-16RT2	Sinclair Interplanetary	158[i]	9 to 34	1	5 / 55	[357]
VST-68M	VECTRONIC Aeropspace	470	9 to 40	3	5 / 30	[358]

[a] Maximum power consumption specified in the data sheet
[b] Cross-boresight / around boresight
[c] Requires external computer to run the star detection algorithm
[d] Value personally enquired as it was not specified in the data sheet
[e] Star tracker with dual heads
[f] Standard version
[g] Co-developed with Berlin Space Technologies
[h] Excluding baffle

Table C.3: Selection of commercially available Sun sensors suitable for the TUBiX20 platform.

Device	Manufacturer	Mass g	Supply voltage V	Power consumption[a] W	Accuracy deg	Reference
BiSon64-ET	Lens R&D	23	n/a[b]	n/a[b]	0.5	[359]
Fine Sun sensor	GomSpace	2.2	3.3	13.2	0.5[c]	[360]
Mini-FSS	Bradford Engineering	50	n/a[b]	n/a[b]	0.2[d]	[361]
nanoSSOC-A60	Solar MEMS Technologies	4	3.3 or 5	2	0.5	[362]
nanoSSOC-D60	Solar MEMS Technologies	6.5	3.3 or 5	23	0.5	[363]
NCSS-SA05	NewSpace Systems	5	5	50	0.5	[364]
SS200	Hyperion Technologies	3	5	40	1	[365]
SS-411	Sinclair Interplanetary	34	5 to 50	135	0.1	[366]
SSOC-A60	Solar MEMS Technologies	25	3.3 or 5	36	0.3	[367]
SSOC-D60	Solar MEMS Technologies	35	5	70	0.3	[368]
Sun sensor	German Orbital Systems	9.7	3.3 or 5	15	unspecified[e]	[369]

[a] Maximum power consumption according to data sheet
[b] The sensor does not require being supplied with power
[c] With a FoV below 45° and no albedo
[d] With on-board implementation of look-up table
[e] Precision is given with 0.5°

Table C.4: Selection of commercially available magnetometers suitable for the TUBiX20 platform.

Device	Manufacturer	Mass g	Supply voltage V	Power consumption[a] mW	Accuracy %	Reference
3-axis fluxgate	meisei electric	220	12 to 15	1 500	1[b]	[370]
AMR-RS422-LV	ZARM Technik	60	6 to 16	300	1	[371]
DRV425[c]	Texas Instruments	unspecified	3 to 5.5	100[d]	2	[372]
FLC3-70	Stefan Mayer Instruments	30[e]	4.8 to 12	77	1[f]	[373]
HMC5983[g]	Honeywell	0.02	3.3	0.36	unspecified	[374]
HMR2300	Honeywell	98[h]	6.5 to 15	450	0.5	[375]
M315	GomSpace	8	3.3	8.25	0.5[i]	[376]
MAG-3	SpaceQuest	100	5[j]	450[k]	0.75	[377]
NMRM-001-485	NewSpace Systems	6	5	550	1[l]	[378]
NMRM-Bn25o485	NewSpace Systems	85	5	750	1[l]	[378]

[a] Maximum power consumption according to data sheet
[b] Given as “alignment accuracy”
[c] Single axis sensor IC
[d] While measuring a magnetic field of 1 mT
[e] Value personally enquired as it was not specified in the data sheet
[f] Accuracy at 20 °C
[g] 3-axis digital compass IC
[h] Mass of the PCB only
[i] Given as “linearity” at ± 200 µT
[j] Also available with a power supply range of 15 V to 34 V
[k] Voltage dependent with 30 mA at any input voltage
[l] Given as “orthogonality”

Table C.5: Selection of commercially available rate sensors suitable for the TUBiX20 platform.

Device	Manufacturer	Mass g	Supply voltage V	Power consumption[a] W	Angle random walk $\mathrm{deg}/\sqrt{\mathrm{h}}$	Reference
ADIS16334	Analog Devices	12.5	5	0.235	2	[379]
ADIS16485	Analog Devices	48	3.3	0.650	0.3	[380]
AGS-1	AstroFein[b]	1 000	18 to 34	10	0.1	[381]
CRH02	Silicon Sensing System	45	5	0.35	0.017	[382]
HG1120CA50	Honeywell Aerospace	54	3 to 5.5	0.4	0.6	[383]
HG4930CA51	Honeywell Aerospace	140	5	2	0.04	[384]
HGuide i300BA50	Honeywell Aerospace	35	5 to 36	0.5	0.15	[385]
IMU-P S	Inertial Labs	70	5 to 30	0.8[c]	0.08	[386]
SDD3000-A01[d]	EMCORE Corporation	227	11 to 16	2.25	0.01	[387]
EG-120[d]	EMCORE Corporation	90	5	4.5	0.04	[388]
EG-1300[d]	EMCORE Corporation	411	5	5	0.001	[389]
G150Z[d]	Gladiator Technologies	28	5	0.125	-[e]	[390]
G300D	Gladiator Technologies	17.5	3.8 to 5.5	0.250	-[f]	[391]
GYPRO2300[d]	Tronic's Microsystems	2	5	0.125	0.14	[392]
MTi OEM	Xsens Technologies	11	4.5 to 34[g]	0.550[c]	unspecified	[393]
STIM210	Sensonor	52	5	1.5	0.15	[394]
µFORS-6U[d]	Northrop Grumman LITEF	150	5	2.3	0.15	[395]
TA7584	TAMAGAWA SEIKI	1 200	unspecified	3.5	unspecified	[396]

[a] Maximum power consumption according to data sheet
[b] The full name of the company is "Astro- und Feinwerktechnik Adlershof"
[c] At 5 V power supply
[d] Single axis unit
[e] Given as $0.001\,\mathrm{deg}/\mathrm{s}/\sqrt{\mathrm{Hz}}$
[f] Given as $0.002\,8\,\mathrm{deg}/\mathrm{s}/\sqrt{\mathrm{Hz}}$
[g] Can also be supplied with 3.3 V

Table C.6: Selection of commercially available GNSS receivers suitable for the TUBiX20 platform.

Device	Manufacturer	Mass g	Supply voltage V	Power consumption[a] W	Position accuracy m	Reference
GNSS200	Hyperion Technologies	3	3.3	0.165	8	[397]
GPS-601	SpaceQuest	160	3.3[b]	1.4[c]	5	[398]
GPSRM 1[d]	Pumpkin	109	3.3 and 5	1.3	6 000[e]	[399]
GW-CMS-V20	CGWIC	45	5	3	unspecified	[400]
NanoSense GPS[d]	GomSpace	31	3.3	1.32	1.5	[401]
NANT-PTCL1	NewSpace Systems	80	5	0.165	unspecified	[402]
NGPS-03-422	NewSpace Systems	130	3.3 and 5	1[f]	10	[402]
Phoenix	German Aerospace Center (DLR)	22	5	0.85[f]	10[g]	[403, 404]
Venus838FLPx	SkyTraq Technology	0.3	3.3	0.195[f]	2.5	[405]

[a] Maximum power consumption according to data sheet
[b] Build time options 3.3 V regulated, 5 V to 20 V unregulated or 6 V to 42 V unregulated
[c] Given with 1.0 W at 3.3 V, 1.2 W at 7.5 V and 1.4 W at 28 V including active antenna
[d] Based on a NovAtel GPS module [406]
[e] Given as average magnitude in LEO orbits with 24-hour propagation time
[f] Exclusive LNA
[g] Given as 1 m to 2 m for the -XNS variant and 10 m for the other variants

Table C.7: Selection of commercially available reaction wheels suitable for the TUBiX20 platform.

Device	Manufacturer	Mass g	Supply voltage V	Power consumption[a] W	Torque mN m	Momentum mN m s	Reference
CubeWheel S+	CubeSpace	90	6.4 to 16[b]	2.3	2.3	1.6	[407]
CubeWheel M	CubeSpace	150	6.4 to 16[b]	2.3	1	10.8	[407]
CubeWheel L	CubeSpace	225	6.4 to 16[b]	4.5	2.3	30.6	[407]
GSW-600	GomSpace	180	5	2.5	1.5	19	[408]
MAI-400	Maryland Aerospace	110	5	2.2	0.6	11.1	[409]
WHL-50	Space Inventor	180	12 to 16.6	6.33	5	22	[410]
RW-0.03	Sinclair Interplanetary	185	3.4 to 6	1.8[c]	2	40	[411]
RW3-0.06	Sinclair Interplanetary	226	7.5 to 34	23.4[d]	20	180	[286]
RW0	NanoAvionics	137	5	3.0	3.2	20	[412]
RW 35	AstroFein[e]	500	12 to 24	5	5	100	[413]
RWP015	Blue Canyon Technologies	130	12	1.0[f]	4	15	[414]
RWP050	Blue Canyon Technologies	240	12	1.0[f]	7	50	[414]
RWP100	Blue Canyon Technologies	350	12	1.0[f]	7	100	[414]
RW400	Hyperion Technologies	155	5[b]	15	8	15	[415]
RW400	Hyperion Technologies	210	5[b]	15	8	30	[415]
RW400	Hyperion Technologies	380	5[b]	15	8	50	[415]

[a] Maximum power consumption specified in the data sheet
[b] Additionally requires a 3.3 V supply
[c] At 0.02 N m s and 2 mN m
[d] At 0.12 N m s and 10 mN m
[e] The full name of the company is “Astro- und Feinwerktechnik Adlershof”
[f] At full momentum

Table C.8: Selection of commercially available magnetorquers suitable for the TUBiX20 platform.

Device	Manufacturer	Mass g	Supply voltage V	Power consumption W	Magnetic moment A m^2	Reference
CubeRod M	CubeSpace	36	5	750	0.66	[416]
CubeRod L	CubeSpace	72	5	750	1.9	[416]
GST-600[a]	GomSpace	156	3.3	73.6[b]	0.310[c]	[417]
iMTQ	ISIS[d]	196	5	175	0.2	[418]
MT01	EXA	7.5	1.25 to 7.5	250 to 1 750	0.19[e]	[419]
MT0.1-1	ZARM Technik	3	5	295	0.1	[420]
MT0.2-1	ZARM Technik	9	5	140	0.2	[420]
MT0.3-1	ZARM Technik	9	5	315	0.3	[420]
MT0.5-1	ZARM Technik	35	5	300	0.5	[420]
MT1-1	ZARM Technik	60	5	230	1	[420]
MT2-1-02	ZARM Technik	100	5	500	2	[421]
NCTR-M002	NewSpace Systems	30	5	200	0.2	[422]
NCTR-M012	NewSpace Systems	50	5	800	1.19	[422]
NanoTorque	GomSpace	106	3.3	73.6	0.139	[423]
MTQ3X[a]	NanoAvionics	205[f]	3.3 to 6	440[g]	0.30[h]	[424]
MTQ M6P	NanoAvionics	31	5	850	0.42	[424]

[a] Device includes all three axes
[b] Given with 427 mW around the z-axis and 382.1 mW around the x- and y-axis
[c] Given with 0.340 A m^2 around the z-axis and 0.310 A m^2 around the x- and y-axis
[d] The full name of the company is "Innovative Solutions In Space"
[e] Saturation Magnetic moment given with 0.85 A m^2
[f] Value personally enquired as it was not specified in the data sheet
[g] Given with 400 mA around the x- and y axis and 440 mA around the z-axis
[h] Given with 0.30 A m^2 around the x- and y axis and 0.34 A m^2 around the z-axis

Table C.9: Selection of commercially available transmitters and receivers suitable for the TUBiX20 platform.

Device	Manufacturer	Mass g	Supply voltage V	Power consumption[a] W	Type	Reference
CUBE-LCT	Tesat-Spacecom	360	unspecified	8	Laser transmitter	[425]
HiSPiCO	IQ wireless	100	3.3 to 5.0	5	S-band transmitter	[426]
Laser Downlink[b]	Sinclair Interplanetary	335[c]	28	10	Laser transmitter	[427]
PULSAR-STX	AAC Clyde Space[d]	130	6.2 to 17	15	X-band transmitter	[428]
PULSAR-XTX	AAC Clyde Space[d]	100	6 to 12[e]	5	S-band transmitter	[428]
S2DR HRTX	Augustus Aerospace	500	12	23	S- or X-band transmitter	[429]
S-band receiver	EnduroSat	220	10 to 24.5	2	S-band	[430]
S-band transmitter	EnduroSat	250	10 to 24.5[e]	7.2	S-band	[431]
TXS	ISIS[f]	132	7 to 20	13	S-band transmitter	[432]
X-band transmitter	EnduroSat	270	10 to 24.5	12	X-band transmitter	[433]

[a] Maximum power consumption specified in the data sheet
[b] Preliminary data sheet
[c] Including a star tracker
[d] Developed by Cape Peninsula University of Technology, distributed by AAC Clyde Space
[e] Can also be supplied with 5 V
[f] The full name of the company is “Innovative Solutions In Space”

Table C.10: Selection of commercially available radio transceivers suitable for the TUBiX20 platform.

Device	Manufacturer	Mass g	Supply voltage V	Power consumption[a] W	Frequency bands[b]	Reference
CUBECAT	Hyperion Technologies	1 330	9.6 to 21[c]	15	Laser both ways	[434]
PULSAR-TMTC	AAC Clyde Space[d]	100	3.3 or 5	7	UHF / UHF or VHF	[435]
SAT2RF1-1D	NanoAvionics	7.5	3.3	6.8	UHF both ways	[436]
SCR-100	Innoflight	330	9 to 13[e]	10	S-band both ways	[437]
SCR-104	Innoflight	290	9 to 13[e]	10	S-band / L- or S-band	[438]
SCR-106	Innoflight	290	9 to 13[e]	30	X-band / S-band	[439]
SCR-108[f]	Innoflight	370	9 to 13[e]	30	K-band both ways	[440]
SLink	IQ wireless	420	7 to 18	13	S-band both ways	[441]
SRS-3	Satlab	190	5 to 40	5.0	S-band both ways	[442]
S2DR 1000	Augustus Aerospace	435	9 to 28	7	0.07 to 6 GHz both ways	[443]
UHF transceiver	EnduroSat	94	3.3 or 5	2.57	UHF both ways	[444]
VHF/UHF transceiver	ISIS[g]	75	6.5 to 20	4	UHF / VHF	[445]
XLink	IQ wireless	200	8 to 18	15	X-band / S- and X-band	[446]

[a] Maximum power consumption specified in the data sheet
[b] Transmit / receive
[c] Additionally requires to be supplied with 5 V
[d] Developed by Cape Peninsula University of Technology, distributed by AAC Clyde Space
[e] Also supports an input power range of 22 V to 34 V
[f] Preliminary data sheet
[g] The full name of the company is “Innovative Solutions In Space”

Table C.11: Selection of commercially available propulsion systems suitable for the TUBiX20 platform.

Device	Manufacturer	BOL mass[a] kg	Supply voltage V	Power consumption[b] W	Total impulse N s	Reference
BmP-220	Busek	0.5	3.3 and 12	3	175	[447]
BIT-3	Busek	2.9	28	80	unspecified	[448]
Cold gas MiPS	VACCO Industries	2.54	9 to 12.6	55	500	[449]
Comet-1000	Bradford Space	1.44	8 to 34	55	1 155	[450]
Comet-8000	Bradford Space	6.675	8 to 34	55	8 348	[450]
EPSS C1	NanoAvionics	1.2	3.3 and 12	8	650	[451]
Green MiPS	VACCO Industries	5	9.5 and 12.6	15	3 320	[452]
Hybrid MiPS	VACCO Industries	2.065	9 to 12.6	20	855	[453]
IFM Nano Thruster	ENPULSION	0.9	12 or 28	40	5 000	[454]
Micro 100	ENPULSION	3.2	28	100	50 000	[455]
IPS	VACCO Industries	14.7	12 and 28	50	12 000	[456]
MarCO MiPS	VACCO Industries	3.49	9 to 12.6	unspecified	755	[457]
MPS-120-1U	Aerojet Rocketdyne	1.48	6 to 8	11	775	[458]
MPS-120-2U	Aerojet Rocketdyne	2.38	6 to 8	11	2 000	[458]
MPS-130-1U	Aerojet Rocketdyne	1.66	12[c]	39	1 200	[459]
MPS-130-2U	Aerojet Rocketdyne	2.76	12[c]	39	3 360	[459]
NanoProp CGP3	GomSpace	0.300	5 and 12	2[d]	40	[460]
NanoProp 6U	GomSpace	0.9	5 and 12	2[d]	80	[461]
PM200	Hyperion Technologies[e]	1.41	5.0 and 12.0	12	850	[462]
Standard MiPS	VACCO Industries	0.957	9 to 12.6	12	489	[463]

[a] Maximum BOL mass specified in the data sheet
[b] Maximum power consumption specified in the data sheet
[c] Additional supply in the range of 6 V / 8 V required for the valves
[d] Given as average power consumption
[e] Developed by Dawn Aerospace, distributed by Hyperion Technologies